Niet-invasieve methoden voor ruimtelijke en kwantitatieve reconstructies van magnetische nanodeeltjes door middel van elektron-paramagnetische resonantie en magnetorelaxometrie

Non-Invasive Methods for Spatial and Quantitative Reconstructions of Magnetic Nanoparticles Using Electron Paramagnetic Resonance and Magnetorelaxometry

Annelies Coene

Promotoren: prof. dr. ir. L. Dupré, prof. dr. ir. G. Crevecoeur
Proefschrift ingediend tot het behalen van de graad van
Doctor in de ingenieurswetenschappen: biomedische ingenieurstechnieken

UNIVERSITEIT
GENT

Vakgroep Elektrische Energie, Metalen, Mechanische Constructies en Systemen
Voorzitter: prof. dr. ir. L. Dupré
Faculteit Ingenieurswetenschappen en Architectuur
Academiejaar 2016 - 2017

ISBN 978-94-6355-008-6
NUR 954, 981
Wettelijk depot: D/2017/10.500/43

Non-Invasive Methods for Spatial and Quantitative Reconstructions of Magnetic Nanoparticles Using Electron Paramagnetic Resonance and Magnetorelaxometry

Annelies Coene

Dissertation submitted to obtain the academic degree of
Doctor of Biomedical Engineering

Publicly defended at Ghent University on May 29, 2017

Supervisors:

Prof. dr. ir. Luc Dupré
Prof. dr. ir. Guillaume Crevecoeur
Electrical Energy Laboratory
Department of Electrical Energy, Metals, Mechanical Constructions and Systems
Faculty of Engineering and Architecture
Ghent University
Technologiepark 913
9052 Zwijnaarde, Belgium
http://eemmecs.ugent.be

Members of the examining board:

Prof. dr. ir. Patrick De Baets (chairman)	Ghent University, Belgium
Prof. dr. ir. Patrick Segers (secretary)	Ghent University, Belgium
Prof. dr. ir. Luc Dupré (supervisor)	Ghent University, Belgium
Prof. dr. ir. Guillaume Crevecoeur (co-supervisor)	Ghent University, Belgium
Prof. dr. ir. Tom Dhaene	Ghent University, Belgium
Univ.-prof. dr.-ing. Daniel Baumgarten	UMIT, Austria
Prof. dr. Stefaan Vandenberghe	Ghent University, Belgium
Dr. Uwe Steinhoff	Physikalisch-Technische Bundesanstalt, Germany

GHENT UNIVERSITY
FACULTY OF ENGINEERING AND ARCHITECTURE

Dankwoord
(Acknowledgments)

Nu mijn doctoraat stilletjes aan ten einde loopt, wordt het tijd om even terug te blikken op de voorbije 5.5 jaar. Voor mij was het alvast een geweldig avontuur, dat mij mee heeft gevormd tot de persoon wie ik ben vandaag. Onlosmakelijk met de start van mijn doctoraat kwam ook heel vlug het besef dat ik dit niet alleen kon doen. Het staat vast dat dit doctoraat hier niet voor jullie zou liggen zonder de hulp van verschillende mensen. Daarom, voordat jullie een poging ondernemen om dit doctoraat te doorploegen, wil ik deze mensen nog eens expliciet bedanken.

Eerst en vooral wil ik mijn promotoren, Luc en Guillaume, bedanken. Toen ik mijn thesis onder jullie begeleiding uitvoerde, voelde ik al meteen een goede klik. Ik was dan ook heel blij toen jullie mij de kans boden om een doctoraat te starten. Bedankt om mij de nodige onderzoeksvrijheid te gunnen, maar toch ook steeds beschikbaar te zijn voor vragen en advies. De vele discussies hebben van mij een kritischere onderzoeker gemaakt en mij heel wat inzichten bezorgd. Wanneer nodig, stelden jullie mij gerust of gaven jullie dat extra duwtje, zodat het terug wat sneller ging. Ik wil jullie ook bedanken voor het nalezen en polijsten van onze publicaties en teksten.

I would also like to thank the members of my Jury. Thank you for willing to be part of my Jury and for the time and effort spent on reading my dissertation. I appreciate the insightful comments that were raised and the nice discussion we had during the internal defense.

A big thank you goes out to my German colleagues. Thank you Uwe and Frank for inviting me for a scientific stay at the Physikalisch-Technische Bundesanstalt in Berlin. This stay has shown me the importance of collaborating with various experts in order to achieve significant progress in this multi-disciplinary field. Thank you for giving me the opportunity to perform sensitive measurements of magnetic nanoparticles and thank you Maik for your technical expertise and guidance during

these experiments. This experience made me understand the various experimental difficulties associated to the imaging of these particles. Furthermore, I enjoyed our many interesting discussions and the German culture. I appreciate the effort of taking me on many nice journeys after work and during the weekends.

Next, I should thank the CWO (Ghent University), FWO (Belgium) and the Physikalisch-Technische Bundesanstalt (Germany) for funding my mobility. This allowed me to broaden my scientific network and I am very grateful for this.

Beste collega's, ik hou vele leuke herinneringen aan jullie over, niet alleen op de werkvloer, maar ook ernaast. Ik denk bijvoorbeeld aan onze eigen versie van 'komen eten', onze spannende escape en de laser tag. Guillaume, Ben en Nele, ondertussen zitten we niet meer in hetzelfde bureau, maar ik denk nog vaak terug aan de gezellige momenten en de soms hilarische gesprekken. Bedankt ook om mijn muziekkennis wat uit te breiden en mijn muzieksmaak bij te schaven. Mijn huidige bureaugenoten, Jasper, Mariem, Arne, Matthias en Andries, moeten alvast niet onderdoen. Het is een plezier om elke dag te komen werken en ik vind het leuk dat iedereen, op zijn eigen manier, een noodzakelijk stukje vormt van onze 'awesome bureau'. Ik hoop dat ik nog vele jaren met jullie kan samenwerken. Heel erg bedankt om mij tijdens het schrijven van mijn doctoraat te steunen, mij koekjes en koffie te geven wanneer nodig, input voor interessante discussies te voorzien en ook voor de ontspanning te zorgen. Ingrid en Marilyn, bedankt voor het regelen van SAP en administratieperikelen, voor elke dag koffie te zetten (ik vermoed dat de koffie echt een grote bijdrage heeft aan dit doctoraat) en de leuke gesprekken tussendoor. Ingrid, ik waardeer het enorm dat je, zelfs nu je op pensioen bent, zoveel doet voor het labo. Bedankt ook voor je hulp op de receptie. Tony, Vincent en Stefaan: ik heb twee linkerhanden, dus ik ben jullie heel dankbaar voor de praktische ondersteuning. Nic, ik heb gelukkig niet al te veel computerproblemen gehad, maar als er iets van hardware aan het sukkelen was, was je er snel bij om het te fixen. De andere collega's: bedankt voor de leuke lunchpauzes, ik heb heel wat afgelachen. De pauzes vormden de ideale ontspanning tussen het harde werken door.

Een belangrijke plaats in dit dankwoord is ook weggelegd voor mijn vrienden en familie. Ik weet dat ik niet de makkelijkste persoon ben om mee af te spreken, zeker de laatste maanden, en dat onze drukke schema's ervoor gezorgd hebben dat we elkaar niet zoveel hebben gezien, maar ik apprecieer het echt dat jullie moeite blijven doen om mij uit 'mijn cocon' te halen. Onze uitjes, kooklessen, etentjes, ijsjes, sterrenkampen, film- en spelletjesavonden, cafédiscussies en dansfeestjes hebben zeker voor de nodige ontspanning

gezorgd tijdens mijn doctoraat.

Ik wil ook graag mijn schoongrootouders, -ouders en -broer bedanken om mij zo snel thuis te laten voelen en voor hun enthousiasme en interesse in mijn doctoraat. Een grote dankuwel gaat ook uit naar mijn grootouders die mij al van kleins af aan stimuleren en motiveren. Jullie trots maken is echt een grote motivatie voor mij! Charlotte, bedankt om mijn kleine (maar nu toch ook al grote) zus te zijn. Niemand begrijpt onze 'zusjeshumor', maar je slaagt er wel altijd in om een glimlach op mijn gezicht te toveren. Bedankt ook voor het nalezen van de Nederlandstalige teksten in mijn doctoraat, voor je stijladvies en om mij volop te motiveren en voor mij te duimen. Lieve mama en papa, zonder jullie was niets van dit alles waar geweest. Ik kan jullie niet genoeg bedanken voor jullie onvoorwaardelijke steun, het vele geduld en het vertrouwen. Jullie stonden altijd met raad en daad klaar en hebben mij geleerd dat je alles kan bereiken, zolang je maar je best doet. Ik apprecieer ook de vele kansen en opportuniteiten die jullie mij gegeven hebben, zoals de mogelijkheid om naar de sterrenwacht te gaan, op verre reizen te vertrekken en natuurlijk ook het aanvangen van mijn studies. Bedankt!

Als er één iemand is die toch wel alle aspecten van dit doctoraatsavontuur van dichtbij heeft mogen beleven, dan is het mijn man. Jonathan, jij bent mijn dagelijkse steun, mijn toeverlaat en mijn beste vriend. Jouw onuitputtelijke energie motiveert mij om te blijven doorgaan. Bedankt om in mij te geloven, mij door alle 'highs en lows' te steunen, mij te laten doorwerken tot in de vroege uurtjes en mij een luisterend oor te bieden. Zeker de laatste maanden heb ik het je niet makkelijk gemaakt. Ik wil je nadrukkelijk bedanken voor het nalezen van mijn doctoraat en je inzichtelijke opmerkingen en vragen. Ik ben ook blij dat we de stap genomen hebben om samen te werken, we vormen ook op dit vlak een prachtig team! Ik kijk al uit naar wat de toekomst brengt!

Annelies Coene, Mei 2017

Contents

Samenvatting

Magnetische nanodeeltjes vertonen interessante eigenschappen die hen zeer geschikt maken voor een verscheidenheid aan biomedische toepassingen. Dankzij hun typische afmetingen in de orde van enkele nanometer tot honderden nanometer, laten zij toe om rechtstreeks te communiceren met biologische entiteiten zoals genen en cellen, en kunnen ze vrijwel elk gebied in het menselijk lichaam bereiken. Door het feit dat de nanodeeltjes magnetisch zijn, kunnen ze ook vanop afstand bestuurd worden met behulp van magnetische gradiëntvelden. Dit laat bovendien ook toe om de deeltjes vanop afstand te registeren met gevoelige meetsensoren. Verder kunnen de deeltjes in resonantie gebracht worden door hen bloot te stellen aan een tijdsvariërend magnetisch veld met een specifieke frequentie. Op deze manier zetten de deeltjes de energie van het magnetisch veld om in warmte en gedragen ze zich als warmtebronnen die de omgevingstemperatuur van de deeltjes gevoelig kunnen verhogen.

Bijgevolg zijn er de laatste jaren heel wat toepassingen ontwikkeld die werken met nanodeeltjes en die baat hebben van voorgenoemde eigenschappen. Een belangrijke applicatie bijvoorbeeld, is magnetische hyperthermie. In deze toepassing wordt het resonante gedrag van de deeltjes gebruikt om kwaadaardige weefsels, zoals tumoren, op te warmen. Dit heeft als gevolg dat er onherstelbare schade aan deze cellen wordt veroorzaakt. Een andere toepassing waarin de nanodeeltjes nuttig zijn, is doelgerichte afgifte van geneesmiddelen. In dit geval worden de nanodeeltjes gebruikt als magnetische omhulsels waarin medicijnen vervat zitten. De deeltjes kunnen dan met behulp van gradiëntvelden naar de gewenste plaats begeleid worden, waar ze dan de medicijnen afleveren. Niettegenstaande het feit dat dankzij de magnetische nanodeeltjes verschillende diagnose- en therapietoepassingen gerealiseerd kunnen worden, zijn er slechts enkele in de klinische praktijk in gebruik. Een van de belangrijkste redenen hiervoor is het gebrek aan kwantitatieve informatie over de ruimtelijk verspreiding van de magnetische deeltjes. Heel wat toepassingen hebben deze kennis betreffende de locatie en hoeveelheid deeltjes nodig, zodat ze in staat zijn om te bepalen of de deeltjes aanwezig zijn op de gewenste locatie, en in de juiste hoeveelheden.

Dit zorgt ervoor dat de toepassingen steeds veilig zijn voor de patiënt en dat ze ook efficiënt werken. Gevestigde medische beeldvormingsmodaliteiten, zoals MRI en CT, verschaffen enkel kwalitatieve beelden van de magnetische nanodeeltjes. Deze beelden hebben voor de meeste toepassingen een onvoldoende nauwkeurigheid. Bovendien is er ook een gebrek aan meetmethoden voor klinisch relevante hoeveelheden aan nanodeeltjes. Daarom wordt dit probleem, waarin de spatiale distributie van magnetische nanodeeltjes op een kwantitatieve en niet-invasieve wijze wordt bepaald, door officiële instanties als een van de belangrijkste uitdagingen in de nanogeneeskunde gezien.

Deze problemen kunnen verholpen worden door gebruik te maken van magnetische veldmetingen. Dergelijke metingen maken het mogelijk om de nanodeeltjes op een rechtstreekse, gevoelige en niet-invasieve manier waar te nemen. Elke meting wordt gekarakteriseerd door het aanleggen van specifieke magnetische velden en het opmeten van de magnetische respons van de deeltjes op deze velden. De technieken laten toe om uit hun metingen de spatiale verdeling van de magnetische nanodeeltjes af te leiden door een *invers probleem* op te lossen. In een invers probleem worden bepaalde externe metingen van een gegeven systeem gelinkt aan zijn eigenschappen. In dit specifieke geval wordt een verband gelegd tussen de magnetische respons van de magnetische nanodeeltjes en hun ruimtelijke verdeling. Om dit verband tussen de metingen en de ruimtelijke partikeldistributie te vinden, is een *voorwaarts model* nodig. Dit model laat toe om metingen te simuleren, vertrekkende van een zekere ruimtelijke partikelverdeling. De ruimtelijke verdeling van de magnetische nanodeeltjes kan dan gereconstrueerd worden door de verschillen tussen de gesimuleerde metingen en de echte metingen te minimaliseren. In het algemeen hebben deze technieken last van onnauwkeurigheden in de reconstructie, die hun oorsprong vinden in de slecht-gesteldheid van het inverse probleem, meetruis, en in modelleringsfouten in het voorwaartse model. Daarom wordt in dit proefschrift onderzoek verricht naar niet-invasieve ruimtelijke reconstructiemethoden. Dit houdt in dat de meettechnieken geoptimaliseerd worden, de stabiliteit van het inverse probleem verbeterd wordt en nieuwe voorwaartse modellen en inverse reconstructieprocedures ontwikkeld worden. Meer specifiek concentreren we ons op twee veelbelovende beeldvormingsmethoden voor de magnetische nanodeeltjes, die gebaseerd zijn op elektron-paramagnetische resonantie (EPR) en magnetorelaxometrie (MRX). Het einddoel van dit werk is om de partikeldistributie kwantitatief in beeld te brengen met behulp van EPR en MRX. Dit heeft als resultaat dat eerdergenoemde biomedische toepassingen, die gebruik maken van magnetische nanodeeltjes, dichter bij hun klinische implementatie komen te staan.

In een EPR-experiment wordt een sample, dat de nanodeeltjes bevat, in een homogeen magnetisch veld geplaatst en bestraald door een radiofrequente elektromagnetische golf. De dynamische respons van de deeltjes op deze velden kan opgemeten worden met behulp van een meetspoel. Deze techniek laat toe om een zeer gevoelig signaal in de meetspoel te induceren, dat lineair afhankelijk is van de partikelhoeveelheid. Initieel liet de EPR-techniek enkel maar toe om de totale hoeveelheid nanodeeltjes te bepalen, zonder daarbij enige informatie omtrent hun distributie te verstrekken. Daarom houdt het eerste onderzoeksonderwerp van dit doctoraat een ontwikkeling in van een voorwaarts model en inverse reconstructieprocedure. Zo kan een spatiale partikelverdeling gelinkt worden aan de EPR-metingen. Om dit te verwezenlijken was het nodig om meetsignalen in de spoel te genereren die informatie bevatten over de partikellocatie. Aangezien deze informatie kan gehaald worden uit de metingen van het sample op verschillende plaatsen in de opstelling, werd het EPR-experiment uitgebreid, waarbij het sample vanaf nu verplaatst werd en voor elke nieuwe positie een EPR-meting werd uitgevoerd. Dit gedrag werd dan in een voorwaarts model geïncludeerd, zodat op een niet-invasieve manier de kwantitatieve partikeldistributie in het sample bepaald kon worden. Het tweede onderzoeksonderwerp omvatte een sensitiviteitsanalyse, waarin foutmodellen en systeemmodellen ontwikkeld werden en hun impact op de reconstructie onderzocht werd. Zo was het mogelijk om de sterktes en zwaktes van deze methode te bepalen. Op basis van deze analyse konden dan de parameters van de opstelling, de inverse reconstructieprocedure en de posities van het sample geoptimaliseerd worden, zodat de reconstructie accurater werd en het inverse probleem een grotere stabiliteit vertoonde. Door bovendien het sample bloot te stellen aan spatiaal veranderlijke magnetische velden in plaats van een homogeen veld, konden specifieke sub-volumes van het sample magnetisch geactiveerd worden. Daarna, in het laatste onderzoeksonderwerp, werd onderzocht welke van deze velden de grootste informatiehoeveelheid bevatte over de locatie van de deeltjes. Door deze veldconfiguraties dan te gebruiken in de EPR-metingen, was het mogelijk om de meetmethode significant te versnellen en daarbovenop een grote vooruitgang in reconstructienauwkeurigheid en in stabiliteit van het inverse probleem te bekomen.

In tegenstelling tot de EPR-beeldvormingsmethode werd de MRX-beeldvormingsmethode in het verleden wel al succesvol toegepast voor de reconstructie van magnetische partikeldistributies. In een MRX-experiment wordt het sample met de magnetische nanodeeltjes in een magnetisch veld geplaatst. Vervolgens wordt dit magnetisch veld plots afgeschakeld en wordt de vertraagde respons van de deeltjes op het plotselinge afschakelen met behulp van gevoelige meetsensoren opgemeten. Deze metingen kunnen de

partikeldistributie reconstrueren door het oplossen van een invers probleem. In dit werk worden specifiek MRX-beeldvormingssystemen bestudeerd die bestaan uit meerdere spoelen. Gelijkaardig als in de EPR-meetmethode zorgt het gebruik van spatiaal veranderlijke magnetische velden, gegenereerd door de specifieke activatie van deze spoelen, voor verbeterde reconstructies van de partikelverdeling. Eerst werd er onderzocht in welke sequenties de spoelen dienden geactiveerd te worden om betere reconstructies te verkrijgen. Hiervoor werd een iteratieve targetprocedure bedacht die op basis van *a priori* informatie over de partikeldistributie de spoelen doelgericht activeerde. Deze spoelactivaties werden dan in een volgende MRX-meting gebruikt, waarvan de nieuwe reconstructie opnieuw als invoer van deze targetprocedure gebruikt kon worden. Op deze manier kon de reconstructie iteratief verfijnd worden, wat resulteerde in zeer accurate beelden van de magnetische partikeldistributie. Een tweede onderzoeksonderwerp met de MRX-beeldvormingsmethode omvatte de ontwikkeling van een kwantitatieve maatstaf die toeliet om verschillende MRX-beeldvormingsmodellen en systemen met elkaar te vergelijken. Dit werd gerealiseerd door *kwantitatieve* MRX-modellen te introduceren die gebruikmaken van statistische parameters. Vervolgens kon er, onafhankelijk van de partikeldistributie, bepaald worden welk beeldvormingsmodel en -opstelling het meest geschikt waren voor de beeldvormingsprocedure op basis van de afmetingen van het sample en de gewenste resolutie van de reconstructie. Het laatste onderzoeksonderwerp ging de mogelijkheid na om meerdere types van nanodeeltjes gelijktijdig te reconstrueren. Hoewel de MRX-beeldvormingsmethode toelaat om een brede waaier aan partikelsystemen te visualiseren, kon altijd maar één partikeltype gebruikt worden in eenzelfde MRX-experiment. Daarom hebben we een voorwaarts model en inverse reconstructieprocedure ontwikkeld, genaamd het *MRX multi-color imaging model*, zodat de lokalisatie en kwantificatie van meerdere partikeltypes gelijktijdig kan gebeuren. In de finale reconstructie wordt dan elk partikeltype geassocieerd met een specifieke kleur. De intensiteit van deze kleur correspondeert dan met de hoeveelheid deeltjes van dit type. Deze drie onderzoeksonderwerpen hebben de performantie van de MRX-beeldvormingsmethode significant verbeterd en zo wordt het mogelijk om in een klinische omgeving, met behulp van deze ontwikkelde techniek, verschillende magnetische partikelverdelingen succesvol te reconstrueren.

Tot slot werden in dit proefschrift niet-invasieve ruimtelijke reconstructiemethoden ontwikkeld die respectievelijk toegepast werden op EPR en MRX. Dit resulteerde in de uitbreiding van EPR van een kwantitatieve detectiemethode voor magnetische nanodeeltjes naar een techniek die toelaat om de ruimtelijke partikeldistributie op een niet-invasieve, snelle en kwantitatieve manier te bepalen. Ook de MRX-beeldvormingsmethode werd

dichter bij zijn klinische realisatie gebracht dankzij de ontwikkeling van het MRX multi-color model, de significante verbeteringen in reconstructie-nauwkeurigheid van de distributies, en het ontwerpen van een kwantitatieve maatstaf voor het vinden van de meest geschikte beeldvormingsmethode voor een gegeven geometrie. De ontwikkelde methoden dragen bij tot de algemene vooruitgang van toepassingen die gebruik maken van magnetische nanodeeltjes. Zo bereiken magnetische hyperthermie en doelgerichte geneesmiddelenafgifte een verbeterde prestatie en veiligheid voor de patiënt dankzij de ontwikkelde technieken in dit proefschrift.

Summary

Magnetic nanoparticles exhibit interesting properties that make them suitable for a variety of biomedical applications. For instance, their small size in the nanometer region allows them to interact directly with biological entities such as cells and genes, and to reach virtually every region in the human body. Additionally, the nanoparticles are magnetic which means that they can be controlled remotely using magnetic field gradients and be measured non-invasively using sensitive sensors. Furthermore, the particles resonate at certain magnetic field frequencies at which they transfer magnetic field energy into heat and act as heat sources to increase the temperature of their surroundings.

In recent years, many applications have emerged that benefit from aforementioned properties. For example, in magnetic hyperthermia, the particles' resonant behavior is exploited with the aim to heat up malignant tissues, such as tumors, in order to cause irreparable damage to their cells. Another application is magnetic drug targeting in which the nanoparticles act as magnetic carriers for therapeutics and are magnetically guided towards the desired location where the therapeutics are released. Despite the fact that many diagnostic and therapeutic applications can be realized with the help of magnetic nanoparticles, not many of these applications have been implemented into clinical practice. One of the main reasons thereof, is the lack of quantitative information on the particles' spatial biodistribution. Indeed, many applications require accurate knowledge on particle location and amount, since they need the particles to be at the target location in the right amounts. This way, safe and efficient operation can be guaranteed. Clinically established imaging techniques such as magnetic resonance imaging (MRI) and computed tomography (CT) only provide qualitative images of the magnetic nanoparticles, which do not meet the accuracy requirements of most applications. Moreover, there exists a gap in measurement techniques for the detection of particles at clinically relevant concentrations. Therefore, the problem of determining the spatial distribution of the magnetic nanoparticles in a quantitative and non-invasive way, is seen by official institutions as one

of the key challenges in nanomedicine.

Fortunately, magnetic field measurements allow the direct, sensitive and non-invasive detection of the particles. Each technique is characterized by the application of specific magnetic fields and measures the magnetic response of the particles to these fields. These techniques allow to find the spatial nanoparticle distribution from their measurements by solving an *inverse problem*. An inverse problem relates certain external measurements of a given system to its properties. In the specific case of this dissertation, the particles' responses are associated to their spatial distribution. In order to find the relation between the measurements and particle distribution a *forward model* is required. This model simulates the measurements for a given particle distribution. By minimizing the differences between the model's solution and the measurements the distribution can be recovered. In general, these techniques suffer from inaccuracies in the reconstructed particle images originating from the ill-posedness of the inverse problem, measurement noise and modeling errors in the forward model. Therefore, in this dissertation, research is conducted on non-invasive reconstruction methods. This includes optimizing the measurement techniques, improving the stability of the inverse problem and developing new forward models and inverse reconstruction procedures. Specifically, we focus on two promising particle imaging techniques, based on electron paramagnetic resonance (EPR) and magnetorelaxometry (MRX). The final goal of this work is to enable quantitative reconstructions of the spatial nanoparticle distribution using EPR and MRX imaging. In this way, the various applications making use of magnetic nanoparticles can be brought closer to clinical implementation.

In EPR, a sample containing magnetic nanoparticles is positioned in a homogeneous magnetic field and additionally excited by a radio frequency wave. The dynamic response of the particles to these magnetic fields can be measured using a pickup coil. This way a very sensitive measurement signal is induced, which depends linearly on the particle amount. Initially, the EPR imaging technique could only recover the total amount of particles present in a sample and did not provide any information about their spatial distribution. Therefore, the first research topic of this thesis was to develop a forward model and inverse reconstruction procedure which related particle distribution properties to the EPR measurements. To realize this, measurement data that included information on particle location, had to be induced in the pickup coil. As movement of the sample encompasses this information, the EPR measurement procedure was extended to perform measurements for various positions of the sample. This behavior could be incorporated in a forward model which then allowed to *non-invasively* determine the

quantitative MNP distribution inside the sample. The second research topic comprised a sensitivity analysis, in which error and setup models were developed and their impact on the reconstructed particle distribution was investigated. Subsequently, the strengths and weaknesses of the method could be pinpointed, enabling the optimization of setup parameters, inverse reconstruction procedures and sample movement. Hence, reconstruction errors could be reduced and the stability of the inverse problem improved. By additionally exposing the sample to spatially varying magnetic fields instead of a homogeneous field, specific sub-regions of the sample could be magnetically activated. Then, in a final research topic, it was investigated which spatial magnetic field configurations contained the largest amounts of information on the particle distribution. By using these magnetic field configurations in the measurement procedure, a significant speed up of the measurement technique was achieved, as well as a tremendous increase in its reconstruction accuracy and in the stability of its inverse problem.

Contrary to the EPR imaging technique, MRX imaging was already successfully employed in the reconstruction of magnetic nanoparticle distributions. In a MRX imaging experiment, the sample is placed in a magnetic field and the delayed response of the magnetic nanoparticles to a sudden shutdown of this magnetic field is measured using sensitive sensors. The sensors' measurements can be related to properties of the spatial particle distribution by solving an inverse problem. This work focuses on MRX imaging setups that use an array of coils for generating the magnetic field. Similarly as in the EPR approach, the application of spatially varying magnetic fields by the activation of specific coil sequences, results in improved reconstructions of the particle distribution. First it was investigated in which sequences the coils should be activated in order to improve the accuracy of the reconstructions. An iterative targeting procedure was devised based on *a priori* information on the particle distribution. Taking into account this preliminary information, sub-regions of the sample were magnetized in the subsequent MRX measurement using specific activations of the coil array. The obtained particle reconstruction could then be used again as input to the targeting procedure. This way the particle distribution could be iteratively refined resulting in accurate images of the particle distribution. A second research topic in the MRX-based reconstruction of MNP distributions, concerned the development of a quantitative measure in MRX imaging which allowed to compare various MRX imaging models and setups. This was achieved by introducing *quantitative* MRX models which make use of statistical parameters. Hence, it could be determined which imaging model and setup were best suited for the imaging procedure, given sample geometry and desired reconstruction resolution, independent of particle distribution. The final research topic investigated the

imaging of different particle types simultaneously. Although MRX allows to image a broad collection of particle types, in each experiment only a single particle type could be used. Therefore, we developed a forward model and reconstruction procedure, referred to as the *MRX multi-color imaging model*, for the localization and quantification of multiple particle types simultaneously. In the final reconstruction each particle type is associated with a specific color and its intensity represents the reconstructed amount of particles for the given type. These three research topics have significantly improved the MRX imaging technique, which opens the pathway to clinical examinations in which this technique could be successfully employed to reconstruct various magnetic nanoparticle distributions.

To conclude, in this dissertation non-invasive spatial reconstruction methods were developed which were applied to EPR and MRX respectively. This resulted in the extension of EPR from a quantitative particle detection technique, to a technique capable of recovering the three dimensional magnetic nanoparticle distribution in a quantitative, fast and non-invasive way. Similarly, the MRX imaging technique is now closer to clinical realization by the accomplishment of multi-color imaging, the significant improvement in particle reconstruction accuracy, and by the development of a quantitative measure for finding the most suitable imaging procedure for a given sample geometry. The developed methods contributed also to the general advancement of the magnetic nanoparticle field, as applications such as magnetic hyperthermia and drug targeting can reach an increased efficiency and patient safety, because of the improvements made to the MNP imaging techniques in this dissertation.

List of abbreviations

1D	One Dimensional
2D	Two Dimensional
3D	Three Dimensional
ACS	AC Susceptibility
ASI	AC Susceptibility Imaging
CC	Correlation Coefficient
CT	Computed Tomography
CW	Continuous Wave
DLS	Dynamic Light scattering
EEG	ElectroEncephaloGraphy
EMA	European Medicines Agency
EPR	Electron Paramagnetic Resonance
FDA	Food and Drug Administration
FFP	Field-Free Point
HCS	High Concentration Selection
LRT	Linear Response Theory
MARIA	MAgnetic Relaxation ImmunoAssay
MEG	MagnetoEncephaloGraphy
MI	Mutual Information
MM	MagnetoMotive
MNE	Minimum Norm Estimates
MNP	Magnetic NanoParticles
MPI	Magnetic Particle Imaging
MPS	Magnetic Particle Spectroscopy
MRI	Magnetic Resonance Imaging
MRX	MagnetoRelaXometry
MSM	Moment Superposition Model
NMR	Nuclear Magnetic Resonance
NNLS	Non-Negative Least Squares
NP	NanoParticles

PE	Positioning Error
PET	Positron Emission Tomography
PSF	Point Spread Function
PTB	Physikalisch-Technische Bundesanstalt
QSM	Quantitative Susceptibility Mapping
RD	Relative Deviation
RF	Radio Frequency
SAR	Specific Absorption Rate
SLP	Specific Loss Power
SMI	Susceptibility Magnitude Imaging
SNR	Signal-to-Noise Ratio
SSR	Spatial Separation Ratio
SVD	Singular Value Decomposition
SVT	Sub-Volume Targeting
TEM	Transmission Electron Microscopy
US	UltraSound

List of symbols

Mathematical notations and operators

$\mathbf{A}^T$	transpose of matrix $\mathbf{A}$
$\mathbf{A}(i,:)$	i-th row of $\mathbf{A}$
$\mathbf{A}(:,j)$	j-th column of $\mathbf{A}$
$\mathbf{a} \cdot \mathbf{b}$	dot product of $\mathbf{a}$ and $\mathbf{b}$
$\|\mathbf{a}\|$	L2-norm of $\mathbf{a}$
$\frac{dR(n)}{dn}$	derivative of $R(n)$ to n

Greek letters

α	position shift
α_0	weighting parameter for HCS
α_1	weighting parameter for HCS
β	condition number
γ	gyromagnetic constant
$\mathbf{\Gamma}$	Tikhonov matrix
δ	amount of bound MNP in total MRX signal
$\boldsymbol{\delta}_\lambda$	relative contribution of particle type λ
$\zeta(B)$	weighting factor
η	viscosity of the liquid surrounding the particle
$\boldsymbol{\theta}$	θ axis
Θ	number of rotations of the sample
$\kappa(t)$	function describing decay of MRX signal
$\Delta\kappa_{t_1,t_2}$	decay of MRX signal between time points t_1 and t_2
$\Delta\kappa_\lambda(t_1,t_2)$	$\Delta\kappa_{t_1,t_2}$ for MNP type λ

λ	particle type
Λ	total number of particle types
μ	average deviation
μ_0	permeability of free space
μ_c	mean V_c
μ_h	mean V_h
ν	HCS selection parameter
$\nu(z)$	weighted HCS selection parameter
ξ	argument of Langevin function: $\frac{\mu_0 m H_{sat}}{k_B T}$
ρ	mass of iron divided by the core volume
ρ_c	mass density of the magnetic material
σ	standard deviation
σ_{avg}	average eigenvalue
σ_c	standard deviation of V_c
σ_h	standard deviation of V_h
σ_{max}	maximal eigenvalue
σ_{min}	minimal eigenvalue
σ_r	regularization parameter
Σ	matrix containing eigenvalues
τ_0	inverse of the attempt frequency
τ_B	Brownian relaxation time
τ_{eff}	effective relaxation time
τ_N	Néel relaxation time
ϕ	phase difference
χ	magnetic susceptibility
χ'	real part of the complex magnetic susceptibility
χ''	imaginary part of the complex magnetic susceptibility
χ_0	quasi-static magnetic susceptibility
Ψ	total number of histogram intervals
ω_0	Larmor frequency
Ω	region in which $R(n)$ is defined

Latin letters

a	coil activation a
$\mathbf{A}$	interaction matrix
B_s	measured induction in sensor s
B_{sv}	measured induction in sensor s originating from $\mathbf{m}_v$
ΔB	relaxation amplitude
$\mathbf{B}$	magnetic induction
$\mathbf{B}_0$	magnetic induction from Helmholtz coil pair
$\mathbf{B}_1$	magnetic induction from excitation coil
$\mathbf{B}_{1\mathrm{att}}$	feed-through of $\mathbf{B}_1$
$\mathbf{B}_\mathrm{b}$	MRX signal of immobilized MNP
$\mathbf{B}_{\mathrm{MRXref}_\lambda}(t_\mathrm{window})$	MRX reference measurement of particle type λ
$\mathbf{B}_\mathrm{ub}$	MRX signal of free MNP in solution
c_calib	calibration sample
$c_{\mathrm{calib}_\lambda}$	calibration sample for particle type λ
c^*_max	maximum value of $\mathbf{c}^*$
c_v	MNP amount in voxel v
$\mathbf{c}$	unknown MNP distribution
$\mathbf{c}^*$	reconstructed MNP distribution
$\mathbf{c}_\mathrm{act}$	actual MNP distribution
$\mathbf{c}_\lambda$	$\mathbf{c}$ of particle type λ
$\mathcal{C}$	conversion factor
d_c	core diameter
d_h	hydrodynamic diameter
$\mathbf{D}_q$	source normalization matrix
ΔE	required energy for moment reorientation
f	frequency of alternating magnetic field
$\mathbf{F}_\mathrm{D}$	drag force
$\mathbf{F}_\mathrm{M}$	magnetic force
G	gradient of the magnetic field
H_K	magnetic anisotropy field amplitude
$H(\mathbf{X})$	entropy of $\mathbf{X}$
$\mathbf{H}$	magnetic field
$\mathbf{H}_\mathrm{mag}$	applied external magnetic field in MRX
$\mathbf{H}_v$	magnetic field at voxel v

i	imaginary unit: $\sqrt{-1}$
$\mathbf{I}$	identity matrix
$\mathbf{I}_{\text{coil}}$	activation currents in the coils for N_a activations
$\mathbf{I}_{\text{coil}_a}$	activation currents in the coils for a-th activation
J	total number of time points
k_{B}	Boltzmann constant
K	anisotropy constant
L_{sv}	sensitivity coefficient of the forward model
$\mathbf{L}$	sensitivity matrix
$\mathbf{L}_\lambda$	$\mathbf{L}$ for particle type λ
$\mathbf{L}_q$	$\mathbf{L}$ for coil q
$\mathbf{L}_{\text{type}}$	$\mathbf{L}$ of certain imaging technique
$\mathcal{L}(\xi)$	Langevin function
$\mathbf{m}$	magnetic moment of a single-domain MNP
$\mathbf{m}_v$	magnetic moment of voxel v
$\Delta\mathbf{m}_v$	change in $\mathbf{m}_v$ between two time points
$M(t)$	time-dependent magnetization
M_0	initial magnetization amplitude
M_{r}	remanent magnetization
M_{sat}	saturation magnetization
$\mathbf{M}$	magnetization
$\mathbf{M}_v$	magnetization of voxel v
$\mathbf{M}_y$	magnetization along $\mathbf{y}$ direction
n	sample position number
n_v	position of voxel v
$\mathbf{n}$	noise vector
$\mathbf{n}_{\text{att}}$	attenuated $\mathbf{n}$
N	total number of sample positions
N_a	number of spatially varying magnetic fields
N_{calib}	total number of calibration positions
ΔN	distance between consecutive positions of the sample
ΔN_{calib}	ΔN of the calibration sample
$\mathbf{N}_q$	sensor normalization matrix
P_{noise}	average noise power
P_{sig}	average noise-free signal power

$P(V_\mathrm{c})$	distribution function of V_c
$P(V_\mathrm{c}, V_\mathrm{h})$	distribution function of V_c and V_h
$P(x_\mathrm{rv})$	probability of $\mathbf{X} = x_\mathrm{rv}$
$P(x_\mathrm{rv}, y_\mathrm{rv})$	probability of $\mathbf{X} = x_\mathrm{rv}$ and $\mathbf{Y} = y_\mathrm{rv}$
Q	number of coils
r	eigenvalue cut-off
$\mathbf{r}_q$	position coil q
$\mathbf{r}_s$	position sensor s
$\mathbf{r}_v$	position voxel v
R	number of response values
$R(n)$	system response function
$R(n, B)$	system response function for heterogeneous magnetic fields
s	sensor number
S	total number of sensors
S_{f_n}	simulated signal from position n
S_{f_s}	simulated signal in sensor s
$\mathbf{S}_\mathrm{f}$	solution of the forward model
$\mathbf{S}_\mathrm{m}$	actual measurement values
$\mathbf{S}_{\mathrm{m}_\mathrm{sim}}$	simulated measurement values
$\mathbf{S}_\mathrm{p}$	spatial sensitivity
t	time
$t_{1/e}$	relaxation time
t_c	characteristic time
t_delay	required time between shut-down of $\mathbf{H}_{mag}$ and start of $M(t)$
t_end	end of t_window
t_mag	duration of $\mathbf{H}_{mag}$
t_meas	measurement time of $M(t)$
t_start	start of t_window
t_window	time window
T	temperature
T_1	longitudinal relaxation
T_2	transverse relaxation
$\mathbf{T}(\mathbf{L})$	transformed $\mathbf{L}$
$\mathbf{U}$	matrix with left-singular vectors

v	voxel number
$\Delta\mathbf{v}$	difference in speed between the particle and fluid
V	total number of voxels
V_c	magnetic core volume
V_h	hydrodynamic volume or volume of a MNP cluster
V_v	volume voxel v
$\mathbf{V}$	matrix with right-singular vectors
$\mathbf{V}_\mathrm{pickup}$	measurement signal pickup coil
$\mathbf{V}_\mathrm{pickup+}$	pickup signal at maximum field amplitude
$\mathbf{V}_\mathrm{pickup-}$	pickup signal at minimal field amplitude
$\mathbf{V}_\mathrm{sub}$	subtracted measurement signal
$\mathbf{w}$	dual vector in NNLS
$\mathbf{W}_q$	weighting matrix
$\mathbf{x}$	x axis
$\mathbf{xy}$	$x = y$ axis
$\mathbf{X}$	random variable
$\mathbf{y}$	y axis
z_p	distance to the main sensors' plane
$\mathbf{z}$	z axis
Z	number of translations of the sample

List of publications

Articles in international SCI journals

1. A. Coene, G. Crevecoeur, and L. Dupré, ”Adaptive control of excitation coil arrays for targeted magnetic nanoparticle reconstruction using magnetorelaxometry”, *IEEE Transactions on Magnetics*, 48(11):2842-2845, 2012.

2. A. Coene, G. Crevecoeur, L. Dupré, and P. Vaes, ”Quantitative Estimation of Magnetic Nanoparticle Distributions in One Dimension Using Low-frequency Continuous Wave Electron Paramagnetic Resonance”, *Journal of Physics D: Applied Physics*, 46(24):245002, 2013.

3. M. Liebl, U. Steinhoff, F. Wiekhorst, A. Coene, J. Haueisen, and L. Trahms, ”Quantitative Reconstruction of a Magnetic Nanoparticle Distribution Using a Non-negativity Constraint”, *Biomedical Engineering/biomedizinische Technik*, 58(1), 2013.

4. A. Coene, G. Crevecoeur, M. Liebl, F. Wiekhorst, L. Dupré, and U. Steinhoff, ”Uncertainty of Reconstructions of Spatially Distributed Magnetic Nanoparticles Under Realistic Noise Conditions”, *Journal of Applied Physics*, 115(17):17B509, 2014.

5. J. Leliaert, A. Coene, G. Crevecoeur, A. Vansteenkiste, D. Eberbeck, F. Wiekhorst, B. Van Waeyenberge, and L. Dupré, ”Regarding the Néel Relaxation Time Constant in Magnetorelaxometry”, *Journal of Applied Physics*, 116(16):163914, 2014.

6. A. Coene, G. Crevecoeur, and L. Dupré, ”Magnetic Nanoparticle Imaging Using Multiple Electron Paramagnetic Resonance Activation Sequences”, *Journal of Applied Physics*, 117(17):17D105, 2015.

7. J. Leliaert, A. Vansteenkiste, A. Coene, L. Dupré, and B. Van Waeyenberge, ”Vinamax: a Macrospin Simulation Tool for Magnetic Nanoparticles”,

Medical & Biological Engineering & Computing, 53(4):309-317, 2015.

8. A. Coene, G. Crevecoeur, and L. Dupré, "Robustness Assessment of 1-D Electron Paramagnetic Resonance for Improved Magnetic Nanoparticle Reconstructions", *IEEE Transactions on Biomedical Engineering*, 62(6):1635-1643, 2015.

9. J. Leliaert, B. Van de Wiele, J. Vandermeulen, A. Coene, A. Vansteenkiste, L. Laurson, G. Durin, B. Van Waeyenberge, and L. Dupré, "Thermal Effects on Transverse Domain Wall Dynamics in Magnetic Nanowires", *Applied Physics Letters*, 106(20):202401, 2015.

10. A. Coene, G. Crevecoeur, J. Leliaert, and L. Dupré, "Toward 2D and 3D Imaging of Magnetic Nanoparticles Using EPR Measurements", *Medical Physics*, 42(9):5007-5014, 2015.

11. A. Coene, J. Leliaert, L. Dupré, and G. Crevecoeur, "Quantitative Model Selection for Enhanced Magnetic Nanoparticle Imaging in Magnetorelaxometry", *Medical Physics*, 42(12):6853-6862, 2015.

12. J. Leliaert, A. Coene, M. Liebl, D. Eberbeck, U. Steinhoff, F. Wiekhorst, B. Fischer, L. Dupré, and B. Van Waeyenberge, "Thermal Magnetic Noise Spectra of Nanoparticle Ensembles", *Applied Physics Letters*, 107(22):222401, 2015.

13. M. Harabech, J. Leliaert, A. Coene, G. Crevecoeur, D. Van Roost, and L. Dupré, "The Effect of the Magnetic Nanoparticles Size Dependence of the Relaxation Time Constant on the Specific Loss Power of Magnetic Nanoparticle Hyperthermia", *Journal of Magnetism and Magnetic Materials*, 426(22):206-210, 2017.

14. J. Leliaert, D. Eberbeck, M. Liebl, A. Coene, U. Steinhoff, F. Wiekhorst, B. Van Waeyenberge, and L. Dupré, "The Complementarity and Similarity of Magnetorelaxometry and Thermal Magnetic Noise Spectroscopy for Magnetic Nanoparticle Characterization", *Journal of Physics D: Applied Physics*, 50(8):085004, 2017.

15. A. Coene, J. Leliaert, G. Crevecoeur, and L. Dupré, "Sensor Fusion of Electron Paramagnetic Resonance and Magnetorelaxometry Data for Quantitative Magnetic Nanoparticle Imaging", *Journal of Physics D: Applied Physics*, 50(8):085008, 2017.

16. A. Coene, J. Leliaert, M. Liebl, N. Loewa, U. Steinhoff, G. Crevecoeur, L. Dupré and F. Wiekhorst, "Multi-Color Magnetic Nanoparticle Imaging Using Magnetorelaxometry", *Physics in Medicine and Biology*, 62(8):3139-3157, 2017.

17. J. Leliaert, D. Schmidt, O. Posth, M. Liebl, D. Eberbeck, A. Coene, U. Steinhoff, F. Wiekhorst, B. Van Waeyenberge and L. Dupré, "Interpreting the magnetorelaxometry signal of suspended magnetic nanoparticles with Kaczmarz' algorithm", *Journal of Physics D: Applied Physics*, 2017.

Conference contributions

1. A. Coene, G. Crevecoeur, and L. Dupré, "An Adaptive Current Selection Method for Coil Arrays Used in Magnetorelaxometry to Quantitatively Reconstruct Magnetic Nanoparticles", *12th International Workshop on Optimization and Inverse Problems in Electromagnetism (OIPE)*, Ghent, Belgium, September 19-21, 2012.

2. A. Coene, G. Crevecoeur, and L. Dupré, "Adaptive Control of Excitation Coil Arrays for Targeted Magnetic Nanoparticle Reconstruction Using Magnetorelaxometry", *International Conference on Magnetism (INTERMAG)*, Vancouver, Canada, May 7-11, 2012.

3. A. Coene, G. Crevecoeur, and L. Dupré, "Nanoparticle Imaging Using Electron Paramagnetic Resonance with a Non-negativity Constraint", *12th Belgian Day on Biomedical Engineering*, Brussels, Belgium, December 6, 2013.

4. A. Coene, G. Crevecoeur, M. Liebl, F. Wiekhorst, L. Dupré, and U. Steinhoff, "Spatial Error Distributions of Magnetic Nanoparticles Using Magnetorelaxometry Noise Data", *58th Annual Conference on Magnetism and Magnetic Materials (MMM)*, Denver, USA, November 4-8, 2013.

5. A. Coene, M. Liebl, F. Wiekhorst, G. Crevecoeur, U. Steinhoff, L. Dupré, and J. Haueisen, "How to Adapt Magnetorelaxometry Activation Setups for Quantitative Magnetic Nanoparticle Imaging Under Realistic Noise Conditions", *19th International Conference on Biomagnetism (BIOMAG)*, Halifax, Canada, August 24-28, 2014.

6. J. Leliaert, A. Coene, G. Crevecoeur, L. Dupré, and B. Van Waeyenberge, "Dipolar Interactions Between Magnetic Nanoparticles in Magnetorelaxometry", *19th International Conference on Biomagnetism (BIOMAG)*, Halifax,

Canada, August 24-28, 2014.

7. A. Coene, G. Crevecoeur, and L. Dupré, "Towards 2D and 3D Imaging of Magnetic Nanoparticles Using EPR Measurements", *13th International Workshop on Optimization and Inverse Problems in Electromagnetism (OIPE)*, Delft, the Netherlands, September 10-12, 2014.

8. A. Coene, G. Crevecoeur, and L. Dupré, "Imaging of Magnetic Nanoparticles Using Multiple Electron Paramagnetic Resonance Activation Sequences", *59th Annual Conference on Magnetism and Magnetic Materials (MMM)*, Honolulu, USA, November 3-7, 2014.

9. A. Coene, J. Leliaert, G. Crevecoeur, and L. Dupré, "Quantitative Comparison of Magnetorelaxometry Models", *15th German Ferrofluid Workshop*, Rostock, Germany, June 15-17, 2015.

10. J. Leliaert, A. Coene, A. Vansteenkiste, G. Crevecoeur, B. Van Waeyenberge, and L. Dupré, "Vinamax: a Simulation Tool for Nanoparticle Magnetization Dynamics", *15th German Ferrofluid Workshop*, Rostock, Germany, June 15-17, 2015.

11. A. Coene, J. Leliaert, G. Crevecoeur, and L. Dupré, "Comparative Study of Particle Electron Paramagnetic Resonance and Magnetorelaxometry for Quantitative Magnetic Nanoparticle Imaging", *20th International Conference on Biomagnetism (BIOMAG)*, Seoul, South Korea, October 2-6, 2016.

12. J. Leliaert, A. Coene, M. Liebl, D. Eberbeck, U. Steinhoff, F. Wiekhorst, B. Fischer, L. Dupré, and B. Van Waeyenberge, "Thermal Magnetic Noise Spectra of Nanoparticle Ensembles", *20th International Conference on Biomagnetism (BIOMAG)*, Seoul, South Korea, October 2-6, 2016.

Preface

Situation

As might be expected from the prefix *nano*, nanoparticles (NP) are extremely small particles with a diameter ranging in the nanometer (10^{-9} meter) region. Generally speaking, they have sizes between 1 and 100 nm, although examples of larger NP of several hundreds of nanometers in size also exist [1]. Due to their extremely small sizes and the link with *nanotechnology*, one might think that nanoparticles only emerged recently. Nevertheless, they have always occurred in nature and already had applications in ancient times [2, 3]. One example is the use of metallic nanoparticles, such as gold and silver, to color pottery and glass [4]. At that moment, it was not clear where these effects originated from, as these techniques were solely based on empirical experience. It was only in 1857 that Michael Faraday presented the scientific explanation behind these effects in a lecture for the Royal Society of London entitled: *'Experimental Relations of Gold (and other Metals) to Light'* [5]. He mainly used gold NP as he was familiar with the phenomenon that only a small variation in the nanoparticle's size resulted in a variety of colors. This talk is generally considered as the emergence of nanoscience and nanotechnology [6]. It illustrates that nanoparticles often have special, unexpected and new properties compared to their bulk counterparts. Depending on their size and shape, these effects can be optical, but also electrical, magnetic, or mechanical effects can arise [7]. This so-called *quantum size effect*, which occurs due to confinement of electrons in a small volume, was first explained in the beginning of the 1980's by Rossetti et al. [8]. Scientists soon realized that by carefully tailoring the particles' sizes and shapes, many new and interesting materials and applications could be developed, with often a superior performance [2].

One special class of nanoparticles are *magnetic* nanoparticles (MNP) [9]. An ensemble of magnetic nanoparticles shows *superparamagnetic* behavior [10, 11]. This behavior is explained in detail in Section 1.1.3 and can be summarized as follows: 1) magnetic nanoparticles each individually exhibit

a large magnetic moment because each particle contains several aligned atomic moments, hence the name *super*paramagnetism, 2) in the absence of an external magnetic field, no net magnetization of the ensemble is observed due to the random orientation of the magnetic moments of the individual magnetic nanoparticles and 3) when the MNP ensemble is placed in an external magnetic field, a net magnetization of the MNP ensemble in the direction of the external magnetic field can be measured, originating from the partial alignment of the particles' magnetic moments with the external magnetic field. Increasing the amplitude of the external magnetic field results in a higher magnetization of the MNP ensemble. For small magnetic fields the relationship between field strength and the magnetization of the MNP ensemble is nearly linear, while at higher fields the relationship becomes non-linear. Furthermore, from a certain field strength no increase in the magnetization can be observed: this is the maximum achievable magnetization of the ensemble defined as the *saturation magnetization*. As can be seen from previous points, the ensemble's behavior depends on the orientation of the individual magnetic moments of the magnetic particles. A magnetic particle can change the orientation of its magnetic moment in two ways: by rotating as a whole, thereby altering the orientation of its magnetic moment or by moving the direction of the magnetic moment internally in the magnetic core of the particle. Both mechanisms are characterized by a certain time constant, the Brownian relaxation time [12] and the Néel relaxation time [13] respectively. These temporal dynamics depend on the environment, temperature, material and size of the particle. Therefore different particle types respond to changes in the external magnetic field with different speeds. This unique and special behavior associated to these particles has been beneficial for many applications in different areas.

One area that has been particularly influenced by the emergence of MNP, is the biomedical field. There, magnetic nanoparticles have been increasingly employed in many biomedical applications because of their suitable properties [14–17]. According to Pankhurst et al., three important features can be defined [14]: first, they are magnetic, which means that they can be measured from a distance using sensitive sensors such as fluxgates [18] or SQUIDs [19] and that they can be moved from a distance by means of a magnetic field gradient [20]. The human body is penetrable by magnetic fields, thus the MNP can easily be manipulated and measured from the outside without the need to harm the body. Secondly, the MNP are extremely small so they can reach almost every region in the human body. This is convenient in *drug targeting* in which the MNP are used as drug carriers [21]. This application is a huge step forward compared to the traditional way of drug delivery in which the whole body is targeted by the medicine. Because the drug is now

locally applied, a lower medicine dosage can be employed, no systemic side effects are created and thus the efficiency of the medicine and patient safety is increased. The particles' sizes are comparable to biological entities such as cells (10 - 100 μm), viruses (20 - 450 nm), proteins (5 - 50 nm) or genes (2 nm wide and 10 - 100 nm long), which facilitate interactions with these entities and allows for direct tagging by binding specialized chemical markers to the MNP. This way diseases can easily be detected [22] and the interactions with biological entities monitored [23]. Third, they can be made to resonate at a certain alternating magnetic field frequency. When they are in resonance, a maximum amount of energy from the magnetic field is transferred to the MNP which results in heating of the particles. Due to the heating of the MNP, also the surrounding tissues see an increase in temperature. Many types of tumors show a larger sensitivity towards heat compared to healthy tissues, making this technique ideal for the destruction of cancer cells. When temperatures between 41 and 46 °C are achieved, this is called *magnetic hyperthermia* [24]. These temperatures allow to damage or kill cancer cells if the temperature increase can be maintained for at least half an hour [14].

Although many diagnostic and therapeutic applications can be realized with the help of magnetic nanoparticles, in order for these applications to operate in a clinical environment, many steps still need to be taken to ensure efficacy of aforementioned applications and patient safety. One important step, seen as one of the key challenges in nanomedicine by official institutions [25], is to determine the spatial distribution of the magnetic nanoparticles in a *quantitative* and *non-invasive* way. Hence, questions such as *'Did the particles reach the target?'* and *'Is the amount of particles at the target sufficient to reach the desired heating/drug dosage?'* need to be answered.

One promising technique for visualizing the MNP biodistribution is *magnetorelaxometry* (MRX). In these experiments the delayed magnetic response of the MNP ensemble to sudden changes in the external magnetic field is measured. In 1995 Kötitz et al. performed the first MRX measurements on magnetite MNP with different sizes for the case of a sudden shutdown of the magnetic field [26]. They discovered that the MRX measurements yield information about MNP properties and their environment. Soon MRX was employed for recovering the binding state of MNP to biological entities [27], characterizing MNP properties such as their size distribution [28] and agglomeration [29] and determining the amount of MNP in small tissue samples (*ex vivo*) [30]. In the last approach the tissue of interest (tumor, liver, lung,...), containing the MNP, is cut into smaller samples. For each sample separately, the amount of MNP is obtained using MRX [31, 32]. When the position of each sample in the tissue is known, the MNP distribution can be

reconstructed. This approach is very cumbersome when large organs or areas are considered and additionally the MNP distribution cannot be obtained *in vivo*. Because only *one* sensor is used (i.e. *single channel* MRX) for measuring the relaxometry signal in aforementioned applications, the samples have to be small. This drawback can be solved by moving a SQUID over the region of interest [33] or, more effectively, by measuring simultaneously with multiple sensors (i.e. *multi-channel* MRX) [34, 35].

By employing multiple magnetometers on various positions and directions the magnetization *vector* of the MNP ensemble can be mapped on various positions and thus a magnetic field pattern can be obtained. Finding the MNP distribution starting from these sensor signals is an *inverse problem*. In this thesis, we refer to this inverse problem as *magnetorelaxometry imaging* to make the distinction between magnetorelaxometry for characterizing MNP and their environment, and magnetorelaxometry imaging for finding the MNP biodistribution. In order to be solved, the inverse problem requires a *forward model*. The forward model links a certain spatial MNP distribution to a measurement signal in the sensors. The way of solving the inverse problem and the chosen forward model have a large impact on the obtained solution (i.e. the reconstructed MNP distribution). By fitting a magnetic dipole model to the multi-channel MRX data, Wiekhorst et al. were able to determine the center of magnetization and total amount of MNP accumulations *in vivo* after drug targeting [35].

However, to obtain detailed information about the spatially varying MNP amounts, a more extensive model is needed. As this is an *ill-posed* problem, it is important to state the forward model and inverse calculations so that the inverse problem becomes stable and an accurate and detailed MNP distribution can be found. In 2008 Baumgarten et al. used minimum norm estimates (MNE) on MRX data to solve the inverse problem [36]. This allowed a two dimensional (2D) reconstruction of the MNP distribution, although the reconstructions showed a strong blur effect originating from the used approach. Consequently, a lot of research has been performed on inverse procedures and forward modeling to increase the reconstruction quality of the 2D MNP distributions [37–39]. It is possible to stabilize the inverse problem in MRX measurements further, by using the susceptibility tomography principle presented by Wikswo et al. [40]. This is done by bringing different parts of the volume into relaxation and measuring the relaxation signals with multiple sensors simultaneously. Because independent information is added from the sensors, the inverse problem shows an increased stability and now allows the reconstruction of the three dimensional (3D) spatial MNP distribution in simulations [41, 42]. In this thesis the MRX inverse problem is further

stabilized using different techniques and inverse procedures as to increase the resolution and the accuracy of the reconstructed MNP distribution.

Magnetorelaxometry is not the only technique capable of retrieving the MNP distribution. In 2005 Gleich and Weizenecker developed a technique called *magnetic particle imaging* (MPI) to visualize the 2D MNP distribution [43]. MPI takes advantage of the non-linear magnetization of the MNP ensemble and its saturation at a certain external magnetic field. First the region of interest is placed in a magnetic field (*selection field*) that saturates the MNP ensemble except for one point in space (*field-free point*, (FFP)). Then an oscillating magnetic field (*modulation field*) is applied that results in a time-varying magnetic magnetization from the MNP ensemble in the FFP with the same frequency and its harmonics as the oscillating field. The MNP outside the FFP do not contribute to this signal as they are in saturation. The harmonics of the oscillating field in the spectrum of this signal contain information related to the MNP amount in the FFP. By moving the FFP over the region of interest, the spatial MNP distribution can be reconstructed. In 2009, MPI was employed to visualize the beating heart of a mouse in 3D [44]. Currently, many reconstruction methods and setup adaptations are under research in order to improve this imaging technique [45–48].

A similar approach to visualize the MNP distribution is to measure the magnetization response of the MNP ensemble to a small oscillating external magnetic field [49]. Because of the small field, compared to MPI, the MNP show a linearly varying magnetization with the same frequency as the oscillating field. The difficulty lies in separating the magnetization signal of the MNP ensemble from the oscillating magnetic field as the latter one is several orders of magnitude larger. Therefore compensation is necessary, both active, by generating opposing oscillating fields at the sensors' location, so the total magnetic field is zero, as well as passive, by placing the sensors in such way that their measurement direction is orthogonal to the direction of the oscillating field. This approach, called *susceptibility magnitude imaging* (SMI), was presented by Ficko et al. [50]. They showed that the magnetic response varied linearly with the MNP amount and that it was possible to reconstruct a one dimensional (1D) MNP distribution *ex vivo*.

Although it does not yet allow the reconstructions of MNP distributions, a very accurate technique for obtaining the total MNP amount in a sample is *electron paramagnetic resonance* (EPR) [51]. In this approach the MNP sample is placed in a small magnetic field that results in a magnetization of the MNP ensemble. The sample is then radiated by a radio frequency wave, which results in a precession of the magnetization around the direction of the applied

magnetic field at a fixed angle. A pickup coil is placed with its measurement direction orthogonal to the magnetic field and radio frequency wave, to minimize the disturbances to the measured signal from the magnetic field and radio frequency wave. Due to the precessional motion of the ensemble's magnetization around the magnetic field, the sample's magnetization can be separated from the magnetic field. The pickup coil measures the component of the magnetization that is perpendicular to the applied magnetic field and radio frequency wave. This component is dependent on the amount of MNP present in the sample [52]. This measurement is performed for anti-parallel directions of the applied magnetic field, so a high signal-to-noise ratio (SNR) can be achieved and therefore the obtained MNP amount is very accurate. In this thesis the EPR principle is extended to allow reconstructions of MNP distributions in 1D, 2D and 3D. Furthermore, inverse reconstruction procedures are presented that allow fast and accurate measurements.

Aims and objectives

The previous section showed the need for a *non-invasive* technique for reconstructing the spatial MNP distribution. Although in recent years many approaches emerged, they are still in the initial state of research and many developments are required in order for these approaches to find clinical practice. In the end, the imaging technique should be low-cost, fast, sensitive, accurate, specific (only MNP contribute to the signal) and usable for many MNP types. Additionally, it should have a large field of view and should result in high-resolution images of the particles. To date, no technique is able to fulfill all these requirements. Therefore, in this dissertation, research is conducted on non-invasive methods for spatial and quantitative reconstructions of magnetic nanoparticles. More specifically, this work aims at improving MRX imaging and EPR by optimizing their measurement procedures and setups, developing new forward models and by increasing the stability of their inverse problems. The final goal of this work is to enable quantitative reconstructions of the spatial nanoparticle distribution using EPR and MRX imaging.

A first specific aim is to extend EPR from a sensitive and accurate MNP detection technique to an imaging modality that allows the spatial reconstruction of MNP distributions in 1D, 2D and 3D. To realize this, a forward model and measurement procedure is developed that includes spatial information in the EPR measurements. In a next step, the robustness and limitations of the presented EPR imaging modality are analyzed through a sensitivity analysis. It investigates the impact of different error types and setup parameters on

reconstruction quality and resolution. This enables the targeted optimization of the measurement procedure, the stabilization of the inverse problem, and an improved reconstruction accuracy. Finally, by introducing a heterogeneous magnetic field in the EPR setup (instead of a homogeneous magnetic field), specific parts of the particle sample can be magnetically activated. This way a speedup of the EPR imaging technique is possible, while also achieving an improvement in its stability and accuracy.

A second specific aim is to bring MRX imaging closer to clinical applications. This is achieved by optimizing the MRX measurement procedure by taking into account preliminary information about the MNP sample. Additionally, a quantitative measure is developed that allows to find the most suitable MRX imaging model and setup for any given sample geometry and desired reconstruction resolution. It also allows to compare and optimize MRX imaging setups and models independent of the MNP distribution. This way, an increased reconstruction quality can be obtained together with a speedup of the measurement procedure. Finally, the MRX forward model is extended so that instead of using a single particle type in each MRX experiment, now multiple MNP types can be employed and reconstructed simultaneously. This extension enables the combination of multiple diagnoses and therapies in a single experiment.

Outline

This dissertation comprises three main parts. The first part (Chapter 1) provides a general introduction to the biomedical research field of magnetic nanoparticles and supplies all necessary knowledge and background to understand the scientific results obtained in this work. The second part (Chapter 2) describes the EPR imaging technique and discusses our main research results with respect to this imaging technique. The last part (Chapter 3) focuses on the MRX imaging technique and covers the general principles of MRX and details the obtained progress for this technique during this PhD. Finally, in Chapter 4, the general conclusions from this work are discussed and an outlook is given.

In Chapter 1, the most important properties of the magnetic particles are discussed, including their structure and dynamic behavior in magnetic fields and in the human body (Section 1.1). It also shows how these properties can be useful in a variety of MNP-based biomedical applications such as magnetic targeting, magnetic hyperthermia and image contrast enhancement (Section 1.2). Furthermore, the possibilities and limitations of MNP imaging using

clinically established and newly developed imaging techniques are reviewed (Section 1.3). This first chapter ends with a general introduction to inverse problems and gives an overview on forward models and inverse solution procedures, and explains how the quality of the MNP reconstructions is evaluated throughout this dissertation (Section 1.4).

Chapter 2 starts with a general introduction to the EPR measurement technique and discusses its main biomedical applications (Section 2.1). Then it describes the development and experimental evaluation of a measurement procedure and forward model for 1D MNP imaging using EPR (Section 2.2). This is followed by a sensitivity analysis in which the impact of various system parameters and errors on the reconstruction is investigated (Section 2.3). Based on these results, an extension of the forward model is made to allow the imaging of 2D and 3D MNP distributions (Section 2.4). Finally, the EPR setup is adapted so that spatially varying magnetic fields can be generated with the aim to magnetize specific parts of the MNP sample and hence improve reconstruction quality and the stability of the inverse problem (Section 2.5).

In Chapter 3, the various MRX signal and imaging models are reviewed and an overview of the main biomedical applications is given (Section 3.1). This is followed by the introduction of an adaptive measurement procedure in which reconstructions are iteratively refined based on previous reconstruction results (Section 3.2). In a next step, statistical parameters from information theory are employed to realize quantitative MRX imaging models which can be used directly to optimize and compare MRX imaging setups and models for a desired sample geometry and reconstruction resolution (Section 3.3). This chapter ends with the development and experimental validation of an advanced MRX imaging model that allows to localize and quantify multiple particle types simultaneously (Section 3.4).

Chapter 4 elaborates on the general conclusions of this research and shows the importance of inducing the right responses from the MNP (Section 4.1). This is further demonstrated in a preliminary numerical study in which the EPR and MRX measurement techniques are combined in a single setup (Section 4.2). The conclusion chapter ends with ideas for future work based on the performed research and the preliminary study (Section 4.3).

1

Introduction

In this chapter an overview of MNP-based research is given to increase understanding and to provide a general situation of the work performed in this dissertation on MNP imaging. Section 1.1 describes the main properties (structure, behavior and magnetic dynamics) of magnetic particles. Section 1.2 explains how these properties can be useful in many MNP-based applications, such as magnetic targeting, magnetic hyperthermia, and contrast enhancement, among others and gives an overview on their recent progress. In Section 1.3, the recent advances in MNP imaging are discussed. A distinction is made between MNP imaging using clinically established techniques and MNP imaging with newly developed techniques especially for this purpose. The final section (Section 1.4) is an introduction to inverse problem formulations and reviews the typical forward models, inverse procedures and quality measures used in MNP imaging.

1.1. Magnetic nanoparticles

1.1.1 Introduction

Magnetic nanoparticles appear in many shapes and sizes and are only roughly defined as having a size in the nanometer (10^{-9} meter) region and the fact that they are magnetic. In this dissertation the focus is on magnetic nanoparticles for biomedical applications. MNP are ideally suited for these applications, because they can interact with biological entities such as cells and proteins, because of the comparable sizes and their high surface-to-volume ratio. Additionally, they can be measured non-invasively using magnetic sensors and be manipulated with external magnetic field gradients [14, 53]. Therefore, in recent years, many MNP-based biomedical applications appeared in diagnosis, actuation, therapy and imaging [14–17] (for more details, see Section 1.2). This however poses many requirements of the MNP, they should be [17, 54, 55]:

- non-toxic
- biocompatible, meaning that the body shows no immune and repair responses
- stable, the MNP should be stable in biological solutions and the MNP should stay as long as possible in the body (in some applications however, it is desirable that the MNP leave the body very fast)
- monodisperse, i.e. the used MNP do not vary much in size, although not required for every application, some biomedical applications need specific MNP behavior, which is size-dependent
- have a high maximum magnetization, M_{sat}, enabling sensitive registration using magnetometers and increased manipulation possibilities
- have interactive functions on their surface to interact with biological entities

A lot of research has been done on magnetic materials, surface coatings and fabrication procedures to tailor the MNP specific to an application's needs. In literature many excellent review papers can be found on this topic [17, 53–56]. In general, iron oxides, and especially magnetite (Fe_3O_4) and maghemite (γ-Fe_2O_3), are the most employed magnetic materials for MNP-based biomedical applications because of their biocompatibility, biodegradability, widespread abundance in nature and they can be readily synthesized in the laboratory [56, 57]. Furthermore, the medical use of magnetic iron oxide nanoparticles has been approved by the US Food and Drug Administration (FDA) and the European Medicines Agency (EMA) [53].

Nevertheless, research is still being conducted on many types of particles and recently *multifunctional* NP emerged in which the particles have other useful properties, besides being magnetic. This added functionality is mostly with respect to imaging and extended targeting possibilities combined with

multiple drug types [58–60]. Examples of extended imaging capabilities are having different types of imaging agents, optical contrast and fluorescence to allow the use of multi-modal and molecular imaging (Section 1.2.4). Multifunctional NP are very useful, especially from the viewpoints of *theranostics* [61] (Section 1.2) and *personalized medicine* [62]. In the first field, research is done on simultaneously performing diagnoses and therapies in one experiment, such as the monitoring of cancer progress and adequate response (thermoablation and drug targeting) [63] and in the latter, the patient inter-individual variability in therapeutic responses is tackled [64]. Recently however, Cheng et al. raised the question of the benefit of additional functionality compared to the increased complexity of manufacturing the NP and analyzing their behavior, not to mention the greater regulatory hurdles and higher costs [65]. Furthermore, standardization in MNP manufacturing and characterization already proves difficult and might even hinder the introduction of innovative MNP-based biomedical applications [66]. Therefore many projects, such as the EU FP7 project, NanoMag, are currently working on standardizing the different MNP analyzing techniques [67] as to be able to provide improved particle characterization and understanding of how their structure affects their behavior. As these are difficult concepts, Sections 1.1.2 and 1.1.3, provide a small introduction to the general structure of MNP and how this affects their behavior and magnetic dynamics.

1.1.2 Structure and biodistribution

Iron oxide particles can be divided into single-core magnetic iron oxide nanoparticles with sizes from a few nanometers and iron oxide based multi-core particles with sizes up to several micrometers [66]. A single-core magnetic nanoparticle consists of an iron oxide core, while the multi-core case contains multiple iron oxide cores (nanocrystals) grouped together in different configurations. The magnetic material allows for the non-invasive measurement of the MNP and manipulation/interaction with external magnetic fields. The core(s) can be made biocompatible, stabilized and functionalized with a coating. Typical examples are starch or dextran coatings. The coating, although mostly non-magnetic, plays an important role in agglomeration and oxidation prevention of the particles and their measurable magnetization [53]. Furthermore, the coating and the particle's size determine the biological fate of the particle [55]. We define V_h as the hydrodynamic volume of the particle and it refers to the total volume of particle (iron core(s) and coating) and V_c is the volume of the magnetic core. Figure 1.1 depicts the differences between single-core and multi-core iron oxide MNP.

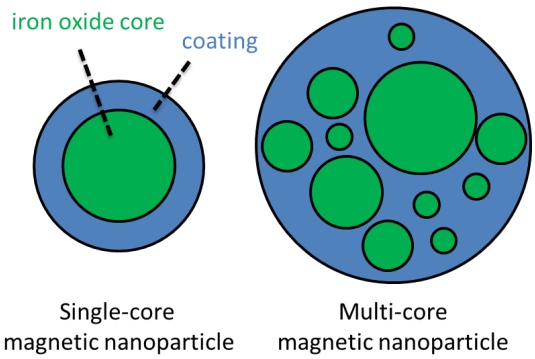

Figure 1.1: A single-core iron oxide particle consists of one single iron core, while a multi-core has multiple iron oxide cores. Because of the magnetic core(s), the MNP can be manipulated by means of external magnetic fields and be measured non-invasively. Both particle types can be stabilized with a coating that governs interactions between particles themselves and with the body and allows for possible functionalization (targeting or detection) of the particles.

Many biological mechanisms exist that might hinder the MNP during their journey in the body, such as 1) removal of the particles from the body before they can reach their desired target and 2) structural limitations [17]. For example, when the particles are injected into the bloodstream, plasma proteins easily attach themselves to the MNP due to their high surface-to-volume ratio. These proteins enable the detection by macrophages (type of white blood cell that digests foreign objects) and as such the MNP are removed by the body. This behavior is ideal when one wants to target a region containing many macrophages such as the liver, bone marrow, spleen or inflammatory areas [53]. However, if another target is favored, the MNP should be able to reach this target before they are removed from the blood stream. Typically, larger MNP show an increased sensitivity to plasma protein adhesion compared to smaller MNP [55]. Also the diffusion from the capillaries into the tissues depends on the size of the MNP, i.e. healthy capillaries from most organs allow the penetration of MNP with sizes up to 6 nm, while the typical leaky vasculature of tumors (the enhanced permeability and retention effect) or inflammation can allow MNP with sizes up to 700 nm . Particles with sizes < 5.5 nm are filtered by the kidneys, while MNP having sizes > 200 nm are cleared in the liver and spleen [53, 55]. The way of confining the MNP in the cells also greatly depends on the size. After they entered the cell, the MNP are clustered in lysosomes (waste disposal system of the cell) in which they are degraded into iron and oxygen. The Fe ions are further used by the normal metabolic pathways of the cell [55]. This is a simplified picture

as the interaction of the particles with the body also depends on the way of injecting the MNP, their concentration, material, shape, surface, charge and functionalisation. It is for example possible to extend blood circulation of the MNP by using 'stealth coatings' such as poly-ethylene-glycol. Furthermore, the diffusion of larger MNP can be temporarily improved with local heating or radiation. Most important for this dissertation are effects that change the magnetic dynamics of the MNP. This can occur when high MNP concentrations are achieved, for example when many MNP are confined in a cell, and inter-particle relations change the magnetic behavior of the MNP, or when the hydrodynamic size of the particle changes due to interactions with for example proteins [17, 53]. Section 1.1.3 explains this magnetic behavior into detail.

1.1.3 Magnetic dynamics

Magnetic materials that are subject to an external magnetic field **H**, can be classified according to their magnetization **M** in an external magnetic field, **H**. **M** is a material property and originates from the magnetic moments of the material's electrons. Figure 1.2 shows an overview of the different magnetic responses considered here. More details about these magnetic materials and their properties can be found in [68]. The magnetic induction, **B**, is defined as:

$$\mathbf{B} = \mu_0(\mathbf{M} + \mathbf{H}) \tag{1.1}$$

with μ_0 the permeability of free space. Certain materials exists in which **M** varies linearly with **H**:

$$\mathbf{M} = \chi\mathbf{H} \tag{1.2}$$

with χ, the magnetic susceptibility, $\chi > 0$ in the case of a paramagnetic material and $\chi < 0$ for a diamagnetic material. Additionally, magnetic materials exist in which regions arise where the magnetic moments are aligned to each other, called *magnetic domains*. Due to this coupling between the electrons, very high values for **M** can be achieved. These materials are ferromagnetic, ferrimagnetic or antiferromagnetic each with a specific coupling. For ferromagnetic materials, neighboring magnetic moments want to align in the same direction, while in the ferrimagnetic case some magnetic moments want to align anti-parallel, thereby reducing **M**. In the antiferromagnetic case, neighboring magnetic moments cancel each other, as such no magnetization is visible when no external magnetic field is applied, while in the other two cases, due to the magnetic ordering, a remanent magnetization, $\mathbf{M}_r$ is observable after removal of the magnetic field. In these magnetically ordered structures χ depends on **H** and the previous magnetization state, which gives

rise to *hysteresis loops* between **H** and **M**. This irreversibility in magnetization is due to pinning of the magnetic domains at grain boundaries and impurities and anisotropy effects of the material. The maximum achievable magnetization (in which all the magnetic moments are aligned to **H**) is referred to as the *saturation magnetization*, M_{sat}.

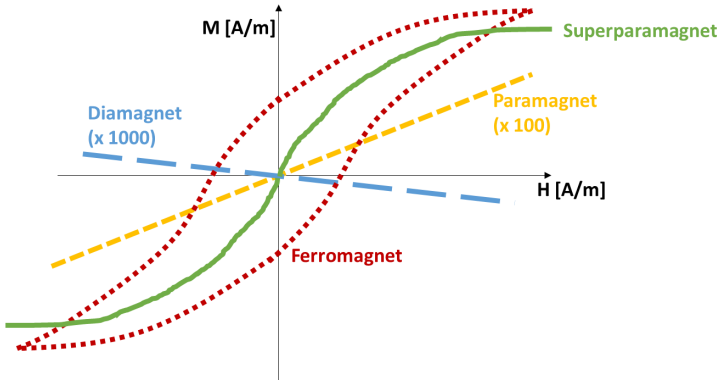

Figure 1.2: Responses of different magnetic materials to an external magnetic field **H**.

The MNP considered in this work are ferromagnets or ferrimagnets. Their magnetic dynamics are, among others, determined by the size of the magnetic core. Larger MNP have multiple magnetic domains (multi-domain NP) comparable to their bulk counterparts, while for smaller MNP, starting from a certain critical size (which is material-dependent), it is energetically favorable to have only one magnetic domain (single-domain NP) and hence a uniform magnetization in which all the particle's magnetic moments lie in the same direction [69]. This uniform magnetization can be represented by one magnetic moment, **m**, which is the sum of the particle's individual magnetic moments. Consequently, the saturation magnetization becomes:

$$M_{\text{sat}} = \frac{m}{V_{\text{c}}} \tag{1.3}$$

with V_{c} the volume of the magnetic core. The transition from multi-domain to single-domain depends on the crystalline structure and particle composition, although for many MNP types it ranges between 50 and 100 nm [17, 53]. Reducing the size of the MNP even further, results in *superparamagnetic* behavior (superparamagnetic MNP) [10, 11], in which the thermal energy allows to change the orientation of the particle's magnetic moment. This happens on a

characteristic time scale defined by the Néel relaxtion time [13], τ_N:

$$\tau_N = \tau_0 \exp\left(\frac{\Delta E}{k_B T}\right) \tag{1.4}$$

ΔE is the required energy to change the direction of the particle's moment and depends on the particle's anisotropy, k_B is the Boltzmann constant, T the temperature and τ_0 is the inverse of the attempt frequency with values in the literature between 10^{-8} s and 10^{-12} s. $\Delta E = KV_c$, for MNP having uniaxial anisotropy, with K the anisotropy constant. In practice this signifies that the magnetic moment of the particle lies in one of two possible directions along an axis, called the easy axis. When the measurement time is longer than τ_N, no remanent magnetization is observed (therefore, it is a form of paramagnetism), on the other hand the acquired **M** values are significantly larger than in the case of a paramagnetic material (similar to the ferromagnetic response), therefore we refer to this behavior as *super*paramagnetism. When the measurement time is smaller than τ_N, a single-domain NP is observed. Figure 1.3 depicts the magnetization states of the magnetic core depending on its size.

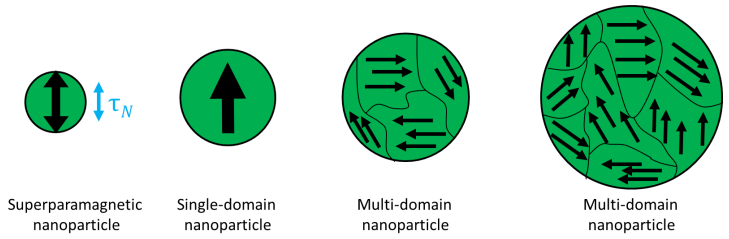

Figure 1.3: Depending on the magnetic core's size the particle can be superparamagnetic (when the measurement time is longer than τ_N), single-domain or multi-domain.

The Néel relaxation is an example of internal rotation of the particle's magnetic moment. Additionally, the particle can rotate as a whole when it is dispersed in a liquid with viscosity η, thereby changing the orientation of its magnetic moment. This second behavior also happens on a characteristic time scale, called the Brownian relaxation time, τ_B [12]:

$$\tau_B = \frac{3\eta V_h}{k_B T} \tag{1.5}$$

with V_h the hydrodynamic volume of the particle. When both relaxation phenomena act on the particle its temporal behavior is represented by an effective

relaxation time, τ_{eff}:

$$\tau_{\text{eff}}(V_{\text{c}}, V_{\text{h}}) = \frac{\tau_{\text{N}}(V_{\text{c}})\tau_{\text{B}}(V_{\text{h}})}{\tau_{\text{N}}(V_{\text{c}}) + \tau_{\text{B}}(V_{\text{h}})} \tag{1.6}$$

Eq. (1.6) represents the fact that the fastest relaxation of both mechanisms will define the effective relaxation of the particle. Figure 1.4 illustrates the impact of the magnetic core diameter (d_{c}) and hydrodynamic diameter (d_{h}) on the particle's relaxation time for an iron oxide particle with K = 10000 J/m^3 and T = 290 K, suspended in water ($\eta = 10^{-3}$ Pa·s). It shows that the magnetic dynamics of the single-core particle are determined by the size of its iron core and its hydrodynamic diameter with τ_{N} prevailing for smaller MNP and τ_{B} for the larger ones. In the multi-core case, also the size distribution of the cores in the particle, their geometrical configuration and their interactions play a vital role in the magnetic dynamics [70]. Additionally the relaxation times might change for high MNP amounts due to interactions between the MNP [71–73]. In 2013, Kolhatkar et al. provided an overview of the most important magnetic requirements for each MNP-based application and how this related to particle properties such as size, shape, composition and core-shell design [74].

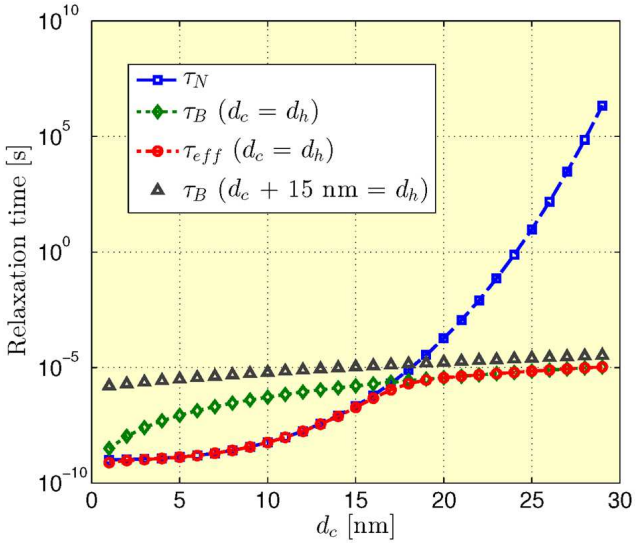

Figure 1.4: The influence of an iron oxide core with diameter d_{c} and hydrodynamic diameter d_{h} on it's relaxation time for the case of K = 10000 J/m^3, T = 290 K and $\eta = 10^{-3}$ Pa·s.

In this dissertation, we consider ensembles of MNP and assume that each particle individually is superparamagnetic or single-domain. The MNP ensemble shows superparamagnetic behavior [10, 11] even when all MNP are single-domain, provided they can rotate through Brownian relaxation. In the absence of an external magnetic field, the relaxation mechanisms, Brownian or Néel, randomly orient their magnetic moments, resulting in no net magnetization of the ensemble. Note that Eqs. (1.4) and (1.5) are only valid for zero magnetic field and no interaction of the magnetic core with other magnetic cores. When an external magnetic field $\mathbf{H}$ is applied, the energy barrier in Eq. (1.4) is reduced and in Eq. (1.5) the external field acts as a torque on the particle and therefore the direction of its magnetic moment can change on smaller time scales. Thus, by increasing the amplitude of the external magnetic field, increasing amounts of MNP are aligned to the field. For extended formulas in the case of a magnetic field, we refer the interested reader to [75–78]. The quasi-static magnetization of a superparamagnetic ensemble of non-interacting, identical MNP and with $KV_\mathrm{c} \ll k_\mathrm{B}T$ is often described by the Langevin function $\mathcal{L}(\xi)$:

$$\mathbf{M} = M_\mathrm{sat}\mathcal{L}(\xi) \tag{1.7}$$

$$\mathcal{L}(\xi) = \coth(\xi) - \frac{1}{\xi} \tag{1.8}$$

with $\xi = \frac{\mu_0 M_\mathrm{sat} V_\mathrm{c} H}{k_\mathrm{B}T}$. This function corresponds to the superparamagnet curve in Fig. 1.2. Fig. 1.5 depicts the superparamagnetic behavior of the MNP ensemble. In general the MNP ensemble consists of a distribution of particle sizes, denoted as $P(V_\mathrm{c}, V_\mathrm{h})$. In most cases a lognormal distribution of V_c and V_h is considered. Eq. (1.7) can be made MNP dependent by weighting it with the magnetic core size distribution.

In this work, the spatial distribution of MNP ensembles in samples is investigated. To this end, the sample is tessellated in cubic volume-elements, called *voxels*, and the MNP amount in each voxel is reconstructed. The magnetization of voxel v then becomes:

$$\mathbf{M}_v = \frac{c_v}{\rho V_v}\mathbf{M} \tag{1.9}$$

with c_v the mass of iron in the voxel (expressed in grammes of Fe), ρ the mass of iron divided by the core volume ($\rho = \frac{c_v}{V_\mathrm{c}}$) and V_v the volume of the voxel. In the remainder of this dissertation c_v is referred to as the MNP amount in voxel v, as the mass of iron in a voxel is related to its MNP amount. This way it is possible to link magnetic measurements to the spatial MNP distribution.

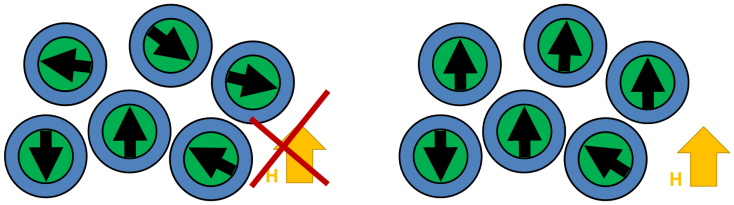

Figure 1.5: An ensemble of MNP shows superparamagnetic behavior. When no external magnetic field is applied (left), the average magnetization of the ensemble is zero, while with increasing **H**, increasingly more MNP are aligned with the direction of **H** (right).

Note that the ensemble behavior described above is only valid in case the MNP have sufficient time to align with the applied magnetic field. Hence, when the applied field changes in amplitude, for example a temporal varying magnetic field with frequency f, the changes should be sufficiently slow in order for the MNP to follow (i.e. quasi-static regime or $\tau_{\text{eff}} \ll f^{-1}$). When $\tau_{\text{eff}} > f^{-1}$ or when $\tau_{\text{eff}} \approx f^{-1}$ hysteretic behavior is observed. When $\tau_{\text{eff}} \approx f^{-1}$, the particles' magnetic dynamics can be modeled using the linear response theory (LRT). LRT assumes a linear relationship between H and M and no interactions between the MNP. LRT is valid for superparamagnetic MNP as long as small magnetic field amplitudes are considered and $\mu_0 M_{\text{sat}} H V_{\text{c}} \ll k_{\text{B}} T$. This theory describes how the MNP lag behind the applied field trough the, now complex, magnetic susceptibility χ (Eq. (1.2)), with $\chi = \chi' + i\chi''$. The imaginary part (χ'') represents the out-of-phase component and the real part (χ') represents the in-phase component:

$$\chi' = \chi_0 \frac{1}{1 + (2\pi f \tau_{\text{eff}})^2} \tag{1.10}$$

$$\chi'' = \chi_0 \frac{2\pi f \tau_{\text{eff}}}{1 + (2\pi f \tau_{\text{eff}})^2} \tag{1.11}$$

with χ_0 the quasi-static magnetic susceptibility ($\tau_{\text{eff}} \ll f^{-1}$). In the case of the Langevin function, which is linear for small fields, $\chi_0 = \frac{\mu_0 M_{\text{sat}}^2 V_{\text{c}}}{3 k_{\text{B}} T}$. As an MNP ensemble in practice consists of MNP with a size distribution $P(V_{\text{c}}, V_{\text{h}})$, it also has a distribution of effective relaxation time constants and corresponding magnetic susceptibilities.

1.2. Biomedical applications of magnetic nanoparticles

1.2.1 Introduction

The preface section showed that MNP are very advantageous for biomedical applications: by specifically tailoring their structure, they can reach different places in the body, by '*tagging*' them, they allow the detection of diseases and enzymes or the targeting of certain parts in the body such as tumors or inflammations. Additionally, by applying magnetic field gradients, they can be guided and kept at certain positions in the body and because of their superparamagnetic properties they can be measured from a distance non-invasively, to locate their exact position. Thanks to these interesting properties many biomedical applications exist. Figure 1.6 gives an overview of the main applications. Applications that provide both therapy and diagnostic services are referred to as *theranostic* applications. In these applications, the MNP are made suitable to allow the simultaneous visualization of disease progress (often multi-modal) and adequate response (targeted delivery of medicine or heating) [61, 63, 79–82]. In this section we focus on the diagnostic and therapeutic applications separately, but it should be noted that, through careful tailoring of the NP, both can be applied simultaneously.

The main examples of therapeutic applications are *magnetic hyperthermia*, in which the MNP heat their surrounding environment, and a collection of applications making use of *magnetic targeting*, in which the MNP are magnetically targeted towards certain points of interests. Applications include *drug targeting*, *tissue engineering*, *regenerative medicine* and *magnetofection*. Sections 1.2.2 and 1.2.3 give a description of their underlying mechanisms and the progress made in these domains.

MNP are also employed in diagnostic applications, which can be subdivided into *in vitro* and *in vivo* applications. Examples of *in vitro* applications are *magnetic separation* in which biological entities such as viruses, proteins, molecules, bacteria etc. are labeled by the MNP and then magnetically removed from their environment [14, 53, 55, 83]. The separated entities are then further prepared for other analysis techniques. Similarly, MNP find their use in determining the presence and concentration of said biological entities in solutions, called *immunoassays*. In this case the MNP bind, through the antibodies on their surface, with the entity of interest. Based on the changing magnetic dynamics (see for example Section 1.1.3, Eqs. (1.4),(1.5)) the presence and amount of the biomolecule can be determined [16, 27, 53, 55, 76]. Sections 3.1.3 and 3.1.5 explain into detail how MRX can be employed to measure these changes in dynamics and how to relate them to the biological entities. Section 1.2.4 describes the principles behind *contrast enhancement*,

an important *in vivo* diagnostic application used in many clinical settings, in which the MNP are used to increase the contrast of MRI and other imaging modalities. Sections 1.3, 3.1.4 and 3.1.5 discuss the specific imaging of MNP themselves in which the biodistribution of the MNP is acquired *in vivo*. This can be used to the benefit of previously mentioned applications such as drug targeting, hyperthermia, disease detection, molecular imaging and etc.

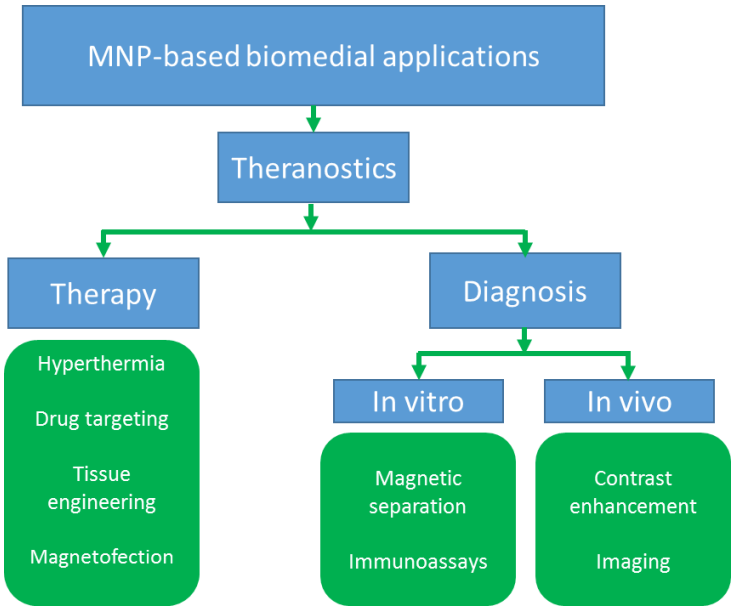

Figure 1.6: An overview of the main MNP-based biomedical applications (Adapted from [1, 17]).

1.2.2 Magnetic targeting

Most pharmaceuticals suffer from the problem that they are non-specific, i.e. unhealthy as well as healthy cells are targeted by them, and furthermore, they struggle to overcome biological barriers resulting in only a small portion of the medicine reaching the desired target. Therefore large dosages need to be employed to have an effective amount of medicine at the location. Hence, many patients suffer from systemic side effects from their medication [14, 55]. Magnetic drug targeting arose in the late 1970s to provide a solution to these problems, by specific targeting of drugs with magnetic carriers to reduce the systemic distribution and required dosage of therapeutics [84]. In magnetic

drug targeting, particles are injected into the arteries, veins or directly into the target region. The particles contain a therapeutic agent (drug, genes, radionuclide) and are targeted to a desired location. When they arrive, their therapeutic agent is released trough mechanisms such as enzymatic activity or external stimuli such as changes in pH, osmolarity and temperature [21]. For example p-NIPAAM is a temperature-sensitive polymer that can be in a swollen or collapsed state based on the temperature. The drug is released when the polymer collapses due to higher temperatures [17]. Temperature increase can be obtained by applying an AC magnetic field to the MNP (see Section 1.2.3). Porous pH-sensitive coatings are also employed in which a drug is encapsulated and, due to the lower pH in tumors, the pores etch and as such the drug release rate increases [85].

Generally, targeting is done by a combination of following methods: 1) passive targeting, 2) active targeting and 3) magnetic targeting [57, 61, 86]. In the first approach, use is made of abnormalities in the vasculature at inflammatory sites or the enhanced permeability and retention effect associated to most tumor tissues (see Section 1.1.2). However, this way of targeting requires NP that have a long circulation time in the blood in order to accumulate sufficient particles in the region. This problem can be reduced by using active targeting in which the coating of the particles is functionalized by for example targeting molecules that attach to tumor receptors. Functionalized MNP can be used to target many biological entities besides tumors, such as cells, viruses, proteines, etc. Accumulation in the desired region can be further increased by using a magnetic field gradient in combination with magnetic NP. The magnetic field gradient is typically generated by a permanent magnet, such as Nd-Fe-B, which is placed outside the body over the target region [14]. A magnetic force, $\mathbf{F}_\mathrm{M}$, acts on the MNP in the presence of an external magnetic field gradient:

$$\mathbf{F}_\mathrm{M} = (\mathbf{m} \cdot \nabla)\mathbf{B} \tag{1.12}$$

with $\mathbf{m}$ the magnetic moment of the single-domain particle and $\mathbf{B}$ the magnetic induction (see Section 1.1.3). This force should overcome the drag force in e.g. a bloodstream, which is given by:

$$\mathbf{F}_\mathrm{D} = 6\pi\eta\frac{d_\mathrm{h}}{2}\Delta\mathbf{v} \tag{1.13}$$

with $\Delta\mathbf{v}$ the difference in speed between the particle and fluid. In humans, blood flow speeds range from 0.05 cm/s in capillaries to 2 cm/s in arteries [17]. As $\mathbf{F}_\mathrm{M}$ depends on the third power of the particle's core radius ($\mathbf{m}$ is proportional to V_c, see Eq. (1.3)), while $\mathbf{F}_\mathrm{D}$ depends only linearly on its hydrodynamic radius, particles with large V_c are preferred. On the other hand, the MNP should be sufficiently small to overcome biological barriers

(Section 1.1.2) and to reduce the risk on embolization [14]. Additionally, the magnetic gradient from permanent magnets reduces with the distance, making magnetic drug targeting most suitable for regions in the body that can be positioned near the magnet (i.e. limited tissue depth) and in which the blood flow is sufficiently slow, hence the residence time of the MNP at the desired target is optimal [1, 14]. Recent work includes the use of invasive magnetic meshes and extensive magnetizing setups such as Halbach arrays, to increase magnetic field gradients in deeper regions in the body and thus improve deep magnetic targeting [87, 88] and the use of MRI to realize the simultaneous steering and imaging of magnetic drug carriers, called *magnetic resonance navigation* [89]. Although many papers have investigated the impact of fluid viscosity, magnetic field and particle properties on their drug targeting efficiency and drug targeting experiments have been performed in animal studies and clinical trials, still many challenges exist (the diminishing magnetic field gradient, possible embolization, drug retention in target region after release from MNP, and toxic response) for magnetic drug targeting to become a clinical practice [14, 20, 90, 91]. Recent reviews of magnetic drug targeting and their open challenges can be found in Refs. [92–95].

Magnetic targeting strategies for MNP are also employed in the field of *tissue engineering* and *regenerative medicine* in which research is aimed at generating or repairing functional tissue [15, 55, 85]. This can be done by magnetically targeting stem cells (a special type of cell which can differentiate into multiple cell types), labeled by MNP, to injuries in the body [96, 97]. Another approach is to use cells from a patient biopsy and then grow a tissue from these cells on porous 3D scaffolds (which are later on again placed in the body). The problem is to achieve enough cell seeding, structural complexity and effective communication between the cells (also in the deeper region of the scaffold). Aforementioned problems can be reduced by loading the cells with MNP and applying external magnetic (gradient) fields to the culture plate, to generate desired structures of tunable size and geometry [98] and to use mechanical actuation which has been shown to force cell differentiation and growth [99]. Recently, magnetic scaffolds with MNP and magnetic gradients were introduced to achieve magnetically deformable scaffolds and drug and hyperthermia services [100]. Based on previous principles, cells can also be magnetically actuated, in which MNP can open ion channels or deform the cell by magnetic gradient fields. Using these concepts it is possible to investigate and actively control cellular functions and mechanics using MNP [101]. Another therapeutic application is *gene therapy*, in which genes are delivered as a drug into the cells to cure genetic diseases. The difficulty lies in the rapid degradation of DNA and RNA and the troublesome insertion into the cells. By using MNP, containing the genes, and targeting them into cells

through magnetic fields, called *magnetofection*, it is possible to overcome these hurdles [93, 102, 103].

Based on previous applications one can also clearly observe that the success of magnetic targeting is inherently entwined with an accurate measurement system that allows to determine the spatial MNP distribution.

1.2.3 Magnetic hyperthermia

Hyperthermia, using magnetic nanoparticles, was done for the first time in 1957 by Gilchrist et al. in which tissue samples were heated [104]. Magnetic hyperthermia was then presented as a means to provide precision heating. The concept is as follows: MNP are targeted to the area where heat should be applied (Section 1.2.2) or are directly injected into the desired site. Then an AC magnetic field is applied, with a certain amplitude (in general < 50 kA/m) and frequency (in general 50 - 1200 kHz), to increase the temperature of the MNP and hence of their surrounding tissues.

Although alternating magnetic fields induce currents which can heat up the medium, it is not a source of heating for the MNP, as the considered MNP (iron oxides) are bad conductors and their sizes are too small. On the other hand, induced currents can appear in the human body and result in heating. Therefore regulations exist (for the frequencies applied in hyperthermia) that limit the product of the field's frequency and strength. This limit was experimentally determined for the case of a 30 cm coil by Atkinson et al. and states that the product should not exceed $4.85 \cdot 10^8$ $\mathrm{Am^{-1}s^{-1}}$ [105]. Note that the absorbed power in the tissues, due to induced currents, scales with the square of the radius of the exposed region, hence in practice a limit of $5 \cdot 10^9$ $\mathrm{Am^{-1}s^{-1}}$ is employed, because generally smaller coils of 10 cm are used in hyperthermia [106]. The heating of MNP in magnetic hyperthermia finds its origin in hysteretic losses. Hence, the heat released by an amount of MNP, the specific loss power (SLP), is proportional to the area of the hysteresis loop (Section 1.1.3) for the considered field strength H :

$$\mathrm{SLP} = \frac{\mu_0 f}{\rho_\mathrm{c}} \int M(H)\mathrm{d}H \tag{1.14}$$

with ρ_c the mass density of the magnetic material. To calculate the SLP, it is important to consider the frequency of the applied magnetic field (f) in relation to the thermal fluctuations (τ_eff) of the magnetic material, as the hysteretic behavior of the MNP is determined by these two parameters (see Section 1.1.3). In the case of a magnetic material with $\tau_\mathrm{eff} \ll f^{-1}$ superparamag-

netic behavior is observed (Fig. 1.2) and the SLP becomes zero. When $\tau_{\text{eff}} \approx f^{-1}$, Eq. (1.14) can be solved by LRT for small magnetic field amplitudes and as long as $\mu_0 M_{\text{sat}} H V_{\text{c}} \ll k_{\text{B}} T$ (see Eqs. (1.10) and (1.11)):

$$\text{SLP} = \frac{\mu_0}{\rho_{\text{c}}} \chi_0 \pi f H^2 \frac{2\pi f \tau_{\text{eff}}}{1 + (2\pi f \tau_{\text{eff}})^2} \tag{1.15}$$

H and f are chosen as such to maximize the SLP for the given particle type. An overview of the different models for obtaining hysteresis loops, and their assumptions, is given in Refs. [107–109]. In literature, SLP values of a few 100 W/g are found for MNP, with exceptions of 1650 W/g [110]. Hergt and Dutz assume that through further particle optimization SLP values of 10 000 W/g can be obtained [111]. From the SLP values, the temperature profiles in the targeted tissues can be calculated by heat conduction [112] or by solving the bio-heat equation [113]. In general, temperature increases with the SLP and amount of particles on the site. In order to sustain a temperature the generated heat needs to overcome the heat outflow of the tissue which depends on parameters such as its size and vasculature.

Depending on the achieved temperatures in the tissue, a distinction is made between *hyperthermia* and *thermoablation*. In hyperthermia temperatures range between 41 and 46 °C, while in thermoablation temperatures above 48 °C up to 56 °C are used. In the latter case, cells are irreversibly damaged and cell death may occur after an exposure of only a few minutes [114]. In hyperthermia use is made of the increased heat sensitivity of tumor cells due to their low pH, low oxygen content and nutritional deprivation [17]. Therefore, realizing a temperature of 42 °C for at least 30 minutes can kill them [14]. However, all cells are affected by temperatures above 41 °C as these temperatures have an impact on enzymatic and structural proteins [17] and cell survival rate is determined by temperature and exposure time [106]. Hyperthermia is not only employed for the destruction of tumors, it is also helpful in increasing the permeability of biological barriers (Section 1.1.2) and the blood perfusion of tissues and hence enhances the targeting of MNP [55, 115] (Section 1.2.2). Furthermore, it has been shown that hyperthermia improves therapeutic effects in combination with chemotherapy or radiotherapy at even modest temperatures of 39 and 40 °C [15, 17]. Recently, it has also been associated to heat-induced immune responses of the body towards tumor cells [17, 53, 115].

In 2007, the Jordan group from the Charité in Berlin published the first magnetic hyperthermia experiments in humans [116]. In this experiment, MNP injections were done on multiple sites in the tumor based on MRI data. Then computed tomography (CT) data and planning software, NanoPlan®

(MagForce Nanotechnologies AG, Berlin, Germany) were used to calculate the temperature profiles at a certain magnetic field strength. The study showed that it was possible to increase the temperature in the tumor without patient discomfort. Since then, many hyperthermia experiments have been successfully applied in humans for different type of cancers such as breast, brain and prostate cancer and numerous companies are now working on hyperthermia devices [15, 53, 117]. Furthermore, magnetic hyperthermia has been approved by the FDA for treatment in specific cases. Prigo et al. wrote a nice overview of recent advances in hyperthermia with respect to modeling, measurement techniques and experiments [118].

One of the main challenges reported in previous experiments, is to achieve a homogeneous MNP distribution in the tumor [115]. Using MNP injections, irregular MNP distribution patterns arise, due to the high pressure at the tumor site. Therefore, therapy results vary significantly, because the temperature is not well controlled and distributed throughout the tumor. Homogenous MNP distributions could be achieved with passive or active targeting of the MNP to the tumor. Although, in contrast to MNP injections, the obtained MNP amount in the tumor is much lower and the MNP amounts are not controllable. Additionally, the MNP distribution may vary depending on the pathophysiology of the tumor [115]. The required heat depends on tumor size and is higher for smaller tumors than larger ones due to the increased surface-to-volume ratio. Hergt and Dutz calculated the required SLP in order to heat the tumor by 5 or 15 degrees [111]. This showed that hyperthermia through (homogeneous) injections (assuming MNP amounts between 100 and 10 mg per ml tumor tissue) and active targeting (1 mg/ml) is feasible for tumors with a minimum size of 3 mm and 10 mm respectively.

Another issue observed in some experiments, is that many MNP systems produce a different amount of heat than theoretically calculated. In magnetic hyperthermia, the generated heat is commonly modeled using Eq. (1.15). The assumptions of this model, such as small magnetic fields and non-interacting particles, do not necessarily hold for the considered hyperthermia experiments and employed particle systems, and might thus explain the differences. Dutz et al. also showed a discrepancy between the experimentally measured heat in ferrofluids and the observed heat *in vivo*, which is due to immobilization of the MNP in tumors and cells, hence τ_B (proportional to η, see Eq. (1.5)) is suppressed [119]. Another source of error is that in practice MNP distributions have a lognormal distribution of sizes and as such, the magnetic field parameters will not be ideal for most particles in the system and hence the SLP will be significantly lower. Therefore, researchers started to investigate the effect of various parameters such as dipolar interactions,

particle distribution, biological constraints and magnetic core properties on the generated heat for various MNP [120–122] and modeling approaches are undertaken which include dipolar interactions [73, 123–126].

Also the need of a MNP distribution imaging system is clearly demonstrated here, as therapeutic effects (and hence number of therapies, injections) tremendously depend on the MNP distribution [127].

1.2.4 Contrast enhancement

MNP have also found applications in the enhancement of imaging techniques in which they overcome sensitivity or resolution problems, i.e. they improve the imaging contrast. This way, imaging techniques are made suitable to monitor and measure biological processes by visualizing cells and molecules, called *molecular imaging* [128]. The most important example thereof is MRI. MRI provides anatomical images with a very fine resolution, large soft tissue contrast and utilizes no radiation [129]. Nevertheless, its sensitivity is too low to accurately measure cells and molecules. First the principles behind MRI are explained to understand how MNP can increase the sensitivity of MRI. In MRI a large homogeneous magnetic field, **B**, is generated (in the order of a few T), which results in a measurable net magnetization originating from the protons, referred to as the longitudinal magnetization. The protons precess around the direction of **B** with a characteristic frequency called the *Larmor frequency*:

$$\omega_0 = \gamma B \tag{1.16}$$

with γ the gyromagnetic constant which equals $2.67{\cdot}10^8$ $\mathrm{rad\,s^{-1}T^{-1}}$ in the case of a proton. When additionally a perpendicular time-varying magnetic pulse is applied with frequency ω_0, the protons will absorb energy from this field, referred to as *resonant absorption*. The net magnetization of the protons changes direction due to this absorbed energy. Certain pulses exist that rotate the magnetization over specific angles of 90° and 180°. When the pulse is removed, the protons relax to equilibrium (aligned with **B**) in two ways: 1) through longitudinal relaxation, T_1, in which the longitudinal magnetization is regained due to loss of energy to the surrounding tissue and 2) through transverse relaxation, T_2, in which the transverse magnetization (net magnetization perpendicular to **B**) decays due to loss of phase coherence between the protons. This dephasing originates from interactions between the protons and small changes in their local magnetic field which affect their Lamor frequency. Figure 1.7 gives an overview of the different steps in a MRI experiment for the case of a 90° pulse.

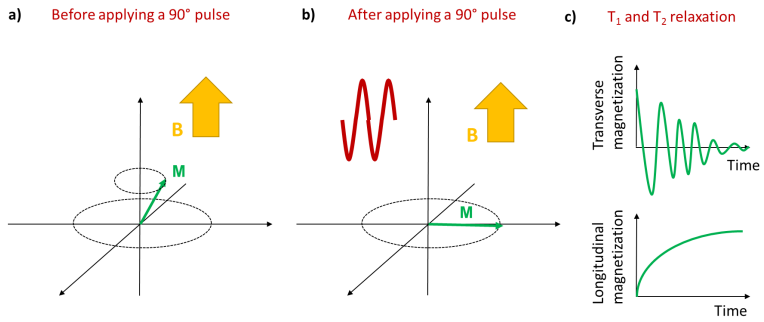

Figure 1.7: a) The longitudinal magnetization of the proton precesses at the characteristic Larmor frequency around the direction of **B**. b) When a 90° pulse is applied, the proton's magnetization becomes transverse. c) After removal of the pulse, the protons relax to equilibrium through T_1 and T_2 relaxation.

Tissues can be separated based on their varying relaxation times, which are reflected in grayscale values. MRX images can be T_1 or T_2 weighted. In the first type, tissues expressing a fast T_1 relaxation, have a bright signal in the obtained image, while tissues with longer T_1 relaxation, result in dark values. In the latter type, tissues with a fast T_2 relaxation have a dark signal. Although MRI has a fine resolution, in some cases it is a challenge to create enough contrast between pathological tissue and its surrounding healthy tissue. This contrast can be achieved by introducing MRI contrast agents which speed up T_1 and/or T_2 at the unhealthy tissue. Contrast agents typically employed in MRI, consist of a heavy metal ion, such as gadolinium or manganese, which is encompassed by a chelate that is used to make the agent non-toxic. Similar as for MNP (Section 1.1.2), the biodistribution of the contrast agent depends on the chelate properties. For example, some contrast agents have a long residence time in the vascular system, making them ideal for visualizing blood vessels. Likewise, smart contrast agents exist that react on changes of biochemical parameters such as pH, temperature or oxygen pressure. In general, MNP are considered as safer contrast agents for MRI, because they consist out of iron oxide. Moreover, the particles express an increased sensitivity and have many tailorable properties that make them ideal contrast agents [130]. Although MNP have been mostly used as T_2 contrast agents, they can also be employed as T_1 contrast agents, or even have both contrast mechanisms simultaneously [131–134]. Furthermore, by functionalizing the MNP, they can target specific diseases/molecules and as such give contrast where it is needed. Additionally, they can be adapted by adding radioisotopes or fluorescent molecules to be visible in other imaging modalities such as SPECT/PET and optical imaging which have, in contrast

to MRI, a high sensitivity [135–137]. Combining these modalities with MRI (i.e. *multi-modal imaging*) can significantly increase image accuracy.

To be a proper T_2 contrast agent, the MNP should have a high magnetic moment, as this changes the local field of the protons and hence, the protons dephase faster. This can be achieved by using larger particle sizes (**m** is proportional to V_c, see Eq. (1.3)), changing the particle's composition (for example metal doping to boost M_{sat}) and producing specific shapes and MNP clusters that promote an increased magnetic moment. Similarly, T_1 contrast is realized by having unpaired electrons at the surface of the particle (canted surface spins) that improve energy exchange with the protons. T_1 is improved by increasing the portion of canted surface spins, by decreasing particle size and doping the particle with rare-earth metals that disrupt spin ordering. Finally, specific particle shapes exist that enhance energy interaction with the protons. More details about MNP properties and their relaxation effects can be found in Refs. [131, 133]. A nice overview of biomedical applications using MRI with MNP as contrast agents (detection of lymph nodes, atherosclerotic plaques, inflammatory responses, macrophages infiltration and cell imaging) can be found in Ref. [55].

MNP with high T_2 contrast can generate artifacts, which present themselves as dark regions, referred to as *blooming effects*. These blooming effects can obscure the pathological tissue and healthy tissue and therefore it is difficult to locate them. Furthermore, artifacts, which can be both dark or bright signals, arise in MRI images due to air, fat and blood clots. Therefore, it is hard to make the distinction between MNP signals, artifacts and low tissue signals [133, 138, 139]. Additionally, MRI experiments had to be delayed in some cases by several hours in order to reduce blood circulating MNP and their resulting artifacts [132]. Fortunately, MNP artifacts can be reduced by employing specific MRI pulse sequences, although these require specialized MRI scanners [131] (Section 1.3.2). Also recently, MNP were developed that express as well improved T_1 as T_2 relaxation to overcome problems with differentiating between artifacts and pathological conditions. Now self-confirmation of the pathology is possible in T_1 and in T_2 weighted images [132, 133]. This problem could also be solved by combining MRI with MPI, because MPI allows to determine the position of the particles non-invasively without background signal [44] (Section 1.3.3).

MNP are also used as contrast agents in ultrasound (US). US is a non-ionizing, portable and cost-efficient imaging technique and allows imaging in real-time. It requires the use of contrast agents to improve its sensitivity and resolution to enable molecular imaging. Microbubbles have been used

before, but these are not small enough to cross biological barriers (Section 1.1.2) and have stability issues. On the other hand, iron oxide NP are too small to be visualized in US and show low reflexivity [140]. To enable MNP detection with US, a pulsed magnetic field gradient (6 - 10 ms) is applied, which exerts a force on the MNP, see Eq. (1.12). It is then possible to map the magnetically induced internal displacement of the tissue with US. This technique is referred to as pulsed magnetomotive (MM) ultrasound and has been successfully applied in the visualization of xenograft tumors and MNP loaded cells [141, 142]. Similarly, in magneto acoustic tomography, μsecond magnetic pulses are applied to the MNP to realize acoustic vibrations in the medium which can be measured with US [143, 144]. Another way of improving the resolution of US, is used in photoacoustic imaging. In this technique efficient light absorbing NP are excited with laser pulses which are converted into heat that is measurable as acoustic waves in US [145, 146]. MM ultrasound and photoacoustic imaging are combined in MM photoacoustic imaging, which further improved imaging performances [147–150]. The MM principle has also been employed in optical imaging methods, such as in MM optical coherence tomography [151].

1.3. State-of-the-art magnetic nanoparticle imaging techniques

1.3.1 Introduction

The previous sections clearly showed the need of a quantitative imaging technique to determine the biodistribution of the MNP. It can be used to investigate the clearance time and biological fate of different particle types (Section 1.1.2), and the therapeutic effect of magnetic targeting and hyperthermia can be determined (Sections 1.2.2 and 1.2.3). Moreover, the technique could be used to further improve the accuracy of other imaging modalities (Section 1.2.4). Ideally, it should be able to capture the versatile nature of particle distributions, as some particles will form clustered configurations and chains, while others remain separated. Their behavior also depends on their surroundings. It has, for example, been observed that MNP in cells and tumors can be immobilized, which affects how they react to magnetic fields. It would thus be beneficial if the imaging technique could monitor particle interactions and possible binding state to targets or therapeutics. Furthermore, the technique should work on many particle types, preferably allow the imaging of multiple particle types simultaneously, be non-invasive, cost-efficient and allow real-time monitoring. Moreover, it should be able to *quantify* small MNP amounts (in the order of μg Fe ml^{-1} [152]) in the case of drug targeting and larger MNP amounts in the case of hyperthermia (in the order of 10 - 100 mg Fe ml^{-1} [111]). Finally, the obtained images should have a fine resolution and be acquired using short measurement times.

In this section an overview is given of the main approaches and their recent advances for determining the MNP distribution. For each technique its respective advantages and drawbacks are discussed. First, approaches with well-established clinical techniques such as MRI, CT and US are considered. Then newly developed techniques, based on magnetic field measurements, are described such as MPI, susceptibility magnitude imaging and AC susceptibility imaging. These latter techniques have the advantage that they measure the particles directly through their intrinsic magnetic properties in contrast to clinically available techniques such as MRI, CT and US. EPR and MRX are separately discussed in Chapters 2 and 3, as these methods were specifically adopted in this dissertation for reconstructing MNP distributions. An overview is given in Fig. 1.8.

1.3.2 Established imaging techniques

The working principles of MRI were explained in Section 1.2.4. There it was shown that MNP are mainly used as contrast agents in MRI to allow molecu-

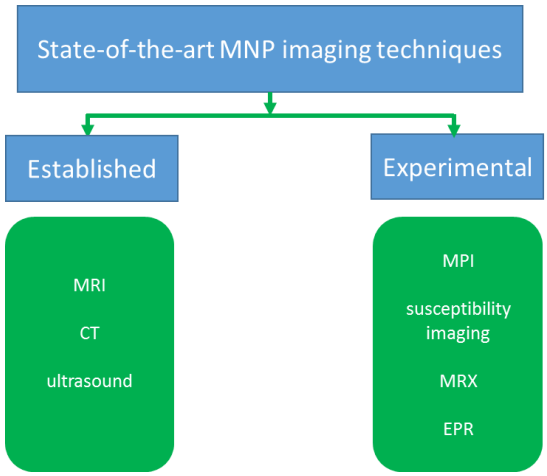

Figure 1.8: Overview of the discussed state-of-the-art MNP imaging techniques. MNP imaging using established techniques (MRI, CT, ultrasound) is in general indirect, which makes them at the moment less suitable than the newly developed (experimental) techniques such as MPI, susceptibility imaging, MRX and EPR.

lar imaging. Over the last 10 years, many approaches have been undertaken to quantify MRI data [153], however MRI is rather a semi-quantitative analysis technique for MNP distributions because it is prone to many artifacts [139]. Nevertheless, the effect of the particles on the protons' relaxation can be employed to detect and quantify MNP. Because MNP are mainly used as T_2 contrast agents, the first (qualitative) attempts of recovering MNP locations were with T_2 mapping [154]. As the MNP amount increases, T_2 becomes faster, at a certain MNP amount resulting in signal loss. In general using these techniques, qualitative information of the MNP can be obtained up until 0.1 mg Fe/mL [155, 156]. Applications such as hyperthermia require larger MNP amounts which results in a short T_2, and thus signal loss. Hence, it is difficult to obtain quantitative information about the MNP when using traditional imaging sequences [157, 158]. Recently, specialized imaging sequences, such as SWIFT [155, 158, 159], UTE [138, 160] and PETRA [161], are being developed that allow to obtain quantitative information by investigating the MNP's slower T_1 relaxation. This way it is possible to measure MNP concentrations up until 3.2 mg Fe/mL, with resolutions of ≈ 200 μm. Nevertheless, these techniques require state-of-the-art scanners and significant programming. Consequently, translation to a clinical environment might be difficult [162]. Furthermore, the impact of a single MNP on the proton's signal is assumed to be the same, while in practice it will depend on clustering behavior of the MNP, their distribution, cell internalization, particle degradation and

the microstructure of the tissue [155]. Moreover, *in vivo* signal artifacts, such as flow and organ movement, complicate the relationship between MNP amount and relaxation. Therefore the particle's impact will vary both in time as space [153]. All this combined, can lead to modeling errors of up to 30 % [160]. Recent studies now perform mapping of various parameters (i.e. multiparametric mapping) such as T_1, T_2, field inhomogeneities and magnetic susceptibility to further improve MNP information [162, 163]. Sillerud found using this approach a detection limit of 0.1 μg Fe/mL with MRI. Note that the mentioned Fe amounts greatly depend on the used MRI setup, imaging sequence and particle system, but give a general idea about the sensitivity and limitations of MRI. In the context of further improving multiparametric mapping, quantitative susceptibility mapping (QSM) is very promising, as it results in quantitative measurements of the magnetic susceptibility distribution related to the phase information in the magnetic resonance signals [164, 165]. On the other hand the technique requires solving a complex ill-posed inverse problem and suffers from susceptibility jumps at tissue boundaries and magnetic field variations in the scanner [153, 162]. As can be observed, still many challenges exist for MRI to become a quantitative method for recovering MNP biodistributions and therefore it is now mostly used in MNP studies to give a qualitative idea of the MNP distribution and to provide background anatomical information. For example, MRI has been used together with MPI (see Section 1.3.3) [44].

Another clinically established method is CT. It measures the absorption of X-rays in materials. In a clinical setting, the patient is placed in the scanner and X-rays are generated by an X-ray tube, which can rotate around the patient. The detector measures the attenuation of the X-rays and is opposite to the source on the other side of the patient and turns together with the source [166]. The CT scan results in images with values representing the amount of absorption of the X-rays. A high grey value (in Hounsfield units) represents a high attenuation of the X-rays. Although CT does not directly detect MNP (in general it has a resolution between 50 - 200 μm [17, 86]), their accumulation results in a region with higher density, thus increasing X-ray absorption. In contrast to MRI, it only allows the detection of high amounts of MNP, starting from MNP amounts $>$ 10 mg Fe/mL [156, 167]. Therefore, CT has been employed in clinical studies with hyperthermia, and hence large MNP amounts, in which it was used to visualize intra-tumoral MNP injections and to calculate the achieved heating [116, 117] (Section 1.2.3). Quantitative approaches are under development with μCT, a smaller version of CT with resolutions of a few μm, in which the sample is rotating instead of the X-ray tube and detector [168]. It allows the visualization of specimen up to 6 cm in dimension [169]. First steps towards quantitative mapping have been done *ex vivo* by relating Hounsfield units directly to the MNP amount [169, 170], using μCT in combination with MRX [171] and by relating the Hounsfield units to

MNP concentrations obtained with a vibrating sample magnetometer [172] and MRX [152]. Bayer et al. believe it is possible to quantitatively reconstruct MNP distributions with only 0.044 mg Fe/mL and a resolution of 56 μm, as such μCT could be employed in drug targeting experiments (although *ex vivo*).

In Section 1.2.4 US was introduced. This section showed how MNP could be employed to enable molecular imaging with US. Nevertheless, these techniques can also be used to visualize the MNP distribution. Magneto acoustic tomography, for example, has been able to visualize the qualitative MNP distribution in prostate tumors in mice with a resolution of 1.5 mm [144]. It is believed that when the technique will be extended for varying magnetic fields, it will be possible to obtain quantitative information up to a depth of 10 cm. Using MM US, is possible to determine MNP locations, interaction and accumulation, due to the MNP's effect on the US signal [142, 173, 174]. On the other hand, there is a relatively uniform displacement in the magnetically labeled tissues and therefore MM US does not allow to visualize variations in the MNP distribution [148]. Photoacoustic imaging has also been successful at imaging of MNP, although it suffers from background tissue signals [145, 147, 148]. These background signals cover the NP's signal or are misclassified as originating from the NP while coming from endogenous sources such as hemoglobin. By combining MM US and photoacoustic imaging into MM photoacoustic imaging, it was possible to remove background signals (as these did not move due to the magnetic field) and to visualize MNP variations in the distribution based on the photoacoustic signal. Nevertheless, the technique was inherently sensitive to physiological motion of the tissue and therefore recently *cyclic* MM photoacoustic imaging was introduced in which field pulses are timed and signal time coherence with respect to these pulses is used to separate magnetically induced motion from background motions [149, 150]. This way it was possible to visualize cancer cells *in vivo* in a mouse. Although this technique can be very promising for recovering MNP distributions, this has not been validated. The largest drawback of these US techniques is the limited penetration depth of a few cm, although resolutions in the μmeter range are achievable.

1.3.3 Experimental imaging techniques

Magnetic particle imaging

In 2005, Gleich and Weizenecker presented a new measurement technique for the quantitative visualization of MNP distributions, referred to as magnetic particle imaging or MPI [43]. The technique makes use of the non-linear magnetic dynamics of the MNP and their saturation behavior. In the first

generation of MPI, a large time-independent magnetic field, (the *selection field*) is applied except in one point, the field-free point. MNP are brought into saturation by the large magnetic field (see Section 1.1.3 for details on the magnetic dynamics of the MNP). When additionally an oscillating field (the *modulation field*) is applied, the MNP at the FFP express a time-dependent magnetization, while MNP outside the FFP stay saturated. Due to the non-linear MNP dynamics, the time-dependent magnetization contains harmonics of the oscillating field. Figures 1.9a) and b) depict the principle of MPI for particles at the FFP and outside the FFP respectively. Using this approach, only the MNP at the FFP respond to the modulation field.

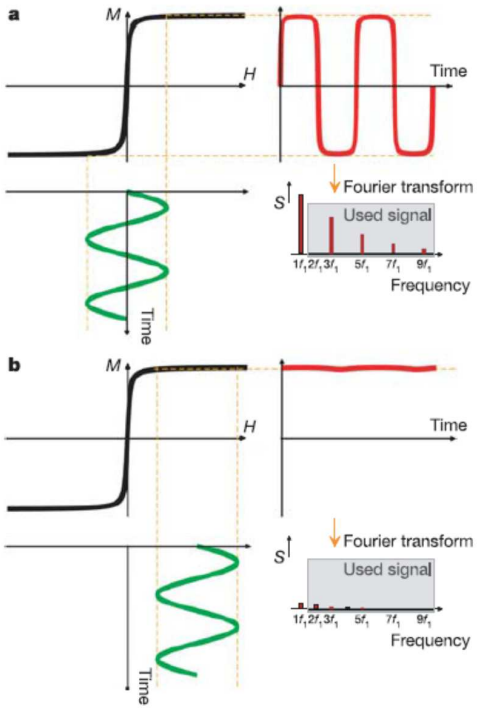

Figure 1.9: a) When an alternating magnetic field of sufficient amplitude (green curve) is applied to MNP, their non-linear magnetic dynamics (black curve) result in a magnetization (red curve) having the frequency of the AC field and a series of harmonics. This represents the situation for MNP at the FFP. b) MNP exposed to a time constant magnetic field of sufficient amplitude and an oscillating field stay in saturation, hence their magnetization does not vary in time. This is the case for MNP outside the FFP. Figure taken from [43].

The amplitude of the harmonics in the obtained spectrum is related to the MNP amount at the FFP. The frequency of the modulation field is not used

in determining the MNP amount, as it is difficult to separate the signal of the modulation field from the signal of the MNP. By moving the FFP over the region of interest a tomographic image of this region can be obtained. This can be done by moving the sample or the coil setup generating the magnetic fields. This results in slow scanning speeds, therefore additionally so-called *drive coils* are employed. These are coil pairs that generate a time-varying homogenous magnetic field in between them. By placing 3 pairs orthogonally, it is possible to change the three coordinates of the FFP. Typically, the coil pairs are driven with sinusoidal currents with a high frequency to generate fast and continuous trajectories over the sample. High currents are required to cancel the selection field at the edges of the sample. In this approach, signals in the measurement coil with harmonics of the drive frequency are induced. This originates from changes in local magnetization at each new location of the FFP. Hence, the drive coils now act as the modulation field. The theoretically achievable resolution according to Gleich and Weizenecker is $2H_K/G$ with H_K the amplitude of the anisotropy field, in which lower values express larger non-linearity of the magnetic dynamics, and G being the gradient of the selection field. Starting from magnetic field values of $2H_K$, particles are assumed to be in the non-linear region of their magnetization dynamics.

In order to reconstruct MNP distributions of a given particle type, the relationship for the MPI system between measured harmonics and spatial position of the particle type, which depends on magnetic dynamics, needs to be known. Therefore a sample with known MNP amount of the given particle type is placed at each position and the resulting harmonics are measured. This is the so-called *system function*. Simulations of the MPI signal (i.e. forward simulations) can then be done using this system function. The MNP distribution is found by solving an inverse problem which minimizes the differences between simulated and actual MPI measurements. For more details on forward simulations, inverse problems and MNP reconstruction procedures, we refer to Section 1.4. By using mechanical movement of the sample and one drive coil pair, Gleich and Weizenecker showed it was possible to reconstruct a 2D (9.4×9.4 mm^2) MNP distribution with a resolution of 0.5 mm [43]. In 2007, an extensive simulation study was done to predict 2D image quality for different field of views, MNP properties, MNP concentrations, resolutions and acquisition times in which the FFP was magnetically moved on a 2D Lissajous trajectory [175]. The study showed that MPI can have fast encoding and acquisition times and sufficient resolution for biomedical applications. This was experimentally validated in 2008, in which a 2D MNP distribution (9.4×9.4 mm^2), having dots of 28 mg Fe/mL, was reconstructed [176]. The reconstruction had a resolution of < 1 mm and could be acquired in 4 ms,

although an accurate reconstruction took 40 ms. In 2009 MPI was used for the real-time imaging of Resovist® particles *in vivo* and in 3D. Resovist® is a discontinued MNP-based contrast agent in MRI that is often employed in MPI. Three drive coil pairs were employed, so that the FFP could follow a 3D Lissajous trajectory. This way the flow of a Resovist® MNP bolus through a beating mouse heart (field of view: $20.4 \times 12 \times 16.8$ mm^3) could be visualized with a high spatial (approximately 2 mm) and temporal (21.5 ms) resolution.

MPI is a very popular imaging technique with promising results. Hence, since 2005, many groups have been working on MPI and developed their own setups and imaging approaches, which significantly differ from the first MPI generation described above. The next paragraphs try to summarize the recent advancements in the MPI community. In general the research is focused on 6 topics: development of 1) MPI systems, 2) acquisition schemes, 3) image reconstruction procedures, 4) particles with a high MPI signal and their accurate dynamic modeling, 5) applications making use of MPI and 6) measurement and safety procedures with smart coil designs to allow MPI for humans. Each paragraph is dedicated towards a certain topic.

Although many MPI systems are under development, they still operate at similar frequencies. The drive fields are around 25 kHz and have an amplitude of about 10-20 mT and the FFP gradients are between 1-7 T/(μ_0m). Most noteworthy is the development of single-sided scanners in which all the coils generating and measuring the magnetic fields are placed on one side of the object of interest [46, 177]. The single-sided configuration overcomes sample size limitations in the conventional design, where closely positioned coil pairs were employed because of the required large magnetic fields. At the moment only 1D imaging is possible with the single-sided scanner and penetration depth is limited to 15 - 24 mm. Additionally, the resolution becomes coarser for increasing distances to the scanner. Another configuration for MPI applies a small static field perpendicular to the oscillating field [178]. This allows to generate the MPI signal perpendicular to the oscillating field. In the first generation of MPI, this signal was parallel to the oscillating field and therefore required harmonic filtering and oscillating magnetic field compensation.

Additionally, research has been conducted on new acquisition schemes. In the case of a FFP, the most suitable trajectories, that result in a dense and fast acquisition and in quantitative reconstructions, are Lissajous and radial figures [179]. It was found in 2D simulations, that when using a field-free line instead of a field-free point, a significant increase in image quality and acquisition speed could be obtained [45]. This is due to the fact that more voxels contribute simultaneously to the signal and hence the SNR increases.

This concept was recently validated in 2D experiments [180] and used to reconstruct 3D MNP distributions using a filtered backprojection similar as in CT [181].

Two main reconstruction approaches are found in MPI. The first approach, which was also employed in the first generation of MPI, uses the measured system function. Here, research is directed towards the structure and properties of the system function [182] with the goal to reduce its time-consuming measurement and redundant information. This way sparser representations can be found of the system function, memory requirements reduced and MNP reconstructions sped up. The measurement time of the system function and its inherent noise can also be reduced by modeling (parts of) the system function. Therefore a lot of research in this approach is also oriented towards modeling the system function. Knopp et al. successfully applied a hybrid system function (i.e. a modeled system function and few measurements) to experimental data from a single-sided scanner [183]. Recently, basis transformations were applied to the system function to enable compressed sensing [184], which reduced measurement positions of the system function significantly. The measurement positions could be further reduced, without significantly affecting the image quality, when taking into account MPI symmetries [185]. The transformations have also been used to reduce the noise floor [186]. Additionally, the system response function can be adapted to improve reconstruction results, by giving more or less weight to certain harmonics in the system function [47]. The second reconstruction approach, called x-space MPI, is based on a theoretical framework. In this framework a MNP image can be expressed, under certain assumptions, as a convolution between the spatial MNP distribution and a point spread function (PSF) [48, 180, 187–189]. Image reconstruction is done by relating the raw signal to the known position (with velocity correction) of the FFP trajectory. X-space does not require a system function and allows fast, real-time and robust reconstructions of MNP distributions. Moreover, the framework allows the easy determination of several imaging parameters such as resolution, SNR and bandwidth [187]. Recently, a hybrid procedure was presented in which system function and x-space approaches were combined [190]. Neural networks have also been applied in simulations to reduce the required data, although reconstruction time significantly increases [191].

A lot of work still needs to be done on finding suitable MNP (tracers) for MPI [192]. In practice, the suitability of MNP for MPI is measured with a magnetic particle spectrometer (MPS), which works similar to MPI but without spatial encoding [193]. Gleich and Weizenecker predicted in their initial experiment that only 3% of the Resovist® particles contributed to the MPI signal [43].

Hence, SNR in MPI could be drastically improved if MPI tracers could be optimized, so they fully contribute. Eberbeck et al. attributed the Resovist® performance to a bimodal size distribution with a peak at 4 nm diameter (the actual MNP) and a peak at about 20 nm (the particle aggregations). The peak at 20 nm explained the good MPI performance of Resovist®. Indeed, larger particles have a higher magnetic moment ($\mathbf{m}$ is proportional to d_c^3, see Eq. (1.3)) and hence produce more measurable harmonics which increase the SNR of the MPI signal [175, 182, 187, 193]. Moreover, as previously mentioned, the resolution is determined by how easily the particles saturate (H_K). By employing dynamic magnetic separation it is possible to select only the larger diameters contributing to the MPI signal, which resulted in a signal increase of 100 % for Resovist® [195]. The MNP employed in MPI have at least a diameter of 15 nm. Because these particles are easily removed from the bloodstream (see Section 1.1.2), they limit particle imaging to only a few minutes. Therefore, in parallel, research is directed towards finding appropriate coating for the particles to allow prolonged imaging. First steps towards permanent 3D real-time visualization of the vessel tree have been set by the recent visualization, 24 hours after injection, of long circulating MNP encapsulated in red blood cells [196]. Resovist® concentration was in the order of 2.8 μg Fe/mL. Besides size distribution and clearance time, tracer performance is also affected by the MNP's delayed response to the applied oscillating fields. In practice the MNP will lag behind the oscillating field and this lag increases for larger MNP (see Section 1.1.3 for more details). Relaxation phenomena in MPI can result in localization errors of the MNP, decrease in SNR and image artifacts, such as asymmetric blurring in the scan direction of the system [197, 198]. Ferguson et al. were one of the first who took MNP relaxation into account and also experimentally validated the effect of MNP properties on the MPI signal. They showed that the particles should be preferably monodisperse with the largest size allowed, determined by their desired relaxation time τ_{eff} (Eq. (1.6)) (which depends on the drive field frequency, see Section 1.1.3) [199]. Currently many groups are working on investigating and manufacturing optimized tracers for MPI and preserving relaxation dynamics *in vivo* [200–209]. Recently, in order to increase reconstruction quality, attempts at incorporating relaxation dynamics into the x-space reconstruction procedure have been introduced [188, 197, 210]. It has also been observed in the system function approach that the MPI signal suffers from changes due to particle variations from batch to batch, particle interactions, disintegration of the MNP and differences in MNP aggregation and dynamics for various biological environments [182, 196, 208, 211–214].

Many efforts are undertaken in developing applications for MPI. In some of these applications, it is a desired property of the system function to be

dependent on particle environment and characteristics. This is for example useful in assessing molecular binding state, viscosity, temperature or cell-labeling efficiency of the MNP and in quantifying multiple MNP types in MPS [215–219]. In MPI this effect has been used to image blood coagulation [220] and to enable the imaging of multiple particle types simultaneously, by incorporating multiple MNP system functions in the reconstruction process. In the latter application, each particle type has a certain color in the final image, hence it is often referred to as *multi-color magnetic particle imaging* [221]. MPI multi-color has also been applied for the separation of a MNP-coated interventional device (guide wire) from MNP in a vessel [222]. Multi-color image reconstructions could be further enhanced by extending MPI to multiple frequencies. This has been done in *mobility MPI*. In this approach the mobility (i.e. viscosity) of the MNP is mapped using a similar reconstruction procedure as in multi-color MPI. At the moment, only a 1D proof of concept of mobility MPI, without quantitative information, has been presented[223]. Many MNP-based applications benefit from MPI's real-time imaging possibilities and its high resolution. Subsequently, the use of MPI in these applications resulted in an improved efficiency and patient safety of the applications and allowed to assess and predict their therapeutic performance. Examples in literature can be found in the case of magnetic hyperthermia [127, 224–226], magnetic targeting [227] and (longterm, 4-87 days) cell tracking [82, 228, 229]. This way, first steps are set toward theranostic applications. It is expected that more applications will follow soon, as the possibility recently emerged to buy pre-clinical MPI scanners for small animal imaging purposes from Bruker and Magnetic Insight at a respective cost of 3 million and 700 000 €. This should significantly lower the entry barriers to this field as it removes the difficult requirement of building and controlling excitation and gradient coils having a large power consumption.

One drawback still observed in the applications described above, is the small field of view. Meeting power requirements of the coils and handling noise levels will become even more demanding when MPI scanners are scaled to human size [230]. Therefore, to allow a large field of view and sufficient resolution in human MPI experiments, the FFP needs to be enabled to shift far enough using sufficient steep gradients. Hence, large currents in the coils and large magnetic fields are required. Another important consideration are safety-limits for these large time-dependent magnetic fields. They can induce currents that heat up the body, and/or can stimulate peripheral and cardiac nerves (i.e. magneto-stimulation). The generated specific absorption rate (SAR) due to this current-induced heating, is limited by the FDA to 4 W/kg [187]. When moving to human-sized setups, and thus when large fields of view are considered, SAR might become a problem, especially considering

the fact that MPI setups now already have a SAR of about 2 W/kg and might thus exceed the restrictions [231]. In hyperthermia for example, the product of the magnetic field and amplitude is limited, to not exceed the induced current safety threshold (Section 1.2.3). This boundary is the limiting threshold in the frequency range of hundredths of kHz [15]. Saritas et al. determined that it is not the SAR but magneto-stimulation, that is the critical safety limit for the frequencies used in MPI and therefore performed human magneto-stimulation experiments. They found a peak-to-peak value of 15 mT in the human torso for frequencies between 25 and 50 kHz [232]. Fortunately, this limit can be overcome, by using higher frequencies (although these increase the SAR again) [207, 230]. To reduce the required power of the drive fields and SAR, smart coil designs, including combinations of Maxwell coils, single-side devices and interleaved multi-layer coils, are being developed with optimized varying currents flowing trough them [233, 234]. To obtain a large field of view, so-called focus fields are employed [235]. These magnetic fields shift very slowly in time, while the fast drive-fields encode the current focus field position. The reconstructions for different focus field positions are then combined to acquire the final image. This way a field of view of $50 \times 43 \times 28$ mm^3 could be achieved in the *in vivo* imaging of a mouse. Recently, *traveling wave MPI* was introduced, which combines the coil configuration and focus field approaches by using an array of coils and two perpendicular saddle coil pairs. This way two FFPs are created and only low-power gradients are needed [231]. It has been successfully applied in *in vivo* quasi-projections of a mouse with a field of view of $65 \times 25 \times 25$ mm^3 [236]. Another attempt at reducing power requirements, at the moment still for small fields of view, is to use small gradient fields (0.2 T/m) and a small drive field (1.6 mT), but using multiple pickup coils [237].

Susceptibility imaging

In AC susceptibility (ACS) measurements, a sample is exposed to a small alternating magnetic field with varying frequencies, and the in-phase and out-of-phase components (Eqs. (1.10) and (1.11)) of the magnetization are measured. ACS measurements have been commonly employed in the characterization of MNP as the magnetization response of MNP to time-dependent magnetic fields depends on many particle parameters [66, 122, 202, 205, 238–246]. Based on these measurements, Eqs. (1.10) and (1.11)) allow to determine the effective relaxation time (Eq. (1.6)) of the MNP. Note that this model is only valid in case of non-interacting MNP and magnetic field amplitudes in the linear regime. Many groups have worked on equations describing relaxation dynamics in the non-linear regime and for larger magnetic fields [75, 76, 78, 108, 247]. From τ_{eff}, particle parameters such as $P(V_c, V_h)$, binding

state and environment can be obtained using Eqs. (1.4) and (1.5). These Eqs. are approximately correct for the very low magnetic fields employed in ACS.

AC susceptometry can also be employed to determine spatial MNP distributions [49]. The principle is similar to the one used in magnetic susceptibility tomography of para- and diamagnetic materials for their non-destructive evaluation [40, 248]. In magnetic susceptibility tomography of a magnetic sample, the 3D internal distribution of the magnetic susceptibility is obtained, by employing the tomography principle. This principle measures the sample's response (Eqs. (1.1) and (1.2)) to different configurations of magnetic fields. These configurations are obtained by moving the sample, by spatially varying the magnetic fields, or by using multiple measurement sensors. Similar as in MPI, a model simulates the measurements of the sample's response for the different configurations. The MNP distribution is found through solving an inverse problem, which minimizes the differences between simulated and actual measurements (see Section 1.4 for more information on inverse problems). Instead of relating the measurements to a susceptibility distribution, Steinhoff et al. linked them to a distribution of MNP amounts [49]. Indeed, because of the small magnetic fields employed, a linear relationship exists between the magnetization of a voxel and the amount of MNP it contains (see Section 1.1.3, Eqs. (1.7)) and (1.9). Steinhoff et al. showed the possibility of imaging MNP distributions with ACS measurements by moving a MNP sample in a coil that generated the AC field. They observed a difference in sensor signal depending on the position of the MNP sample in the coil. One needs to keep in mind that the magnetic induction of the MNP is several orders smaller than the induction of the applied magnetic field. Therefore it is difficult to separate both signals. Contrary to MPI, the magnetization lies in the linear regime so no harmonics are created in the measurements. Hence, it it not possible to separate the MNP signal by investigating harmonics. Therefore, at least passive compensation is necessary, in which the sensitive axis of the measurement sensor is placed orthogonally with respect to the direction of the externally applied field.

The first MNP reconstructions using ACS measurements were presented in 2014 by Ficko et al. [50]. They used both passive as well as active compensation to increase the sensitivity of the measurements. In active compensation, the feed-through by the AC field is nullified by generating a compensating magnetic field at the position of the sensor. Their setup consists of three *drive* coils that produce the AC field, two Fluxgate magnetometers that measure the magnetic induction and two *compensation* coils that nullify the AC field at the position of their corresponding sensor. Figure 1.10 depicts an overview of their susceptibility magnitude imaging (SMI) setup. MNP response was kept

in the linear range by limiting the generated magnetic fields to 10 - 100 μT in the imaging region. The drive coils had unique frequencies of 625, 725 and 825 Hz which were activated simultaneously. By using a digital lock-in amplifier the resulting in- and out-of-phase components for each frequency can be separated. Similar as in the system function approach in MPI, a well-known MNP amount is measured at each position and the resulting measurements are used to obtain the forward model of the setup. This calibration is needed to take into account uncertainties in sensor and coil manufacturing, hardware delays and magnetic dynamics of the particles. Using this first prototype setup, 1D imaging of MNP distributed over 6 voxels with a resolution of 1 cm was possible. A depth sensitivity of 2 cm with respect to the fluxgate sensor for a MNP sample of 12.5 mg Fe mL^{-1} was obtained. For this approach to be accurate, the dynamic susceptibility should be accurately known.

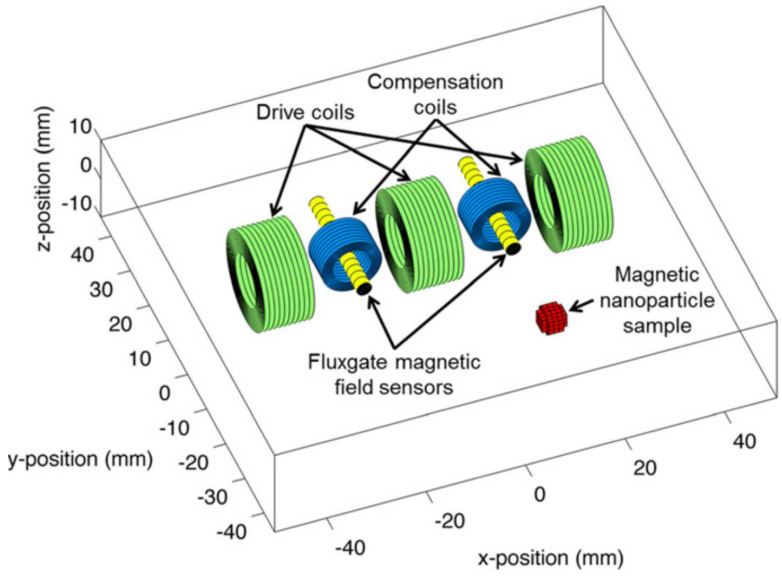

Figure 1.10: Overview of the setup presented by Ficko et al.. The drive coils generate the AC field. The fluxgates measure the magnetic induction from the MNP. The residual AC field at the position of the fluxgates is compensated by the compensation coils. Figure taken from [50].

Another possibility in the linear regime is to time-multiplex coils with a sequence of frequencies, i.e. each coil has a unique frequency that is changed after a predefined amount of measurement time, until each coil has been driven with each frequency [249]. This approach is called AC susceptibility imaging (ASI) and, in contrast to SMI, it allows to determine the dynamic

susceptibility and amount of the MNP. Hence, this extension allows to image multiple types of MNP simultaneously and the dynamic susceptibility does not need to be known. In a first step the in- and out-of-phase susceptibilities are reconstructed for each frequency. Using these susceptibilities it is then possible to determine the MNP amount through least-squares fitting by comparing to the susceptibility values in the same voxels of the MNP types with a known amount. Ficko et al. showed that using SMI for multiple particle types resulted in cross-talk, while this is not the case for ASI.

SMI can be improved when the magnetic field amplitudes are increased to about 5 mT to enable non-linear MNP responses i.e. non-linear SMI [250]. Similar as in MPI, particle saturation creates frequency harmonics. Moreover, because the drive coils each have their own frequency (instead of only 1 frequency as in MPI), signal components at intermodulation frequencies appear. Due to the harmonics and intermodulation, no compensation coils are needed, which significantly reduces hardware complexity. It is further reduced by using only two drive coils and one sensor. Next to the drive coils permanent magnets are placed, this way AC and DC gradients are generated in the imaging field. They aid in the spatial encoding of the MNP, because the degree of saturation, and hence the generated harmonics, vary spatially. Ficko et al. found that by using the signal at harmonics and intermodulation frequencies, the *ill-posedness* of the inverse problem (Section 1.4) significantly decreased and image quality improved. Moreover, time-multiplexing methods (varying of amplitude, phase and frequency of the coils in time) were applied and shown to be further enhancing image quality, although they require longer acquisition times. Recently, a non-linear SMI setup was introduced with 3 drive coils each with 327 and 350 Hz signals, 3 detection coils, 3 stacks of permanent magnets and 61 cylindrical wells with a spacing of 5 mm [251]. By using a phase encoding scheme, in which the phase between both signals for every coil is changed, and measuring harmonics and intermodulation frequencies, huge amounts of data could be generated, which allowed dense 2D reconstructions of complex MNP patterns. Recently, a combination of non-linear SMI and time-multiplexing with a sequence of frequencies (similar to ASI, but in the non-linear region) was developed to quantitatively determine the bound and unbound MNP to different cell lines, although imaging has not yet been performed [252]. Similar as in MPI, efforts are undertaken to accurately model non-linear dynamic MNP behavior [253]. Therefore, measurements of MNP magnetization dynamics have been done for various magnetic field frequencies, amplitudes and DC magnetic fields. Using these measurements to build a Volterra model, first attempts at capturing the non-linear MNP dynamics could be achieved. A model-based system function could overcome the time-consuming empirical calibration,

such as in x-space MPI.

An advantage of the susceptibility imaging techniques presented in this section, is that they can be built from off the shelf components. Depending on requirements, such as the desired field of view, resolution and properties of the employed magnetic field, costs for sample imaging are estimated to be between 6000 to 150 000 €. Currently the company Lodestone Biomedical is working on the first commercial nanoparticle imaging system for histological tissue sections based on these techniques.

1.4. Inverse problems

1.4.1 Introduction

In this dissertation two techniques are developed for determining the spatial MNP distribution, namely EPR (chapter 2) and MRX (chapter 3). Both techniques have in common that they solve an *inverse problem*. Also other state-of-the art MNP imaging techniques such as MPI and susceptibility imaging (Section 1.3.3) require use of an inverse problem. Therefore, this section explains the basic principles behind inverse problems and discusses how to solve them to obtain accurate MNP reconstructions using these techniques.

An inverse problem relates certain external measurements or observations to parameters of the system under investigation. The required number of observations depends greatly on the model used to describe the system, its assumptions and the wanted model parameters. In this work *magnetic* inverse problems are studied, in which the observations are typically magnetic field values at certain spatial positions and time points, and the considered systems are magnetic sources (here MNP ensembles). A detailed description of magnetic inverse problems, using SQUIDs as measurement devices of the magnetic fields, can be found in Ref. [254]. More specifically, the magnetic inverse problem in this work is stated as follows: *What is the spatial distribution of the MNP, taking into account the measurements of their magnetic dynamics?* EPR and MRX have a different way of obtaining the observations, but both can relate their measurements to the spatial MNP distribution. In order to link the spatial distribution to the observations, a model is required, referred to as the *forward* model. The forward model simulates the measurements starting from a given MNP distribution, and the inverse problem minimizes the differences between the model solution and the measurements to obtain the MNP distribution. Figure 1.11 depicts the relationship between the forward model and inverse problem for the specific problem considered in this dissertation. Section 1.4.2 describes the general forward model and Section 1.4.3 discusses different ways of finding the inverse solution, each with their respective drawbacks and advantages. In Section 1.4.4, it is explained how adaptations in the forward model and inverse reconstruction procedure can be quantified. This allows to compare the performance of the various methods developed in this dissertation and to assess their reconstruction accuracy.

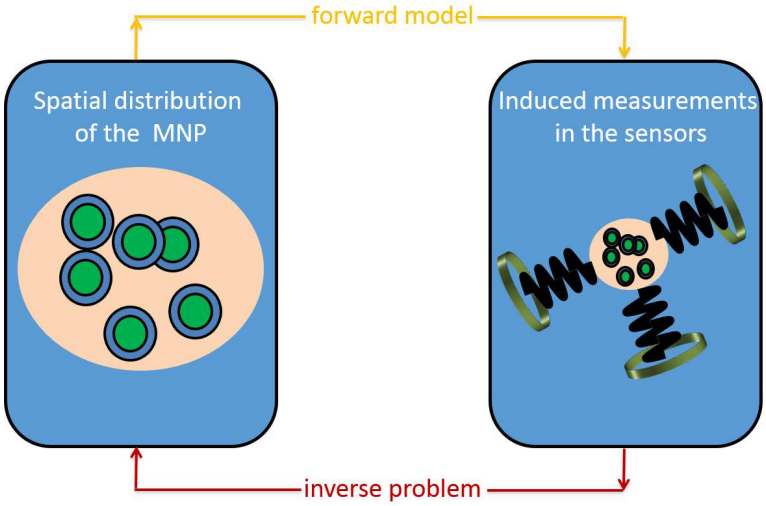

Figure 1.11: Relationship between the forward model and the inverse problem. The forward model calculates the signal in the sensor for a given MNP distribution, while the inverse problem reconstructs the MNP distribution starting from the actual measurements. The found distribution is the one that minimizes the differences between the model solution and the actual measurements.

1.4.2 Forward modeling

In this part the forward model of magnetic measurements, originating from MNP ensembles, is developed. The forward model should at least depend on the distribution of the MNP and return certain external observations such as magnetic field vectors at certain positions and time points. The MNP ensemble is virtually tessellated into small volume elements with the same size, called *voxels*. Each voxel v has a parameter c_v associated to it. c_v represents the iron (Fe) amount in that voxel, as the MNP considered in this work are iron oxides. The forward model between an MNP amount c_v in voxel v and the signal in sensor s can then be stated as follows:

$$S_{\mathrm{f}_s} = L_{sv} c_v \tag{1.17}$$

S_{f_s} is the modeled signal in sensor s and L_{sv} is the *sensitivity coefficient* that relates the MNP amount in voxel v to the signal in sensor s. Most MNP imaging techniques make use of multiple sensors and analyze the distribution over multiple voxels. Hence, Eq. (1.17) can be extended to V voxels and S sensors:

$$\mathbf{S}_{\mathrm{f}} = \mathbf{L} \cdot \mathbf{c} \tag{1.18}$$

with $\mathbf{c}$ a $V \times 1$ vector containing the V MNP amounts in each voxel, $\mathbf{L}$ the *sensitivity matrix* (or also sometimes called the gain matrix or lead field matrix), with dimensions $S \times V$, encompassing all the sensitivity coefficients between the voxels and sensors and $\mathbf{S}_\mathrm{f}$, a $S \times 1$ vector, containing the S *simulated* measurement values in the sensors. The values of $\mathbf{L}$ can be obtained in various ways:

1. by modeling the particles' magnetic dynamics, the employed external magnetic fields and the sensor sensitivities [76, 210] (see Sections 1.1.3, 3.1.3 and 3.1.4)
2. by a calibration procedure [43, 50, 255]
3. by a hybrid approach [183, 253] (Section 1.3.3)

The calibration procedure is as follows: a MNP sample with known Fe amount, c_calib, is moved from voxel to voxel and coupled to the resulting sensor signals. It is assumed that a different MNP amount in the voxel generates a signal scaled with $\frac{c_v}{c_\mathrm{calib}}$. This is done in MPI, susceptibility imaging and EPR (Sections 1.3.3, 2.2 and 2.4) and has the drawback that it is time-consuming, especially when there are many voxel positions. Moreover, the magnetic response of the MNP can change from particle batch to batch, depends on setup properties such as magnetic field amplitude and frequency and can suffer from dipolar interactions between the MNP. On the other hand, it allows to take dynamic MNP properties and hardware delays into account which are difficult to model. The modeling procedure of the sensitivity coefficients in MRX is discussed in detail in Section 3.1.4.

Possible sensors for measuring MNP signals include pickup coils [43, 251, 256], magnetoresistive sensors [242, 257], fluxgates [50, 258, 259], SQUIDs [34, 76, 260, 261] and optical magnetometers [262]. $\mathbf{S}_\mathrm{f}$ in Eq. (1.18) is only a general description and, based on the imaging method, might contain a different representation of the measurement data. For example in MPI, the spectrum of the measurements is investigated, so in this case $\mathbf{S}_\mathrm{f}$ represents the amplitude of the different frequency harmonics in the recorded signal. On the other hand, in SMI the in- and out-of-phase components of the MNP response with respect to the magnetic field are used.

A lot of research is conducted towards increasing the stability of the forward model (see Sections 1.4.3 and 1.4.4) and gaining the maximum amount of information from the system through the forward model. Therefore, measurement techniques are extended to bring the MNP in as many states as possible. This can be done in various ways. For example, in some imaging procedures the behavior of the MNP ensemble changes over time and hence, the sensor signal is measured at multiple time instances: $\mathbf{S}_\mathrm{f}$ can then be extended to a $S \times J$ matrix with J the number of time points [37] (Section 3.4). Additionally,

the sample can be moved, in which new measurements are obtained for each sample position n, with N the total number of positions. Hence, $\mathbf{S}_\mathrm{f}$, becomes a $NS \times 1$ vector. This last approach is used in this dissertation to include spatial information in the EPR measurements (see Sections 2.2 and 2.4) [255, 256]. In MRX we obtain additional measurements by applying spatially varying magnetic fields [263] (Section 3.1.4). Consequently, $\mathbf{S}_\mathrm{f}$, becomes a $N_a S \times 1$ vector, with N_a the number of spatially varying magnetic fields. Other approaches include using various magnetic field frequencies [249] and performing mathematical operations on $\mathbf{L}$ [47, 264] (Sections 1.3.3 and 3.3).

1.4.3 Inverse procedure

The MNP distribution can be retrieved by solving an inverse problem that calculates the MNP distribution starting from $\mathbf{S}_\mathrm{m}$. The inverse problem is in most cases *ill-posed*, which means it does not have the three requirements of a well-posed problem (in the sense of Hadamard): 1) a solution exists, 2) it is a unique solution and 3) the solution depends continuously on the input data. More specifically, the solution is determined by the number of observations S with respect to the number of unknowns V. If $S > V$, the problem is *overdetermined* and only an approximation is possible. If $S < V$, the ill-posed inverse problem is *underdetermined* and has multiple solutions resulting in multiple possible MNP distributions. When $S = V$, a unique solution is possible when $\mathbf{L}$ is nonsingular, although in practice, $\mathbf{L}$ is not invertible because it contains linearly dependent information, i.e. the observations are not independent. Hence, the inverse problem determines $\mathbf{c}^*$, starting from the actual measurements $\mathbf{S}_\mathrm{m}$, and minimizes the differences between $\mathbf{S}_\mathrm{m}$ and the model solution $\mathbf{S}_\mathrm{f}$ as a unique solution is not possible. This approximation is often referred to as minimum norm estimates (MNE):

$$\mathbf{c}^* = \arg\min_{\mathbf{c}} \|(\mathbf{L} \cdot \mathbf{c}) - \mathbf{S}_\mathrm{m}\| \tag{1.19}$$

with $\|\cdot\|$ the L2-norm. The solution to this equation is as follows:

$$\mathbf{L}^T\mathbf{L}\mathbf{c}^* = \mathbf{L}^T\mathbf{S}_\mathrm{m} \tag{1.20}$$

with ^{T} the transpose operator. $(\mathbf{L}^T\mathbf{L})$ is invertible when the columns of $\mathbf{L}$ are linearly independent, else its inverse does not exist. In order to still find a solution, a generalized inverse can be obtained, the Moore - Penrose inverse $\mathbf{L}^\dagger$, by calculating the singular value decomposition (SVD) of $\mathbf{L}$ [265]:

$$\mathbf{L}^\dagger = (\mathbf{U}\Sigma\mathbf{V}^T)^\dagger \tag{1.21}$$

Σ is a diagonal matrix containing the eigenvalues of $\mathbf{L}$ and $\mathbf{U}$ and $\mathbf{V}$ are matrices with the left- and right-singular vectors. This generalized inverse can in turn be used to calculate $\mathbf{c}^*$:

$$\mathbf{c}^* = \mathbf{L}^{\dagger}\mathbf{S}_{\mathrm{m}} \tag{1.22}$$

For most MNP imaging methods, this solution suffers from instability issues such as errors in the data and rounding errors in which small variations in $\mathbf{S}_{\mathrm{m}}$, result in large changes for $\mathbf{c}^*$. Therefore, additionally regularization techniques are applied that damp instabilities while trying to maintain accurate approximate solutions. In this work the SVD is truncated, so that only eigenvalues larger than σ_r contribute and the solution becomes more stable [266]:

$$\mathbf{c}^* = \mathbf{L}_r^{\dagger}\mathbf{S}_{\mathrm{m}} \tag{1.23}$$

The smaller eigenvalues, which have the largest impact on the inverse problem, correspond to instabilities and noise sources and the higher eigenvalues are related to the signal space. Therefore, it is important to select the right r, hence only instabilities and noise are removed. This approach has been applied in many MNP reconstruction procedures [37, 42, 50, 263]. Another popular approach in MNP imaging is to use a Tikhonov regularization term [36, 175, 267]:

$$\mathbf{c}^* = \arg\min_{\mathbf{c}}(\|(\mathbf{L}\cdot\mathbf{c}) - \mathbf{S}_{\mathrm{m}}\| + \|\mathbf{\Gamma}\cdot\mathbf{c}\|) \tag{1.24}$$

$\mathbf{\Gamma}$ is the Tikhonov matrix and is often chosen to be $\lambda\mathbf{I}$ (with $\mathbf{I}$ the identity matrix), such that small amplitude MNP distributions are favored (zero order regularization) or preference is given to a solution with certain smoothness or low-pass behavior in which derivatives (first and second order) of $\mathbf{L}$ are used for $\mathbf{\Gamma}$. The solution then becomes:

$$(\mathbf{L}^T\mathbf{L} + \mathbf{\Gamma}^T\mathbf{\Gamma})^{-1}\mathbf{L}^T\mathbf{S}_m \tag{1.25}$$

Combined with Eq. (1.21) and $\mathbf{\Gamma} = \lambda\mathbf{I}$, it becomes clear that the Tikhonov regularization filters eigenvalues which are small compared to λ, while keeping those that are large with respect to λ. It is a smoother filter than the truncated version (Eq. (1.23), which has a sharp cut-off at σ_r. Although in both approaches sharp edges in the MNP distribution are difficult to reconstruct due to the penalization of the L2-norm. In general, both approaches perform well on smooth MNP distributions. The problems with sharp edges can be reduced in the Tikhonov approach by using for example the L1-norm and a derivative of $\mathbf{L}$ as $\mathbf{\Gamma}$. The Tikhonov approach has the drawback that the regularization parameter is continuous and hence difficult to determine, while in the truncated SVD it has a discrete character. One needs to take care that when too much regularization is imposed (i.e. a very smooth solution) larger

deviations from the data fit occur (Eq. (1.19)), although instabilities have less impact. When the regularization is too low, a good data fit is obtained, although the solution is dominated by instabilities and will hence have a large norm. A popular approach to determine the regularization parameter (discrete and continuous) is the L-curve, in which a log-log plot is made of the norm of the fit error (Eq. 1.19) and the norm of the solution ($\|\mathbf{c}^*\|$) for each value of the regularization parameter [268]. This way, insight is gained in their respective trade-offs. In this work the truncated SVD is employed for the reconstruction of smooth distributions.

In this work Eq. (1.19) is also solved iteratively using the non-negative least squares (NNLS) approach with the constraint that the solution $\mathbf{c}^*$ should only contain elements ≥ 0. The algorithm is described in detail in [269]. Basically, it adapts the dual vector $\mathbf{w}$ iteratively so that it only has elements ≤ 0:

$$\mathbf{w} = \mathbf{L}^T(\mathbf{S}_\mathrm{m} - \mathbf{L}(\mathbf{c})) \tag{1.26}$$

In contrast to SVD, it performs well on MNP distributions containing sharp edges and it does not allow negative MNP amounts. Therefore, this approach was used in the reconstruction of discontinuous MNP distributions. It has also found its use in other MNP imaging techniques [249, 251, 270]. Another popular iterative reconstruction approach in MNP imaging is called Kaczmarz's algorithm [271]. It has mostly found its use for very large $\mathbf{L}$ in which computing the inversion or factorization is computationally expensive [44, 47, 221]. Moreover, Kaczmarzs algorithm also has the possibility to add *a priori* information into the iteration, such as non-negativity and real-valued MNP amounts.

1.4.4 Quality of reconstructions

As Sections 1.4.2 and 1.4.3 showed, the MNP reconstructions highly depend on the forward model used and the way of solving the inverse problem. A quantitative measure is needed in order to find which adaptations to the forward model increase stability of the inverse problem and which reconstruction approaches generate improved reconstruction results. Throughout this work different *quality parameters* are used each with a specific target. The most important ones are discussed here.

The main quality parameter is the correlation coefficient (CC). It shows the correspondence between the actual distribution of the MNP $\mathbf{c}_\mathrm{act}$ and the re-

constructed distribution $\mathbf{c}^*$ [263, 272] and it is calculated as follows:

$$CC = \frac{\sum_{v=1}^{V}(c_v^* - \bar{c^*})(c_{\text{act}_v} - \bar{c_{\text{act}}})}{\sqrt{\sum_{v=1}^{V}(c_v^* - \bar{c^*})^2 \sum_{v=1}^{V}(c_{\text{act}_v} - \bar{c_{\text{act}}})^2}} \tag{1.27}$$

$\bar{c^*}$ and $\bar{c_{\text{act}}}$ are the averages of the reconstructed and actual MNP amount. A CC of 1 implies a perfect reconstruction. Two other important measures that reflect reconstruction quality are the mean and standard difference between $\mathbf{c}_{\text{act}}$ and $\mathbf{c}^*$, denoted as μ and σ respectively. Reconstruction quality is additionally affected by stability of the sensitivity matrix $\mathbf{L}$. The condition number β captures the rate of decrease in amplitude of the eigenvalues (Eq. (1.21)). β is defined as:

$$\beta(\mathbf{L}) = \frac{\sigma_{\text{max}}}{\sigma_{\text{avg}}} \tag{1.28}$$

with σ_{max} and σ_{avg} the maximum and average eigenvalues respectively. This definition of β, instead of the more common definition $\frac{\sigma_{\text{max}}}{\sigma_{\text{min}}}$ (with σ_{min} the minimum eigenvalue), makes the calculation of the condition number less sensitive to numerical errors [39]. Moreover, it depends to a decreased extent on the smaller eigenvalues, therefore it is more convenient to compare sensitivity matrices of different dimensions. β should be as low as possible. This evaluation is closely related to the eigenvalue analysis in this dissertation, in which the normalized eigenvalues of the sensitivity matrix are visualized and arranged according to their sizes. In practice, slower decaying eigenvalues are favorable. The last quality parameter is the spatial sensitivity $\mathbf{S}_{\text{p}}$. It is a measure for the impact of a voxel on the measurements and is calculated by taking the column norm of the sensitivity matrix [42, 272].

2

Electron paramagnetic resonance

This chapter starts with a general introduction to electron paramagnetic resonance (EPR). It highlights the differences with MRI that works on similar principles. The general introduction also discusses biomedical applications of EPR and the initially used EPR setup (Section 2.1). This setup can accurately quantify MNP amounts, but does not allow to determine MNP distributions. In Section 2.2 methods are developed that extend the capabilities of the EPR setup to 1D imaging. In a next step, the robustness of the newly developed technique is investigated by analyzing the impact of different errors and setup parameters (Section 2.3). In Section 2.4 the EPR imaging method is extended to 2D and 3D imaging. To realize quantitative 2D/3D MNP reconstructions, requirements for the EPR setup are formulated and a new measurement procedure is introduced. In Section 2.5 the technique is significantly sped up and its accuracy and stability are increased by introducing specific magnetic field configurations in the setup.

2.1. Basic concepts

2.1.1 Introduction

EPR is a measurement technique based on the absorption of electromagnetic radiation by a sample containing unpaired electrons placed in a constant magnetic field [273, 274]. In general, the irradiation frequency is kept fixed and the magnetic field amplitude is varied. For each static field value, the absorption (in practice the derivative of the absorption) is measured to obtain an absorption spectrum of the sample. It is also possible to operate at fixed magnetic field values and excite the sample with a radiation pulse. EPR finds applications amongst others in the fields of physics, chemistry, biology, medicine, archeology, geology, mineralogy, radiation damage, and radiation dosimetry [275]. EPR is sometimes also called electron spin resonance or electron magnetic resonance. The latter expresses the analogy to nuclear magnetic resonance (NMR) spectroscopy and its use in the well-known MRI. We refer to Section 1.2.4 for the NMR working principles used in MRI and to Section 1.3.2 in the specific case of MNP imaging. EPR and NMR both consider the interaction between electromagnetic radiation and magnetic moments. NMR however, studies the magnetic moments of nuclei rather than electrons [274]. The progress in EPR imaging has been noticeably slow compared to MRI, especially considering the fact that Zavoisky already measured the EPR phenomenon in 1944 [276], which was three years before the NMR measurements by Bloch [277]. This is caused by several technical challenges, especially in the case of *in vivo* EPR due to the physical and chemical differences between the resonant species (electrons in EPR and mainly protons in MRI) which can be summarized as follows [278, 279]:

- The magnetic moment of the unpaired electron is significantly larger than the magnetic moment of a proton, resulting in the requirement of higher frequencies for a given magnetic field to achieve the resonance condition. This is reflected in their gyromagnetic constants, see Eq. (1.16), in which γ equals $1.76{\cdot}10^{11}$ rad s^{-1}T^{-1} in the case of an electron and $2.67{\cdot}10^{8}$ rad s^{-1}T^{-1} in the case of a proton.
- The associated relaxation times of the electrons are in the nanoseconds to microseconds range, whereas for protons these are between milliseconds and seconds.
- Only a limited amount of paramagnetic elements can be found in the body. Protons on the other hand are abundant.

Note that the points, discussed above, showed the case of MRI using protons, but in fact each nucleus with a net spin can be used such as carbon, nitrogen, phosphorus and fluorine. Except for above mentioned points, the principles behind EPR are the same as those explained in Section 1.2.4. The differences between EPR and NMR have three important consequences [278]. We list

them here below.

Firstly, most commercial EPR setups use frequencies at 9 GHz with magnetic field amplitudes of 0.34 T, due to the readily availability of the required hardware components. These EPR setups are referred to as X-band EPR setups because of their frequencies situated in the X-band range (8 - 12 GHz) of the electromagnetic spectrum. At these frequencies, sample sizes for the setup are restricted to 1 mm due to non-resonant absorption of water. Frequencies lower than 1.2 GHz (in the case of excised organs) and preferably between 250 - 500 MHz (in the case of *in vivo* EPR) must be applied to avoid non-resonant absorption of water and to allow sufficient penetration into the tissue, although at the drawback of a lowered sensitivity and spatial resolution [278, 280]. EPR scanners operating at 1 GHz (L-band, 1-2 GHz) already allow sample sizes of 1 cm [281]. Especially, noteworthy are the 300 MHz EPR scanners employing the same frequency as clinical MRI setups. They can hence be easily combined for anatomical imaging through MRI [282]. In recent years, a tendency towards developing high frequency EPR setups operating at 3.4T/95 GHz up to 12.8T/360 GHz is observed to allow extremely sensitive measurements with a high resolution [283]. As these techniques are not suitable for *in vivo* imaging we do not detail these.

Secondly, in MRI and NMR it is common practice to excite the sample with radiation pulses. In the case of EPR it becomes technically challenging to implement pulsed irradiation (pulsed EPR), because of the fast relaxation dynamics of the unpaired electrons. Therefore, the sample is mostly irradiated continuously with a low-power wave at fixed frequency, called continuous wave (CW) EPR. The resonance condition is then reached by sweeping the magnetic field. Nevertheless, pulses have been shown to increase sensitivity and information content of the measured signal compared to CW techniques [283]. Therefore, in the last years also pulsed EPR setups have been under development, although few groups are able to overcome the technical hurdles and care should be taken that the high-intensity pulses do not exceed SAR regulations [279, 282, 284, 285]. A detailed comparison between pulsed and CW excitation procedures on a 300 MHz EPR scanner, in the specific case of *in vivo* imaging, has been described by Yamada et al. [286]. The study showed, among others, that the pulsed excitation limits the number of possible paramagnetic compounds and can generate artifacts, although it has an increased sensitivity and resolution compared to CW. On the other hand, CW was able to produce artifact-free images, did not limit tracers, but required significantly more measurement time. To remove the artifacts in pulsed EPR, many innovative reconstruction algorithms have found their way, although in general most EPR images are reconstructed by filtered backprojection

methods similar as in CT [280, 284, 285].

Thirdly, since EPR can only measure unpaired electrons and most stable molecules only have paired electrons, EPR has a larger specificity compared to MRI. Hence, it is more sensitive in detecting free radicals produced in certain pathological conditions. On the other hand, in the case of *in vivo* imaging, it necessitates the injection of paramagnetic compounds, so-called tracers, in order to overcome the lack of endogenous paramagnetic samples [278]. Therefore, a lot of research is conducted towards tracer development, as the tracers should be non-toxic with optimized pharmaceutical properties and require simple EPR spectra that can be acquired at room temperature [287]. An advantage of using tracers, is the ability to analyze the local environment of their unpaired electrons by inspecting changes in their EPR spectrum. For example, spectrum broadening of the tracer occurs in the presence of the paramagnetic material oxygen. Hence, it is possible to measure oxygen concentration, as the broadening is directly related to the oxygen amount. This principle has also been successfully applied to assess pH, charge and microviscosity of tissues both *in vitro* and *in vivo* [278, 279, 288, 289]. An overview of the most important biomedical applications using EPR is given in Section 2.1.2.

In general, a EPR setup consists of three main components: a source that generates the electromagnetic wave, the sample, and a detector that measures the changes in absorption by the sample. In order to amplify the small absorption signals, the sample needs to be placed in a resonator. In general, a cavity is employed as resonator. A cavity is simply a metal box of certain dimensions that allows it to resonate with the electromagnetic waves. When the cavity is in resonance, it stores the energy of the wave and hence the electromagnetic wave remains in the cavity. The cavity is tuned as such that it is in resonance with the applied electromagnetic wave. When the sample absorbs energy (i.e. the sample is in resonance due to the right magnetic field value), the cavity is no longer critically coupled with the source and hence the wave is reflected out of the cavity. This is the EPR signal. The sensitivity is further improved by using a phase sensitive detection. To realize this, the magnetic field at the sample is modulated sinusoidally at a certain modulation frequency, so that, when in resonance, the EPR signal becomes a sine at the modulation frequency. The phase sensitive detection only allows signals having the modulation frequency, so that system noise and electrical interference can be suppressed. As the EPR signal is linear along the modulation amplitude, the amplitude of the modulated signal is proportional to the derivative of the sample's absorption. In section 2.1.3 the EPR setup employed in this

dissertation is described.

2.1.2 Biomedical applications

It is clear from the previous section that EPR has several properties that make it suitable for many biomedical applications. For example, EPR has a high sensitivity compared to NMR, because of the electron's higher γ, and has the ability to probe the immediate environment. Therefore, EPR imaging has found its use in many clinical applications [279, 288, 289], with the most widespread application being EPR oximetry [290]. EPR oximetry encompasses the possibly repeated, long-term and accurate mapping of the oxygen distribution in different tissues. These measurements influence diagnosis and therapy directly, especially in the case of oncology, peripheral vascular diseases and wound healing [287, 288, 291]. For example the tumor oxygen status determines the success of various cancer therapies such as chemotherapy and allows targeted treatment planning. Currently, research is performed on upscaling from small animals to humans, with the first experiments running on humans [289]. Another important *in vivo* application is EPR dosimetry [289, 292]. In EPR dosimetry the presence of radiation-induced free radicals in calcified tissues such as teeth and fingernails can be determined. This way the radiation dosages after a major radiological incident can be assessed.

Of specific importance for this dissertation is the use of EPR for *in vivo* imaging of MNP distributions. EPR studies have been mostly targeted towards the quantification of MNP amounts in tissues. In 1992, Iannone et al. were the first to use EPR (X-band, CW) to detect and quantify MNP amounts [293]. They determined the MNP amount in the liver, spleen, blood and bone marrow *ex vivo* by using biopsies. This was achieved by measuring the EPR spectra (which correspond to the first derivative of the absorption, see Section 2.1.1) for known MNP amounts in blood and buffer solutions. Then in each measurement, the known MNP amount was related to the intensity of the EPR signal at the MNP's resonance condition by taking the double integral of the measured first derivative absorption spectrum. It was found that the MNP amount was linearly related to the intensity of the EPR signal. For both blood and buffer solutions the same calibration curve was obtained. The calibration curve was then used to determine MNP amount in the experimental spectra from the biopsies.

This principle has been used to determine (*ex vivo*) elimination kinetics and MNP biodistributions of various MNP types in different tissues [294–297]

even over the course of 3 months [298]. EPR has also been employed to assess cell labeling efficiency for different cell and MNP types by evaluating MNP uptake by cells [299, 300] and to monitor the fate of those labeled cells *ex vivo* [297, 301]. These studies all confirmed that in each organ, containing MNP, a similar resonance peak could be observed as for the calibration measurements and this peak was not present in organs without MNP. Moreover, they noted that the resonance peak only represented the MNP amount and was hence distinguishable from the resonance frequency of other sources of iron in the body. Therefore, it was possible to monitor the degradation of the MNP, by relating the measured MNP amount to techniques measuring total iron amount in the body [298]. Figure 2.1 depicts the two main MNP applications in which EPR is used to estimate the MNP amount, namely cell tracking and the determination of the MNP biodistribution. EPR is also mentioned as a possible technique for unambiguously determining the source of the MRI signal, i.e. if the low signal is arising from e.g. tissues, MNP, blood cloths or air (see also Section 1.2.4) [279, 300]. The Fe quantification limit for X-band EPR is in the order of nanogrammes Fe/mL, which is very sensitive compared to previous MNP imaging techniques described in Section 1.3.

The first *in vivo* experiments were performed in 2002, by Fujii et al. using both L-band (for *in vivo* measurements of the liver) and X-band (for biopsies) CW EPR [302]. Next, *in vivo* experiments were focused on the evaluation of molecular markers (MNP with targeting possibilities) in which it was measured how many MNP reached the target [281, 303]. This was done both *in vivo* with L-band for measuring kinetics curves and *in vitro* with X-band for MNP quantification. Attempts at cell tracking *in vivo* with L-band EPR have been made, although the sensitivity was too low to detect the labeled cells and the depth was limited by the use of surface coils [297].

At the moment, no *in vivo* MNP quantification using EPR has been performed, because of the low sensitivity of L-band EPR setups. In general, no experiments have been performed with EPR that showed the spatially varying MNP distribution, only the total MNP amount in biopsies was determined each time. In Section 2.1.3 a recently developed EPR setup with a higher sensitivity is presented that should allow *in vivo* determination of the MNP distribution.

2.1.3 Setup

Previous section showed the need of developing a sensitive EPR spectrometer that operates at low frequencies (250 MHz - 500 MHz) to allow *in vivo* imaging of MNP distributions. Recently, a 300 MHz/10 mT EPR spectrometer was

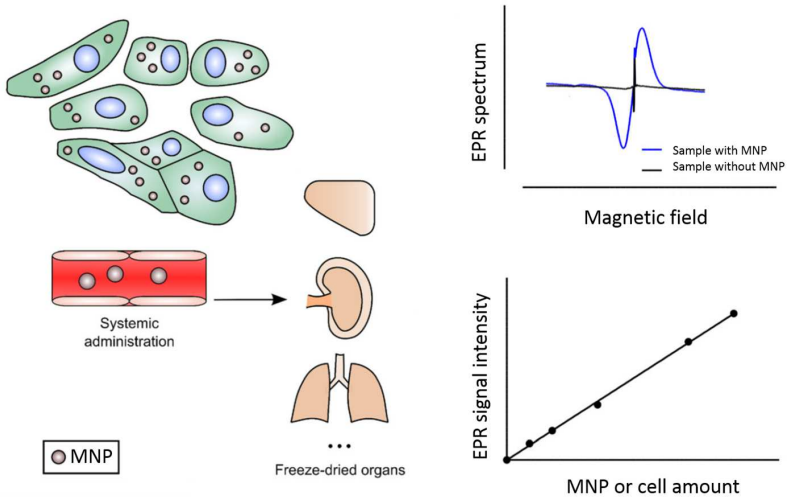

Figure 2.1: EPR is used in the tracking of cells and finding the MNP biodistribution. This is done by relating the measured EPR spectra of excised organs (in the case of L-band EPR) to calibration curves that link the EPR intensity signal to the MNP or MNP-tagged cell amounts. The calibration curve shows a linear relationship between EPR signal intensity (obtained by taking the double integral of the EPR measurements) and MNP amount or number of cells. EPR has the advantage that the signal at the MNP's resonance frequency is only sensitive to the MNP amount and is not affected by endogenous sources of iron. Adapted figure from [279].

developed by the Belgian company PEPRIC NV. PEPRIC NV was founded in 2009 as a spin-off of the institute IMEC, which is a world player in research on nano-electronics. The goal of PEPRIC NV was to build an EPR spectrometer working at a low frequency, and hence low magnetic field, with a sensitivity comparable to EPR setups operating at higher frequencies and magnetic fields. Pulsed as well as CW excitation procedures have been investigated using this setup [304–306]. In this dissertation, measurements were only performed on the 300 MHz CW EPR spectrometer. This section provides an overview of the working principles of the CW setup. These principles are also described in Refs. [51, 52, 305].

Section 2.1.1 mentioned that existing EPR setups use a resonator to amplify the weak absorption signal and measure the absorption or derivative of the absorption by the sample. The proposed setup introduces a new detection method by measuring the MNP directly through their magnetization instead of using their absorption. The setup consists of three orthogonally placed coils: a Helmholtz coil pair that generates the homogeneous magnetic field $\mathbf{B}_0$ with an amplitude of 10 mT, an excitation coil that produces the radio

frequency (RF) wave of 300 MHz with its magnetic field, $\mathbf{B}_1$, perpendicular to $\mathbf{B}_0$, and a pickup coil with measurement axis perpendicular to $\mathbf{B}_0$ and $\mathbf{B}_1$. The excitation and pickup coil are placed orthogonal in order to isolate them from each other and hence to limit feed-through of the RF wave. The sample is positioned in the center of the excitation and pickup coils. Side and top view pictures of the setup are shown in Fig. 2.2 and Fig. 2.3 depicts a schematic representation of sample and coil placement.

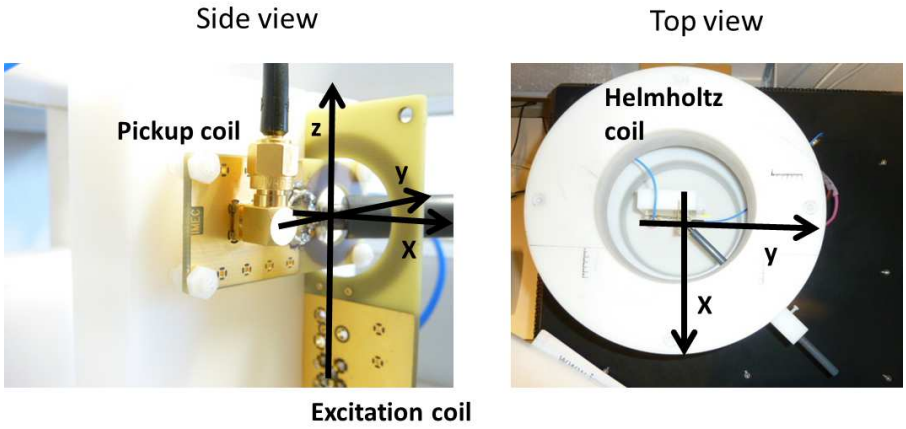

Figure 2.2: Side and top view of the EPR setup with the Helmholtz coil pair, excitation coil and pickup coil. The MNP sample is at the origin of the coordinate system.

The MNP sample is placed in $\mathbf{B}_0$ which aligns the magnetization of the MNP to the direction of $\mathbf{B}_0$. At these low fields, only the MNP produce a measurable magnetization, thanks to their large magnetic susceptibility (Section 1.1.3), while the magnetization of the endogenous iron is negligible. When the sample is irradiated by an electromagnetic wave with $\mathbf{B}_1$ and its frequency chosen equal to the Larmor frequency (Eq. (1.16)), the MNP are in resonance and will absorb energy. This absorption results in a precession of the magnetization at the Larmor frequency around the direction of $\mathbf{B}_0$ at a fixed angle. The angle depends on particle parameters, such as T_1, T_2, the difference between the actual frequency of the RF wave and resonance frequency, and B_1 [274]. Figure 2.4a) shows the magnetization response of a MNP sample placed in the origin of the coordinate system when in resonance for the case of $\mathbf{B}_0$ along the positive **z** axis, $\mathbf{B}_1$ along the positive **x** axis and the pickup coil with its sensitive direction along the **y** axis (the same configuration as in Fig. 2.2). M_y is the magnetization component of the MNP measured by the pickup coil. M_y is proportional to the MNP amount of the sample [52]. Even though the

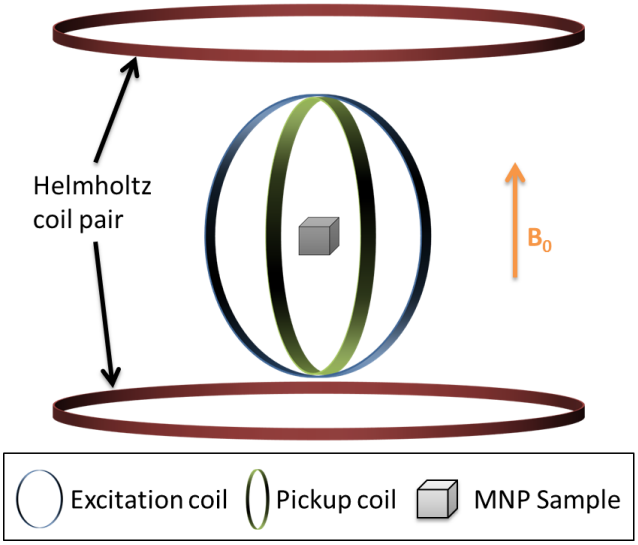

Figure 2.3: Schematic representation of the EPR setup (not to scale).

excitation and pickup coil are placed orthogonally, in practice some RF feed-through is still measured by the pickup coil:

$$\mathbf{V}_{\text{pickup}} = \mathcal{C}(\mathbf{B}_{1\text{att}} + \mu_0 \mathbf{M}_y + \mathbf{n}) \tag{2.1}$$

with

$$\mathbf{B}_{1\text{att}} = B_{1\text{att}} \cos(2\pi f t) \tag{2.2}$$
$$\mathbf{M}_y = M_y \cos(2\pi f t + \phi) \tag{2.3}$$

and $\mathbf{V}_{\text{pickup}}$ is the measurement signal in the sensor at different time points t, $\mathcal{C}$ is a conversion factor expressed in V/T, $B_{1\text{att}}$ is the feed-through of the RF wave, ϕ is the phase difference between the MNP response and the RF excitation wave and $\mathbf{n}$ represents the noise. The frequency f equals 300 MHz. ϕ is approximately 90°, as the electron's Larmor frequency is around 280 MHz for the considered B_0.

Contrary to the EPR setups described above, a magnetic field sweep is no longer necessary, as this setup measures the EPR signal at a fixed frequency and magnetic field amplitude. On the other hand, an AC magnetic field is used instead of a DC field. By temporally varying $\mathbf{B}_0$, the field will have two opposite orientations, in the case of Figure 2.4, along positive (Fig. 2.4a)) and negative (Fig. 2.4b)) $\mathbf{z}$ values respectively. Hence, $\mathbf{M}_y$ has the opposite sense

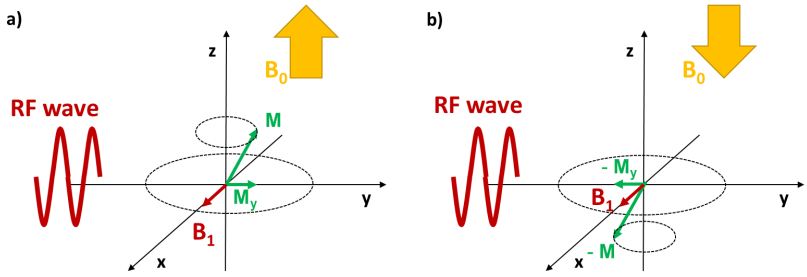

Figure 2.4: a) When a MNP sample is placed in a magnetic field $\mathbf{B}_0$ and additionally radiated by an electromagnetic wave at the Larmor frequency, its magnetization precesses around the direction of $\mathbf{B}_0$ at an fixed angle. In this case $\mathbf{B}_0$ is directed towards positive **z** values. b) When $\mathbf{B}_0$ is directed towards negative **z** direction, the measured magnetization component $\mathbf{M}_y$ is now directed towards negative **y** direction.

in both configurations, but the same size. By measuring at these two opposite configurations, and subtracting both measurements, it is possible to further reduce the feed-through of the RF wave and hence increase EPR sensitivity:

$$\mathbf{V}_{\text{sub}} = \mathbf{V}_{\text{pickup}+} - \mathbf{V}_{\text{pickup}-} \tag{2.4}$$

with $\mathbf{V}_{\text{sub}}$ the subtraction of the signals obtained at maximum ($\mathbf{V}_{\text{pickup}+}$) and minimum ($\mathbf{V}_{\text{pickup}-}$) amplitude of $\mathbf{B}_0(t)$.

$$\mathbf{V}_{\text{sub}} = \mathcal{C}\left(2\mu_0 M_y \cos(2\pi f t + \phi) + \mathbf{n}_{\text{att}}\right) \tag{2.5}$$

with $\mathbf{n}_{\text{att}}$ the attenuated noise compared to the noise signal in the pickup coil. The feed-through signal can be obtained by adding both signals. Figure 2.5 visualizes the phases of the different signals and Fig. 2.6 shows the effect of the polarity of $\mathbf{B}_0$. The sensitivity is further increased by taking into account the phase difference of the RF wave and MNP response and only measuring at the zero-crossings of the RF wave, where the RF signal is minimal and $\mathbf{M}_y$ maximal. The noise levels can be reduced by averaging the measured signals for each RF wave and multiple polarities. For example, taking 125 measurements for each field polarization and do this for 400 polarizations $2\times(125\times400)$ results in an averaging of 100 000. By increasing the frequency of $\mathbf{B}_0$ it was shown that the noise could be further reduced [51, 305]. However, increasing the switching rate of $\mathbf{B}_0$, results in less measurements per polarization, therefore a trade-off exists between frequency increase and number of measurements for averaging. The optimal frequency for $\mathbf{B}_0$ of 200 Hz was used in the measurements in this dissertation. In Ref. [305] different sampling and averaging techniques are investigated into detail. Note that the presented methodology is applicable for the broad ranges of parameters mentioned in

Ref. [51], i.e. a electromagnetic wave frequency between 60 and 500 MHz and a magnetic field amplitude between 0 and 50 mT.

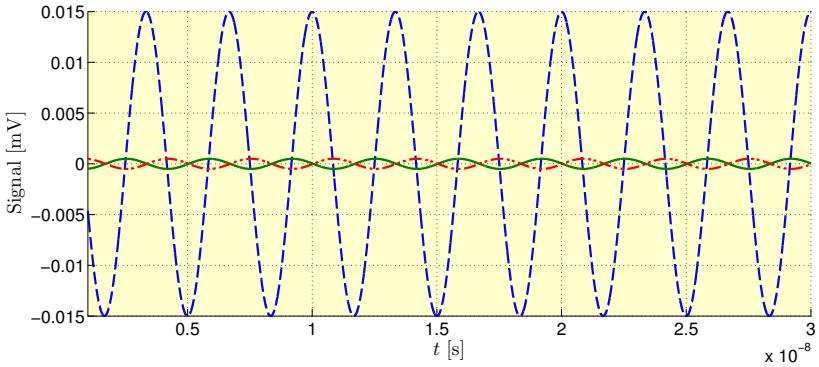

Figure 2.5: Dashed curve: attenuated RF wave, full green line: $\mathbf{M}_y$ in the case of maximum field, dash-dotted line: $\mathbf{M}_y$ in the case of minimal field.

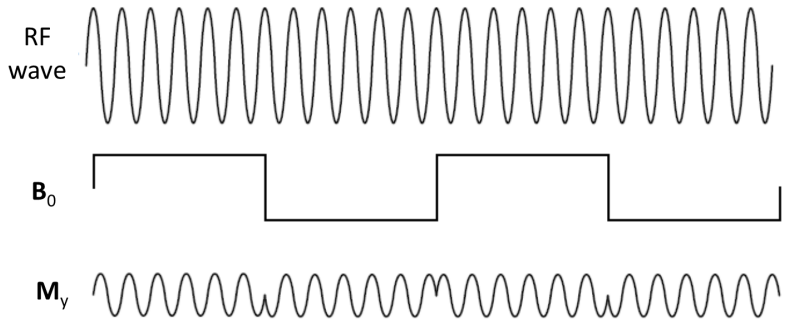

Figure 2.6: Measured MNP response taking into account polarization of $\mathbf{B}_0$. Figure adapted from [305].

Similar as in Section 2.1.2, a calibration curve needs to be measured that links the sensor signals to an MNP amount. Because M_y varies linearly with the MNP amount, the calibration curve is also linear [52]. New samples can then be quantified by relating new measurements to the calibration curve. As the intensity of the measurement signal depends on the temperature, B_0 and B_1, care needs to be taken to keep these parameters stable during the measurements [307]. The setup has been successfully used in *ex vivo* biodistribution

and pharmacokinetic studies of MNP [308, 309] and its sensitivity is in the order of nanogrammes of Fe (depending on particle type) which becomes μg Fe $(\text{mL})^{-1}$ for the typical PCR tubes employed in the setup [52, 309]. The studies showed that this novel detection approach is sensitive, reliable and specific, although it only allows to determine the total MNP amount at the center of the setup and does not tell anything about the spatial MNP distribution in the sample. To allow sensitive measurements of the MNP, strict requirements are imposed on the hardware, such as it should be stable, have low jitter and be low noise. Moreover, a precise control and timing of the acquisition of the measurement signal (see e.g. Fig. 2.6) is necessary. These requirements result in the need of specialized hardware. Fortunately, the setup is commercially available from PEPRIC NV for a price of 220 000 €. Compared to the imaging methods described in Section 1.3, EPR has the potential to become a very sensitive MNP imaging technique if spatial information could be retrieved. In this dissertation methods are presented (Sections 2.2, 2.3 and 2.4) to allow 1D up until 3D imaging of the particle distribution using this setup.

2.2. 1D imaging

2.2.1 Introduction

In this section an approach is developed for assessing the 1D MNP distribution using the CW EPR setup described in Section 2.1.3. As noted before, EPR is able to accurately determine the total MNP amount in a single volume, but does not permit to obtain the MNP distribution throughout this volume. Section 1.3 showed that a large variety of techniques exist to recover the MNP distribution each with their own advantages and drawbacks. EPR has a high potential of becoming a biomagnetic imaging method if spatial information can be extracted from the EPR measurements. Especially, its ability to directly measure the magnetization, contrasting established techniques, is particularly advantageous. Moreover, EPR quantification has been shown to be highly specific, sensitive and accurate and is therefore the ideal candidate to capture the versatile nature of the magnetic particles.

The aim of this section is to recover quantitative 1D reconstructions in order to aid in the progress of many MNP-based applications, such as magnetic hyperthermia, drug targeting and diagnostics (Section 1.2) which require accurate reconstructions. A new approach, that exploits the solution of inverse problems for the correct interpretation of the measured EPR signals is investigated. An advantage of the proposed method is the lack of imaging gradients. Imaging gradients are commonly used in EPR imaging because the image is obtained through filtered backprojection methods. In the backprojection method, different gradient orientations are needed and for every gradient orientation a magnetic field sweep needs to be performed. The addition of gradients would result in an increased complexity of the setup and a higher cost. Our method does not alter the original EPR setup as no additional magnets are needed to create the field gradients and no field sweep is necessary, i.e. the measurements are performed at a fixed magnetic field value.

Here the first results of imaging a 1D distribution of superparamagnetic nanoparticles using low-frequency EPR are presented. Previous approaches applying EPR for the quantification of MNP had no spatial information (Section 2.1.2). Spatial information is retrieved from our EPR measurements by moving the sample through the magnetic field along one direction. Every new position of the sample along the line yields a distinct measurement, asthe field of view of the coils of the EPR setup induces a measurement response which depends on the position of the sample. This way a 1D reconstruction of the MNP distribution is achieved by solving the corresponding inverse problem (Section 1.4). These inverse problems require a forward model being function of the spatial distribution of the MNP, i.e. the forward model

simulates the measurements and is evaluated for different MNP distributions. Figure 2.7 schematically illustrates the methodology.

In Section 2.2.2 the forward model of 1D EPR imaging is detailed and it is explained how the 1D EPR measurements should be performed. In a next step a numerical validation is made of the proposed model and method where artificial measurement data is generated for certain MNP distributions (Section 2.2.3). More specifically, measurement data is created by using synthetic system properties, measured system properties and measured system properties with added noise. Numerical evaluation follows from comparing the reconstructed MNP distributions to the distributions used for generating the measurement data. In a second stage the method is experimentally validated using actual CW EPR measurements as measurement data (Section 2.2.4). The accuracy on the reconstructed MNP amounts is investigated by comparing the calculated reconstruction with the actual magnetic nanoparticle distribution that was placed in the holder. Numerical and experimental validation both happen according to the quality measures described in Section 1.4.4. Measurements are executed on two distinct setups, i.e. a temperature-controlled setup and non-controlled. This allows to evaluate the robustness and universality of the method. Furthermore, the impact of temperature control on the reconstructed distributions can be analyzed. The work in this section has been published in Refs. [256] and [310] and was done in the light of a collaboration project with PEPRIC NV.

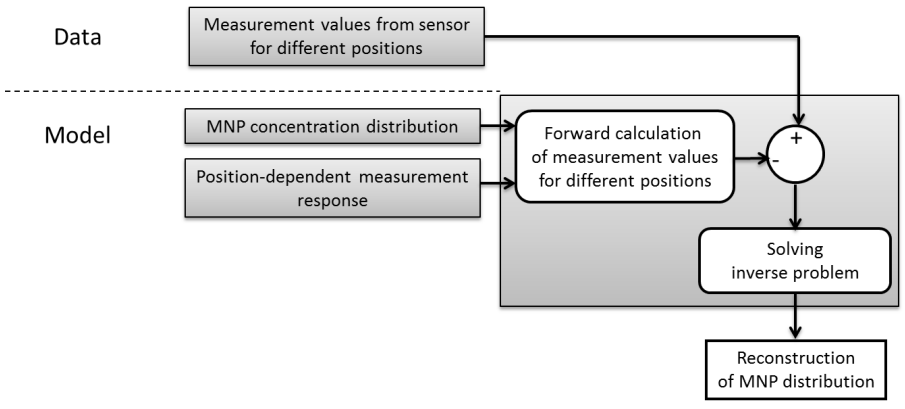

Figure 2.7: Measurement data is interpreted by the model and an inverse problem is solved to recover the MNP distribution.

2.2.2 Forward modeling & measurement procedure

Here, the forward model and measurement procedure for 1D EPR imaging of MNP distributions is developed. In order to relate particle distribution properties to EPR measurements, measurement data needs to be induced in the pickup coil that includes information on particle location. This is achieved by moving the sample along a line through $\mathbf{B}_0$, which yields position-dependent measurements. In the specific case of this section, the sample is moved along the **xy** axis (see Fig. 2.8a)) in the region where $\mathbf{B}_0$ and $\mathbf{B}_1$ can be measured. The position-dependent response of the particles is included in the forward model by measuring a well-known MNP amount on the different positions in $\mathbf{B}_0$. This model allows to simulate EPR measurement data for various MNP distributions, as the particles' response on each position, linearly depends on particle amount. This way, by solving an inverse problem, 1D imaging can be realized.

In a standard measurement approach with EPR, the sample is fixed in the origin of the coordinate system. This is also the place where the excitation and pickup coil are positioned (see Figs. 2.2 and 2.3). The first step of our method is the calibration procedure. The system response function is determined in a similar way as in MPI and susceptibility imaging (see Sections 1.3.3 and 1.4.2). The calibration sample is moved through $\mathbf{B}_0$ along $x = y$ (called the **xy** axis), see figure 2.8a). In total, the calibration sample is moved to N_{calib} positions with a spacing of ΔN_{calib}. The calibration sample is a tube where a single compartment is filled with a well-known MNP amount, c_{calib}, expressed in μmol Fe. When the calibration sample is on the edge of the region where $\mathbf{B}_0$ is defined, it is on the point furthest from the excitation and pickup coil. On this position, the electron spins are only moderately excited by the RF wave and only partially registered by the pickup coil, resulting in a relatively small measurement value. The highest measurement value is obtained for $xy = 0$ due to the complete excitation and sensing of the particles in the sample. The response function, $R(n)$, is the degree of particle registration by the system in function of the n'th sample position along **xy**. n is used as a variable instead of xy to keep the representation general. The positions along **xy** are linearly mapped to n. This is also convenient for Sections 2.4 and 2.5 in which the response function is extended to multiple dimensions. The response function corresponds to the measurement values obtained from a unit MNP amount (1 μmol). In case a different MNP amount was used in the calibration, the measurement values are divided by its MNP amount c_{calib}. This can be done because the EPR signal scales linearly with MNP amount. $R(n)$ is defined in the region Ω, which corresponds to the region where $\mathbf{B}_0$ and $\mathbf{B}_1$ can be measured. In the simulations and measurements in this section and Section 2.3 movement of the sample is limited to this region. Figure 2.8b) shows a

typical response function that we measured.

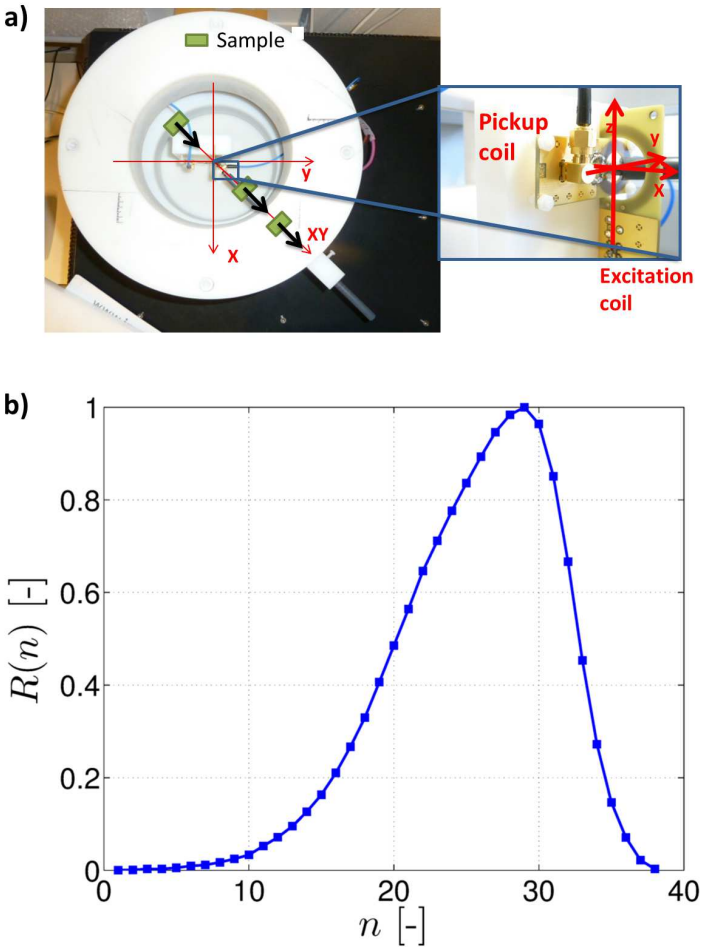

Figure 2.8: a) Definition of the different axes. The particle distribution is obtained by moving the volume under study along **xy**. b) Example of a response function. These are the response values of the EPR setup for the N positions along the **xy** axis or equivalent $n = 1,...,N$.

Let us now consider the measurement of an unknown MNP distribution **c** with particle amounts c_v ($v = 1,...,V$). In our simulations and experiments the particle distribution is contained in a tube consisting of 10 compartments (Fig. 2.9). Each compartment has a length of 2 mm and allows to hold a certain particle amount. The compartments are separated from each other with a spacing of 1 mm. This tube is moved along **xy** in a similar manner as the calibration

sample. To allow for multiple measurements, the sample is measured at N positions along **xy**. A forward model can be reconstructed analogous to Eq. (1.17). A n-th measurement can then be modeled as:

$$S_{\mathrm{f}_n} = \sum_{v=1}^{V} L_{nv} \cdot c_v = \sum_{v=1}^{V} R(n_v) c_v \tag{2.6}$$

L_{nv} is the system's response value for the position n of voxel v, n_v, with amount c_v. The response function acts as a weighting function: when voxel v is in the origin we obtain the actual amount in our signal S_{f_n}, i.e. L_{nv} equals 1, and this value decreases when moving to compartments near the edges of $\mathbf{B}_0$. This implies that compartments positioned near the center have a greater impact on the measured signal. Every new position n of the tube corresponds to a new measurement.

Figure 2.9: Example of a tube with three compartments filled with a certain particle amount. The compartments have a length of 2 mm and are separated by a spacing of 1 mm. In total ten compartments can be used for the representation of various particle distributions. When it is used in the calibration procedure a single compartment is filled.

The set of simulations $S_{\mathrm{f}_n}(n = 1, ..., N)$, with N the number of different positions of the tube are represented by:

$$\mathbf{S}_{\mathrm{f}} = \mathbf{L} \cdot \mathbf{c} \tag{2.7}$$

This equation corresponds with Eq. (1.18) in Section 1.4.2, but has different dimensions as there is only 1 sensor ($S = 1$). Multiple measurements are introduced by moving the sample. The sensitivity matrix **L** used in Eq. (1.18) now only contains information from 1 sensor and N movements, hence it becomes a $N \times V$ matrix. Similarly, it links a MNP distribution to measurements in the pickup coil. $\mathbf{S}_f$ is analogous to Eq. (1.18) and is a $N \times 1$ vector. **c** represents the V MNP amounts in the tube and V depends on the discretization of the tube. These values are *unknown* and need to be recovered.

The stability of **L** depends on $R(n)$, the step sizes ΔN and $\Delta N_{\mathrm{calib}}$ and the ratio of N to V. The ratio determines the type of problem, i.e. overdetermined or underdetermined, see Section 1.4.3. The step sizes reflect the distance between subsequent positions of the sample and calibration sample, respectively. If

$\Delta N > \Delta N_{\text{calib}}$, faster measurements are done compared to the calibration measurement, albeit reconstruction accuracy could change due to increased ill-posedness of the inverse problem. When $\Delta N < \Delta N_{\text{calib}}$, the respective $\mathbf{L}$ values need to be interpolated. This can reduce accuracy, as these interpolated values are not measured. Moreover, the stability of $\mathbf{L}$ might deteriorate due to the addition of linearly dependent information. For more details on this subject, see Section 2.3. In practice, the resolution of $R(n)$ is smaller or equal than the resolution of the measurements. Figure 2.10 explores the construction of $\mathbf{L}$ into detail.

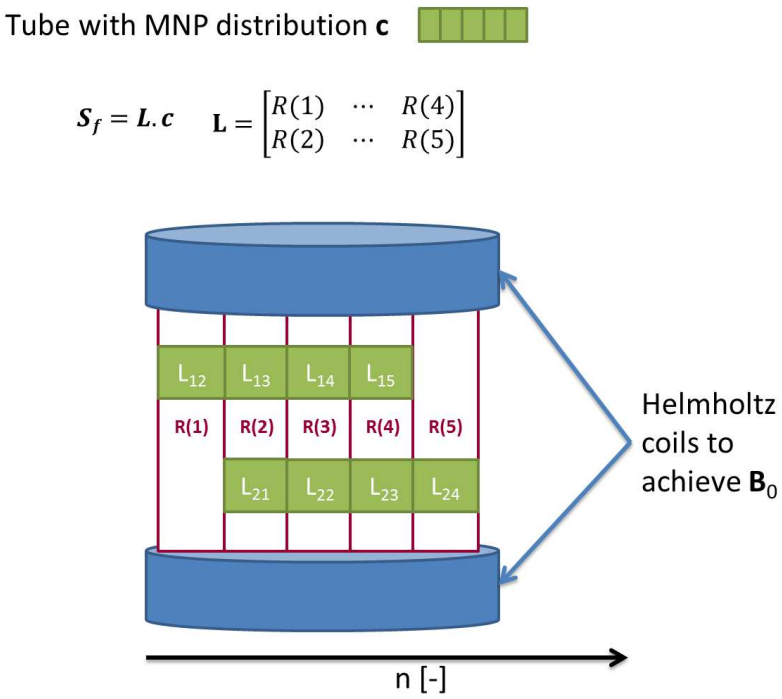

Figure 2.10: Construction of $\mathbf{L}$ for a volume with a certain particle distribution with $V = 5$, $N_{\text{calib}} = 5$, $\Delta N_{\text{calib}} = 1$ mm, $N = 2$ and $\Delta N = 1$ mm.

Equation (2.7) allows to calculate the measured signals in the sensor for different positions of the spatial MNP distribution $\mathbf{c}$. This is the so-called *forward model* for EPR. In practice it is crucial to acquire the response function very precisely, since the accuracy of the forward model depends on the response function. The model can be altered by making modifications, such as changing the positions of the pickup or excitation coil, measuring other

positions of the sample, varying $\mathbf{B}_0$ or by adding theoretical information of the MNP (see Section 1.4.2). The MNP distribution can be obtained by solving the inverse problem starting from the actual EPR measurements $\mathbf{S}_\mathrm{m}$. The reconstructed MNP distribution, $\mathbf{c}^*$, is realized by minimizing the differences between modeled measurements and actual measurements (Eq. (1.19)). This is solved by truncated SVD, as described in Section 1.4.3.

2.2.3 Numerical validation

The forward model for 1D EPR imaging presented in Section 2.2.2 is numerically validated for five spatial MNP distributions. This is done by *simulating* measurement data through the forward model Eq. (2.7):

$$\mathbf{S}_{\mathrm{m}_\mathrm{sim}} = \mathbf{L} \cdot \mathbf{c}_\mathrm{act} \tag{2.8}$$

with $\mathbf{c}_\mathrm{act}$ the known, actual MNP distribution in the experiment. For the various considered distributions, see Fig. 2.11. Measurements are simulated in three ways by varying the elements of $\mathbf{L}$:

1. Using an artificial $R(n)$ with and without measurement noise.
2. Using a measured $R(n)$.
3. Using a measured $R(n)$ and added white Gaussian noise to $\mathbf{S}_{\mathrm{m}_\mathrm{sim}}$.

Additionally, a comparative study between the performance of two setups is carried out. Both setups operate as described in Section 2.1.3, but one setup has additional cooling to keep the temperature constant and its edges are covered to avoid reflections of the electromagnetic wave. The first setup is denoted as setup A and the temperature-controlled setup is referred to as setup B. We expect an increased accuracy and more stable results for setup B.

Figure 2.11 depicts the different MNP distributions and the calibrating sample of the setups. These distributions were implemented in the software to realize a numerical validation of the proposed methodology. Measurements of these distributions can be simulated through including the distributions as $\mathbf{c}_\mathrm{act}$ in Eq. (2.8). MNP distributions 2 - 5 are lab-made MNP distributions that are also measured with both setups. Because the compartments of the tube are separated by 1 mm, no continuous distribution is measured in the experimental validation.

An artificial response function is constructed and is used in the forward model for the simulation of measurements (Eq. (2.8)). These simulated measurements are used in the inverse reconstruction procedure (Eq. (1.23)) as $\mathbf{S}_\mathrm{m}$ to obtain the different reconstructions. Additionally, numerical simulations

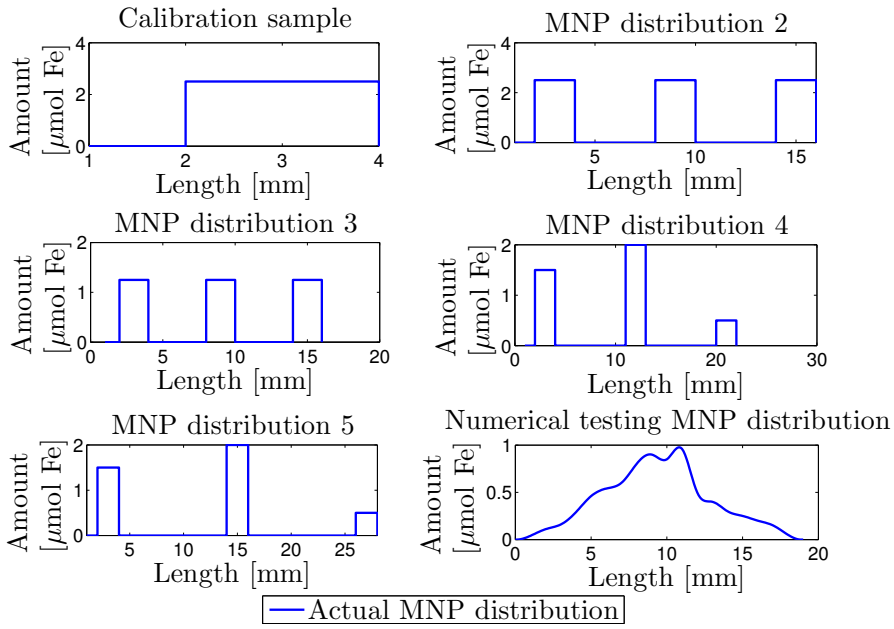

Figure 2.11: MNP distributions that are implemented in the software. The calibration sample and MNP distributions 2 - 5 are also measured experimentally.

are performed where noise is added to the simulated measurements. This allows to investigate the influence of noise on the reconstruction quality. These numerical simulations can also be used to obtain the minimal requirements of a response function (certain amplitude, steepness, etc.), which is investigated in Section 2.3. A perfect reconstruction is possible when an artificial response function is used. However, it should be noted that the reconstruction quality depends on the response function. This is only a numerical validation of the principle in software, therefore these results are omitted and only the results with a measured response function are given.

In a next step, the measured response function is used for building up the forward model (Eqs. (2.6) and (2.7)). The generated values trough Eq. (2.8) are then again inserted in Eq. (1.23). To acquire the response function, the EPR signal is measured on different positions ($N_{\text{calib}_{\text{setupA}}} = 34$, $N_{\text{calib}_{\text{setupB}}} = 38$, $\Delta N_{\text{calib}} = 1$ mm) of a 5 μmol Fe Resovist® (Schering AG, Berlin, Germany) calibration sample (Fig. 2.11). The Resovist® particles used to be applied as contrast agents in MRI (see Sections 1.2.4 and 1.3). For more information on these particles, we refer to Ref. [134]. Figure 2.12 shows the typical shape of $R(n)$ for setup A and B. As stated before, the response function

has an important impact on the accuracy of the proposed methodology. The two response functions were differentiated to analyze their steepness. Setup B is steeper especially in the center of the field. This means that noise has a smaller influence on the measurements as there is a larger difference between consecutive values of the response function. When this difference is small, the added noise can reach response values associated to other positions and in this way induce displacement errors (see Section 2.3).

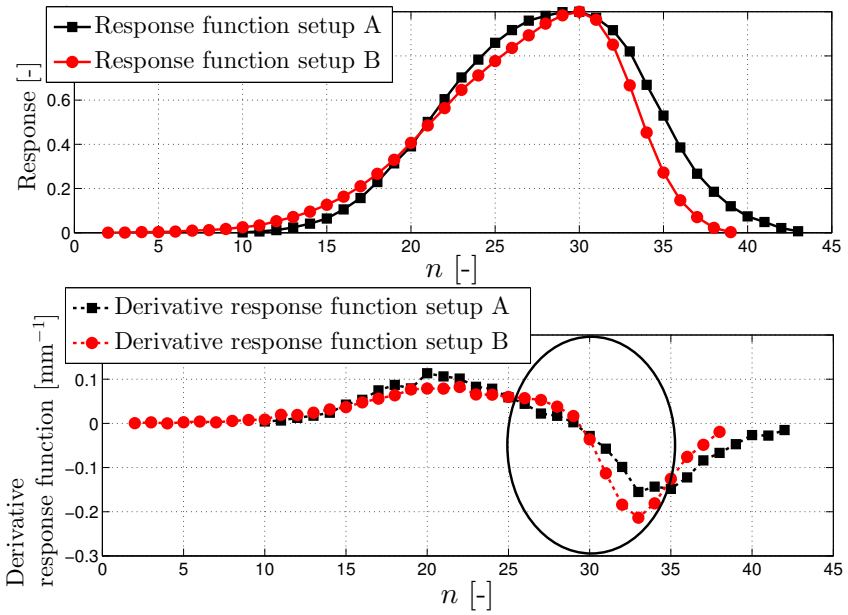

Figure 2.12: Comparison of the response functions from setup A and B. The response functions are differentiated to analyze the steepness as this influences the noise sensitivity.

The sensitivity matrix depends on the measured response function (Eqs. (2.6) and (2.7)) and is different for setup A and setup B. Figure 2.13 shows the simulated measurements for MNP distribution 3 (through Eq. (2.8)), compared to the actual performed measurements of MNP distribution 3 with both setups. For setup B, a close agreement can be observed between the simulated measurement and the actual measurement. This is not the case for setup A. From Table 2.1 one can deduce that this is also the general conclusion when considering all the measurements, i.e. μ and σ on the deviations between measured and simulated measurements are considerably lower for setup B compared to A. Setup A retrieves increased absolute EPR

signals when compared to setup B for equal MNP distributions, but due to the relatively high error of the forward model, this advantage is lost.

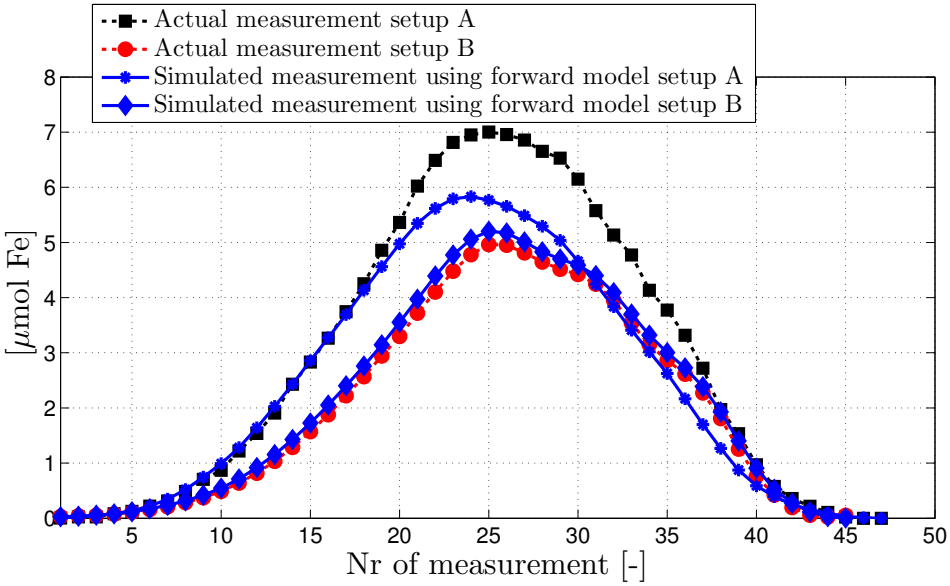

Figure 2.13: Comparison between simulated and actual measurement of MNP distribution 3. The simulation should be as close as possible to the real measurement.

Table 2.1: The average deviation, μ, and the standard deviation, σ, of the simulated and actual measurement for setup A and setup B when measuring different MNP distributions. Setup B achieves simulated measurements which are closer to the actual measurements.

	Setup A	
MNP distribution	μ **[μmol]**	σ **[μmol]**
2	1.63	1.64
3	0.51	0.56
4	0.48	0.41
5	1.34	1.13
	Setup B	
MNP distribution	μ **[μmol]**	σ **[μmol]**
2	0.74	0.65
3	0.13	0.08
4	0.22	0.16
5	0.75	0.65

The MNP distributions from Fig. 2.11, are perfectly recovered in case no noise is added to $\mathbf{S}_{\mathrm{m_{sim}}}$ with the simulated measurements generated by

measured $R(n)$. However, real experiments contain noise originating from e.g. the hardware and the environment. This is also the cause of the observed differences between the simulated and real measurement in Fig. 2.13.

Hence, white Gaussian noise was added to the simulated measurements to analyze the noise robustness of the methodology. Different noise levels, ranging from 1% to 10% compared to the amplitude of $R(n)$, are generated. The reduction in reconstruction quality is shown in Figs. 2.14 and 2.15 for MNP distribution 3. For each noise level, 200 different noisy data sets were generated. The CC was calculated by comparing $\mathbf{c}_{\text{act}}$ and $\mathbf{c}^*$. We refer to Section 1.4.4 for more information on the CC. The average CC for each noise level is depicted in Fig. 2.14 for setup A and B. The corresponding averaged reconstructions for each noise level are depicted in Fig. 2.15.

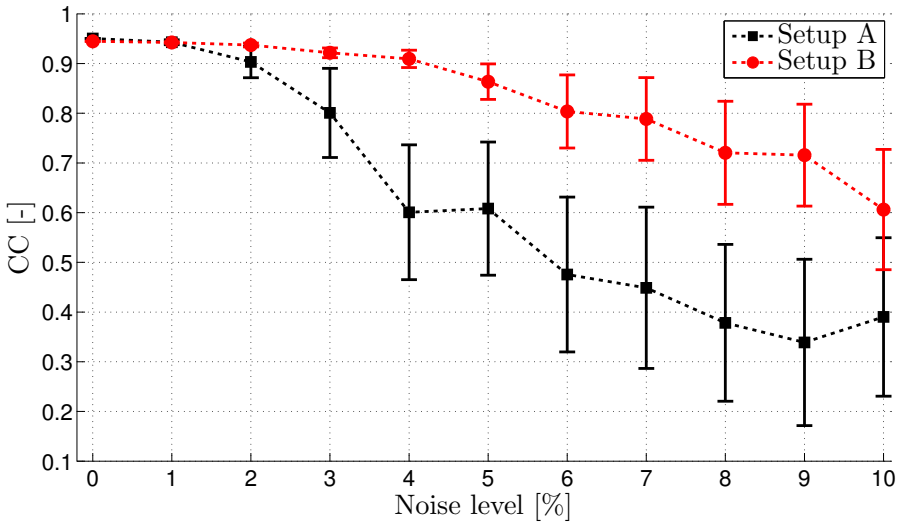

Figure 2.14: The average reconstruction quality (CC) for increasing noise levels when measured with setup A and setup B. Results are obtained from 50 simulations with MNP distribution 3.

2.2.4 Experimental validation

In Section 2.2.3, the proposed methodology was numerically tested by using simulated measurements of the MNP distributions. In this section, actual measurement signals of the MNP distributions are used from the two EPR setups. The focus is on the selection of σ_r, associated to eigenvalue r (Eq. (1.23)).

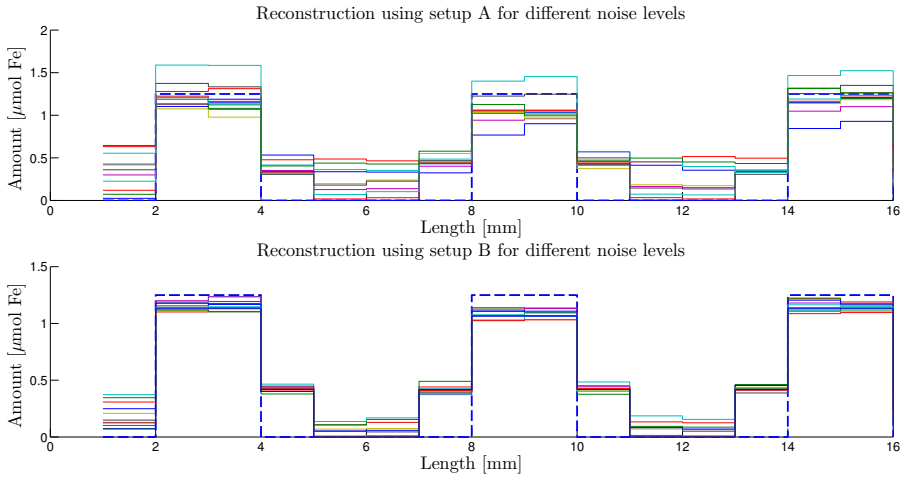

Figure 2.15: The corresponding reconstructions for setup A and B from Fig. 2.14. The actual distribution is the blue dashed line. Results are obtained from 200 experiments.

Here, the correspondence between the reconstructed MNP distribution, using the inverse problem, and the *a priori* known distribution in the sample is investigated.

σ_r (Eq. (1.23)) is determined by analyzing the eigenvalues of $\mathbf{L}$. Figure 2.16 depicts the normalized eigenvalue distribution of setup A and setup B. Higher eigenvalues are associated to the signal space, while lower eigenvalues correspond to noise sources. The eigenvalues which are signal sources should be selected by choosing the proper r. In a first step, reconstructions for different r (1 - 12) and different MNP distributions are performed. Based on these results an r for the system is selected. MNP distributions 2,3,4 and 5 from Fig. 2.11 were measured. Overall, the most accurate reconstructions with setup A were obtained for $r = 7$. Only for distribution 5 a large difference of 21% for the CC score is seen when 11 eigenvalues are retained instead of 7. When analyzing Fig. 2.16 we observe that this r is close to the inflection point ($r = 8$) of the eigenvalue distribution. When $r = 8$ instead of 7, there is only a mean difference (considering all the reconstructions) of 5% for the CC score. Setup B obtains the most accurate reconstructions for $r = 10$ or 11. Again, a larger difference of 8% (when r equals 5 instead of 10) is obtained for distribution 5. The r based on the most accurate reconstructions also corresponds to the inflection point ($r = 10$) of Fig. 2.16. This allows to determine r based on the eigenvalue distribution of $\mathbf{L}$ and an extensive reconstruction analysis is no longer needed. Again the lower noise sensitivity of setup B is represented in

this figure, since the first eigenvalues are higher in amplitude compared to the first eigenvalues of setup A.

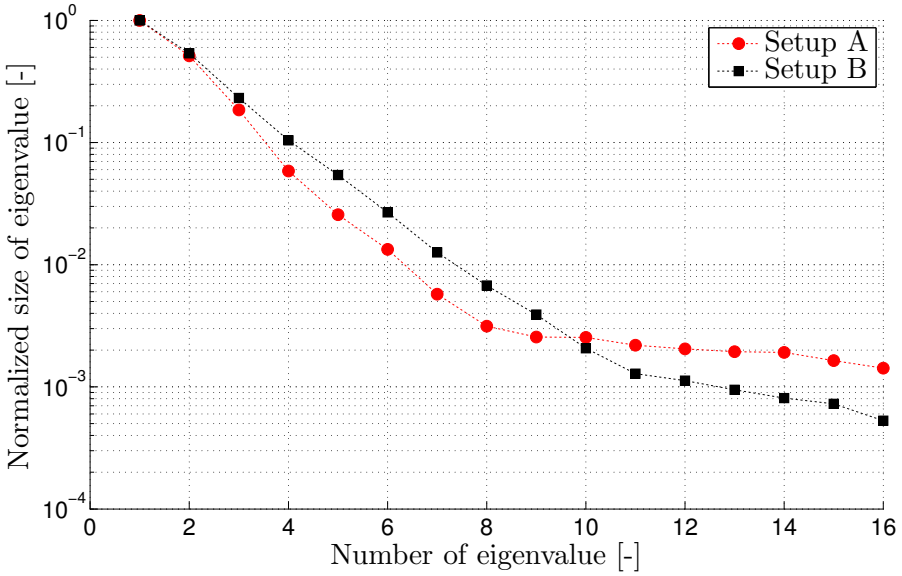

Figure 2.16: Normalized eigenvalue distributions. r corresponds to the inflection point of the distribution.

Figure 2.17 shows a reconstruction of MNP distribution 3 (Fig. 2.11). These are three compartments with a length of 2 mm filled with 2.5 μmol of Resovist®. The compartments are separated by a compartment edge of 1 mm. MNP distribution 3 is the most difficult distribution to reconstruct due to the lower iron amounts in this distribution and the closer spacing of the filled compartments. The reconstruction resolution is chosen to be 1 mm (equal to the measurement resolution). The CC score is 93% for setup B and 80% for setup A. When all the reconstructions (MNP distributions 2 - 5) for different eigenvalues (r = 6 - 12) are considered, setup B achieves a CC increase of $\approx$ 5% compared to setup A. However, in the case of distribution 3, a mean difference ($r = 6 - 12$) of 23% between the CC scores of both setups is achieved (Table 2.2). Table 2.2 gives an overview of the CC scores for different eigenvalues for distribution 3 measured with setup A and setup B. Because of the smaller Resovist® amounts and the higher resolution, the resulting measurement values are smaller in amplitude and change more gradually (Fig. 2.18). This means that the influence of the noise becomes more important. Because setup B is less sensitive to noise we have better results

compared to setup A. This is due to the differences in response function shape and the additional temperature control of setup B. The temperature control decreases the temporal changes in the response function. Also the CC score of setup B changes only gradually in the neighborhood of the inflection point (Table 2.2). In case r is erroneous, the reconstruction quality will be less affected than when a measurement is performed with setup A. It should be noted that there could be an influence of particle dehydration on the measurements. We expect better results when particle distributions are made and then measured directly.

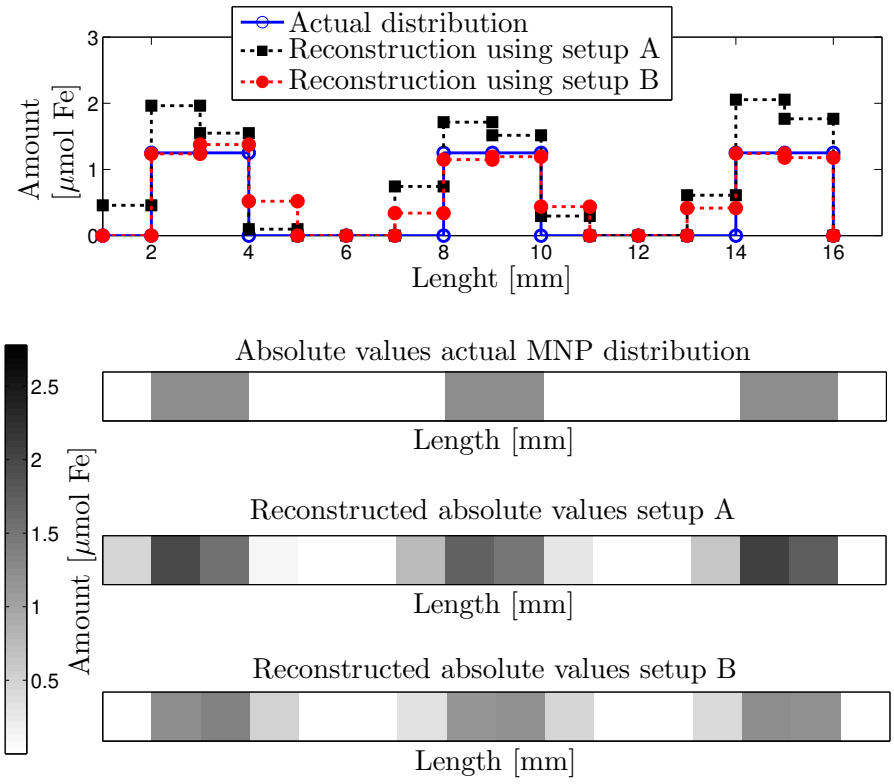

Figure 2.17: Reconstruction of a spatial nanoparticle distribution. The reconstruction of the temperature-controlled setup is closer to the actual distribution of the particles. A CC score of 80% and 93% is achieved for r equal to 8 and 10 for setup A and setup B respectively.

Based on previous results it is clear that setup B is less sensitive to noise. Setup B recovers MNP distributions better than setup A with an increase of 13% for the most demanding reconstruction and an average increase of $\approx$ 5% when all the measured MNP distributions are taken into account. Setup

Table 2.2: Reconstruction scores (CC) of MNP distribution 3 for different r measured by setup A or setup B.

Eigenvalue cut-off r	Setup A	Setup B
6	6%	19%
7	85%	95%
8	80%	94%
9	66%	94%
10	57%	93%
11	57%	93%
12	57%	92%

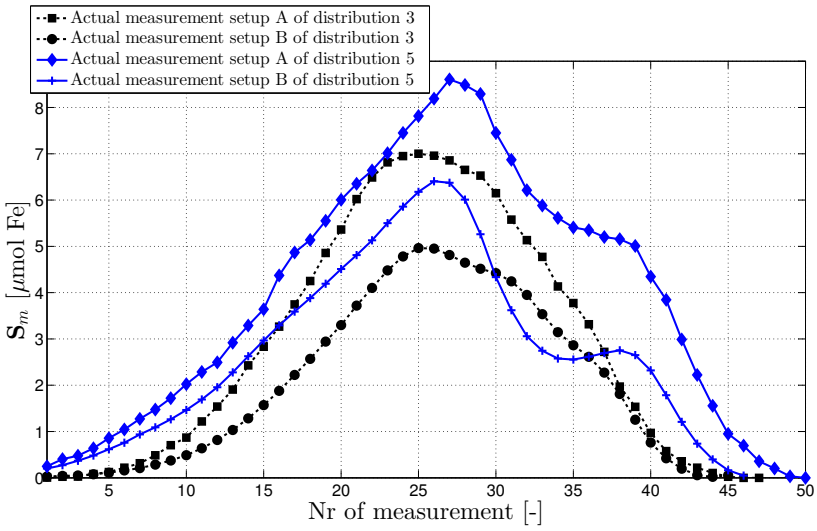

Figure 2.18: Measurements of MNP distribution 3 have a lower amplitude and change more gradually compared to for example MNP distribution 5.

B was then employed for measurements of more continuous distributions (Fig. 2.19). These measurements were performed just after the distributions were synthesized to minimize the influence of dehydration of the MNP. The reconstructions are somewhat smoothed because of the position error on the sample during the movement through $\mathbf{B}_0$. Figure 2.19 proves that we are able to reconstruct the location and absolute values of different MNP amounts.

2.2.5 Conclusion

In this section a measurement procedure and forward model were devised in order to incorporate spatial information in the EPR measurements. Combin-

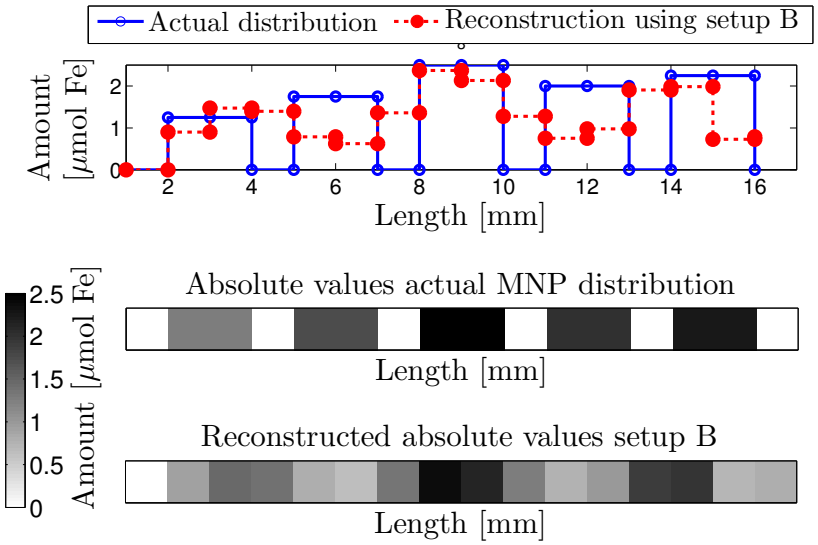

Figure 2.19: Measurement of a MNP distribution with setup B where adjacent compartments are filled with MNP.

ing our new measurement approach with inverse problems allows to interpret the EPR measurements correctly, resulting in an accurate 1D reconstruction of magnetic nanoparticles. This is the first quantitative 1D reconstruction of the spatial distribution of superparamagnetic nanoparticles using EPR measurements. The proposed methodology has been validated both numerically as experimentally. Additionally, a comparison is performed between two setups, where the second setup has additional temperature control of the environment. Following our numerical and experimental results we can conclude that the temperature-controlled setup is less sensitive to noise and shows an increased robustness of the response function compared the other setup. This results in an increase of the reconstruction quality by 13% for the most difficult particle distribution and an average increase of 5%, when all the measurements are considered. In Section 2.3 more measurements and numerical simulations are performed to analyze the influence of different errors and setup parameters on the reconstruction of the particle distribution and to determine the limits of our method.

2.3. Robustness assessment

2.3.1 Introduction

In Section 2.2 a method was developed to recover the 1D spatial MNP distribution using a 300 MHz EPR setup. EPR is a promising and quantitative technique for the visualization of MNP distributions. In order to further improve this method and to retrieve 3D spatial information from the particles (further detailed in Sections 2.4 and 2.5), we investigate the impact of different setup parameters and errors on the inverse solution. This is important because the inverse problem encompasses uncertainties, such as measurement noise, modeling errors, inherent setup errors and the ill-posedness of the problem.

This section investigates which requirements the MNP distribution needs to fulfill to achieve an accurate reconstruction with EPR. For this purpose, various MNP distributions are considered and examined. Additionally, the impact of setup errors and properties (grid, forward model properties, noise), and sample positioning errors is explored. The importance of the inverse solving method is shown by comparing reconstructions with truncated SVD (Eq. (1.23)) and NNLS (Eq. (1.26)). Moreover, a combination of both methods is studied. Figure 2.20 gives a schematic overview of the studied methodology. The aim of this section is to inspect the limits of the EPR setup and to understand the influence of different types of errors on the MNP reconstructions. This allows to optimize the EPR setup towards more accurate reconstructions of MNP distributions.

In Section 2.3.2, various error models are developed. These error models are independently tested in Section 2.3.3 for investigating the impact of:

1. Setup parameters: the ideal properties of the response function are investigated and how resolution requirements of $\mathbf{S}_\mathrm{m}$ and $\mathbf{c}^*$ affect numerical stability, moreover the impact of system noise is investigated.
2. Sample positioning errors: the effect of a single positioning error of different sizes and on various positions is analyzed.
3. Impact of the inverse solution method: the inverse problem is solved with truncated SVD (similarly as in Section 2.2), which allows to generate non-plausible negative solutions, therefore additionally NNLS is investigated which solves the inverse problem iteratively until no negative MNP amounts are found in the solution, moreover, an innovative approach is introduced in which both algorithms are combined.

This work has been published in Ref. [311]. The quality parameters described in Section 1.4.4, more specifically the condition number β (Eq. (1.28)) and the reconstruction quality CC (Eq. (1.27)), μ and σ are used for testing.

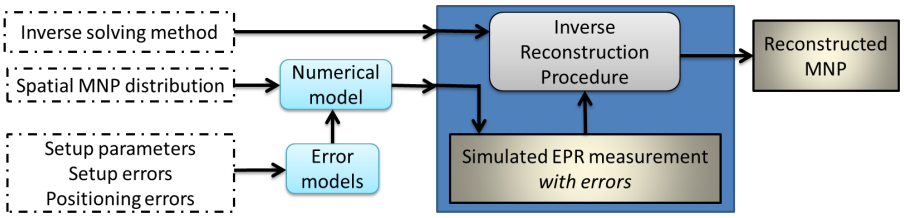

Figure 2.20: Schematic overview of the studied methodology. The dash-dotted rectangles represent necessary model inputs.

2.3.2 Error models

Setup parameter changes, setup errors and sample positioning errors are included in the error models developed in this section.

A change in a *setup parameter* of the EPR setup results in a change of $\Delta\mathbf{L}$ in the model:

$$\mathbf{S}_{\mathrm{f}} = (\mathbf{L} + \Delta\mathbf{L}) \cdot \mathbf{c} \tag{2.9}$$

The setup parameters differ from the assumed parameters leading to errors in the reconstruction, i.e. *setup errors*. This can be the case when the used response function, $R(n)$, in the forward model differs from the response function in the experiment or when the response function is affected by noise. Additionally, the stability of the inverse problem is determined by $\mathbf{L}$. So, in order to have accurate reconstructions, a sensitivity matrix with setup parameters that minimize its condition number (Eq. (1.28)) should be employed. Examples of setup parameters are the resolution of $\mathbf{c}^*$, the resolution of $\mathbf{S}_m$ and the ratio of N to V. Moreover, properties of $R(n)$ such as its shape and spatial variation are of importance, as these properties alter $\mathbf{L}$. We investigate the effect of these parameters to assess in a first stage the robustness of the EPR setup and in a second stage optimize the EPR setup for improving the reconstructions of MNP distributions.

A measurement with a positioning error (PE) can be represented by:

$$\mathbf{S}_{\mathrm{PE}}(n,\alpha) = \mathbf{L}\Big(\mathbf{L}(n,:) = \mathbf{L}(n+\alpha,:)\Big) \cdot \mathbf{c} \tag{2.10}$$

Row n of $\mathbf{L}$, denoted $\mathbf{L}(n,:)$, consists of all the response values for the positions of the voxels at measurement position n. If we erroneously measure at position $n + \alpha$ instead, these response values are the values from $n + \alpha$ where α is the shift in mm units from the actual position n.

2.3.3 Sensitivity analysis

The error models described in Section 2.3.2 allow to study the sensitivity of EPR to many types of errors. Here, we investigate the impact of setup parameters, sample positioning errors and the inverse solver. To this end, various MNP distributions are considered in the analysis, each with their specific challenges, to thoroughly investigate the effects of different error types. The measurements containing the errors can be simulated by incorporating the actual MNP distribution into the respective error model (similar as in Eq. (2.8)). The necessary requirements for the quantitative detection of the MNP distributions follow from this study. The considered error sizes in this study, such as the system noise, are based on observed differences between measurements of the same MNP sample over the course of days and years. To account for the deterioration of the MNP sample, the sample was also made multiple times. Setup parameters and inverse solution parameters such as resolutions and properties of the response function are in correspondence with actual performed measurements, hardware properties or typical values employed in MNP imaging.

The distributions considered in this section are depicted in Fig. 2.21. The upper row represents MNP distributions in the lab, measured according to the method described in Section 2.2.2. Each distribution has specific properties to allow targeted testing of the setup. The first distribution is an example of a calibration sample, $\mathbf{c}_{\text{calib}}$ (see Section 2.2.2). In this way the impact of different parameters and errors on the calibration can be investigated. Errors in the calibration result in an inaccurate forward model (Eq. (2.7)) and thus in inaccurate reconstructions. The bottom row represents numerically simulated MNP distributions. We investigate constant (i.e. homogeneous) distributions, $\mathbf{c}_{\text{con}}$, with slope equal to zero and gradient distributions, $\mathbf{c}_{\text{grad}}$ with constant slope different from zero to assess the impact of slope sizes. Multiple $\mathbf{c}_{\text{grad}}$ MNP distributions are tested, but only two of them are shown for clarity reasons. The red $\mathbf{c}_{\text{grad}}$ distribution corresponds to the measured MNP distribution 2 (upper row), but without discontinuities. This is also the case for the $\mathbf{c}_{\text{con}}$ distribution and MNP distribution 1. These distributions are used to investigate the impact of discontinuities and to see whether they lead to improved or deteriorated reconstructions compared to the continuous distributions found in biomedical applications. We also consider 100 random MNP distributions, $\mathbf{c}_{\text{rand}}$, generated with uniformly distributed pseudo-random numbers in the open interval (0,1). Additionally, we simulate a realistic MNP distribution, $\mathbf{c}_{\text{rea}}$, corresponding to a MNP injection.

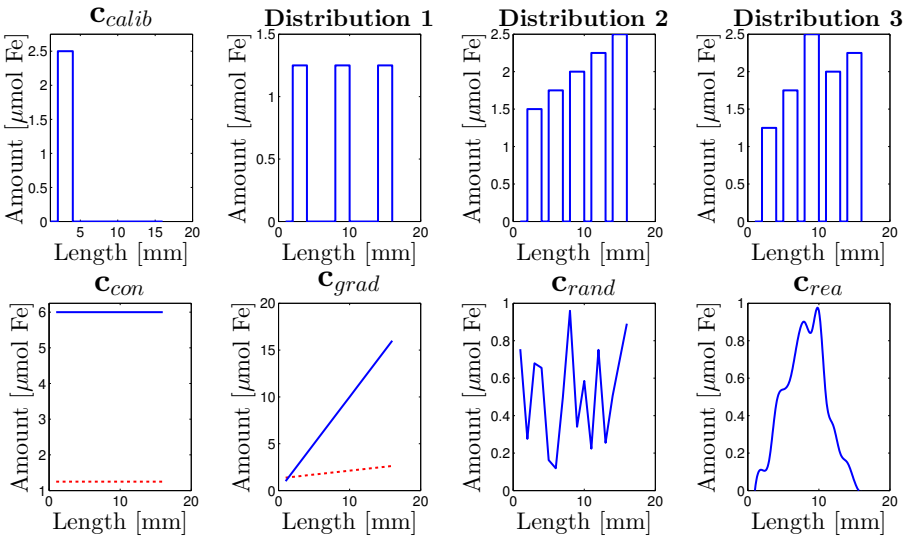

Figure 2.21: The upper row shows lab made MNP distributions. The bottom row depicts numerically simulated distributions. The dotted lines represent simulated distributions of MNP distributions 1 and 2 respectively, but without empty compartments.

Impact of setup errors: noise

First the impact of setup parameters is investigated. These parameters change $\mathbf{L}$ by $\Delta\mathbf{L}$ (as in Eq. (2.9)). We regard noise as a setup parameter, which originates for example from the coils and increases as the coils heat up. This *setup noise* results in a different response function and thus in a different setup behavior:

$$\mathbf{S} = (\mathbf{L} + \Delta\mathbf{L}_{\text{noise}}) \cdot \mathbf{c} \tag{2.11}$$

$\Delta\mathbf{L}_{\text{noise}}$ represents the changes in the final sensitivity matrix due to setup noise. Figure 2.22 depicts the noise robustness of the EPR setup towards the distributions from Fig. 2.21. Noise levels relative to the signal intensity of the distributions are used as MNP distributions with higher MNP amounts are less sensitive to noise. The white Gaussian noise is increased in steps of 1 % and for every noise level 200 simulations (noise measurements) are performed which are then averaged. The shadow band around the average represents the standard deviation due to the noise. The influence of the noise is similar as in Section 2.2: the average CC decreases for increasing noise levels. The presence of noise requires a cut-off of the eigenvalues (r, from Eq. (1.23)). To determine the cut-off value we use the method from Section 2.2. The calibration sample remains largely unaffected by the noise, which means that the calibration results will not differ in time due to small changes

in setup noise levels. The random and constant distributions (omitted for clarity) reach a CC close to zero starting from noise levels of 1%, suggesting a lesser performance for these type of distributions with this setup. The CC of the random distributions can also be explained due to the combined randomness of the noise and the distribution. Distributions 2 and 3 obtain similar CC scores, but are lower compared to distribution 1 because of the smaller spacing between the filled compartments. The $\mathbf{c}_{\text{grad}}$ distributions obtain a CC between distribution 2-3 and distribution 1. The best results are found for the realistic distribution, $\mathbf{c}_{\text{rea}}$.

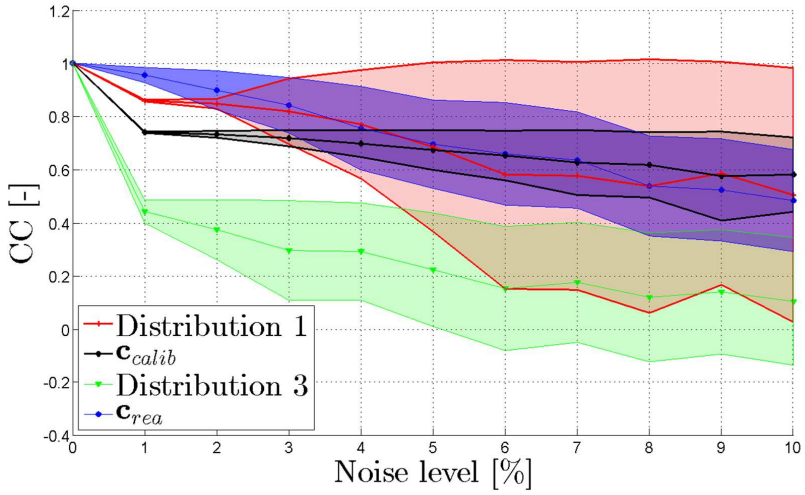

Figure 2.22: Impact of the setup noise level on the MNP distributions from Fig. 2.21. Both the mean and standard deviation are depicted.

Impact of setup parameters: response function

Next, the impact of the response function $R(n)$ on the reconstruction is investigated. Changes in response generate the following measurement:

$$\mathbf{S}_f = \Big(\mathbf{L}\left(R_1(n)\right) + \Delta\mathbf{L}\Big) \cdot \mathbf{c} = \mathbf{L}\left(R_2(n)\right) \cdot \mathbf{c} \tag{2.12}$$

$R_1(n)$ and$R_2(n)$ represent two different response functions. We assess the impact of $R(n)$ on the reconstruction quality and want to define necessary requirements for $R(n)$ to improve reconstructions. Two types of response functions were investigated in Section 2.2 and Ref. [256], but it remained unclear what properties of the response function caused the differences

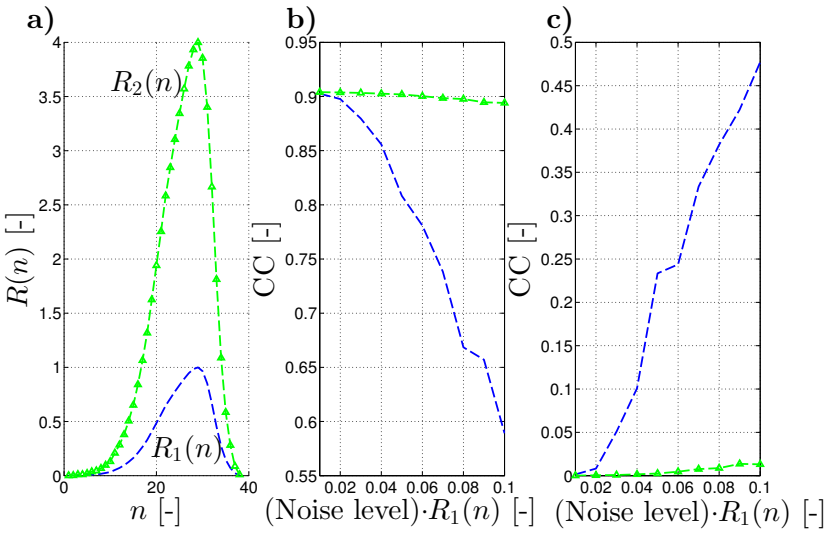

Figure 2.23: a) Response functions $R_1(n)$ and $R_2(n)$ with $R_2(n) = 4 \cdot R_1(n)$. The dotted line depicts a measured response. b) CC for every response as function of noise level. c) Standard deviation for every function due to the noise levels.

in reconstruction quality. Previously, numerical investigations of artificial responses were only used as a validation of the developed software (Section 2.2.3). First we regard $R_2(n) = D \cdot R_1(n)$, $D \in \mathbb{R}$ (i.e equal shape, but changed slope). $R_1(n)$ corresponds to a measured response function. An increased slope should show an increased robustness towards setup noise and thus increased reconstruction performance. Starting from $D = 4$ the impact of the noise is negligible for all distributions shown in Fig. 2.21. In this case the noise level is considered relatively to $R_1(n)$. Figure 2.23 shows an example with $D = 4$ for MNP distribution 1. However, no reconstructions are obtained with a CC of 1. This suggests that other properties such as the spatial variation of $R(n)$ also have an impact.

We therefore introduce three synthetic response functions $R_a(n)$, $R_b(n)$ and $R_c(n)$ with following properties:

$$\frac{dR_a(n)}{dn} = \text{constant} \quad n = 1,...,N$$

$$\begin{cases} \dfrac{dR_b(n)}{dn} = \text{constant} & n = 1,...,N/2 \\ \dfrac{dR_b(n)}{dn} = \text{-constant} & n = N/2+1,...,N \end{cases}$$

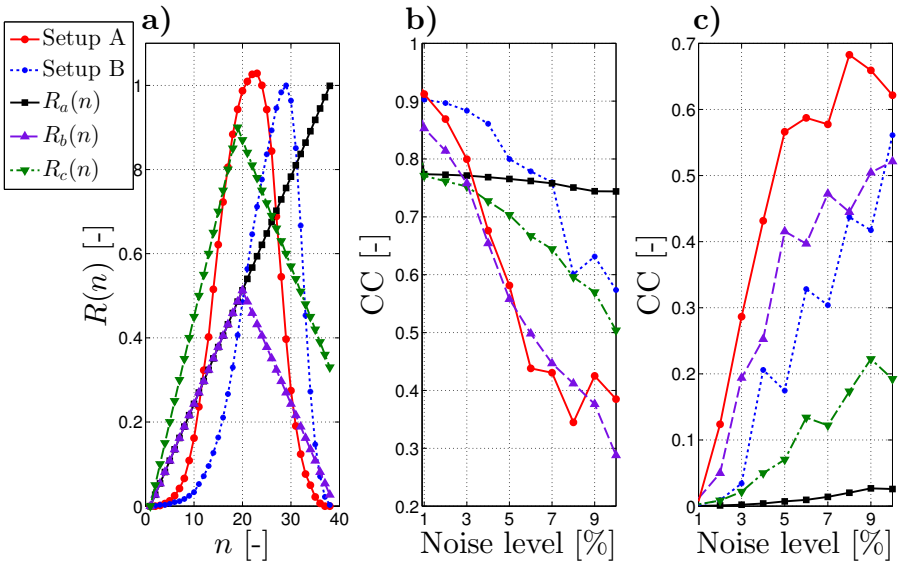

Figure 2.24: a) The different response functions. b) CC for every type of response function for MNP distribution 1 as function of noise level. c) Standard deviation on the CC in b) due to the noise.

$$\begin{cases} \dfrac{dR_c(n)}{dn} = l \cdot \text{constant} \quad n = 1,...,N/2, \;\; l \in \mathbb{R} \\ \dfrac{dR_c(n)}{dn} = \text{-constant} \quad n = N/2+1,...,N \end{cases}$$

Fig. 2.24 depicts these response functions and the associated CC when reconstructing MNP distribution 1 for increasing noise levels. Here the setup noise is relative to the mean amplitude of each $R(n)$ to remove the impact of the slope (as shown in Fig. 2.23). Additionally, two measured response functions from two EPR setups, denoted as setup A and setup B, are plotted (for more detailed information see Section 2.2 and Ref. [256]). Lab measurements of MNP distribution 1 obtain a CC of 80 % for setup A and a CC of 93 % for setup B. We observe that a constant slope is noise robust ($R_a(n)$). Having similar up and downward slopes ($R_b(n)$) results in similar response values and therefore a decreased noise robustness. However for lower noise values, a higher CC is observed. This is also the case for setup A, which has similar slopes. Setup B has two different slopes (similar to $R_c(n)$) and is therefore more noise robust. Hence, the unknown volume should be moved in the region of a constant slope response to improve reconstruction results. When extending the use of the current setup for 2D and 3D reconstructions of MNP distributions, we have to take into account these requirements on the response function.

Impact of setup parameters: resolution

$\mathbf{L}$ also depends on the required resolution (i.e. the step size between consecutive values) of the measurement $\mathbf{S}_\mathrm{m}$ and the reconstructed MNP distribution $\mathbf{c}^*$. The resolutions of these parameters determine the N to V ratio of $\mathbf{L}$ and the resolution of $R(n)$. In this case, the resolution of $R(n)$ is considered the same as of $\mathbf{c}^*$. Our aim is to have the smallest possible resolution for the reconstruction $\mathbf{c}^*$, by performing the least possible amounts of measurements so to realize fast measurements. Lab measurements were performed of MNP distribution 2 with $\mathbf{S}_\mathrm{m}$ having a resolution of 1 mm. Starting from this measurement, reconstructions, $\mathbf{c}^*$, with resolutions of 1 mm, 0.1 mm and 0.01 mm were realized (Fig. 2.25a)). The response was interpolated for reconstructions with a resolution < 1 mm. A similar reconstruction quality is observed for these reconstructions, suggesting no numerical impact of increasing the resolution. If $\mathbf{S}_\mathrm{m}$ is linearly interpolated to smaller resolutions (0.01 and 0.1 mm) and the resolution of $\mathbf{c}^*$ is kept on 1 mm, similar results are seen. When both $\mathbf{S}_\mathrm{m}$ and $\mathbf{c}^*$ are linearly interpolated to smaller resolutions (0.01 and 0.1 mm), a decrease in reconstruction quality due to numerical instability of $\mathbf{L}$ can be observed, as only linearly dependent information is added to $\mathbf{L}$. This decrease also depends on the resolution of $\mathbf{c}^*$; for smaller resolutions there are more unknowns and the problem is increasingly ill-posed. The performance of the selected resolutions highly depends on the numerical stability (Eq. (1.28)) of $\mathbf{L}$ in Eq. (2.7), see Table 2.3. In Fig. 2.25b), values of the measurement $\mathbf{S}_\mathrm{m}$ are omitted to acquire resolutions of 2 and 3 mm. Their reconstruction quality decreases, because of the reduction in information made available in the inverse problem solving. Starting from a resolution of 3 mm for $\mathbf{c}^*$, the problem is overdetermined to such extent, that the approximated solution does insufficiently characterize the spatial variations of the MNP distribution. This also corresponds to the spacing between the filled compartments.

Table 2.3: Performance of the relative resolutions of $\mathbf{c}^*$ and $\mathbf{S}_\mathrm{m}$ from Fig. 2.25 highly depend on the numerical stability (β [-]) of $\mathbf{L}$.

Resolution $\mathbf{S}_\mathrm{m}$ \ Resolution $\mathbf{c}^*$	**0.01**	**0.1**	**1**
1	23.569	23.491	8.059
0.1	232.186	79.239	8.106
0.01	790.321	79.244	8.106

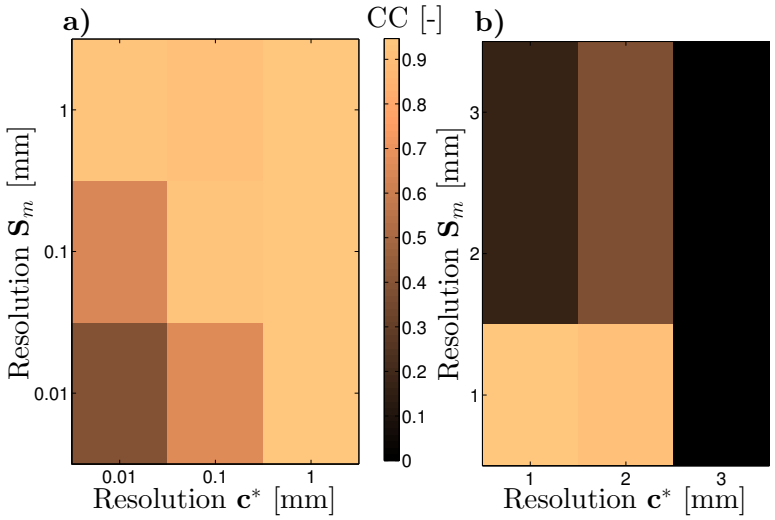

Figure 2.25: Impact of the resolution of $\mathbf{S}_\mathrm{m}$ and $\mathbf{c}^*$ on the reconstruction accuracy starting from a measurement with a resolution of 1 mm. a) For resolutions between 0.01 and 1 mm, e.g. effect of linear interpolation. b) For resolutions between 1 mm and 3 mm.

Impact of positioning errors

In this subsection the impact of positioning errors is investigated:

$$\mathbf{S}_{\mathrm{PE}}(n,\alpha) = \mathbf{L}\Big(\mathbf{L}(n,:) = \mathbf{L}(n+\alpha,:)\Big) \cdot \mathbf{c} \tag{2.10}$$

For each measurement position n an error of $\alpha = 1$ mm is introduced resulting in N shifted measurements of 1 mm. The first positions (smaller n) only have small relative changes to one another (small gradient in the response function), and therefore an error of 1 mm has almost no impact, while the last measurement positions (larger n) have a higher slope and thus a higher associated impact of the PE (Fig. 2.26a)). This results in a lower average CC (i.e. the average of these N reconstructions) for PE's (Fig. 2.26b)). The largest impact (lowest CC) is for the $\mathbf{c}_{\mathrm{con}}$, $\mathbf{c}_{\mathrm{grad}}$ and $\mathbf{c}_{\mathrm{rand}}$ distributions. The lab MNP distributions 1, 2 and 3 obtain similar scores. $\mathbf{c}_{\mathrm{calib}}$ has the highest CC scores and therefore is only slightly affected by the positioning error. The CC correlates directly with the gradient of the measurements (Fig. 2.26c)). The measurement of $\mathbf{c}_{\mathrm{rea}}$, for example, contains steeper gradients than the MNP lab distributions. The $\mathbf{c}_{\mathrm{rand}}$ and $\mathbf{c}_{\mathrm{grad}}$ distributions are sensitive to the size of α due to their larger gradients. For α = 3 and 5 mm, $\mathbf{c}_{\mathrm{calib}}$ obtains similar scores as the distributions due to a larger gradient for higher n.

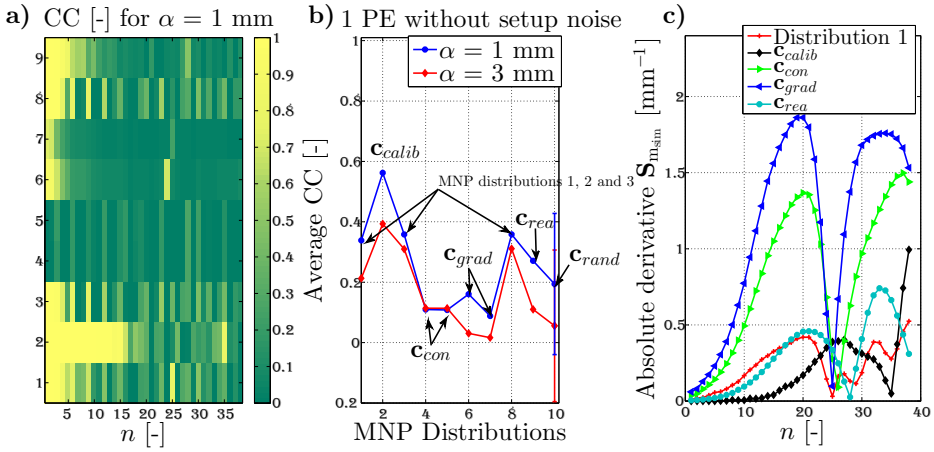

Figure 2.26: a) The positioning error depends on n ($\alpha = 1$ mm). The same mapping between distribution number and name is employed as in b). b) Average CC for one positioning error with $\alpha = 1$ and 3 mm without setup noise. c) The impact of the positioning error is correlated with the local gradient.

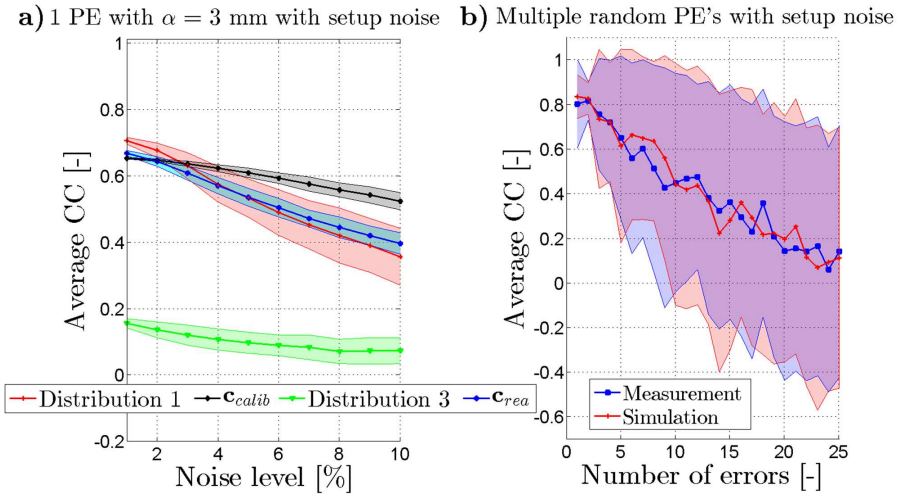

Figure 2.27: a) Impact of one positioning error on the reconstruction quality (average CC) for α equal to 3 mm with setup noise. b) Comparison of the impact on the reconstruction quality of distribution 1 for increasing number of simulated and measured random positioning errors.

In a second step, setup noise was added (Fig. 2.27a)). Comparison with Fig. 2.22, in which only setup noise was considered, reveals that adding noise and positioning errors results in a similar relative performance of

MNP reconstructions than when only adding setup noise, although lower correlations are observed. This means that automating the setup is a higher priority than stabilizing the measurement system.

In a final step we deliberately introduced large positioning errors in the measurements (to compensate already existing errors). Then we compared if the effect on the reconstruction quality of the distribution scaled similarly to the case of using simulated positioning errors. This was achieved by performing 100 simulations for increasing number (1-25) of random positioning errors (random sizes, random positions) with setup noise. Fig. 2.27b) depicts the reconstruction quality of distribution 1 using simulated and measured random positioning errors for increasing number of errors. We obtained similar results (average CC difference of only 0.05) for the simulated impact and the actual impact, suggesting that our method assesses positioning errors well.

Impact of inverse solver

Finally, the impact of the inverse solution method on the obtained MNP reconstructions is investigated. In Section 2.2 the inverse problem was solved by truncated SVD (Eq. (1.23)) in which only the eigenvalues equal to or larger than σ_r were retained. A detailed description of the EPR 1D reconstruction methodology and how to select the correct r can be found in Section 2.2 and Ref. [256]. The SVD solution procedure allows negative values in the reconstruction, which were artificially set to zero in Section 2.2. The inverse problem is now additionally solved through NNLS (Eq. (1.26)) to remove negative MNP amounts from the solution. Moreover to further enhance reconstruction quality, both algorithms are combined in the following way: first the inverse problem is solved using truncated SVD, then it is solved by NNLS. The positive MNP amounts from the NNLS reconstructions are substituted by the values of the SVD algorithm at the same position. The latter approach should increase the reconstruction scores for the typical MNP distributions used in the lab. The reconstructions are performed on actual measurement data.

Figure 2.28 depicts a reconstruction example of MNP distribution 1. Using truncated SVD following quality parameters (Section 1.4.4) are obtained: CC = 89.4%, μ= 0.02 μmol and σ = 0.3 μmol, while for NNLS a general improvement in quality parameters is achieved: CC = 93.5%, μ = 0.02 μmol, σ = 0.2 μmol. NNLS is able to pinpoint the filled compartments in the tube, however, a large discrepancy exists between the actual MNP amounts in the compartment and the reconstructed amount (a mean difference of 0.3 μmol).

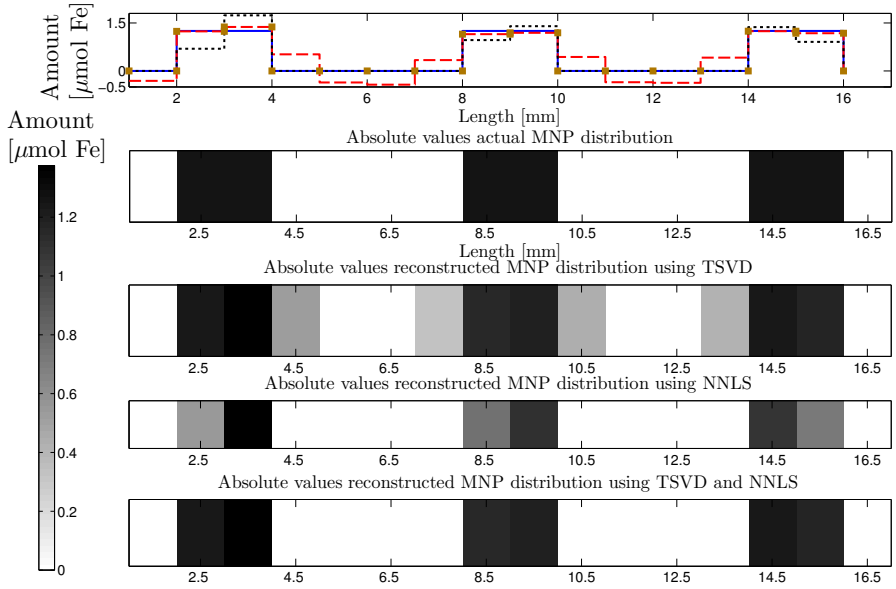

Figure 2.28: Reconstruction of MNP distribution 1 with truncated SVD (dashed curve), NNLS (dotted curve) and with truncated SVD and NNLS combined (filled squares) and respective subfigures with absolute values. The actual MNP distribution is the full line.

Truncated SVD on the other hand, shows a MNP concentration similar to the actual concentrations for the compartment positions (a mean difference of 0.06 μmol), but the compartments are broadened by an average of 2 mm. By combining SVD and NNLS, we can achieve a reconstruction with CC = 99 %, μ = 0.08 μmol and σ = 0.04 μmol. This is an increase of 10% and 6% in CC compared to the separate use of NNLS and SVD.

2.3.4 Conclusion

In this section the robustness of EPR towards setup parameters, noise and positioning errors was numerically investigated. Results showed that the EPR measurements need to be preferably carried out in a region where the response function exhibits a high continuous slope. Positioning errors have a larger impact than measurement errors so the automation of the sample positioning setup should be prioritized above improving the EPR measurement sensitivity. A gradient magnetic field can additionally improve setup noise errors as lower spatial variations of the MNP distribution are required while a larger variation in the EPR measurement is obtained. Additionally, a combination of truncated SVD and NNLS was proposed which improved the

solution of the inverse problem. The reconstruction quality is further affected by the stability of the inverse problem and therefore the sensitivity matrix should be constructed as such that it has a low condition number. The EPR setup used for the reconstructions in this dissertation, is not well suited for measuring homogeneous (constant) MNP distributions, but in biomedical applications these are rarely encountered. High quality reconstructions were achieved in case of MNP distributions with large spatial variations in their distribution and measurement.

2.4. 2D and 3D imaging

2.4.1 Introduction

In this section the 1D imaging procedure developed in Section 2.2, is extended to 2 and 3 dimensions using simulations. The possibility of using the EPR setup for multidimensional imaging is investigated in depth. In Section 2.4.2 the measurement procedure, forward model and 3D response function are discussed in detail. A new measurement procedure is introduced, since the approach used in 1D EPR can only be employed for the reconstruction of small volumes in 2D and 3D EPR. This new approach is here referred to as *partial volume excitation* and encompasses the partial activation of the MNP sample in order to stabilize the inverse solution.

In Section 2.4.3 the condition of the linear inverse problem is analyzed for different EPR implementations and it is numerically investigated how the associated inverse problem needs to be adapted to cope with the added dimensions. These added dimensions require a different way of obtaining measurement data. The goal is to achieve fast measurements and to attain an increased stability of the inverse problem. The investigation includes the reconstruction of multiple 2D and 3D MNP distributions with various response functions for different noise levels. The stability and reconstruction quality of each configuration is evaluated by calculating β (Eq. (1.28)) and by comparing the actual MNP distribution to the reconstructed MNP distribution (Eq. (1.27)). Based on these simulations, we state requirements for the EPR system to handle 2D and 3D MNP reconstructions. This work has been published in Ref. [255].

2.4.2 Forward modeling & measurement procedure

First, the differences with 1D EPR in terms of measurement procedure are highlighted and a new measurement approach is introduced. Secondly, the model for multidimensional EPR imaging, which includes the forward simulations and 3D response function, is discussed.

Recall that the unknown MNP distribution is denoted as the $1 \times V$ dimensional vector $\mathbf{c}$. It contains all the iron amounts on the different grid points, with V being the total number of grid points. In the case of 1D EPR this is a 1D grid (Sections 2.2 and 2.3), in 2D and 3D EPR these are 2 and 3 dimensional grids respectively. An EPR measurement is then represented by:

$$\mathbf{S}_{\mathrm{m}} = [S_1, ..., S_n, ..., S_N] \tag{2.13}$$

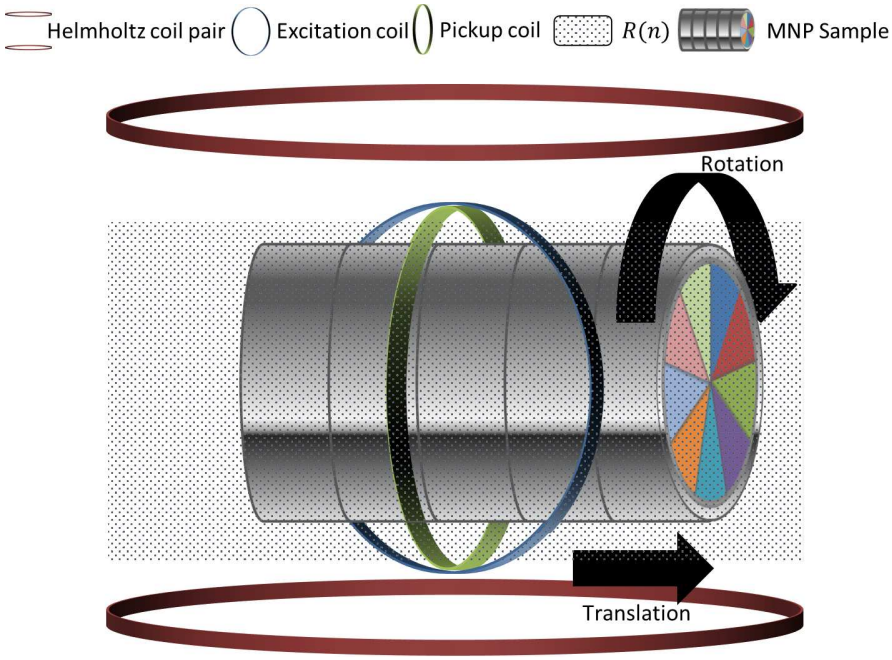

Figure 2.29: Schematic representation of the placement of MNP sample and coils in the EPR setup (not to scale) with possible movement directions for multidimensional imaging.

These N measurements originate from the N positions of the sample during a translation and/or rotation of the sample through the magnetic field. In 1D EPR the sample is translated along a line through the magnetic field (see Fig. 2.8a)). In 2D EPR similar translations are performed but in a plane instead of along one line. In 3D EPR additionally, rotations of the sample are allowed. For every step of the 1D translation, a full rotation of the sample is performed. Figure 2.29 gives an overview of possible movement options in case of multidimensional imaging.

Because of the changing distances with respect to the excitation and pickup coil for every position n, a different measurement value is obtained for an equal iron concentration, similar to the 1D case. These varying measurements are incorporated in the system response function $R(n)$ which contains the different measurement values as function of the position n in the magnetic field for a unit iron concentration. A unit concentration is chosen as the signal linearly scales with the iron concentration. n represents the spatial variables, for example, $R(z)$ in 1D EPR, $R(x,z)$ in 2D EPR and $R(x,\theta,z)$ or $R(x,y,z)$ in

3D EPR depending on the employed type of coordinate system.

As will be detailed further in Section 2.4.3, a simple extension of the 1D EPR principles to a 3D grid does not work to reconstruct larger samples due to instability issues when solving the inverse problem. For that reason, the inverse problem needs to be stabilized in order to achieve quantitative 3D reconstructions of larger samples. Therefore, *partial volume excitation* is introduced in the measurement procedure. In this approach only a part of the sample volume is placed in the region Ω where $R(n)$ is defined, see Fig. 2.30. In this case $R(n_v)$ is zero for c_v with $n_v \notin \Omega$. Partial volume excitation limits the zone of particle response and hence increases information content in the measured EPR signal. The sample is moved to measurement positions such that Ω comprises a different region of the sample. These positions are at the edges of Ω. In the previous approach (Section 2.2) the complete sample was placed in Ω. In practice, Ω corresponds to the region in which $\mathbf{B}_0$ and $\mathbf{B}_1$ can be measured (Section 2.2). Partial volume excitation can reduce the number of measurements by selectively activating parts of the volume, thus reducing the requirement of a complete translation of the volume through the magnetic field. The use of a coil array, which allows to generate spatially varying magnetic fields, can further improve this measurement method by actively targeting certain areas of the sample. This principle is further exploited in the EPR setup described in Section 2.5.

The forward simulations in multidimensional MNP imaging are done in a similar way as in 1D EPR, see Section 2.2.2. To find the response of a certain MNP amount on grid position n, the response value on n, $R(n)$, is multiplied with the MNP amount on grid position n. $\mathbf{S}_\mathrm{f}$ can then be modeled in a similar way as Eq. (2.7) by:

$$\mathbf{S}_\mathrm{f} = \mathbf{L} \cdot \mathbf{c} \tag{2.14}$$

$\mathbf{L}$ is a $N \times V$ system matrix consisting of the associated response values for every grid concentration for the N positions of the sample. Row n of $\mathbf{L}$, i.e. position n of the sample, is constructed from all the corresponding response values $R(n_v)$ for every unknown local c_v, $v = 1, ..., V$ on position n_v. In 3D EPR measurements N typically equals $Z \cdot \Theta$ with Z the number of translations of the sample and Θ the maximum number of rotational movements of the sample.

To allow forward simulations of 3D EPR measurements, a 3D response function is required for $\mathbf{L}$ in Eq. (2.14). Synthetic 3D responses are made to investigate the necessary requirements for the system response function and to show the impact of variations in system response on the inverse

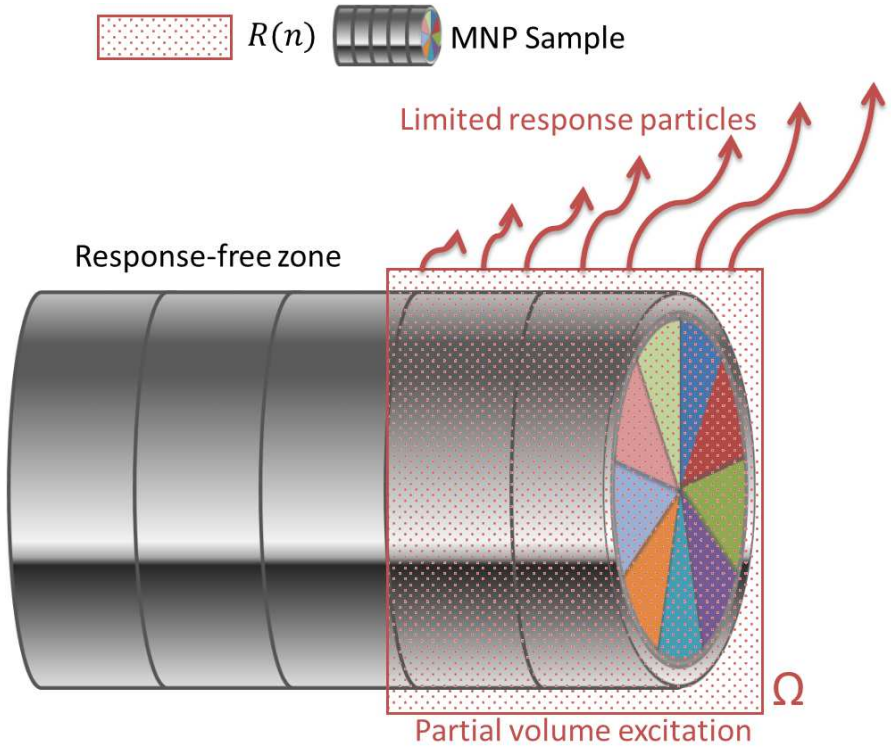

Figure 2.30: By placing only a part of the sample in Ω (and thereby limiting the zone of particle response) more independent information is available to solve the inverse problem which results in improved reconstructions of the MNP distribution.

problem. A 3D response function was modeled based on the measured 1D system response (Fig. 2.31a)). Recall that the response function $R(n)$ is a weighting function that represents how well a certain MNP amount on position n is registered by the pickup coil. Hence, particles further away from the excitation and pickup coil are moderately excited by the RF wave and only partly registered by the pickup coil, resulting in a lower response value. The maximum value, which is equal to 1, corresponds to the position where the particles are completely excited and sensed by the coils. A similar behavior with respect to the two coils is also assumed for the 3D response, i.e. a decrease of the response value in the directions further away from the two coils. Furthermore, we assume a certain circular symmetry with respect to the coils, as is also observed in the 1D case (see Fig. 2.31a) and Sections 2.2 and 2.3). No exact symmetry is modeled as noise and small displacements in hardware result in small variations in the response values. Therefore

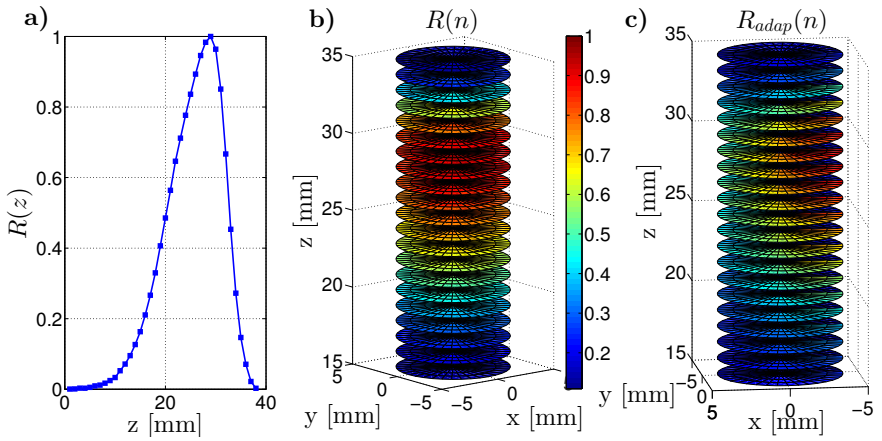

Figure 2.31: a) Measured 1D response function. b) Synthetic 3D response function with radius of 4 mm. c) Synthetic 3D response function with radius of 4 mm and reduced $\boldsymbol{\theta}$ symmetry.

white Gaussian noise with a noise level of 1 % with respect to the local response values was added to the model. Figure 2.31b) depicts the modeled 3D response function. We defined the 3D response function in cylindrical coordinates (x,z,θ) to focus on the rotational symmetry along the azimuthal direction $\boldsymbol{\theta}$. Due to the present diameter of the pickup coil ($\approx$ 9 mm), and because the sample is moved through this coil, the response is only defined in a region Ω with radius 4 mm. With the prospect of scaling up the EPR setup, additionally two response functions were calculated in regions with radii 8 and 12 mm to assess the influence of larger sample volumes. The model was experimentally validated by performing coarse measurements of the response function on a few positions in the EPR setup. Due to the lack of an accurate 3D positioning system, no precise measurements were possible.

Section 2.3.3 showed that symmetrical structures in the response function could reduce the reconstruction quality. To investigate the impact of symmetry, additionally three response functions (with radii 4, 8 and 12 mm) were modeled with larger variations with respect to the $\boldsymbol{\theta}$ direction. The functions are represented by $R_{\text{adap}}(n)$. Figure 2.31c) shows $R_{\text{adap}}(n)$ with a radius of 4 mm. $R_{\text{adap}}(n)$ allows to analyze the impact of reduced θ symmetry. The reduced symmetry of the response can be implemented in the system by adding magnetic field gradients or using a coil array such as in Section 2.5. This is because the response of the particles depends, among others, on the local magnetic field $\mathbf{B}_0$ surrounding the particle.

The MNP distribution is recovered similarly as in the 1D case by solving Eq. (1.19). This can be done using SVD, NNLS or a combination of both, see Sections 2.2 and 2.3. For the simulations in this section SVD is used because the main focus is on the reconstruction of spread sources. In Section 2.2 a method was devised to acquire the optimal cut-off r for EPR imaging with SVD. A general confidence interval for the recovered MNP distributions can be obtained from numerical simulations for, among others, various MNP distributions, different discretizations and noise levels in which the reconstructed MNP distribution is compared to the simulated one. This was investigated in Section 2.3 and in Ref. [311].

2.4.3 Numerical validation

The stability of the inverse problem and the imaging performance are analyzed for various configurations to investigate the feasibility of using the EPR setup for 3D imaging. The configurations include different MNP sample sizes, response functions ($R(n)$ or $R_{\text{adap}}(n)$), noise levels and measurement procedures (partial volume excitation). The measurements are simulated by incorporating the actual MNP distribution into the respective forward model (similar as in Eq. (2.8)).

The symmetric 3D response was used to generate the sensitivity matrix $\mathbf{L}$. The sample was placed in the magnetic field and translated in steps of 1 mm, no partial activation was employed. For each step of the translation, a full rotation (360 $^\circ$ in steps of 10 $^\circ$) was performed. The resolution of the volume is fixed at 1 mm. We performed noise-free reconstructions of different samples having dimensions of $x \times y \times z$ mm^3 with $x = y = z = 1,...,10$. We obtained high-quality reconstructions until $V \approx 200$. Figure 2.32 shows an in-plane reconstruction example of a 5 x 5 x 5 mm^3 with $V = 125, N = 170$ and a $10 \times 10 \times 10$ mm^3 volume with $V = 1000$, $N = 729$. For the smaller volume, a perfect reconstruction is obtained, while the larger volume is unrecognizable. This way of performing 3D EPR only allows the imaging of small MNP volumes as the results deteriorate quickly for larger volumes. Furthermore, the measurement procedure is time-consuming.

Because the response function depends on the relative distances of the sample to the two coils, a circular symmetry is observed where values do not differ a lot. By incorporating these values in $\mathbf{L}$ it is possible that linearly dependent information is added and thus the condition of the linear inverse problem deteriorates. This was already observed for the 1D case in Section 2.3.3, in which it was shown that symmetric responses deteriorate reconstruction

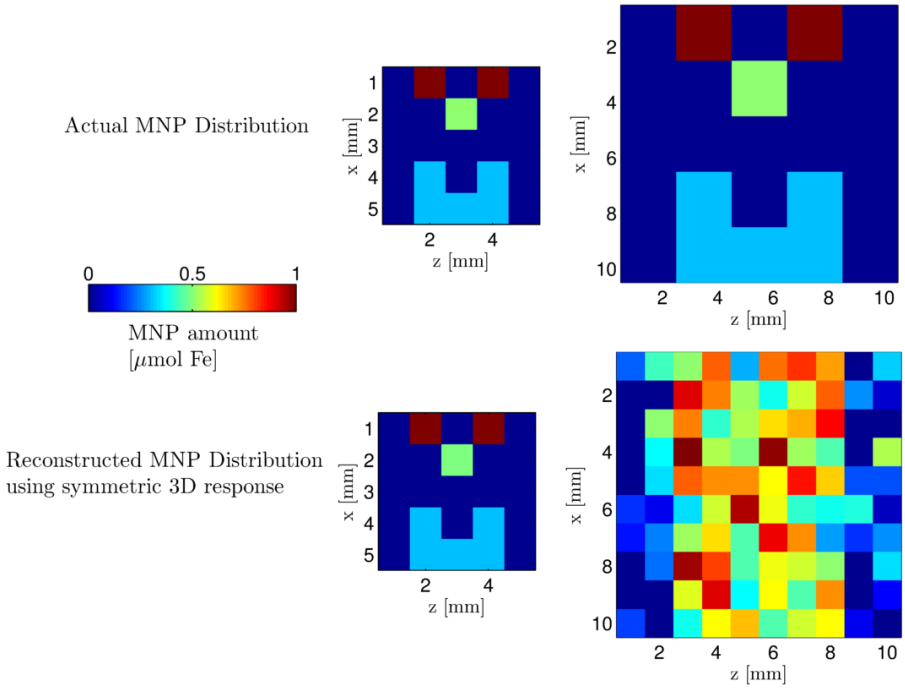

Figure 2.32: 3D EPR imaging of a small $5 \times 5 \times 5$ mm^3 volume and a larger $10 \times 10 \times 10$ mm^3 volume using the symmetrical response function. Using this first approach, with the symmetric response function, only small volumes can be reconstructed.

results. To investigate this effect, sensitivity matrices were made of different sizes corresponding to the reconstructions of different volume sizes. The reconstruction starts with a cylindrical segment with length 5 mm and radius 1 mm having only an angle of 10°. The corresponding condition of this inverse problem is $\beta(\mathbf{L}) \approx 7$ (Eq. (1.28)). Then the volume was increased each time along one dimension ($\mathbf{x}$, $\boldsymbol{\theta}$ or $\mathbf{z}$) and for every increase of the volume, the condition of the inverse problem was evaluated. Figure 2.33a) shows β for all these volumes. In this case the response function with a radius of 12 mm was employed (full lines). It can be seen that increasing the $\boldsymbol{\theta}$ dimension results in a decrease of system stability. These reconstructions were also made with $R_{\text{adap}}(n)$ which does not have this circular symmetry. Then an improved stability for the system matrix is obtained (dashed line). For an increase in the x and z dimensions, the dashed line is equal to the respective full lines as only the $\boldsymbol{\theta}$ direction has changed. Similar results were obtained for the other two response functions with smaller radii (x is limited to their respective radii). Furthermore, Fig. 2.33a) clearly shows that for increasing radius (x) and length (z) the stability is not reducing, making the technique suitable for

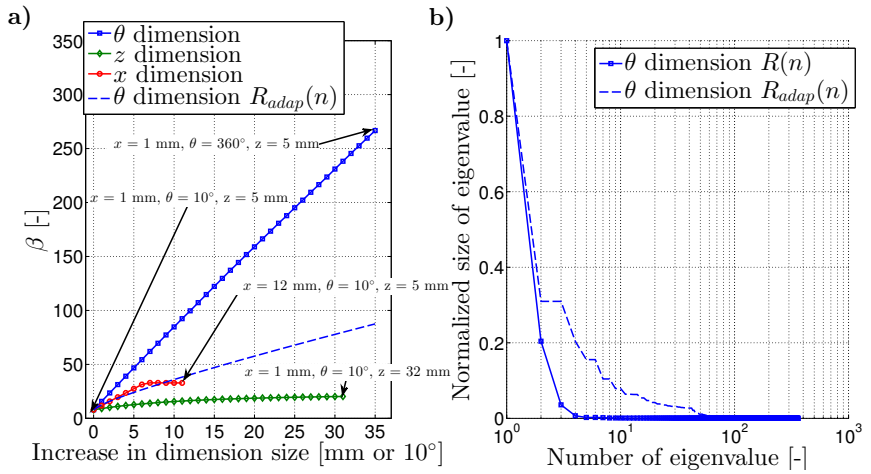

Figure 2.33: a) Numerical stability of **L** for increasing volume dimensions. Because of symmetry reasons an increase in θ dimension results in a decrease in system stability. Using $R_{\text{adap}}(n)$, this system instability is reduced. Furthermore, an increase in x and z dimensions has no large impact on system stability. b) The eigenvalue distribution of $R_{\text{adap}}(n)$ shows a slower decrease which improves the stability of **L**.

samples with larger radii and lengths. Figure 2.33b) depicts the normalized eigenvalue distribution (Eq. (1.23)) for the case of x = 1 mm, θ = 360 ° and z = 5 mm for $R(n)$ and $R_{\text{adap}}(n)$. The slower decrease of the $R_{\text{adap}}(n)$ eigenvalues and their relative larger sizes make the solution more robust compared to $R(n)$, see Section 1.4.4. The cut-off value r was determined according to Section 2.2. By reducing the EPR symmetry, quantitative images of larger MNP samples ($V \approx 800$) like those shown in Fig. 2.32 can be obtained.

The numerical stability of **L** was further improved by placing only a part of the sample in Ω, so only a well-defined segment of the sample generated the particles' response (Fig. 2.30). In Fig. 2.34 a 2D reconstruction example is shown with partial volume excitation (Fig. 2.34b)) and without partial volume excitation (Fig. 2.34c)). In the case of partial volume excitation, the sample was gradually translated, in steps of 1 mm, into the magnetic field generated by the Helmholtz coil, thereby increasing the part of the sample in Ω. Note that, compared to Figure 2.32, the reconstruction quality is lower due to the shape of the sample which allows less measurements (only translations) compared to the number of unknowns. The amount of measurements in Fig. 2.34 was adapted so both measurement methods obtained the same number of measurements (N = 28, V = 77). The reconstruction with partial volume excitations shows an increase in reconstruction quality (a CC of 63 % compared

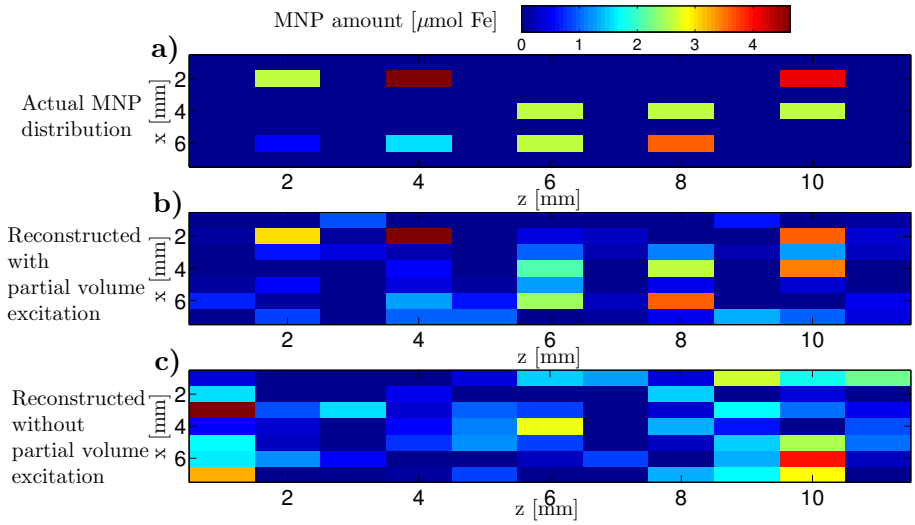

Figure 2.34: Reconstruction of a 2D MNP distribution with and without partial volume excitation. When partial volume excitation is employed, improved reconstructions of the MNP distribution are obtained.

to a CC of only 10 %) and in numerical stability (from $\beta(\mathbf{L}) \approx 28$ to $\beta(\mathbf{L}) \approx 15$ for partial volume excitation). This increase in stability was also observed in the system matrices of Fig. 2.33a) and now a perfect reconstruction of the larger volume of Fig. 2.32 can be attained.

Figure 2.35 depicts the averaged reconstruction scores, and their standard deviation, of 50 randomly generated MNP distributions with and without partial volume excitation for a volume with fixed θ and x dimensions, but increasing z dimension. The larger the MNP sample and thus the more ill-posed the problem, the better the partial volume excitation performs with respect to the conventional measurements. The partial volume excitation was performed by gradually inserting the sample in the magnetic field. In these simulations, the ratio of total number of measurements (N) to the total number of unknowns (V) was kept constant for both methods (by increasing/decreasing the number of measurement positions), because it also has an impact on the inverse problem, see Section 2.3 and Ref. [311]. The improved reconstructions thus only originate from additional information in the inverse problem. This is achieved by only exciting parts of the sample instead of the complete sample. Thanks to the increased stability we can speed up the measurement method, while attaining an increase in reconstruction quality. This way we can increase the measurement speed by ≈ 10 %. This indicates

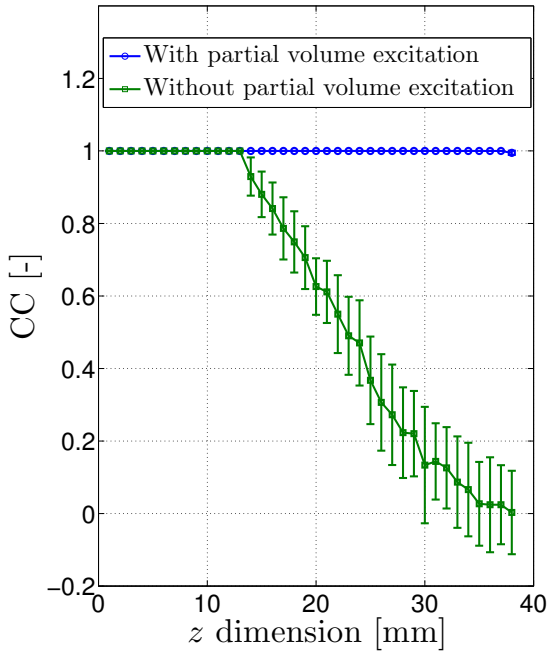

Figure 2.35: Larger 3D MNP volumes deteriorate the condition β of the inverse problem. For every volume 50 randomly generated 3D MNP distributions were reconstructed with and without partial volume excitation. When employing partial volume excitation the condition of the inverse problem deteriorates slower.

that the EPR methodology can be further improved by using magnetic field gradients or a coil array that can actively target certain areas of the sample. This principle is investigated in detail in Section 2.5.

Previous noise-free simulations regarded the stability of the sensitivity matrix. We reduced the symmetry in the original response function to obtain improved solutions to the inverse problem. Additionally, the concept of partially exciting the sample was introduced, further improving stability of the methodology and showing improved reconstructions. Now, the robustness towards noise for these adaptations is investigated. White Gaussian noise was added in steps of 1 %. For every noise level 200 noise measurements are performed which are then averaged. The noise levels of 1 to 10 % are with respect to the system response amplitude and correspond to actual noise values of the setup (Sections 2.2 and 2.3). Figure 2.36a) shows the average CC and standard deviation for increasing noise levels for the different approaches used in this paper. As stated previously, the original response function $R(n)$ is not able to reconstruct larger MNP samples. Now that noise is added, the solution

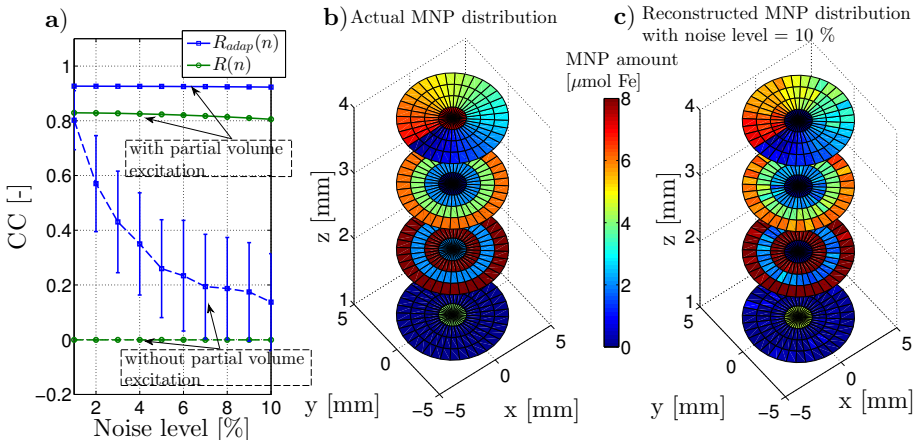

Figure 2.36: a) Noise robustness of the different approaches used in this section. b) Example of a 3D MNP distribution. c) Reconstruction of the 3D MNP distribution from b) using a noise level of 10 % and the adapted system response with partial volume excitation.

deteriorates even faster than before. $R_{\text{adap}}(n)$ delays the deterioration due to the reduced symmetry, but shows significant noise impact (CC goes from $\approx$ 0.8 to $\approx$ 0.13) and a large standard deviation. When using the partial volume excitation, in which we gradually insert the sample in the magnetic field, we observe a tremendous increase in reconstruction quality for both response functions ($R(n) \approx 0.82$, $R_{\text{adap}}(n) \approx 0.92$) and the standard deviation is now significantly lower. Figure 2.36c) shows a reconstruction example of the MNP distribution depicted in Fig. 2.36b) using the adapted response function with partial volume excitation and a noise level of 10 %.

2.4.4 Conclusion

In this section, a general technique was presented to reconstruct multidimensional MNP samples using EPR. Its feasibility was analyzed in depth by using simulations. The extension of the 1D approach from Section 2.2 to 2D and 3D works fine for smaller volumes ($V < 200$), but numerical stability issues arise when imaging larger volumes. Different sensitivity matrices were generated for cylindrical volumes with increasing sizes along one dimension. The deterioration of the solution was especially visible for increasing θ dimensions, which is due to the symmetry of the 3D response function $R(n)$. x and z dimensions only had a minor effect on the stability. The stability of the inverse problem showed that a reduction in symmetry was necessary to assure a sensitivity matrix which is sufficiently stable to allow sensitive

reconstructions of the MNP distribution. To reduce the symmetry of the response function magnetic field gradients or a coil array can be employed (Section 2.5). Based on this principle, the stability of the sensitivity matrix was further increased by exciting only a part of the MNP sample. In this first approach, this was done by gradually inserting/removing the sample in the magnetic field. This adds linearly independent information to the inverse problem to be solved and translates into improved reconstructions. Due to the increased stability and better imaging results, it is also possible to reduce the number of measurement positions and this way speed up the presented technique. A speedup of $\approx$ 10 % can be achieved while still obtaining an increased reconstruction quality. It is expected that this measuring method can be further improved if fields are employed which can target specific areas of the volume (see Section 2.5). Finally, the robustness of the developed method towards noise was investigated, which showed that the adaptations realize an increase in reconstruction quality and the EPR setup maintains its stability with respect to larger multidimensional samples.

2.5. Heterogeneous activation sequences

2.5.1 Introduction

The EPR system described in Section 2.1.3 employes a homogeneous magnetic field $\mathbf{B}_0$ generated by a Helmholtz coil pair. In this section, the EPR setup is adapted such that it can produce distinct heterogeneous magnetic fields. These fields allow to stabilize the solution of the associated inverse problem and to obtain local spatial information. This is based on the *partial volume excitation* principle explained in Section 2.4. The partial volume excitation was shown to stabilize the inverse problem by adding linearly independent information. To realize the heterogeneous fields, the Helmholtz coil pair is replaced by a coil array of 16 smaller coils. The use of coil arrays does not only add independent information, additionally it increases the number of EPR measurements and hence stabilizes the inverse solution. This proposed imaging method is numerically compared to the conventional approach with homogeneous magnetic field. The activation of the coils and the measurement procedure are optimized to obtain the best reconstruction results using a minimal number of measurements, allowing a speedup of the EPR imaging technique.

In Section 2.5.2 the necessary adaptations of the forward model, response function and measurement procedure are discussed. The forward model as well as the response function now need to be adapted to take into account the varying magnetic fields generated by the coil array. First, the resulting change in response due to a different magnetic field was experimentally measured and then incorporated in the modeled response. In Section 2.5.3 the presented model is numerically validated using computer simulations. Both approaches (homogeneous and heterogeneous imaging) are thoroughly investigated by comparing their imaging performance trough calculating their CC (Eq. (1.27)) for various MNP distributions for different noise levels. Furthermore, due to the increased stability obtained in the case of heterogeneous EPR imaging, new measurement procedures are analyzed to reduce measurement time. This work has been published in Ref. [312].

2.5.2 Forward modeling & measurement procedure

Figure 2.37a) depicts the EPR setup which was employed in the previous sections. Recall that it contains a Helmholtz coil pair that produces a homogeneous magnetic field $\mathbf{B}_0$. Therefore we refer to this approach as *homogeneous* EPR imaging. In this case the magnetic field has a fixed amplitude of 10 mT. By additionally applying a RF wave with B_1 at the right frequency,

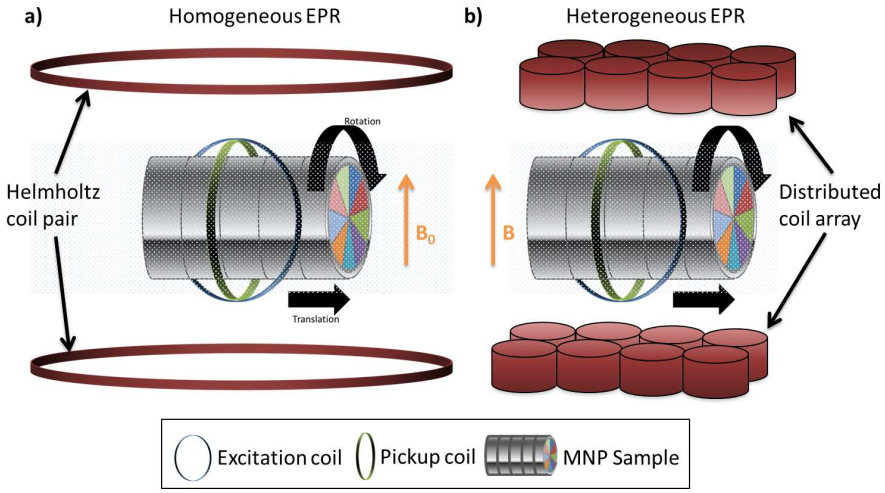

Figure 2.37: a) Example of the setup for homogeneous EPR. b) Example of the EPR setup for heterogeneous EPR.

the MNP absorb its energy and the magnetic moment of the MNP can be measured by the pickup coil (see Section 2.1.3). The resonance condition is determined by the gyromagnetic constant of the electrons. Energy absorption is maximal at the resonance condition, although energy absorption also occurs at magnetic field values near the resonance condition, albeit less efficient (i.e. the angle in Fig. 2.4 will be smaller and hence also M_y). The EPR setup presented in this section exploits this useful property. Instead of using a Helmholtz coil pair with a homogeneous magnetic field fixed at 10 mT, it employes coil arrays that generate heterogeneous magnetic field with amplitudes between 0 and 10 mT. As the response of the MNP depends on their local magnetic field, spatial information can be encoded in the measurement signals this way. Similarly as for the partial volume excitation approach from Section 2.4 this approach allows to stabilize the inverse solution. We refer to this latter approach as *heterogeneous* EPR imaging.

Figure 2.37b) depicts the heterogeneous EPR setup where the Helmholtz coil is substituted by $Q = 16$ smaller coils for generating heterogeneous magnetic fields. Each of these coils consist of 9 winding turns and have a diameter of about 1 cm and are distributed in 2 groups of 8 coils with a spacing of ≈ 1.5 cm in between, where the unknown MNP sample is placed. 16 coils are chosen so the total magnetically activated area is of a similar size as when the Helmholtz coil pair was employed and their diameter is sufficiently small to allow a good imaging resolution. The currents flowing through each coil are called *activa-*

tion currents and are denoted by a $Q \times 1$ vector $\mathbf{I}_{\text{coil}}$. In this case the response function is extended to incorporate responses for different magnetic field amplitudes B, $R(n,B)$. A change in the magnetic field's amplitude alters the required energy of the RF wave, generating a different measurement value S_{m}.

Similarly as in 1D and multidimensional EPR the sample can be moved to N positions. We recall that a measurement is performed at each position, resulting in the following set of measurements:

$$\mathbf{S}_{\text{m}} = [S_1,...,S_n,...,S_N] \tag{2.15}$$

The use of a coil array increases the degrees of freedom as various magnetic fields can be applied for each position of the sample. One possible way of generating various magnetic fields is to activate the coils *sequentially*. In Section 3.1.4 the general formulation for various coil activations can be found. In the sequential activation approach, for each position n, Q magnetic fields are generated with each magnetic field produced by the activation of the q-th coil ($q = 1,...,Q$) with $\mathbf{I}_{\text{coil}_q}$ a vector containing the Q currents for the q-th activation, in which only the q-th element has a value > 0 amps, while the other elements are zero amps. Hence Eq. (2.15) can be extended to:

$$\mathbf{S}_{\text{m}} = [S_1,...,S_{NQ}] \tag{2.16}$$

Instead of having N measurements now a total of NQ measurements can be obtained.

Similarly as in Sections 2.2 and 2.3, Eq. (2.15) can be modeled by:

$$\mathbf{S}_f(\mathbf{I}_{\text{coil}_q}) = \mathbf{L}(\mathbf{I}_{\text{coil}_q}) \cdot \mathbf{c} \qquad\qquad q = 1,...,Q \tag{2.17}$$

In contrast to Eq. (2.7), which was for a fixed magnetic field generated by a Helmholtz coil pair, Eq. (2.17) represents the N measurements of the sample positions in the magnetic field generated by the q-th coil. $\mathbf{L}(\mathbf{I}_{\text{coil}_q})$ is a $N \times V$ matrix and hence has the same dimensions as in Eq. (2.7). Additionally, it is possible to merge the Q magnetic field configurations together in the forward model:

$$\mathbf{S}_f(\mathbf{I}_{\text{coil}}) = \mathbf{L}(\mathbf{I}_{\text{coil}}) \cdot \mathbf{c} \tag{2.18}$$

In this case $\mathbf{L}(\mathbf{I}_{\text{coil}})$ becomes a $(NQ) \times V$ matrix with $\mathbf{I}_{\text{coil}}$ a diagonal matrix having $Q \times Q$ elements corresponding to the currents flowing through the Q coils for the Q coil activations.

To allow forward simulations of EPR measurements for varying B, the response function needs to be extended to include the effect of B, $R(n,B)$. Re-

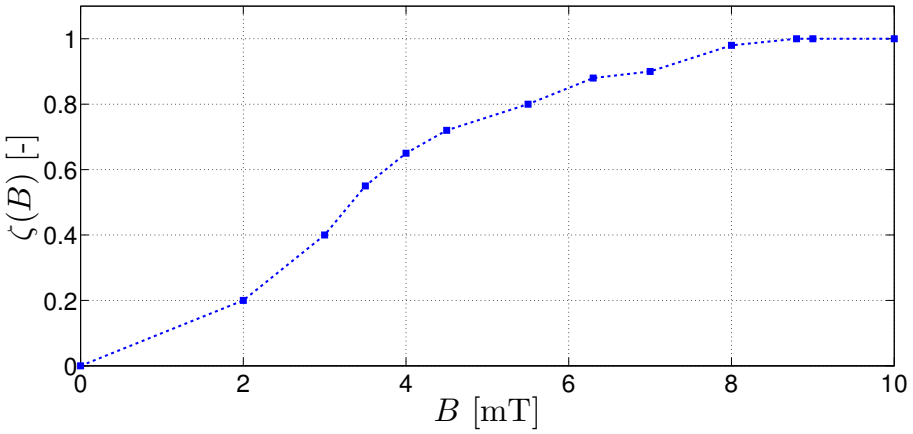

Figure 2.38: Impact of B on the measured response on position n.

sponse values at different B can be modeled by:

$$R(n,B) = \zeta(B) \cdot R(n) \tag{2.19}$$

in which $\zeta(B)$ is an experimentally determined weighting factor depending on the local magnetic field B on position n. $\zeta(B)$ is found by measuring the change in response compared to $R(n)$ for varying B. This was done for a calibration sample in the center of the setup. Figure 2.38 depicts the measured values for $\zeta(B)$. For every grid position the maximum response is obtained at 10 mT (which corresponds to the value $R(n)$). A similar dependence as in Fig. 2.38 is assumed for other grid positions, with respect to their maximum response value at 10 mT. The magnetic field at each grid location is calculated through Biot-Savart and depends on the geometrical details of the coils and their currents. To have magnetic field amplitudes between 0 and 10 mT, the current in the coils is limited to approximately 12 A in the sequential activation approach.

The unknown spatial MNP distribution is obtained in an equal way as in the previous sections: by minimizing the differences between the model solution and the measurement (Eq. (1.19)). In this section Eq. (1.19) is solved by truncated SVD (Eq. (1.23) as was done in Sections 2.2, 2.3 and 2.4. The cut-off value r was determined according to the method described in Section 2.2.

2.5.3 Numerical validation

Five random fractal clustered MNP distributions were generated using fractional Brownian motion [313]. These distributions are ideally suited for the representation of MNP injection sites and allow to thoroughly test and compare both setup configurations. For each distribution a reconstruction is made for increasing noise levels ranging from 1 to 10 % with respect to the response, $R(n)$. The noise is considered to be white Gaussian noise and for each distribution and noise level, 200 noisy reconstructions are performed which are then averaged. The reconstructions are evaluated by calculating the CC (Eq. (1.27)) between the actual MNP distribution $\mathbf{c}$, and the reconstructed MNP distribution $\mathbf{c}^*$.

A first step was to activate the coils from the heterogeneous EPR setup separately and sequentially, see Eqs. (2.17), (2.18). Figure 2.39 shows the average reconstruction results and their standard deviation for each separately activated coil (Eq. (2.17)), all the coils combined in sequential EPR (Eq. (2.18)) and homogeneous EPR (Eq. (2.7)). The purple lines represent the single activation of the outer coils (the 4 coils furthest away from the center of the sample, below and above, 8 in total, see also Fig. 2.37b)). Because these coils magnetically activate regions where $R(n)$ is significantly lower than 1 at 10 mT (further away from excitation and pickup coil) and taken into account the relative decrease from Fig. 2.38, these regions vary only slightly in response values for changing B (a variation of only 1-10 %), which is why the reconstruction results deteriorate. The middle coils (black lines) activate regions where a change in amplitude of $\mathbf{B}$ sufficiently alters the response values (a variation of 70-90 %), adding information to the inverse problem to be solved and resulting in improved reconstructions of the distributions. These variations also reflect in the corresponding eigenvalue distributions which show a slower decrease for the middle coils compared to the outer coils, generally accepted as an increased signal-to-noise ratio (Section 2.2). Differences between coil lines of equal color result from changes in the maximum response value in the region of activation. Combining all these measurements together (blue line) results in an increase in average reconstruction quality of 5% and is 12 times more robust towards noise (12 times smaller standard deviation) compared to the conventional homogeneous approach. This result shows that the combination of coils is necessary in order to obtain localized and general information of each part of the sample and this way increase noise robustness and reconstruction quality.

It is clear that using heterogeneous instead of homogeneous magnetic fields for EPR-based reconstruction of MNP distributions has a significant advantage. However, the proposed method required 16 times more measurements

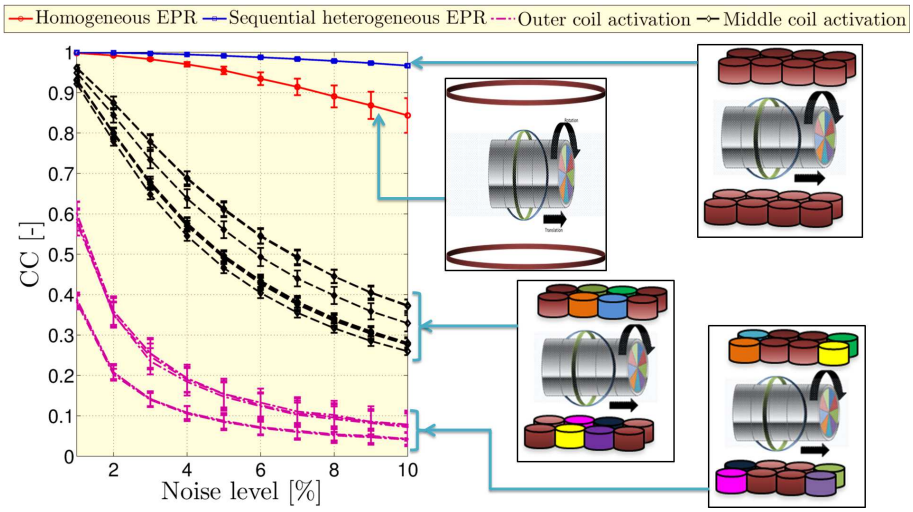

Figure 2.39: CC for increasing noise levels for activation of the coils separately (black and purple lines), all the coils combined (blue line) and homogeneous EPR (red line).

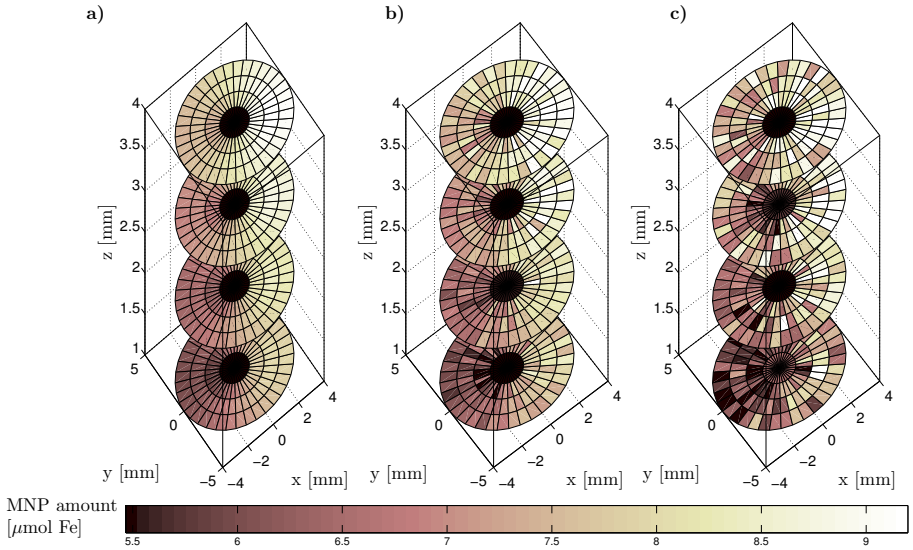

Figure 2.40: a) Actual MNP distribution. b) Reconstructed MNP distribution with sequential EPR and limited movement of the sample. c) Reconstruction using homogeneous EPR with complete movement of the sample.

than the conventional method (Eqs. (2.7) and (2.18)). We therefore decreased the measurements associated to position changes of the sample. This way

an increased accuracy in less measurements compared to the conventional method can be achieved. To reduce number of positions, full rotations of the sample were allowed, but translational movement was limited to the center of the setup (near positions of pickup coil and excitation coil). Only the 4 middle coils were used as the other coils activate this region only slightly. This way, the amount of measurements was reduced by approximately 15 % (or 180 measurements) compared to homogeneous EPR without limited movement while still obtaining an improved accuracy of 4 % and a 2 times improved noise robustness. Homogeneous EPR with limited number of positions of the sample, shows a decrease of the CC with approximately 75 %. Figure 2.40 depicts a reconstruction of a MNP distribution with sequential EPR and limited movement of the sample (Fig. 2.40b)) and with homogeneous EPR and complete movement of the sample (Fig. 2.40c)).

2.5.4 Conclusion

In Section 2.4 it was shown that the partial volume excitation approach had the potential to improve the stability of the inverse problem, resulting in improved MNP reconstructions. This principle was exploited in this section by making use of the varying resonance condition of the MNP. This resonance condition depends on the amplitude of the local magnetic field B. To this end, the setup presented in Section 2.1.3 was adapted to generate heterogeneous magnetic fields and include spatial information in the measurements. Therefore, we replaced the Helmholtz coil from the original EPR imaging setup by a distributed coil array that generates heterogeneous fields instead of the conventional homogeneous magnetic fields. Both approaches were extensively studied and compared by reconstructing various MNP distributions for different noise levels. The accuracy of the MNP reconstructions was increased by 5 % and had a 12 times increased robustness towards noise when using heterogeneous EPR. Furthermore, if the number of positions of the sample was decreased, a speedup of the technique by 15 % could be achieved by using our adapted approach while maintaining an increase in reconstruction accuracy of 4 %. Additionally, we realized a two times improved noise robustness compared to homogeneous EPR.

3

Magnetorelaxometry

This chapter starts with a general introduction to magnetorelaxometry (MRX) (Section 3.1). It explains how a typical MRX measurement is performed, followed by an overview of the main theoretical models useful in MRX imaging and in describing its decaying magnetic signal. The section ends with a discussion of the main biomedical applications making use of MRX. In Section 3.2 it is shown how the MRX measurement procedure can be iteratively adapted to include preliminary information about the particle sample in order to enhance particle reconstructions. Section 3.3 introduces the use of statistical parameters to build quantitative MRX imaging models that allow the direct enhancement of imaging systems and the comparison of different MRX imaging models and setups. This chapter ends with the description of an advanced MRX imaging model, the so-called MRX multi-color model, that enables the localization and quantification of multiple particle types simultaneously (Section 3.4).

3.1. Basic concepts

3.1.1 Introduction

A magnetorelaxometry experiment consists of two phases. First the magnetic moments originating from the MNP are aligned by an external magnetic field. The magnetic field is typically generated by a twin coil [314], a Helmholtz coil pair [34] or an array of coils [263]. The second phase corresponds to switching off the magnetic field and measuring the decaying net magnetic moment of the MNP sample, referred to as the magnetorelaxometry signal. This signal can be measured with sensors such as SQUIDs [19], fluxgates [315], and optical [316] and magnetoresistive magnetometers [257]. Because the biological environment is not able to generate magnetorelaxometry signals, only the specific signal of the MNP is measured. In this dissertation, distinction is made between magnetorelaxometry for characterizing MNP properties and magnetorelaxometry *imaging* for acquiring the spatial MNP distribution. In the first approach the decaying signal is related to MNP properties and their environment (see Sections 1.1.2 and 1.1.3) such as their distribution of energy barriers [317], d_c and d_h [245, 246], the detection of particle aggregation [29, 318] and their interactions [71, 73]. The effect of particle properties on the MRX signal is also conveniently used in immunoassays (Section 1.2) for the detection and quantification of biological entities, such as viruses, proteins, molecules, bacteria, and etc. [16, 27, 53, 55, 76].

In the specific case of MRX *imaging*, an inverse problem is solved in which the measured MRX signals are related to a certain spatial MNP distribution. As detailed in Section 1.4.3, the inverse problem requires a forward model which has a large impact on the reconstructed MNP distribution. Therefore, research has been focused on developing models that increase MRX imaging performance with respect to speed and accuracy. This was mostly achieved by inducing MNP responses that contain increased amounts of independent information on particle location. This includes the use of spatially varying magnetic fields, based on the susceptibility tomography principle presented by Wikswo et al., in which only parts of the sample produce the MRX signals [40]. This can be realized by moving the sample [41], limiting relaxation to a single point that is moved through the sample such as in MPI [319], or by employing coil arrays in which the MRX signal of the MNP can be measured for each generated magnetic field configuration [263]. Specific attention was devoted to how the coils in the array need to be activated in order to reduce measurement time, while improving reconstruction accuracy [42, 264, 272]. Additionally, the forward model has been improved so to stabilize the inverse problem, by including the MRX signal on multiple time points [37] and by determining optimal voxel grid properties [39] and coil and sensor

positions [320, 321]. Finally, also different inverse solution methods have been investigated for MNP reconstructions using MRX [36, 42, 270, 322].

In Section 3.1.2 the general MRX measurement procedure is explained and in Section 3.1.3 an overview of the main models describing the decaying MRX signal is given. This is followed by Section 3.1.4 in which the forward model (Eq. (1.18)) for MRX imaging is derived. Finally, in Section 3.1.5 the main biomedical applications in which the MRX signal is exploited are discussed.

3.1.2 MRX measurement procedure

In a MRX experiment the delayed response of a MNP system to a sudden shutdown of the magnetic field is measured. A typical MRX measurement is schematically illustrated in Fig. 3.1. It consists of two main phases: a *magnetization phase* and a *measurement phase*. We recall from Section 1.1.3 that the MNP ensemble has no net magnetization when no magnetic field is applied due to the random orientation of the MNP's magnetic moments. During the magnetization phase an external magnetic field, $\mathbf{H}_{\text{mag}}$, is applied for a duration of t_{mag} to the MNP sample in which the MNP align their magnetic moments toward the direction of the applied field. The degree of alignment depends on H_{mag}, t_{mag}, T and particle properties such as K, d_{c} and d_{h} (Section 1.1.3). The magnetization time, t_{mag}, is typically of the order of 1 s and H_{mag} is around 1 mT$/\mu_0$. In the measurement phase, the external field is removed and a decaying magnetization of the sample, in the order of nT to pT, is observed. This decaying signal originates from the random orientation of the MNP's magnetic moments through the particle's fastest relaxation mechanism, either τ_{N} (Eq. (1.4)) or τ_{B} (Eq. (1.5)). Recall that τ_{N} expresses the thermal switching of the particle's magnetic moment inside the core and depends exponentially on V_{c}, while τ_{B} reflects the reorientation of the magnetic moment through rotation of the particle as a whole and depends linearly on V_{h}. The decaying signal is therefore highly dependent on particle properties. The signal is measured for a duration of t_{meas} which is generally of the order of 0.2 to a few seconds. The decaying signal can be roughly described by two parameters: its relaxation amplitude ΔB and its relaxation time $t_{1/e}$. ΔB expresses the decrease in amplitude of the MRX signal between two chosen time points (in the case of Fig. 3.1, this corresponds to the start and end of the MRX measurement), while $t_{1/e}$ denotes the time needed for the decaying signal to decrease by a factor $e \approx 2.718$ (corresponding to a 63.2 % decay). As will become clear in Section 3.1.3, this only suffices as an approximation of the decay, even though these two parameters are commonly

employed to compare MRX curves.

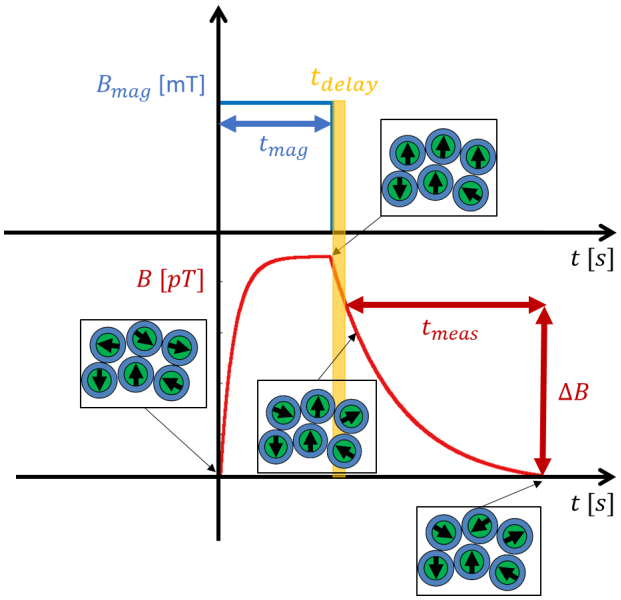

Figure 3.1: Illustration of a typical MRX experiment. First an external magnetic field H_{mag} is applied for a duration of t_{mag}, which aligns the magnetic moments of the MNP. Then, the field is removed and the decaying signal or MRX signal is measured for t_{meas} in which the particles resume their random orientation through Néel and Brownian relaxation. The measurement is typically started after a time delay, represented by t_{delay}.

A time delay, t_{delay}, is required after the magnetic field pulse because of the finite shut-down time of H_{mag}, as well for the recovery of sensor electronics and to allow damping of possible induced currents in the surroundings of the sensors and environment. Note that t_{delay} is highly dependent on the measurement setup and varies in state-of-the-art MRX setups from 200 μs to 35 ms [66, 76, 316, 323]. The measurement procedure is thus among others affected by the type of sensor employed. Frequently used in MRX experiments are low-temperature (low-T_c) SQUID sensors. Although requiring more technical effort, they are amongst the most sensitive sensors with detection limits as small as a few fT/$\sqrt{Hz}$ with a bandwidth of several MHz. Because of their sensitivity they cannot be operated during the application of H_{mag}. Another drawback is the larger distance between the MNP ensemble and the sensor, because of the need of thermal insulation for the sensors. Despite the fact that optical magnetometers and fluxgates have a smaller bandwidth (a bandwidth of a few kHz) and the latter one is less sensitive (pT/$\sqrt{Hz}$),

they can be operated during the application of H_{mag} and be placed closer to the sample. Additionally, because the decaying signal from the MNP is several orders of magnitude smaller than possible magnetic field distortions, magnetic shielding and/or gradiometer configurations (i.e. the difference in induced magnetic field between at least two connected sensors) should be employed to suppress these (far) field distortions [76, 258, 323, 324]. Some systems even additionally employ active shielding [325].

It is important to note that the measurement window determines which particles can be measured by the system. Indeed, the effective relaxation time τ_{eff} (Eq. (1.6)) needs to fall within the measurement window in order for the particles to reorient themselves and to generate a decaying signal in the sensors. Recall from Section 1.1.3 that τ_{eff} corresponds to the prevailing relaxation for the given particle type, i.e. Brownian (τ_{B}) or Néel (τ_{N}) relaxation. If τ_{eff} is faster than the start of the measurement, the particles will have relaxed and the signal will already be zero at the start of the measurements. On the other hand, if τ_{eff} is longer than the measurement window, no decay will be observed. In practice a distribution of particles is present in the system. This means that some of the particles reorient themselves during the measurement, while some particles relax outside the measurement window (i.e. before or after the measurement). We refer to Fig. 1.4 for an example of how τ_{eff} depends on particle properties d_{c} and d_{h}. Furthermore, it is possible to adapt τ_{B} through changing the viscosity of the particles' environment or by binding with other particles or entities. When particles relax according to τ_{B} this can be changed to τ_{N} by immobilizing the particles, so that rotation of the particles themselves is not possible anymore and hence τ_{B} becomes infinite. This can for instance be achieved by freeze-drying the sample or placing the MNP in gypsum cubes.

3.1.3 Modeling the MRX signal

Several models exist that describe the decaying signal each with their own assumptions. These models are used in the pre-processing of sensor signals, the imaging of the spatial distribution of the MNP, or in describing particle properties or binding state of the measured MNP. Remark that in this section no vector notation is used, since the orientation of $\mathbf{M}$ is parallel to the direction of $\mathbf{H}$ at the considered position. For the case of identical particles, without interactions, the decaying magnetization from the MNP ensemble, $M(t)$, can be modeled by [26]:

$$M(t) = M_0 \exp\left(\frac{-t}{\tau_{\text{eff}}}\right) \tag{3.1}$$

with M_0 the magnetization amplitude at the start of the measurement and τ_{eff} the effective relaxation time of the given particle type. In practice however, a distribution of sizes and shapes of the particles is present in the sample, which results in a distribution of τ_{eff} and hence the relaxation behavior of the system is non-exponential. Chantrell et al. derived a formula for the decaying signal of a uniform and broad distribution of (measurable) particles only expressing Néel relaxation, after application of H_{mag} for a time t_{mag} [326]:

$$M(t) \propto \ln\left(1 + \frac{t_{\text{c}}}{t}\right) \tag{3.2}$$

with t_{c} the characteristic time depending on H_{mag} and t_{mag}. The equation fits well for broad particle distributions as these have a high dispersity in anisotropy energy barriers compared to the thermal energy (Section 1.1.3). Particle properties are contained in the proportionality factor [28]. Berkov and Kötitz determined t_c to be equal to t_{mag} for small magnetizing fields [327]. Systems that only allow Néel relaxation are typically samples that are immobilized, so that the MNP cannot rotate physically and hence no Brownian relaxation is possible, or samples in which the MNP are bound or clustered. In some MRX studies Eq. (3.2) has been extended with a single exponential decay term which yields an estimate of the average τ_{B} for systems expressing both relaxation mechanisms [34, 322, 328]. This approximation can be done because of the weak dependence of τ_{B} on d_{h}.

Models that relate particle properties to the decaying signal are of special interest. Hence, the properties of the MNP system under investigation can be determined from a MRX measurement. In the framework of the moment superposition model (MSM), proposed by Chantrell et al. and of which Eq. (3.2) is a result for given assumptions, Eberbeck et al. modeled the relaxation signal for non-interacting, freeze-dried particle systems exhibiting a narrow size distribution [28]:

$$M(t) = \int_{V_{\text{c}}} M_0(V_{\text{c}}) \exp\left(\frac{-t}{\tau_{\text{N}}(V_{\text{c}}, K)}\right) P(V_{\text{c}}) \mathrm{d}V_{\text{c}} \tag{3.3}$$

in which the distribution of V_{c}, $P(V_c)$, was assumed to be lognormal:

$$P(V_{\text{c}}) = \frac{1}{\sqrt{2\pi}\sigma_{\text{c}} V_{\text{c}}} \exp\left(-\frac{\ln^2(V_{\text{c}}/\mu_{\text{c}})}{2\sigma_{\text{c}}^2}\right) \tag{3.4}$$

with μ_{c} the mean particle core and σ_{c} its standard deviation. By fitting Eq. (3.3) with its parameters μ_{c}, σ_{c} and K to measured MRX curves these particle properties can be determined. This was further extended to the cluster moment superposition model in which particle samples are considered expressing both

Néel and Brownian relaxation [29]:

$$M(t) = \int_{V_c} \int_{V_h} M_0(V_c, V_h) \exp\left(\frac{-t}{\tau_{\text{eff}}(K, V_c, V_h)}\right) P(V_c, V_h) \mathrm{d}V_h \mathrm{d}V_c \tag{3.5}$$

with $P(V_c, V_h)$ taking into account the lognormal distribution of V_c and V_h. Note that V_h in this case does not necessarily reflect the hydrodynamic volume of a single particle but can also correspond to the volume of clustered or aggregated particles. Because 5 parameters are involved in the fit, it is often considered to be unreliable and therefore the degrees of freedom are reduced by fitting Eq. (3.3) to the immobilized state of the particle system. This way μ_c, σ_c and K are determined independently and these are then considered as known values in the fitting of Eq. (3.5).

3.1.4 Imaging the biodistribution of particles

In this section, it is described how the MRX signals can be engaged to find the spatial MNP distribution in a sample. The sample is virtually tessellated into V volume-elements (voxels) and for each voxel the MNP amount is determined. It is assumed that the magnetic moment of a voxel containing MNP can be approximated by a magnetic dipole. Subsequently, the well-known *dipole field equation* can be employed to calculate the magnetic induction in a sensor originating from the voxel's magnetic moment $\mathbf{m}_v$:

$$B_{sv} = \frac{\mu_0}{4\pi}\left(\frac{3(\mathbf{r}_s - \mathbf{r}_v)(\mathbf{m}_v \cdot (\mathbf{r}_s - \mathbf{r}_v))}{\|\mathbf{r}_s - \mathbf{r}_v\|^5} - \frac{\mathbf{m}_v}{\|\mathbf{r}_s - \mathbf{r}_v\|^3}\right) \cdot \mathbf{n}_s \tag{3.6}$$

B_{sv} is the magnetic induction in sensor s originating from voxel v, $\mathbf{n}_s$ is the orientation of the sensor, $\mathbf{r}_s$ and $\mathbf{r}_v$ are the position of the sensor and voxel v respectively. The total signal in sensor s contains the contributions from all V voxels weighted by their distance and relative orientation of $\mathbf{m}_v$:

$$B_s = \frac{\mu_0}{4\pi}\sum_{v=1}^{V}\left(\frac{3(\mathbf{r}_s - \mathbf{r}_v)(\mathbf{m}_v \cdot (\mathbf{r}_s - \mathbf{r}_v))}{\|\mathbf{r}_s - \mathbf{r}_v\|^5} - \frac{\mathbf{m}_v}{\|\mathbf{r}_s - \mathbf{r}_v\|^3}\right) \cdot \mathbf{n}_s \tag{3.7}$$

In case of a decaying magnetic moment Eq. (3.7) can be made time-dependent through use of $\mathbf{m}_v(t)$.

Recall from Section 1.1.3 that the magnetization of a voxel v containing MNP can be expressed as:

$$\mathbf{M}_v = \frac{c_v}{\rho V_v}\mathbf{M} \tag{1.9}$$

with c_v the MNP amount in the voxel (expressed in grammes of Fe), ρ the mass of iron divided by the core volume ($\rho = \frac{c_v}{V_c}$), $\mathbf{M}$ the magnetization of the MNP and V_v the volume of the voxel. The magnetic moment of the voxel can be obtained by multiplying its magnetization, $\mathbf{M}_v$, with V_v. For different MNP magnetization models, each with their assumptions, we refer to Section 1.1.3 and the previous section for magnetic decaying models specifically. For the small magnetizing fields and particles employed in MRX, the magnetization (Eqs. (1.7) and (1.8)) can be linearized. Therefore, in this dissertation, the decaying $\mathbf{m}_v(t)$ is modeled as follows:

$$\mathbf{m}_v(t) = \mathbf{H}_v \cdot \kappa(t) \cdot c_v \tag{3.8}$$

$\mathbf{H}_v$ is the magnetic field at the location of voxel v and depends on the geometrical details of the coils that generate the magnetic field and their currents and can be determined by Biot-Savart's law. $\kappa(t)$ takes into account the voxel's detailed temporal information of the decaying magnetic moment depending on t_{mag}, particle material properties and the particle size distribution. $\kappa(t)$ can be obtained by performing a MRX measurement in which $B_s(t)$ is measured for MNP placed in a single sample holder (i.e. $V = 1$) with a well-known iron amount c_{calib}, t_{mag}, $\mathbf{H}_v$, $\mathbf{r}_s$ and $\mathbf{r}_v$, a so-called *reference MRX measurement*. By combining Eqs. (3.7) and (3.8) $\kappa(t)$ can be found. In practice, $\kappa(t)$ is replaced by $\Delta\kappa_{t_1,t_2}$ in which temporal information is included by subtracting the amplitude of the MRX signal obtained at two time points t_1 and t_2:

$$\Delta\mathbf{m}_v = \mathbf{H}_v \cdot \Delta\kappa_{t_1,t_2} \cdot c_v \tag{3.9}$$

Eq. (3.7) then becomes:

$$B_s = \frac{\mu_0}{4\pi} \sum_{v=1}^{V} \left[\left(\left(\frac{3(\mathbf{r}_s - \mathbf{r}_v)(\mathbf{H}_v \cdot (\mathbf{r}_s - \mathbf{r}_v))}{\|\mathbf{r}_s - \mathbf{r}_v\|^5} - \frac{\mathbf{H}_v}{\|\mathbf{r}_s - \mathbf{r}_v\|^3} \right) \cdot \mathbf{n}_s \right) \cdot \Delta\kappa_{t_1,t_2} \cdot c_v \right] \tag{3.10}$$

It should be noted that Eq. (3.8) is only valid for small magnetizing fields so that the magnetization of the particles is linear. Moreover, a similar order of magnitude of MNP amounts should be used because the effective relaxation time can change (and hence the decay behavior is altered) due to particle interactions which depend on the used amount [71]. Additionally, Laslett et al. showed that the particle decay behavior depends on their initialization [72, 73]. Therefore, it is advised to measure the reference measurement under similar conditions as the actual MRX experiment, such as equal t_{mag}. Remark that instead of using the relaxation amplitude between two time points (Eq. 3.9) it is also possible to take into account temporal decay information through the models presented in Section 3.1.3. Baumgarten and Haueisen included the temporal extension from Eq. (3.2) in the inverse problem and showed in

simulations that, especially for low SNR data, improved reconstructions can be obtained [37].

Combining and simplifying Eqs. (3.6) and (3.9) results in:

$$B_{sv} = L_{sv} c_v \tag{3.11}$$

in which L_{sv} is the *sensitivity coefficient* that links a particle amount in voxel v to a measurement signal in the sensor s. This formulation is similar to the one used in Eq. (1.17). Equivalently, Eq. (3.10) can be expressed for each sensor $s = 1,...,S$ and can be rewritten in the same way as Eq. (1.18), which corresponds to extending Eq. (3.11) for just 1 sensor and 1 voxel to S sensors and V voxels:

$$\mathbf{B} = \mathbf{S}_\mathrm{f} = \mathbf{L} \cdot \mathbf{c} \tag{3.12}$$

in which the geometrical parameters of the setup, the particle properties and energy terms are replaced by the $S \times V$ sensitivity matrix $\mathbf{L}$ which contains all the sensitivity coefficients that link the MNP amount in a certain voxel to a measurement signal in a sensor. $\mathbf{c}$ is a vector containing the V MNP amounts in the voxels and $\mathbf{B}$ is a $S \times 1$ vector containing the relaxation amplitudes between t_1 and t_2 for the S sensors. As can be seen from Eq. (3.10), the coefficients in Eq. (3.12) depend on the geometrical details from the setup such as sensor and coil distances and orientations. A change in the setup parameters thus changes the forward model (Eq. (3.12)). Numerical research has been conducted on optimizing the geometrical parameters of the setup, such as the source grid [39] and coils [321], so to stabilize the inverse solution.

In this dissertation, coil arrays are employed for generating the magnetizing fields, similarly as in Section 2.5.2. A MRX imaging setup which makes use of heterogeneous fields, such as those generated by a coil array, shows an increased stability of its inverse problem compared to its counterpart which uses a homogeneous magnetic field [263]. A coil array magnetizes the particles with spatially varying magnetic fields, each of them altering $\mathbf{H}_v$ and thus the sensitivity coefficient L_{sv}. There exist various ways of activating the coils, e.g. the coils can be activated sequentially [49, 263] (Section 2.5.2 for EPR) or multiple coils can be activated simultaneously [42, 272]. The total number of activation sequences, that give rise to distinct magnetic field patterns, is denoted by N_a. In case of sequential activation with Q coils, $N_a = Q$, with each q-th magnetic field produced by the activation of the q-th coil ($q = 1,...,Q$). The forward model for the general case of magnetic field pattern a can then be written as:

$$\mathbf{B} = \mathbf{S}_\mathrm{f} = \mathbf{L}(\mathbf{I}_{\mathrm{coil}_a}) \cdot \mathbf{c} \qquad\qquad a = 1,...,N_a \tag{3.13}$$

$\mathbf{L}(\mathbf{I}_{\text{coil}_a})$ is a $S \times V$ matrix and has the same dimensions as in Eq. (3.12). $\mathbf{I}_{\text{coil}_a}$ is a vector of Q elements containing the currents of the Q coils for the generated magnetic field a. For each spatially varying magnetic field a, S simultaneous MRX measurements are performed using the S sensors. This means that in total $N_a S$ measurements are obtained. The complete activation procedure can be included in the forward model by calculating the sensitivity matrix for each magnetic field a $\left(\mathbf{L}(\mathbf{I}_{\text{coil}_a})\right)$ and concatenating these matrices into a $(N_a S) \times V$ matrix $\mathbf{L}(\mathbf{I}_{\text{coil}})$:

$$\mathbf{B} = \mathbf{S}_{\text{f}} = \mathbf{L}(\mathbf{I}_{\text{coil}}) \cdot \mathbf{c} \tag{3.14}$$

with $\mathbf{I}_{\text{coil}}$ a matrix consisting of $N_a \times Q$ elements which represent the currents in the Q coils for the N_a generated magnetic fields. In most notations in this dissertation the dependance of the 'extended' sensitivity matrix on $\mathbf{I}_{\text{coil}}$ is not written and hence just the notation $\mathbf{L}$ is employed, unless it needs to be emphasized for certain derivations.

A great deal of research has been conducted on how the coils should be activated in order to increase reconstruction quality, while limiting measurement time. For example in Refs. [42] and [272] the currents in the coils are determined based on desired spatial sensitivity profiles throughout the volume. The spatial sensitivity reflects the impact of a voxel on the measurements and is calculated by taking the column norm of the sensitivity matrix. From Eq. (3.10) it can be observed that voxels far away from coils and sensors show a lower sensitivity than the ones closer to coils and/or sensors. Indeed, the signal from voxel v in sensor s decreases with $\|\mathbf{r}_s - \mathbf{r}_v\|^3$ and H_v decreases with $\|\mathbf{r}_v - \mathbf{r}_q\|^2$ with $\mathbf{r}_q$ the position of the q-th coil. By adapting the coil currents, H_v can be changed so that specific spatial sensitivity patterns can be achieved for the whole volume, and voxels with an initial lower sensitivity can have an increased impact on the measurements and thus on the inversion. Crevecoeur et al. found in simulations that voxels expressing a higher spatial sensitivity showed a higher reconstruction accuracy compared to voxels with lower sensitivities [42]. Additionally, Baumgarten et al. could significantly speed up total MRX imaging time in simulations because certain spatial sensitivity profiles required a significantly lower amount of magnetic fields compared to the sequential coil activation, while having a similar reconstruction quality [272]. Another simulation study focused on the random and pseudo-random activation of coils and investigated the resulting effect on the condition of the sensitivity matrix (Eq. 1.28). It was concluded that their activation procedures required significantly less coil activations than the traditional sequential approach, while retaining a similar amount of information in the sensitivity matrix [264].

The MNP distribution can be recovered following the principles described in Section 1.4.3. Liebl et al. successfully reconstructed the 3D MNP distribution of MNP embedded in 1 cm^3 gypsum cubes, comprising an area of 3 cm $\times$ 6 cm $\times$ 3 cm, using the SVD (Eq. (1.23)) [263] and the NNLS approach (Eq. (1.26)) [270]. These are also the approaches used in this dissertation. In the model described above (Eq. (3.10)), the sample is divided into a grid of dipole locations so that only the amplitude of the dipole needs to be determined, as the location is predefined. In contrast to other applications of the dipole model, such as in electroencephalography (EEG) and magnetoencephalography (MEG), the direction of the dipole at each location is known *a priori*, because it is directly given by the direction of $\mathbf{H}_v$. Hence, only the amplitude of the dipole needs to be determined, which is a linear problem. Another approach used in MRX imaging, is to first find the three location parameters of a few dipoles (generally 1-5 dipoles are employed) through a non-linear search algorithm such as Levenberg-Marquardt, as the field in the sensors is proportional to $\frac{1}{\|\mathbf{r}_s - \mathbf{r}_v\|^3}$. Based on their location, their amplitude can be determined according to similar principles as described in this dissertation. For each iteration of the non-linear search algorithm, the linear fit is calculated until the differences between measured and actual induced field are minimal [34, 322]. This type of imaging is generally employed to localize and obtain the MNP amount in distinct regions such as liver and tumor, each with their own dipole [323], while the presented model here reconstructs the spatial variation of the MNP over a constant grid and hence uses significantly more dipoles, varying from 54 to 3000 dipoles in various studies [39, 263]. Baumgarten et al. reconstructed 2D MNP distributions using a combination of both approaches in which the Levenberg-Marquardt algorithm was used to determine the plane of interest and then Tikhonov regularization (Eq. (1.24)), with predefined dipole locations in the plane, to reconstruct the magnetic field in the plane [36]. The magnetic field from the MNP in MRX imaging has also been successfully approximated using other models besides multiple dipoles, such as by multipole expansion, in which multipole moments are determined that describe the main features of the underlying MNP distribution such as center of magnetization, total amount and dimensions, given certain assumptions such as homogeneous magnetization and source geometry [38, 329].

At the moment there is no commercial MRX imaging setup available. The reason thereof is that such a sophisticated system requires many parts that need to be custom-made such as the multi-channel SQUID sensors, and the high-end SQUID electronics. Additionally, cryogenics, coil control and magnetic shielding come into play. Depending on the desired resolution, field of view, number of sensors, etc. the cost of the components can be expected to

be around 300 000 €.

3.1.5 Biomedical applications

In this section only the major applications are mentioned with specific emphasis on how the properties of the MRX signal can be employed to their benefit. Excellent reviews of biomedical applications in which MRX is assisting can be found in Refs. [76] and [330]. A rough distinction can be made between biomedical applications in which a *characterization* of the MNP is required or a *localization* with the latter one referring to MRX *imaging*. First, MNP characterization applications are discussed which make use of the developed MRX models described in Section 3.1.3. Secondly, an overview of MRX imaging applications is given that operate based on the imaging models explained in Section 3.1.4.

One of the main characterization applications using MRX is the magnetic relaxation immunoassay (MARIA) technique in which the properties of the decaying signal are employed in the detection of biological entities or so-called *analytes*. In a first step the MNP are attached to certain recognition molecules, such as antibodies, which specifically bind to the analyte that needs to be detected. The analyte can be immobilized, i.e. attached to a rigid surface (a solid phase assay) or bound to large, micrometer sized, beads (a bead assay), or the analyte can be dissolved in a carrier liquid (a liquid phase assay). Of special interest are analytes and MNP that both have multiple binding sites so that large networks of multiple cross-linked MNP are created (an agglutination assay). Figure 3.2 gives an overview of the different assays. When the MNP bind via their recognition molecules with the immobilized analytes τ_B will be suppressed. Therefore, when particles are employed that express a decaying signal trough Brownian relaxation, the binding of the MNP with the immobilized analyte will result in a slower effective relaxation behavior following τ_N. In case of liquid or agglutination assays, the hydrodynamic diameter of the MNP will become larger due to the binding process and, hence, τ_B will increase and the resulting decay will be slower. This way, the binding between a recognition molecule and analyte can be monitored trough the change in relaxation behavior. Advantages of using MRX are that binding can be monitored while unbound MNP are present and that opaque media can be used as carrier liquids. Moreover, because of the short measurement times a series of MRX measurements can be performed to investigate binding kinetics.

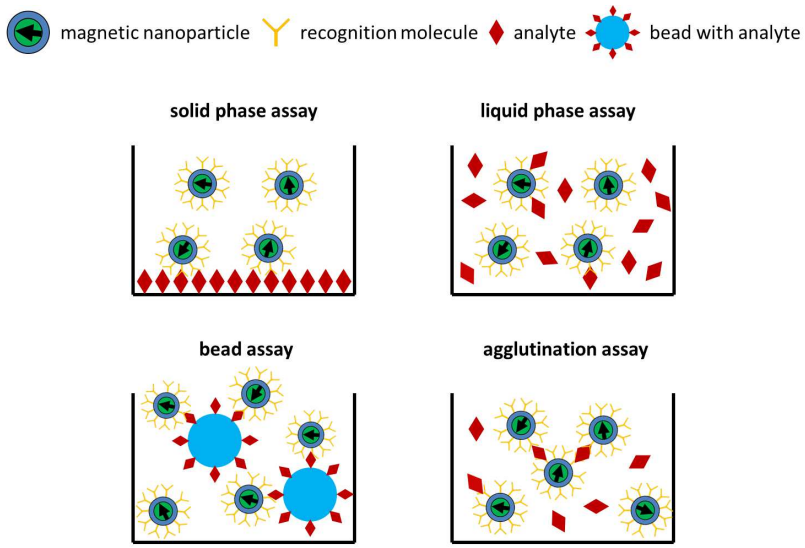

Figure 3.2: Overview of the various MNP-based assays for the detection of analytes (Adapted from [76]).

The MARIA technique was employed for the first time by Weitschies et al. to quantitatively determine the binding of antibodies in a solid phase assay [27]. The principle has been used in the detection of bacteria and human immunoglobuline G [331, 332]. In next experiments, bead and agglutination assays were employed in which the binding kinetics between MNP coated with biomolecules that bind with analytes such as latex beads, yeast cells and blood platelets were quantitatively analyzed. This was done through repetitive MRX measurements every few seconds and comparison of the obtained MRX signal in the sensor to MRX reference curves of immobilized MNP and MNP in suspension without analytes [23, 333, 334]:

$$\mathbf{B}(t) = \delta \mathbf{B}_b(t) + (1-\delta)\mathbf{B}_{ub}(t) \tag{3.15}$$

with $\mathbf{B}(t)$ the MRX signal in the sensor, δ representing the amount of bound MNP contributing to the measured signal, and $\mathbf{B}_b(t)$ and $\mathbf{B}_{ub}(t)$ the respective modeled or measured reference MRX measurements of bound and unbound MNP. By calculating δ for each MRX measurement, the binding kinetics of MNP interacting with biomolecules can be obtained. In case of agglutination, the cluster MSM (Eq. (3.5)) can be employed to characterize the mean and the width of the size distribution of the formed aggregates [335].

Besides analyzing the formed aggregates in agglutination assays, the cluster MSM has also been successfully employed to describe agglomeration behavior of particles with various coatings submerged into various media [318]. The MRX characterization models (Eqs. (3.3) and (3.5)) have also been used in identifying MNP properties in which the MSM is used on freeze-dried MNP samples, as it only takes into account τ_N, and allows to determine μ_c, σ_c and K [28, 77, 336]. These values can then be used in the fitting of the cluster MSM to MNP samples expressing τ_{eff}. Hence finding μ_h, σ_h. It has been successfully used to describe the characteristics of various particle systems [18, 29]. The core and particle size distributions obtained with these models are in good agreement with the distributions found using other characterization techniques such as transmission electron microscopy (TEM), dynamic light scattering (DLS), static magnetization measurements, MPS, and ACS [66, 241, 245, 246]. A description of static magnetization and the MPS and ACS measurement procedures can be found in Sections 1.1.3 and 1.3.3. The other characterization techniques are not detailed as these are out-of-scope for this dissertation. Often the various measurement techniques are used together in which the obtained parameters by one technique are employed in the models of the other techniques to improve fit procedures. Except for TEM, which provides a local number-weighted view of the particle distribution, these techniques require the interpretation of measurement data through different models which are not always representative for the used MNP systems [246]. Therefore, in some cases, discrepancies occur, so no self-consistent set can be obtained. This can be attributed to effects originating from magnetic dynamics, dipolar interactions, the use of parameters independently determined through other techniques, or assumptions on anisotropy and distribution [245]. The decay models have also been used in finding the most suitable MNP characteristics for various applications such as MARIA [336], MPI (Section 1.3.3) [194, 202], MRX [261, 337] and magnetic targeting [338] and for investigating the effect of dipolar interactions on the MRX signal [70–73].

First steps towards quantifying the MNP distribution in biomedical applications using MRX imaging were set by measuring the MRX signal using one sensor (i.e. *single channel* MRX imaging) in which the organ of interest was cut into pieces of 150 μl up until 8 ml. The obtained MRX signal was then compared to a reference MRX measurement of a known MNP amount to determine the MNP in the tissue piece. The pieces are approximated by a dipole source and the distance to the sensor was enlarged for larger sample sizes to fulfill the requirement of this approximation. The various approaches of quantifying tissue samples are summarized in Ref. [76]. Combining the obtained MNP amount with the location of the piece in the complete organ, the

spatial MNP distribution could for example be obtained *ex vivo* for analyzing the performance of magnetic targeting towards the lungs [32, 339] and tumor tissue [31]. Similarly, the MNP amount could be quantified *in vitro* using a bovine artery in which *in vivo* conditions were simulated in a circulating system in which MNP were injected. The MNP were then magnetically targeted to a certain region in the artery using a magnet. Afterward the MNP distribution was recovered using single channel MRX imaging by cutting the artery in lengths of 1 cm [340, 341]. The detection limit is approximately 200 nanogrammes of iron for 8 ml tissue samples, but this value is highly dependent on particle properties.

Flynn et al. used the MARIA principle in MRX imaging, in which vials containing live T-cells conjugated to MNP could be quantified, but also localized non-invasively [342]. Using a sensor setup consisting of 7 SQUID sensors (i.e. multi-channel MRX imaging) [34], two vials in a kidney phantom could be localized. Each vial was represented by a dipolar source and hence its center of magnetization and total bound MNP can be reconstructed. T-cells are important indicators of transplant rejection and should be detected and located as early as possible to target medicine to the appropriate location. The same setup and principles were also employed to detect Leukemia cells *in vitro* collected using a magnetic needle [343] and to localize and quantify different cancer lines such as breast, ovarian and prostate cancer [323]. This could be achieved *in vitro* using live cells [344], *ex vivo* in postmortem mice [157] and *in vivo* in mice [157, 323]. MRX imaging has this way been shown to be several orders of magnitude more sensitive than a mammogram. The platform on which the sample is positioned can be moved in order to increase the number of measurements as function of the considered dipoles. Hence, the stability of the inverse solution can be improved. Multiple dipole sources (up to 4) have been considered in these reconstructions with each dipole corresponding to distinct vials or regions, such as the liver, spleen, kidney and tumor. For each dipole, 4 unknowns (3D position and amplitude) are considered. The achievable resolution using this setup depends on the particle amount, particle type and cell binding sensitivity, and number of measurements compared to dipole sources and distance to the sensors. Generally, it is considered to lie in the range of 0.1 - 0.8 cm. The typical distance to the sensors for this setup is between 2 to 5 cm with a field of view ranging from 4 cm $\times$ 4 cm to 15 cm $\times$ 15 cm.

MRX imaging has not only been used in the detection and localization of biological entities, it has also been employed in analyzing the performance of magnetic (drug) targeting [35, 345]. In this application, MNP, which are coupled to a chemotherapeutic agent, are magnetically targeted towards a

tumor region in a living rabbit. The rabbit was sacrificed and the resulting MNP amount in the liver and tumor was measured by a 304 SQUID sensor multi-channel MRX imaging setup with a sensing area of 25 cm. The center of magnetization and total MNP amount of the two MNP distributions was reconstructed non-invasively by two dipoles (3D position and amplitude) one for each region, determined by least-squares fitting of the measurement data using the Levenberg-Marquardt algorithm. This study showed that 85 % of the MNP were captured in the tumor region. Similarly, using the same setup, the MNP amount and center of magnetization were reconstructed after intra-tumoral MNP injection, to check if the MNP were at the tumor location for thermal ablation experiments (Section 1.2.3). This was achieved in mice killed 24 hours after MNP injection [346] as well as in living mice to monitor the pre and post therapy over seven days [347]. The latter study concluded that the MNP mainly stayed at the tumor site, meaning that magnetic heating and cell death did not affect MNP accumulation and the healthy tissue remained unharmed.

3.2. Adaptive targeting

3.2.1 Introduction

In this section a numerical technique is introduced for the recovery of MNP distributions using MRX imaging systems equipped with a coil array. In this methodology the currents in the MRX coil array are adapted based on *a priori* information on the MNP distribution. It builds on a previous study by Crevecoeur et al. in which the current in the coils was adapted with the aim to achieve a more homogeneous spatial sensitivity profile over the volume [42] (Sections 1.4.4 and 3.1.4). Voxels with a higher spatial sensitivity are correlated with an increased reconstruction accuracy compared to voxels with a lower spatial sensitivity. By making the spatial sensitivity more homogeneous, also the accuracy in the volume under study will vary less, i.e. also regions located far from the sensors and coils (typically with a lower sensitivity) will be more accurately reconstructed [42]. In Ref. [42], the required activations and currents in the coils were determined prior to the MRX measurements, as the activations depended solely on the geometrical parameters of the volume under study, the coil array and the sensor locations. In this work however, previous MNP reconstructions specify the coil currents that need to be enforced in the next MRX measurement.

Crevecoeur et al. first solved an inverse problem to determine the currents required in the coil array so to have a constant spatial sensitivity. Because this is an overdetermined inverse problem, a constant spatial sensitivity can only be approximated. Therefore, most voxels showed a lower than desired sensitivity value. In a next step, voxels with a similar lower sensitivity were grouped together. Then, for each new MRX measurement, the currents required in the coil were determined to target a specific group by setting their desired sensitivity to the original desired sensitivity value, while voxels not belonging to the group obtained a desired spatial sensitivity of zero. This was done until all groups were targeted. By concatenating the sensitivity matrices associated to the determined activations (Eq. (3.14)) a more constant sensitivity could be obtained which resulted in improved MNP reconstructions, especially for particles located further away from the sensors.

In this section the currents in the coil are also determined to achieve a desired spatial sensitivity for the voxels, although no homogeneous sensitivity profile is pursued. Instead, a large spatial sensitivity is given to certain voxels or regions based on *a priori* information on the MNP distribution. This information can originate from other imaging modalities such as MRI or CT. Here, the reconstructed MNP distribution is obtained from a homogeneous MRX imaging experiment. In homogeneous MRX imaging, a homogeneous

magnetic field is applied to the sample. This can be done by placing the sample between a Helmholtz coil pair [35]. Based on the obtained reconstruction using homogeneous MRX imaging, regions containing MNP or voxels having certain MNP amounts are targeted. The targeting is done in a similar way as in Ref. [42] in which the target receives a constant sensitivity value, while non-targeted voxels receive a spatial sensitivity of zero. Then an overdetermined inverse problem is solved to obtain the required currents in the coils so to have the desired sensitivity profile. These obtained currents are then *directly* employed in the MRX imaging procedure to obtain a new reconstruction. Based on this last reconstruction the target regions are refined and the currents adapted. This continues until no significant changes in the obtained reconstruction are observed compared to the previous ones. The complete adaptive update procedure for the currents, based on the reconstructed spatial MNP distributions in the previous iteration of the numerical scheme, is shown in Fig. 3.3.

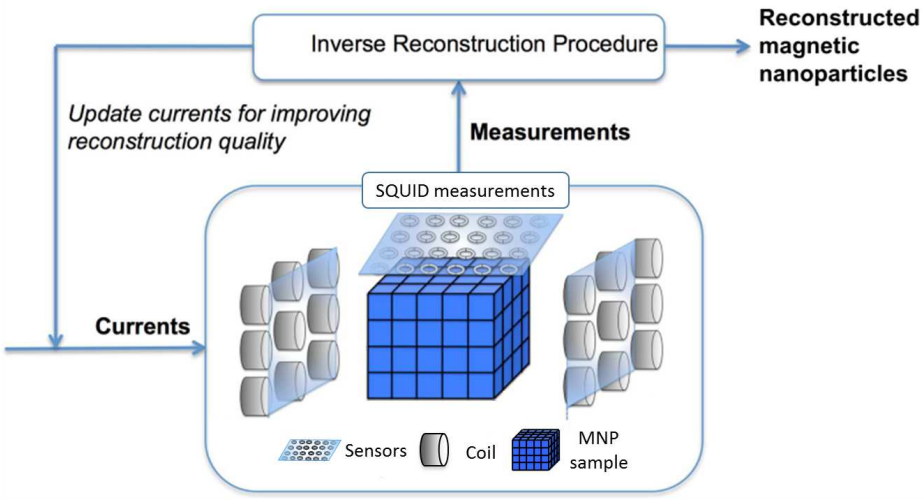

Figure 3.3: Schematic overview of the studied methodology.

In Section 3.2.2, the MRX imaging setup and MNP phantoms are described in detail. In Section 3.2.3 a general explanation is given on how the spatial sensitivity parameter is used to determine the coil currents, followed by an overview of the investigated target procedures and how these translate into a desired spatial sensitivity profile. In Section 3.2.4 the performance of the targeting procedures for clustered and non-clustered MNP distributions is discussed. This is shown first for the case of only one target activation after a

homogeneous MRX imaging experiment. Subsequently, the analysis focuses on multiple iterations of the targeting and their added value. This work was published in Ref. [348]. An extension of the presented procedures, in which specific planes of the volume are targeted, can also be found in Ref. [272].

3.2.2 MRX imaging setup and phantoms

The simulation setup considered in this section has been used before in Refs. [42, 264, 272, 321]. A cubic volume of 96 mm $\times$ 96 mm $\times$ 96 mm consisting of an unknown MNP distribution $\mathbf{c}$ is considered. This cube is tessellated into 4096 voxels ($V = 4096$) with side length of 6 mm. 45 coils ($Q = 45$) with a diameter of 30 mm are arranged in 5 planes around the MNP volume. Each plane has 9 coils and these planes are parallel to the volume and situated in front, behind, to the sides and at the bottom of the sample, each at a distance of 15 mm from the volume. These 45 coils constitute the coil array. The residual parallel plane on top of the volume is used for the SQUID sensors. It contains 81 sensors with sensitive axis along the $\mathbf{z}$ direction and the plane is positioned on a distance of 8 mm from the top of the MNP sample. Another 16 SQUIDs are on a distance of 18 mm with 8 aligned along the $\mathbf{x}$ direction and the other 8 along the $\mathbf{y}$ direction (i.e. $S = 97$). The setup together with the relative axes ($\mathbf{x}$, $\mathbf{y}$, and $\mathbf{z}$) are depicted in Fig. 3.4. For clarity reasons the 16 SQUID sensors at 18 mm are not shown.

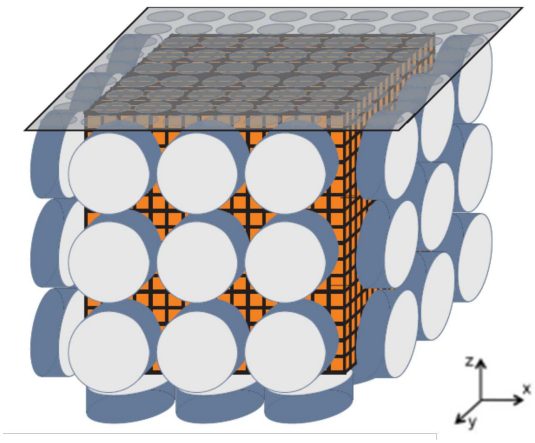

Figure 3.4: Figure of the simulation setup with the MNP sample (cube) in the middle. The 45 cylinders represent the coil array and the plane on top of the volume visualizes the 81 SQUID sensors (Adapted from [264]).

MRX measurements for a known MNP distribution, $\mathbf{c}_{\text{act}}$, can be *simulated* by using this distribution in the forward model (Eq. (3.13)):

$$\mathbf{S}_{\text{m}_{\text{sim}}} = \mathbf{L}(\mathbf{I}^*_{\text{coil}_a}) \cdot \mathbf{c}_{\text{act}} \tag{3.16}$$

with $\mathbf{I}^*_{\text{coil}_a}$ the currents determined for the a-th activation of the coils in order to realize the desired spatial sensitivity pattern. Two types of spatial MNP distributions $\mathbf{c}_{\text{act}}$ are considered: 10 random fractal clustered nanoparticle distributions and a non-clustered, homogeneous distribution. For an example of the distributions, see Figs. 3.5a) and 3.6a) respectively. The first type is used to test multiple random spatial distributions, although with similar properties, which allowed an analysis of the developed methods for clustered MNP distributions. Each cluster corresponds to a MNP injection point. This spatial configuration typically occurs in magnetic hyperthermia experiments in which the MNP are directly injected into the tumor (Section 1.2.3) [115, 117]. The clusters are generated with fractional Brownian motion, similarly as in Section 2.5.3 [313]. The non-clustered distribution is an artificial cross in three planes with a distance $z_{p_1} = 11$ mm, $z_{p_2} = 23$ mm and $z_{p_3} = 53$ mm from the main sensor's plane. The major difference with the first type of MNP distributions is its sharp edges and its continuous and homogeneous distribution. The reconstructions are considered in planes parallel to the sensors because the measured signal in the sensors deteriorates according to z_p^3. The reconstruction quality is investigated by comparing $\mathbf{c}_{\text{act}}$ with the reconstructed $\mathbf{c}^*$ trough the correlation coefficient (CC) (Section 1.4.4, Eq. (1.27)).

3.2.3 Targeting procedure

The adaptive currents are found through the determination of the spatial sensitivity parameter $\mathbf{S}_{\text{p}}$ discussed in Section 1.4.4. $\mathbf{S}_{\text{p}}$ is a vector with V elements containing the spatial sensitivity of each voxel v and is a measure for the contribution of the signal, originating from voxel v, to the sensors. A voxel in a sequential MRX imaging experiment which is close to the sensors and the coils will have a greater impact on the measured signals than a voxel which is far away from the coils and sensors. $\mathbf{S}_{\text{p}}$ is found by taking the sum of the absolute values of column v from the sensitivity matrix $\mathbf{L}$:

$$S_{\text{p}_v} = \sum_{s=1}^{S} \|L_{sv}\| \tag{3.17}$$

As described in Section 3.1.4 and in Ref. [42], $\mathbf{S}_{\text{p}}$ is linearly related to the current in the coils:

$$\mathbf{S}_{\text{p}} = \mathbf{A} \cdot \mathbf{I}_{\text{coil}_a} \tag{3.18}$$

where $\mathbf{I}_{\text{coil}_a}$ is a $Q \times 1$ vector with the currents for the Q coils (Eq. (3.13)) and $\mathbf{A}$ is an interaction matrix with dimensions $V \times Q$. $\mathbf{A}$ depends on setup geometry and can be found based on a reformulation of the sensitivity coefficients (Eqs. (3.10) and (3.12)) in which we separate the $\mathbf{I}_{\text{coil}_a}$ term. Remark that the sensitivity can thus be varied by adapting the currents in the coil array. In order to specificly target a certain sub-region or voxel, a desired sensitivity profile $\mathbf{S}_{\text{p}}^*$ (target) is set. The coil currents to achieve the desired sensitivity profile can then be determined by solving an overdetermined inverse problem [42]. The inverse problem is solved by truncated SVD (Eq. (1.23)) in a similar way as for determining the MNP distributions:

$$\mathbf{I}_{\text{coil}_a}^* = \mathbf{A}^\dagger \cdot \mathbf{S}_{\text{p}}^* \tag{3.19}$$

in which $\mathbf{I}_{\text{coil}_a}^*$ are the currents needed in the coils to approximate $\mathbf{S}_{\text{p}}^*$ and $\mathbf{A}^\dagger$ is the Moore - Penrose inverse of $\mathbf{A}$ (Section 1.4.3). In this work the found coil currents are indexed with a to denote their iteration number in the scheme which corresponds to the a-th activation of the coils. Once $\mathbf{I}_{\text{coil}_a}^*$ is found, it is used to calculate the sensitivity matrix $\mathbf{L}$ (Eqs. (3.10) and (3.12)) and $\mathbf{L}$ can then be employed in the reconstruction procedure to obtain the MNP distribution from the measurements $\mathbf{S}_{\text{m}_{\text{sim}}}$ (Eq. (3.16)) using truncated singular value decomposition (Eq. (1.23)).

The method for determining the coil currents is valid for different target sensitivity patterns. In this section two main targeting procedures are investigated. Both procedures have the result that, starting from a preliminary MNP reconstruction, a desired sensitivity profile $\mathbf{S}_{\text{p}}^*$ is found, which is then used to determine the currents in the coils for the next MRX experiment. The reconstruction from this experiment subsequently serves as input for the procedure, and this is repeated until no significant changes in the reconstructed image are observed. The initial MNP reconstruction is obtained from a homogeneous MRX imaging experiment which is considered as the first activation ($a = 1$).

The first procedure, referred to as the *sub-volume targeting* (SVT) method, targets a predefined sub-volume. The sub-volume is spanned by drawing cuboids around the voxels that contained MNP in the reconstructions. Hence, smaller continuous regions than the original volume are obtained. Voxels inside the sub-volume are given a $S_{\text{p}_v}^* = 1$, while voxels outside the sub-volume are given $S_{\text{p}_v}^* = 0$. Then using $\mathbf{S}_{\text{p}}^*$ in Eq. (3.19) allows for the determination of the currents for the next MRX experiment. Remark that the cuboids also contain empty voxels, which is of interest when for example the actual MNP amount was not recovered in the reconstruction. Indeed, because the voxel is still given a high sensitivity value, chances increase that it will be

reconstructed in the next experiment. A drawback might be that the selected sub-volume does not change much from activation to activation, because the sub-volume is a rather rough outline of the voxels containing MNP.

The second procedure, the so-called *high concentration selection* (HCS) method, targets voxels having a specific amount of MNP. This is done by selecting the voxels for which the condition $c_v^* \geq \frac{c_{\max}^*}{\nu}$ is satisfied. $c_{\max}^*$ is the maximal value of $\mathbf{c}^*$ and ν is a constant determined for the type of experiment, and was found through simulation studies. ν was varied between 1 and 100 (the minimal and maximal MNP amount in the voxels over all distributions) and the chosen value corresponds to the best average reconstruction quality for all considered reconstructions. It has the drawback that MNP amounts not recovered in the initial reconstruction might never be found, because they never receive a higher spatial sensitivity target. They can only be found when voxels with a sufficient MNP amount are in the neighborhood so that their region is excited. Luckily, this is rare for clustered distributions and might only occur for clusters far away from the sensors. To overcome this problem, in addition, a *weighted* high concentration selection methodology was implemented which takes into account the initial lower spatial sensitivity of voxels further away from the sensors' plane. This is achieved by making the concentration selection more strict for MNP in layers close to the sensors than for MNP in layers far away, through the use of the following definition of target:

$$c_v^* \geq \frac{c_{\max}^*}{\nu(z_p)} \tag{3.20}$$

z_p is the distance from the layer in the volume to the sensors' plane and $\nu(z_p)$ is the distance-based weighting. Equation (3.20) enables to focus more on MNP located far from the sensors. For both the HCS and weighted HCS, the selected voxels are given a value $S_{\mathrm{p}_v}^* = 1$, while the other voxels receive $S_{\mathrm{p}_v}^* = 0$. Similarly as for the SVT procedure, $\mathbf{S}_{\mathrm{p}}^*$ is inserted in Eq. (3.19) to find the optimal currents for the next imaging experiment.

In case many voxels are selected through the targeting procedure, Eq. (3.19) might become increasingly ill-posed. Therefore, it could be necessary to apply the procedure from Ref. [42] in which voxels with a similar sensitivity, obtained by Eq. (3.18), are grouped together and for each group an activation is performed. The reconstruction can then be realized by combining the measurements and the associated sensitivity matrices together.

In a nutshell, the new approach targets the sub-region or voxels which are assumed to contain particles based on the previous reconstruction, and $\mathbf{S}_{\mathrm{p}}^*$ is adapted accordingly. This way, more information is available for solving

the ill-posed inverse problem since the signals are originating from MNP in a certain sub-region. The sensitivity matrix in Eq. (3.13) is controlled through $\mathbf{I}_{\text{coil}_a}$ and the reconstruction is optimized through Eq. (3.19). Remark that for each iteration of the scheme, $\mathbf{L}$ has the same dimensions ($S \times V$) and its values are only varied through $\mathbf{I}_{\text{coil}_a}$.

3.2.4 Numerical validation

10 different clustered distributions were generated and their CC calculated in the case of an MRX imaging experiment with a homogeneous activation, SVT and HCS. For the initial studies with SVT and HCS two activations are performed (i.e. $N_a = 2$): first the homogeneous activation ($a = 1$) and then the SVT or HCS is applied ($a = 2$). In the case of the HCS method ν was identified to be approximately 60. Table 3.1 shows the accuracy of the reconstructions (average CC and standard deviation of all clustered distributions) for certain distances to the sensors. In general, the proposed techniques increase the reconstruction accuracy, although the reconstruction scores for MNP located in the plane far away from the sensors are still significantly lower than those for MNP in the closer planes. At larger distances from the sensors' plane, an increase in the CC of on average 20 % for the HCS targeting procedure compared to homogeneous MRX is possible. Figure 3.5 illustrates that MNP located far from the sensors are better reconstructed when using the HCS method (Fig. 3.5c)) as compared to the homogeneous method (Fig. 3.5b)).

Table 3.1: CC for homogeneous MRX imaging experiment, high concentration selection, and sub-volume targeting in case of clustered distributions.

z_p **[mm]**	**Homogeneous**	**HCS**	**SVT**
17	0.55 ± 0.2	0.67 ± 0.2	0.75 ± 0.2
53	0.40 ± 0.4	0.48 ± 0.3	0.45 ± 0.3
77	0.21 ± 0.3	0.40 ± 0.2	0.26 ± 0.3

The reconstruction of the non-clustered distribution, the in-plane crosses, was also studied. The results are shown in Table 3.2 for the three planes containing crosses. Similar results are observed as for the clustered distributions. Again, the targeting methods result in increased CC scores compared to the homogeneous MRX, although the CC decreases for layers further away from the sensors. The in-plane cross distributions are easier to reconstruct through truncated SVD because of their more continuous, homogeneous distribution compared to the clustered distributions. Figure 3.6 visualizes the MNP reconstructions of plane z_{p_3} (the cross furthest away from the sensors)

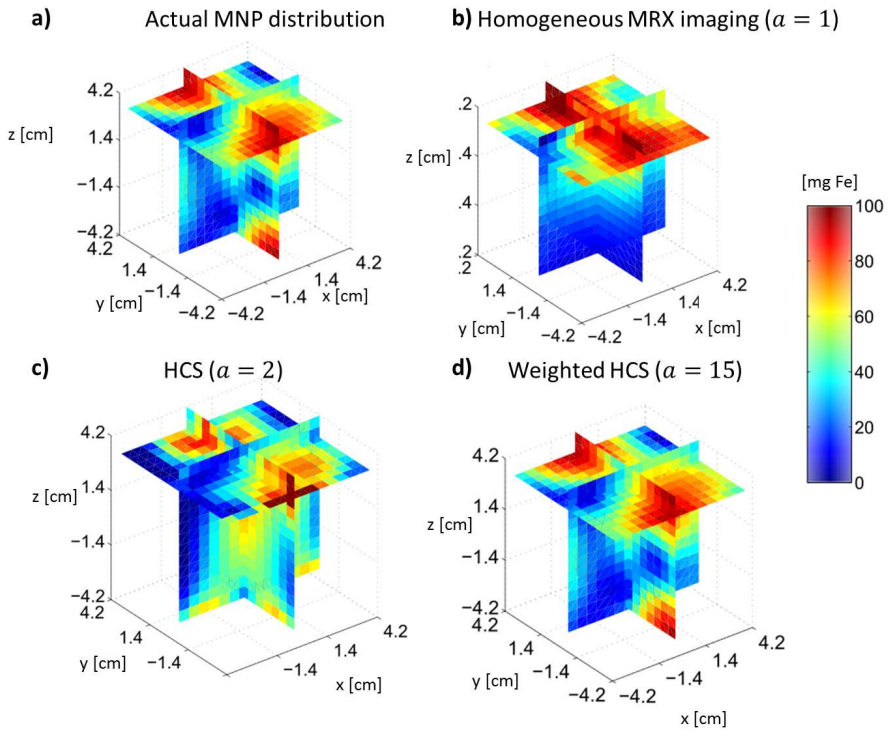

Figure 3.5: Reconstruction of a clustered MNP distribution. a) Actual MNP distribution. Obtained reconstruction using a b) homogeneous activation, c) HCS method with $a = 2$ and d) HCS method with $a = 15$.

obtained with the different techniques. Similarly as for the homogenous MRX imaging experiment, the absolute values of the MNP do not correspond very well to the actual MNP amounts for the distant planes, but the localization of the MNP is improved which results in an increased correlation coefficient (up to 44 %) compared to homogeneous MRX imaging.

Table 3.2: CC for homogeneous MRX imaging experiment, high concentration selection, and sub-volume targeting in case of non-clustered nanoparticle distributions.

z_p [mm]	Homogeneous	HCS	SVT
11	0.94	0.94	0.94
23	0.81	0.89	0.82
53	0.26	0.70	0.64

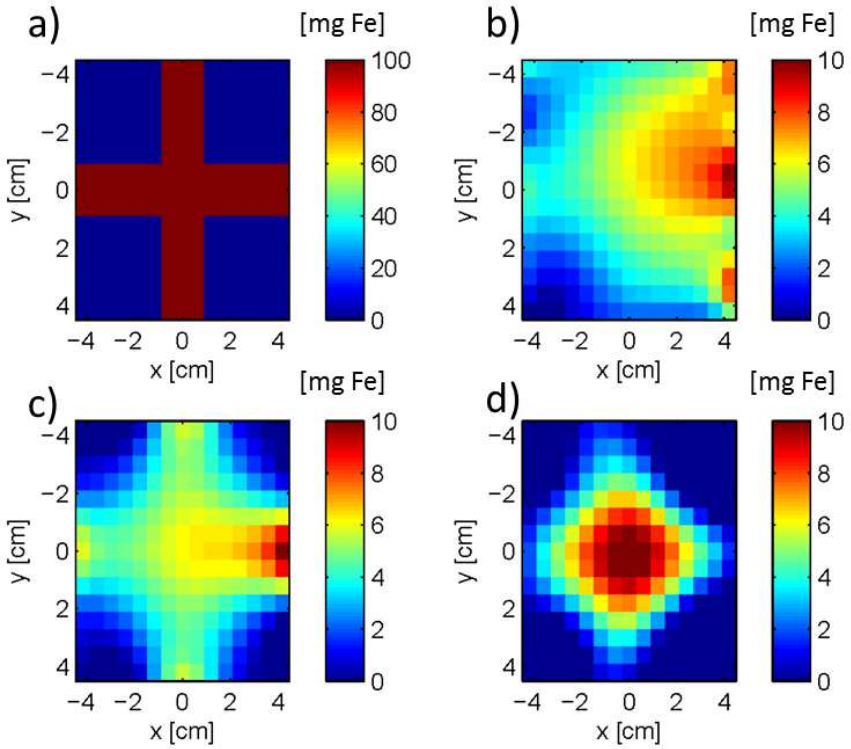

Figure 3.6: Reconstruction of the non-clustered MNP distribution for the plane on z_{p_3}. a) Actual MNP distribution. Reconstruction for b) a homogeneous MRX imaging experiment, c) high concentration selection and d) sub-volume targeting.

When determining the ν constant, it was noted that in some cases HCS reconstructed the MNP amounts in distant planes very accurately. Therefore, the weighted HCS was developed which takes into account the lower spatial sensitivity at more distant planes. A decreasing weight for larger distances was determined based on the largest average CC for all considered MNP distributions. The best results were obtained by decreasing ν with 1 for every distance increase to the sensors by 12 mm. This translates into $\nu(z_p) = \alpha_0 + \alpha_1 z_p$ with chosen $\alpha_0 = \frac{191}{12}$ and $\alpha_1 = -\frac{1}{12}$. This way a far better reconstruction in planes that are further away from the sensors could be achieved, see Fig. 3.7 for the non-clustered MNP distribution. This effect was also noticeable for the clustered MNP distributions. Because of the improved or similar reconstruction results obtained with weighted HCS, weighted HCS is from now on employed in the simulations instead of HCS.

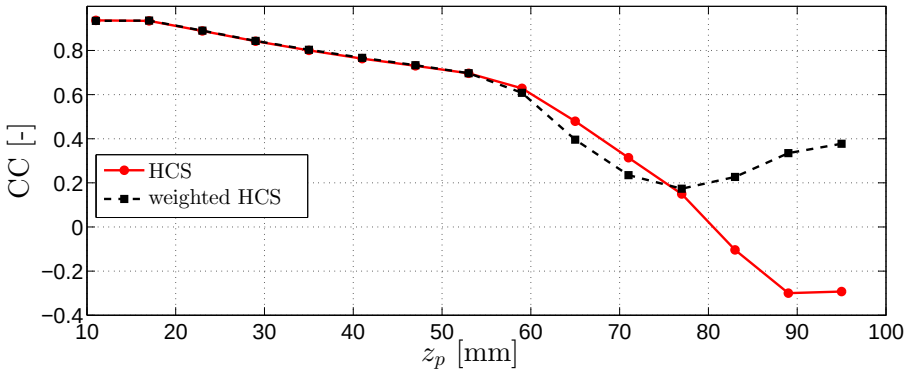

Figure 3.7: Reconstruction accuracy for increasing distance to the sensors' plane using weighted HCS and HCS for the non-clustered distribution.

In the previous simulation studies, a maximum of two activations ($a = 2$) were performed, i.e. homogeneous activation and then HCS or SVT. This approach is now extended to multiple activations ($a > 2$) in which the currents are controlled on the basis of previous MRX measurements. In this way, the reconstructions are adaptively refined. The previous results showed that the proposed methods already obtain a better reconstruction quality for the case of $a = 2$. Especially, a tremendous increase in reconstruction quality can be observed for layers further away. For the SVT approach, not much added value is obtained when using multiple iterations. Only an increase in reconstruction quality for 3 activations is seen. In general, after the third activation no significant changes in reconstruction quality are found for next activations. This is because of the fact that the targeted volume is little changed for the next activations. In the case of the non-clustered distribution $CC(z_{p_1}) = 98$ %, $CC(z_{p_2}) = 92$ % and $CC(z_{p_3}) = 66$ % is obtained for $a = 3$. Compared to the results for $a = 2$ (Table 3.2), this is a small to significant increase in CC up until 10 %.

Fig. 3.8 shows the reconstruction quality for the crosses in the three different planes using the weighted HCS. It is observed that the multiple activations increase the CC significantly. Especially, for particles located in the planes far away from the sensors a tremendous increase in CC (from 26% to 94%) can be achieved. For $a = 14$ the attained reconstruction correlations are $CC(z_{p_1}) = 100$ % $CC(z_{p_2}) = 99.8$ % and $CC(z_{p_3}) = 94$ %. Similar results are found for the clustered distributions, where a maximal improvement of 80 % could be achieved compared to the homogeneous MRX imaging measurement. Figure 3.5d) visualizes a reconstruction example with weighted HCS for $a = 15$. In

general, between 10 to 15 activations are required using the weighted HCS targeting procedure. Further activations yield no increase in reconstruction quality anymore. When HCS is used multiple times, in most cases an almost perfect to perfect reconstruction can be obtained.

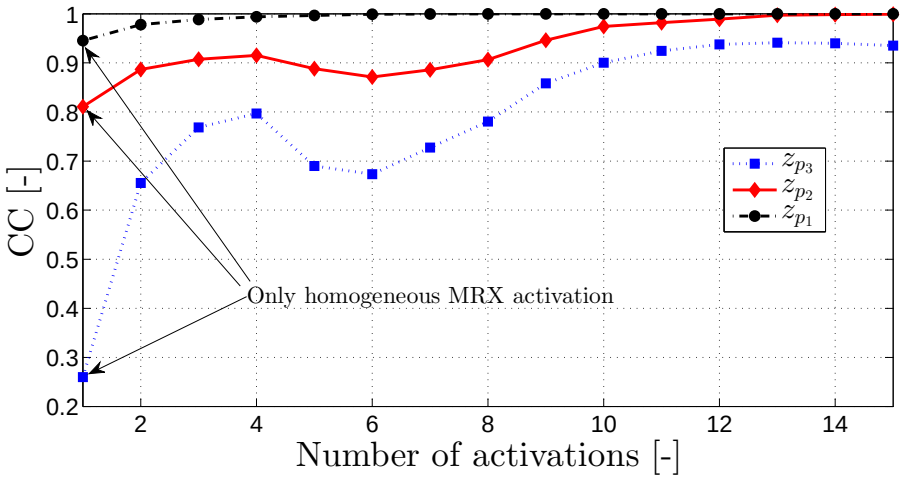

Figure 3.8: Reconstruction accuracy for the non-clustered MNP distribution, for each in-plane cross, when multiple weighted HCS activations are used.

Further improvements are expected by decomposing the selected areas into smaller independent areas that need to be activated. Then, instead of having a single activation and calculating a single $S \times V$ sensitivity matrix in each iteration of the numerical scheme, multiple activations are performed. This decomposition was achieved in Ref. [42] by taking voxels with a similar sensitivity together in the same activation. This approach is also used in the sequential activation of the coil array in which a MRX measurement is done for each coil activated separately, and the associated measurements and sensitivity matrices for all the coils are concatenated (Eq. (3.14), with $\mathbf{I}_{\text{coil}}$ a diagonal matrix) [49, 263]. These approaches improve the discrimination between the areas and reduce the condition number, β, of the inverse problem (Eq. (1.28)). Hence, the reconstruction results are improved, although at the drawback of requiring more MRX imaging measurements which slow down the experiment. The concept presented here was extended in Ref. [272], in which the volume was divided into several planes which were separately targeted. This has the drawback that a MRX measurement needs to be carried out for each selected plane, which can increase measurement time significantly. On the other hand, the activations solely depend on the

geometrical setup and can thus be determined prior to the measurements. The presented approach here requires to perform measurement analysis during the experiment, which is not convenient with current setups.

A general drawback of the sensitivity targeting procedure is that in some cases unrealistic currents can be obtained. Furthermore, due to the underlying principles of the magnetic fields, it is not possible to only select voxels in the center of the MNP sample. On the other hand, layers further away from the sensors' plane can be targeted which improves their sensitivity. The strength of the sensitivity targeting procedures lies in the marking of smaller areas, compared to the original sample, that increase the stability of the inverse solution. Of specific importance for this work is that, starting from a less quantitative preliminary reconstruction, i.e. a general overview of the MNP distribution, sensitivity can be given where needed so to increase the general reconstruction quality.

3.2.5 Conclusion

This section proposes numerical techniques for the quantitative reconstruction of spatial MNP distributions using a MRX imaging setup with a coil array. The possibility to target certain spatial regions, based on *a priori* information on the MNP distribution is introduced. Those regions are given an increased accuracy by adapting the currents in the coils. Two target procedures, sub-volume targeting and high concentration selection, were analyzed on 10 clustered MNP distributions, typically found in magnetic hyperthermia experiments in which MNP are directly injected into the tumor, and on 1 more continuous and homogeneous distribution. Both procedures take a preliminary MNP reconstruction as input and, based on its distribution, target a cuboid or voxels having a specific MNP amount. This target is translated into a sensitivity profile which is employed to calculate the required currents in the coil in order to activate the target regions. These currents are then used in the next MRX experiment of which the reconstruction can again serve as an input.

Starting from a preliminary reconstruction using a magnetorelaxometry experiment with a homogeneous magnetizing field, it could be shown that one activation with the target procedures results in a general increase of the reconstruction accuracy. The improvement in reconstruction quality is especially apparent for layers in the sample further away from the sensors (i.e. in some cases an increase in reconstruction quality of more than 40 % could be achieved). These findings could even be improved further by using a weighted voxel targeting procedure. This procedure takes into account the

initial lower spatial sensitivity in the homogeneous MRX imaging experiment of MNP located further away from sensors. Note that the methods can also be used when *a priori* information from other modalities instead of homogeneous MRX imaging is available.

In a next step, the targeting procedure was employed iteratively, i.e. for multiple activations. For the SVT no large increases in reconstruction quality are seen for multiple iterations of the targeting, as the cuboid only slightly varies from activation to activation. On the other hand, when performing multiple weighted high concentration selections, it is possible to achieve almost perfect to perfect reconstructions after 10 to 15 activations in general. As such it was possible to improve reconstruction quality from 26 % for the first reconstruction to 94 % for the fourteenth reconstruction.

3.3. Quantitative magnetorelaxometry models

3.3.1 Introduction

In this section quantitative measures are introduced for the comparison of different MRX models. This way the most suitable model can be determined for the reconstruction of an unknown particle distribution. Recall that the inverse problem requires a forward model to generate simulated measurements (Eq. (3.12)). These measurements are then compared to the MRX measurements in the inverse problem (Eq. (1.19)) and based on this comparison, the MNP distribution can be recovered. The forward model is represented by sensitivity coefficients that embody the link between the MNP amount in a certain voxel and the signal at a measurement site (Eq. (3.11)). The forward model has a significant impact on the reconstructed MNP distribution and, therefore, research has been conducted on adapting the forward model with the intention to stabilize the inverse solution and to maximize the amount of information, while keeping measurement data to a minimum. For more details, see Sections 1.4.2 and 3.1.4. Previous adaptations include the investigation of different noise models [349], use of multiple time points [37], different inverse solution methods [270], grid and sensors adaptations [39, 320] and different activation patterns and configurations of the coil array [42, 263, 264, 272, 321, 348]. Section 3.2 for example, showed how the adaptive activation of the coils, based on preliminary information on the particle sample, could significantly improve reconstruction quality of the MNP distribution.

The difficulty lies in determining the information content of the forward model and comparing different forward models with each other. Current measures for comparing forward models, such as inspecting the eigenvalue distributions [264], the spatial sensitivity (Section 3.2.3) [42, 272, 348] or performing simulated reconstructions of random distributions for each model [349] are not sufficient and not accurate enough. Furthermore, the different models can not be compared *quantitatively*. For an overview of the main comparison methods, see Section 1.4.4.

In this section a transformation approach on the level of the forward model is presented which enables a quantitative comparison between different forward MRX imaging models and setups, independently of the measurement object. The transformation is an approach adapted from Ref. [350] in which EEG and MEG data were combined into one model by evaluating statistical parameters. Here, the use of statistical parameters is proposed to develop *quantitative* MRX imaging models that can be compared to each other. Using these models, a straightforward optimization of setups and models is possible

resulting in improved MNP reconstructions. An MRX imaging setup is considered with different coil configurations, each corresponding to an MRX imaging model. The models are compared by employing their sensitivity matrices as inputs to statistical parameters from information theory such as conditional entropy and mutual information (MI). The parameters determine the best model to reconstruct the MNP amount for each voxel in the sample. The matrix is transformed by multiplying the columns with different weightings depending on the performance of the MRX imaging model with respect to the other models.

Section 3.3.2 describes the setup and MRX phantom used in the numerical simulations. In Section 3.3.3, a general introduction is given to the statistical parameters employed in this work and how they can be used to transform the sensitivity matrices into *quantitative* MRX models. Section 3.3.4 compares the transformed matrix to the original sensitivity matrix without weightings. This comparison is made by evaluating the reconstruction of an MNP phantom for different noise levels and by calculating the condition number β (Eq. (1.28)), spatial sensitivity (Eq. (3.17)) and eigenvalue distribution (Section 1.4.4) of both matrices. Additionally, two examples are considered in Section 3.3.5 in which the quantitative information associated with the MRX models is *directly* used in order to enhance the MRX imaging setup. In a first example the mutual information between the coils is used to find a reduced number of coils in order to speed up the measurements, while improving reconstruction accuracy. In a second example an optimal voxel size is determined for the setup based on the information content of the statistical parameters. Using the quantitative information associated with each model, an optimal configuration of the given setup can be determined in a very fast and accurate way. This work has also been published in Ref. [351].

3.3.2 MRX imaging setup and phantom

In this section a different MRX imaging setup is employed compared to Section 3.2. To make the numerical simulations more realistic, the geometrical details of the distributed coil array MRX setup at the Physikalisch-Technische Bundesanstalt (PTB) in Berlin were implemented. Liebl et al. developed this setup for the first experimental MNP reconstructions using sequential activation of the coils [263, 270]. The 304 low-T_c SQUID magnetometers sensor setup from the PTB is employed as sensor system [325]. The sensors are arranged in 4 layers in a large liquid helium Dewar vessel of 25 cm. About 3 cm warm-cold distance is needed, so the actual sensor area is about 22 cm. The lowest level has 114 SQUIDs, 30 mm above this layer another layer is

positioned containing 76 SQUIDs. The two residual layers at 70 mm and 140 mm from the lowest layer contain 57 SQUID sensors each. So in total 304 SQUID sensors ($S = 304$) can simultaneously measure the MRX signal. All sensors have a pickup coil with an area of 7 mm $\times$ 7 mm.

The sensor setup is located in a magnetically shielded room, the BMSR-2 [324]. The room has seven magnetic layers of mu-metal and one conductive aluminum layer and additionally employs active shielding. For MRX imaging experiments, it is generally assumed that the complete system has a noise floor of 500 fT [263]. The sensors have orientations in **x**, **y** and **z** direction to allow the measurement of the magnetic induction component in various directions. For example there are 57 **z** direction sensors on the lowest level, arranged as such, that the distance between two sensors measuring the same spatial component equals 29 mm. Because of the different orientations and the spatial arrangement of the sensors it is possible to measure the magnetic induction vector at different locations. Figure 3.9a) shows the measurement system from outside and Fig. 3.9b) depicts a top view of the spatial arrangement of the sensors (i.e. the layers are stacked on each other).

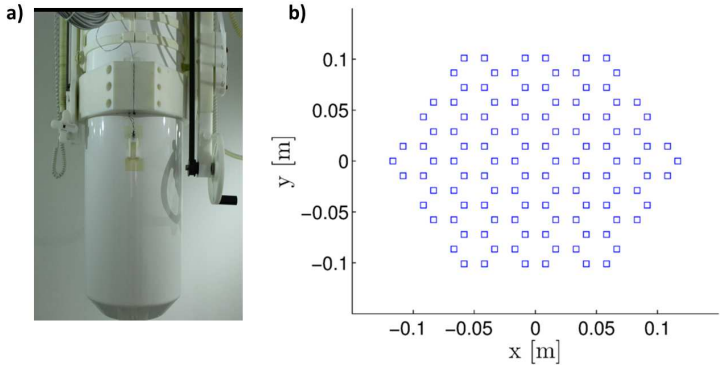

Figure 3.9: a) View of the the helium Dewar vessel in which the SQUIDs are contained. b) Top view of the sensors' spatial arrangement.

The magnetizing part of the imaging setup consists of 48 planar coils ($Q = 48$) with a diameter of about 1 cm. 12 coils are positioned between the SQUIDs and the sample with the unknown MNP distribution, 12 coils are positioned below the sample and 2 $\times$ 12 coils are positioned perpendicular to the other coils, with the sample between them (see Fig. 3.10a)). The upper coil layer is placed at a distance of 4 cm from the lowest SQUID sensors and the upper layer of the phantom has a distance of 5.5 cm to the lowest SQUID sensors. A

sequential activation procedure is used for the coils. This means that before each measurement a single coil of the Q coils is activated with a unit current, here 1 A. The coil magnetizes the MNP and is then switched off. Hereafter the S sensors are measuring the decaying magnetic induction. In total Q measurements are performed so that each coil has been activated once. This way QS sensor signals are obtained.

Similarly as described in Section 3.1.4, each q-th MRX measurement made with this setup can be modeled by a sensitivity matrix:

$$\mathbf{B} = \mathbf{L}_q \cdot \mathbf{c} \qquad q = 1, ..., Q \tag{3.21}$$

$\mathbf{L}_q$ is a $S \times V$ sensitivity matrix with q corresponding to the coil that was activated prior to the measurement. In contrast to Eq. (3.13), in this section the index q is used to differentiate explicitly between the sensitivity matrices of each measurement in order to compare them using the techniques presented in Section 3.3.3. Indeed, Eq. (3.10) shows that an activation of the q-th coil alters $\mathbf{H}_v$ through the law of Biot - Savart, hence, the sensitivity coefficients change (Eq. (3.11)), resulting in distinct $\mathbf{L}_q$. To summarize, each $\mathbf{L}_q$ corresponds to the forward model of a single coil activation from the setup depicted in Fig. 3.10a). Alternatively, it can be stated that each $\mathbf{L}_q$ corresponds to the forward model of an MRX imaging setup consisting of a single coil. In total 48 forward models are considered because the setup consists out of 48 coils.

Because the goal of this section is to find a quantitative measure for comparing different forward models the index q ($q = 1, ..., Q$) is used to differentiate between various forward models. As setup parameters impact the forward model this quantitative measure can also be used to compare different MRX imaging setups. Q is the number of forward models and setups under consideration. A forward model and MRX imaging setup are thus interchangeable. In this dissertation the sensitivity matrix is often referred to as the '(forward) model', because it determines the characteristics of Eq. (3.21).

In Ref. [263] a distributed MNP phantom was made, referred to as the PTB phantom. Because previous findings (Ref. [346]) indicated that the relaxation of MNP in tumors was following the Néel relaxation process (Eq. (1.4)), the MNP in this phantom are fixed in gypsum cubes of 1 cm^3 to suppress their Brownian relaxation (Eq. (1.5)) (Section 3.1.2). In total, 54 cubes are employed, stacked into three layers each of which containing 18 cubes, arranged in a 6 $\times$ 3 pattern. Of these 54 cubes, twelve contained magnetic nanoparticles. In Fig. 3.10b) the phantom is depicted with the resulting iron amounts in the gypsum cubes. The upper layer is the layer which is closest to the SQUID

sensor system, while the bottom layer is furthest away from the SQUIDs.

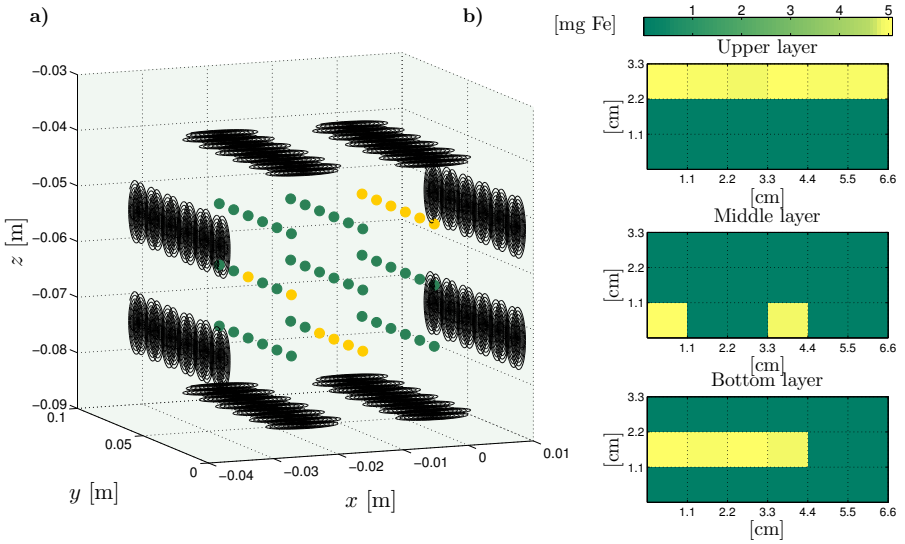

Figure 3.10: a) Visualization of the distributed coil array MRX imaging setup. The filled black circles represent the flat coils and the colored dots show the center of the gypsum cubes with green dots representing cubes without MNP and yellow dots representing cubes with MNP. The upper layer of the phantom is at a distance of 5.5 cm from the lowest SQUID sensors. For clarity reasons the SQUIDs are not shown. Each $\mathbf{L}_q$ corresponds to the activation of a single coil from the distributed coil array with q referring to the activated coil. b) The distributed MNP phantom consisting of 54 gypsum cubes. The upper layer is the layer closest to the sensors, while the bottom layer is furthest away from the SQUIDs. Each layer has a thickness of 1 cm.

3.3.3 Statistical MRX models

This section describes how statistical parameters, working on a random variable, can be employed to perform a quantitative comparison between MRX models. It considers the problem in which one has to determine, starting from Q MRX models and a volume consisting of V voxels, which model is best suited for obtaining the MNP amount in each voxel v. Statistical parameters are used to obtain quantitative information from these models, so to enable their comparison.

In this section each $\mathbf{L}_q(:,v)$ $(v = 1,...,V)$ is assumed to contain the observations of a continuous random variable. $\mathbf{L}_q(:,v)$ represents the v-th column of $\mathbf{L}_q$ and corresponds to the v-th voxel in the sample volume. This means that

each model q contains V random variables with S observations per variable. The motivation for choosing $\mathbf{L}_q(:,v)$ as the random variable is the following: the voxels are considered as sources of the measurement signal and the aim is to determine which model is best suited to reconstruct this source. By comparing the same columns (voxels) of different sensitivity matrices (models) quantitative information is obtained about the reconstruction possibilities with the models for the voxel under consideration. The entropy of a random variable $\mathbf{X}$, $H(\mathbf{X})$, is found by [352]:

$$H(\mathbf{X}) = -\sum_{x_{\mathrm{rv}} \in \mathbf{X}} P(x_{\mathrm{rv}}) \log_2(P(x_{\mathrm{rv}})) \tag{3.22}$$

$P(x_{\mathrm{rv}})$ is the probability that the random variable $\mathbf{X}$ equals the value x_{rv}. The entropy represents the information content of $\mathbf{X}$. Because the 2 base of the logarithm is employed this is commonly expressed in bits. This parameter can be extended to the conditional entropy $H(\mathbf{Y}|\mathbf{X})$ which quantifies the amount of information needed to describe the outcome of the random variable $\mathbf{Y}$ given that the value of $\mathbf{X}$ is known [352]:

$$H(\mathbf{Y}|\mathbf{X}) = -\sum_{x_{\mathrm{rv}} \in \mathbf{X}, y_{\mathrm{rv}} \in \mathbf{Y}} P(x_{\mathrm{rv}}, y_{\mathrm{rv}}) \log_2 \left(\frac{P(x_{\mathrm{rv}}, y_{\mathrm{rv}})}{P(x_{\mathrm{rv}})} \right) \tag{3.23}$$

$P(x_{\mathrm{rv}}, y_{\mathrm{rv}})$ is the probability that $\mathbf{X}$ equals x_{rv} and $\mathbf{Y}$ equals y_{rv}. The mutual information (MI) parameter is defined as [352]:

$$MI(\mathbf{X},\mathbf{Y}) = H(\mathbf{X}) - H(\mathbf{X}|\mathbf{Y}) = MI(\mathbf{Y},\mathbf{X}) \tag{3.24}$$

As can be seen from Eq. (3.24), the amount of information present in $\mathbf{X}$ is subtracted by the uncertainty left on $\mathbf{X}$, when knowing $\mathbf{Y}$. The mutual information is thus a measure for the information both random variables have in common.

These equations quantify a continuous random variable. However, only a limited set of observations (S) is available. Therefore, a discretization of the random variable is needed. Each observation of the random variable is linearly scaled to a value of $1,...,\Psi$, by employing a histogram with Ψ intervals. Ψ is determined according to an equation presented in [350] which depends on the standard deviation on the observations and their number. The histogram shows the number of observations in each interval. The $\mathbf{X}$ and $\mathbf{Y}$ sets employed in Eqs. (3.23) and (3.24) then correspond to the Ψ possible values determined in the discretization step. To obtain the joint probability distribution of two random variables $\mathbf{X}$ and $\mathbf{Y}$, ($P(x_{\mathrm{rv}}, y_{\mathrm{rv}}), x_{\mathrm{rv}} \in \mathbf{X}, y_{\mathrm{rv}} \in \mathbf{Y}$), a joint histogram is made which is then divided by the total number of occurrences. The marginal

distributions ($P(x_{\mathrm{rv}}), x_{\mathrm{rv}} \in \mathbf{X}$ and $P(y_{\mathrm{rv}}), y_{\mathrm{rv}} \in \mathbf{Y}$) are then calculated by:

$$P(x_{\mathrm{rv}}) = \sum_{y_{\mathrm{rv}} \in \mathbf{Y}} P(x_{\mathrm{rv}}, y_{\mathrm{rv}}) \text{ and } P(y_{\mathrm{rv}}) = \sum_{x_{\mathrm{rv}} \in \mathbf{X}} P(x_{\mathrm{rv}}, y_{\mathrm{rv}}) \tag{3.25}$$

In MRX imaging the spatial sensitivity (Eq. (3.17)) is used in evaluating a given model with respect to the voxels, as it is correlated to the achievable accuracy for each voxel. The spatial sensitivity is mostly high for voxels close to the magnetizing coils and sensors and low for voxels further away. A disadvantage of this quantity is that, when the voxel is in close proximity to a sensor or coil, a large value is generated while the contribution of the other (smaller) elements in the summation do not matter anymore. This is why we now employ statistical parameters such as $H(\mathbf{Y}|\mathbf{X})$ (Eq. (3.23)) in order to include the spread on the sensitivity coefficients as an imaging parameter.

Local weighting of quantitative MRX models

This section describes the transformation of $\mathbf{L}_q$. The transformation uses the quantitative information from Eqs. (3.22), (3.23) and (3.24). Based on this information, the transformation gives a weight to each column of $\mathbf{L}_q$ depending on its performances for each voxel with respect to the other sensitivity matrices. The transformation is based on the approach described in [350], where EEG and MEG data was combined. Due to the nature of the inverse problem some modifications of this method were necessary to be able to compare different $\mathbf{L}_q$.

The complete transformation of $\mathbf{L}_q$ is mathematically expressed as:

$$\mathbf{T}(\mathbf{L}_q) = \mathbf{N}_q \cdot \mathbf{L}_q \cdot \mathbf{W}_q \cdot \mathbf{D}_q \tag{3.26}$$

$\mathbf{T}(\mathbf{L}_q)$ is called the transformed sensitivity matrix of forward model q and $\mathbf{L}_q$ the sensitivity matrix of forward model q (Eq. (3.21), Section 3.3.2). In the following all the different steps of this transformation are detailed. Figure 3.11 depicts an overview of the considered transformation.

$\mathbf{N}_q$ is a diagonal matrix and performs the normalization of the sensitivity matrix's rows, so that a similar sensor signal is obtained for each model. Each element s on its diagonal is calculated as follows: $\|\mathbf{L}_q(s,:)\|^{-1}$ with $\mathbf{L}_q(s,:)$ ($s = 1,...,S$) the s'th row of $\mathbf{L}_q$. $\mathbf{W}_q$ is a diagonal matrix with weights based on the performance of the model for each voxel v in comparison to the other $Q-1$ models. $\mathbf{D}_q$ is a diagonal matrix which removes the impact

of source orientation and each element v on the diagonal can be computed by: $\|(\mathbf{N}_q \cdot \mathbf{L}_q \cdot \mathbf{W}_q)(:,v)\|^{-1}$ with the operator $(:,v)$ working on the resulting matrix from the multiplication of $\mathbf{N}_q \cdot \mathbf{L}_q \cdot \mathbf{W}_q$.

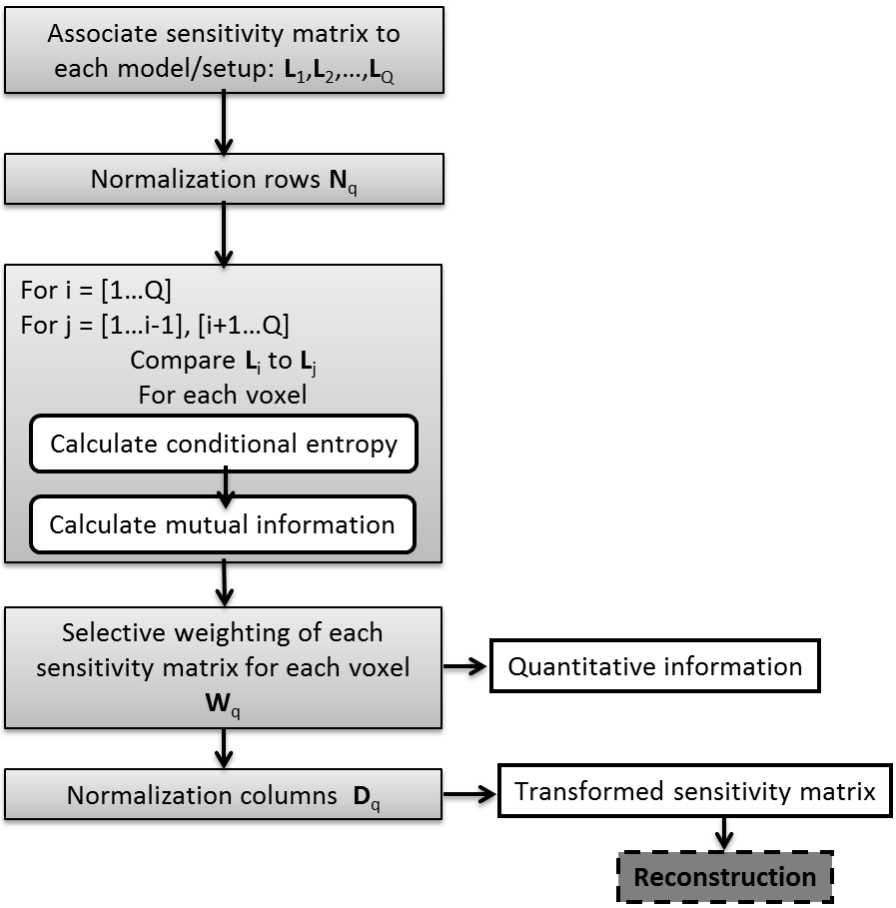

Figure 3.11: Method for quantitative comparison between different MRX forward models using information theory parameters. Based on these parameters a selective weighting of the forward models is possible. The weighting coefficients give quantitative information about the efficiency of each model with respect to the voxels and allow a quantitative comparison between the models.

$\mathbf{W}_q$ is determined by evaluating the conditional entropy (Eq. (3.23)) and mutual information (Eq. (3.24)) for sensitivity matrix q compared to the other $Q-1$ sensitivity matrices for each voxel v. To explain how the weighting works an example is given of two forward models $\mathbf{L}_q$ with $q = j$, $\mathbf{L}_{q=j}$, and

with $q = i$, $\mathbf{L}_{q=i}$. Both models are compared to each other for the voxel v. It is beneficial to use the model that results in the lowest amount of uncertainty left, i.e. the model that gives the largest amount of information about the voxel v to be reconstructed. If

$$H(\mathbf{L}_{q=i}(:,v)|\mathbf{L}_{q=j}(:,v)) < H(\mathbf{L}_{q=j}(:,v)|\mathbf{L}_{q=i}(:,v))$$

this means the model with $\mathbf{L}_{q=j}$ is best suited to reconstruct the v-th voxel. The v-th column of $\mathbf{L}_{q=j}$ then receives a weighting of 1, while the v-th column of $\mathbf{L}_{q=i}$ is given a weighting < 1, determined by minimization of the MI parameter (Eq. (3.24)). This parameter represents the information both models have in common when reconstructing voxel v. The weighting for the v-th column of $\mathbf{L}_{q=i}$ is chosen such that the MI parameter is minimal, to reduce the amount of mutual information and this way reduce the linearly dependent information. It has been shown previously in Ref. [349] that linearly dependent information can deteriorate the solution of the inverse problem. The use of the conditional entropy and MI parameters limits the comparison to only two models at a time. To obtain the final weighting values for forward model j for voxel v the previous comparison is repeated for the other remaining forward models (with q different from j and i). In total thus $Q-1$ weightings originate from the comparison of forward model j to the other $Q-1$ forward models. These $Q-1$ weightings are averaged to obtain the final weighting value for voxel v ($\mathbf{W}_{q=j}(:,v)$). This can be done for each forward model. The models with the largest weightings on the v-th column are then the most favorable for reconstructing the MNP amount in voxel v. Remark that for significantly different weightings, information might be lost by averaging the weightings. For the models considered in this study this is not the case, but this might become a challenge for significantly different models or when many forward models are compared.

To compare the transformed sensitivity matrices to the original sensitivity matrices, the Q sensitivity matrices are concatenated into 1 matrix of dimensions $(QS) \times V$ (similar as in Section 3.1.4, Eqs. (3.13) and (3.14)) defined as $\mathbf{L}$ for the original sensitivity matrices and $\mathbf{T}(\mathbf{L})$ for the transformed sensitivity matrices:

$$\mathbf{T}(\mathbf{L}) = \begin{bmatrix} \mathbf{T}(\mathbf{L}_1) \\ \vdots \\ \mathbf{T}(\mathbf{L}_q) \\ \vdots \\ \mathbf{T}(\mathbf{L}_Q) \end{bmatrix} \tag{3.27}$$

With a similar definition for $\mathbf{L}$ (see, Eq. (3.14)). The forward model of $\mathbf{T}(\mathbf{L})$ becomes:

$$\mathbf{T}(\mathbf{B}) = \mathbf{T}(\mathbf{L}) \cdot \mathbf{c} \tag{3.28}$$

and the inverse solution can be found, similarly as in Section 3.2, by truncated SVD (Eq. (1.23)):

$$\mathbf{c}^* = \mathbf{T}(\mathbf{L})_r^\dagger \cdot \mathbf{T}(\mathbf{B}) \tag{3.29}$$

Remark that the sensor signals generated with the forward model now differ from the measured ones. This is because each column of the transformed sensitivity matrix is multiplied with weightings which are not in accordance with the sensitivity matrices calculated from physical laws (Eqs. (3.10),(3.12)). Luckily, Baillet et al. developed an iterative method, based on a rewriting of Eq. (3.21), to allow the use of measurement data and the transformed sensitivity matrix [350].

3.3.4 Spatial and noise sensitivity

The impact of the complete transformation on spatial and noise sensitivity is investigated here. The spatial sensitivity is analyzed by examining $\mathbf{S}_\mathrm{p}$ (Sections 1.4.4 and 3.2.3) for $\mathbf{L}$ and $\mathbf{T}(\mathbf{L})$. Figure. 3.12a) depicts the normalized spatial sensitivity $\mathbf{S}_\mathrm{p}$. The transformation results in a reduced sensitivity of the layer closest to the sensors, while the sensitivity of the middle and bottom layer is increased. A more equally distributed spatial sensitivity profile is created this way. The middle layer, which originally had the lowest sensitivity, now receives the highest sensitivity. This effect is also observed for other discretizations of the sample. Table 3.3 shows the average normalized sensitivity for each layer when V = 54 (3 layers) and V = 432 (6 layers).

Next, the normalized eigenvalue distributions are inspected as these contain information about the signal and noise sources [264]. In general, a slower decrease for the eigenvalues of $\mathbf{T}(\mathbf{L})$ is seen in Fig. 3.12b), suggesting an improved noise stability (Section 1.4.4). Remark however, that the first eigenvalues of the transformation have a smaller size. The smallest eigenvalues have the largest impact on the inverse solution so the consequences will be minimal. Further evidence for the increased numerical stability is the condition number (Eq. (1.28)) which corresponds to $\beta(\mathbf{L}) \approx 143$ and $\beta(\mathbf{T}(\mathbf{L}))$ ≈ 61. The increased numerical stability should result in an increased noise robustness of $\mathbf{T}(\mathbf{L})$.

The impact of noise on the reconstruction quality can be investigated by considering a noise vector $\mathbf{n}$ in the forward model: $\mathbf{B} = \mathbf{L} \cdot \mathbf{c}_\mathrm{act} + \mathbf{n}$. The actual

MNP distribution, $\mathbf{c}_{\text{act}}$, is the phantom described in Section 3.3.2. A similar expression can be found for $\mathbf{T}(\mathbf{L})$. The noise term is modeled as white Gaussian noise having a certain SNR. The SNR is calculated in dB as: $10\log_{10}\left(\frac{P_{\text{sig}}}{P_{\text{noise}}}\right)$ with P_{sig} the average power of the simulated noise-free signal and P_{noise} the average power of the noise. For each noise level, 50 different noisy data sets were generated. The average CC was calculated by comparing $\mathbf{c}_{\text{act}}$ and $\mathbf{c}^*$ (Eq. 1.27) for each noise level and averaging the obtained values. Figure 3.12c) shows the reconstruction of the PTB phantom for $\mathbf{L}$ and $\mathbf{T}(\mathbf{L})$ for noise with a SNR of 20 dB (a commonly employed noise level, see Refs. [37, 349]). The associated correlation coefficients are 95.5 and 99.8 % respectively. The difference is most striking for the middle layer where a correlation is found of 82.5 % for $\mathbf{L}$ and 99.2 % for $\mathbf{T}(\mathbf{L})$. Using $\mathbf{L}$, lower-lying sources are lifted upwards due to the decreased spatial sensitivity for the lower voxels. For other noise levels (ranging from 1 to 40 dB) $\mathbf{T}(\mathbf{L})$ also outperforms $\mathbf{L}$. Note that the impact of a double transformation, $\mathbf{T}(\mathbf{T}(\mathbf{L}))$, is only marginal ($\approx 1$ %) compared to $\mathbf{T}(\mathbf{L})$ which is why this is not considered further.

Table 3.3: Normalized average spatial sensitivity for each layer for $V = 54$ and $V = 432$ using $\mathbf{L}$ and $\mathbf{T}(\mathbf{L})$. The transformation realizes a homogeneous sensitivity which results in a higher sensitivity for lower layers and a lower sensitivity for the layer closest to the sensors.

Average S_p [-]	$V = 54$		$V = 432$	
	$\mathbf{L}$	$\mathbf{T}(\mathbf{L})$	$\mathbf{L}$	$\mathbf{T}(\mathbf{L})$
Upper layer(s)	0.82	0.60	0.77 0.52	0.49 0.65
Middle layer(s)	0.48	0.72	0.39 0.34	0.73 0.68
Bottom layer(s)	0.47	0.53	0.34 0.39	0.57 0.43

3.3.5 MRX setup optimization

Optimal coil configuration

In this example a statistical parameter (Eq. (3.24)) is directly employed to find a subset of coils that generate similar reconstruction results, while requiring less MRX measurements. The top part of Fig. 3.13a) shows the normalized spatial sensitivity profile (Eq. (3.17)) for the original sensitivity matrix when an upper coil is activated (corresponding to $\mathbf{L}_{q=1}$). The bottom part depicts the mutual information (Eq. (3.24)) of each voxel based on the pairwise

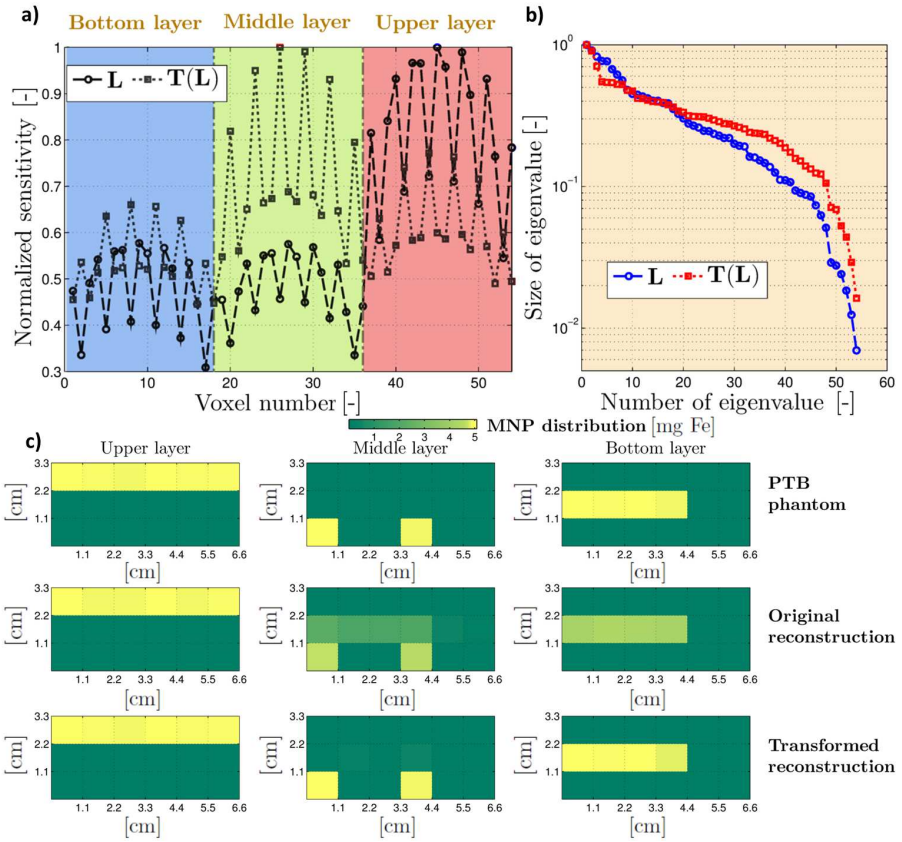

Figure 3.12: a) Normalized spatial sensitivity profile of $\mathbf{L}$ and $\mathbf{T}(\mathbf{L})$. $\mathbf{T}(\mathbf{L})$ shows a homogeneous sensitivity profile responsible for an increased reconstruction quality compared to $\mathbf{L}$. b) The normalized eigenvalue distribution for $\mathbf{L}$ and $\mathbf{T}(\mathbf{L})$ shows an increased numerical stability for $\mathbf{T}(\mathbf{L})$. c) Reconstruction of the PTB phantom for $\mathbf{L}$ and $\mathbf{T}(\mathbf{L})$ using simulated white Gaussian noise of 20 dB. Lower sources are shifted upward and are less accurately reconstructed when $\mathbf{L}$ is employed due to the inherent lower sensitivity of these layers and the decreased numerical stability of this matrix.

comparison between the same coil and the 47 other coils. The mutual information parameter shows the information content the coils have in common and should be as low as possible to increase the stability of the inverse problem. As can be seen from the spatial sensitivity profile, the considered coil strongly magnetizes voxels in the upper plane, while other voxels are not well activated. The other coils in the upper plane have sensitivity profiles with peaks which are slightly shifted in the upper layer compared to this coil, resulting in a small MI for the upper voxels. The lower voxels have a similar sensitivity profile and this results in a high MI. An analogous reasoning can

be made for the other coils. Fig. 3.13b) shows differences in spatial sensitivity for this coil compared to the other coils. Here, similar values are obtained for most voxels because only a summation of the sensitivity coefficients is considered (Eq. (3.17)), while the MI parameter takes into account their spread (Eq. (3.24)). Another approach is to correlate sensitivity profiles of the coils with each other (see Fig. 3.13c)). This however gives one correlation score for all the voxels and does not allow for voxel-based information. The mutual information is thus a parameter which allows to correlate sensitivity profiles of coils in a quantitative way compared to other measures.

Now a subset of coils needs to be found that minimizes the mutual information over all voxels. A coil is randomly selected and added to the coil selection. Then the MI of each voxel for this coil is investigated by pairwise comparison to the other 47 coils (comparable to Fig. 3.13a) below). The voxel with minimum MI and its neighbors are kept. A new randomly chosen coil is added to the coil selection as long as the coil has low MI values on different voxels compared to the previously selected coils. This results in a subset of 18 coils (see Figure 3.14a)). Although the coil selection is random, the results are reproducible because the coils with similar mutual information are chosen (similar effect on similar voxels). Despite the fact that this is a very rough optimization, the results are in agreement with coil selections found in Refs. [349] and [264]. By using the quantitative modeling approach it is thus possible to configure the coil array in a very fast way compared to the techniques used in previously mentioned papers. Fig. 3.14b) shows the CC function of SNR for $\mathbf{T}(\mathbf{L})$ using $Q = 48$ coils, $Q = 18$ coils and for $\mathbf{L}$ using $Q = 48$ coils. The subset of 18 coils shows a small decrease in reconstruction accuracy compared to $\mathbf{T}(\mathbf{L})$ with all coils employed, but has an improved performance (increase in correlation of 3 %) compared to $\mathbf{L}$ with 48 coils. Now only 18 measurements need to be made which correspond to a measurement speedup of about 65 %. Figure 3.14c) shows a reconstruction example of the phantom for a noise level of 20 dB using a subset of 18 coils with a low MI over all voxels. As can be observed, using the MI as a selection criteria for the coils, it is possible to select those coils which achieve a similar performance as when 48 coils are employed. This makes using the MI as a selection criteria a valuable tool.

Optimal spatial resolution

In this example the statistical parameters (Eqs. (3.23),(3.24)) and the transformation approach from Section 3.3.3 are used to estimate the optimal voxel size for the MRX imaging setup. The phantom is tessellated in the following cubic voxels with lengths: 3 mm, 5 mm, 1 cm, 1.5 cm and 2 cm. In a first step the MI

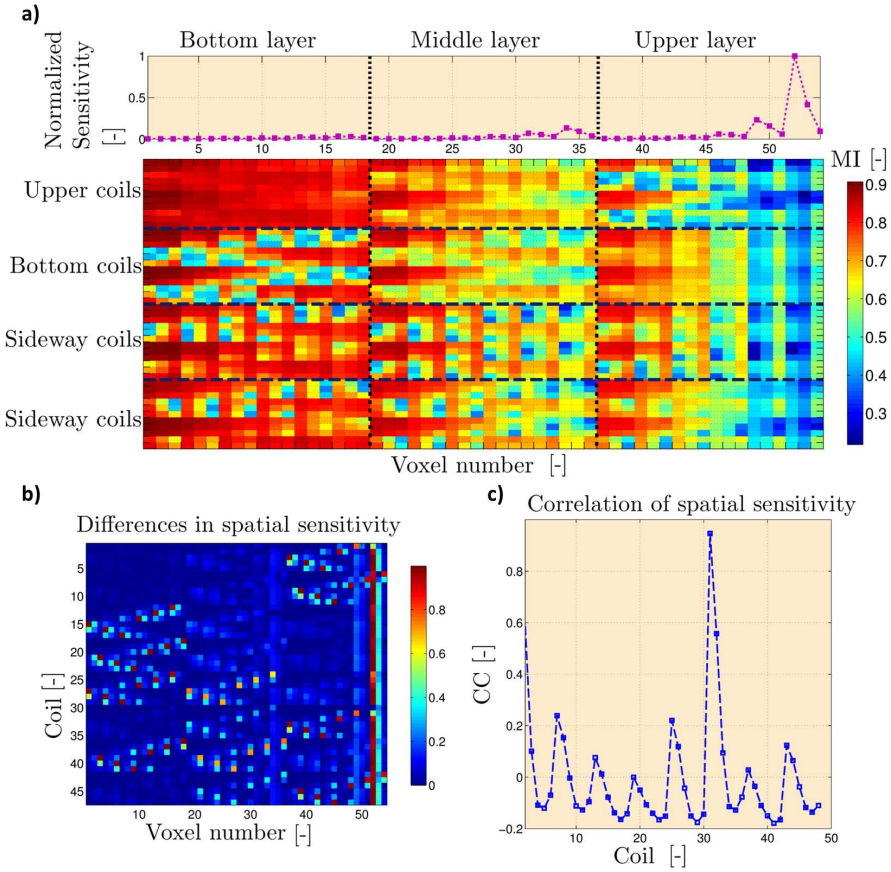

Figure 3.13: a) Above: sensitivity profile of coil $q = 1$ in the layer between volume and SQUIDs. Below: Mutual information for this coil and the other 47 coils. The MI gives a measure of the information both coils have in common for each voxel and should be as low as possible to increase stability of the inverse problem. b) Differences in spatial sensitivity profile for the same coil with respect to the 47 other coils. The spatial sensitivity does not take into account the spread on the sensitivity coefficients and is thus less accurate. c) Correlation of spatial sensitivity profile for this coil with respect to the 47 other coils. This does not allow for voxel-based information.

parameter is calculated based on a pairwise comparison of a given coil and the 47 other coils for the different voxels (comparable to Fig. 3.13a) below). Next, an averaging over all voxels for each comparison is performed. This way the average MI for each voxel size and coil comparison can be found. Figure 3.15a) shows an example for an upper coil and the other 47 coils. The smaller the voxel size, the larger the average MI. It is observed however that the relative information content (the shape of the curve) remains the same

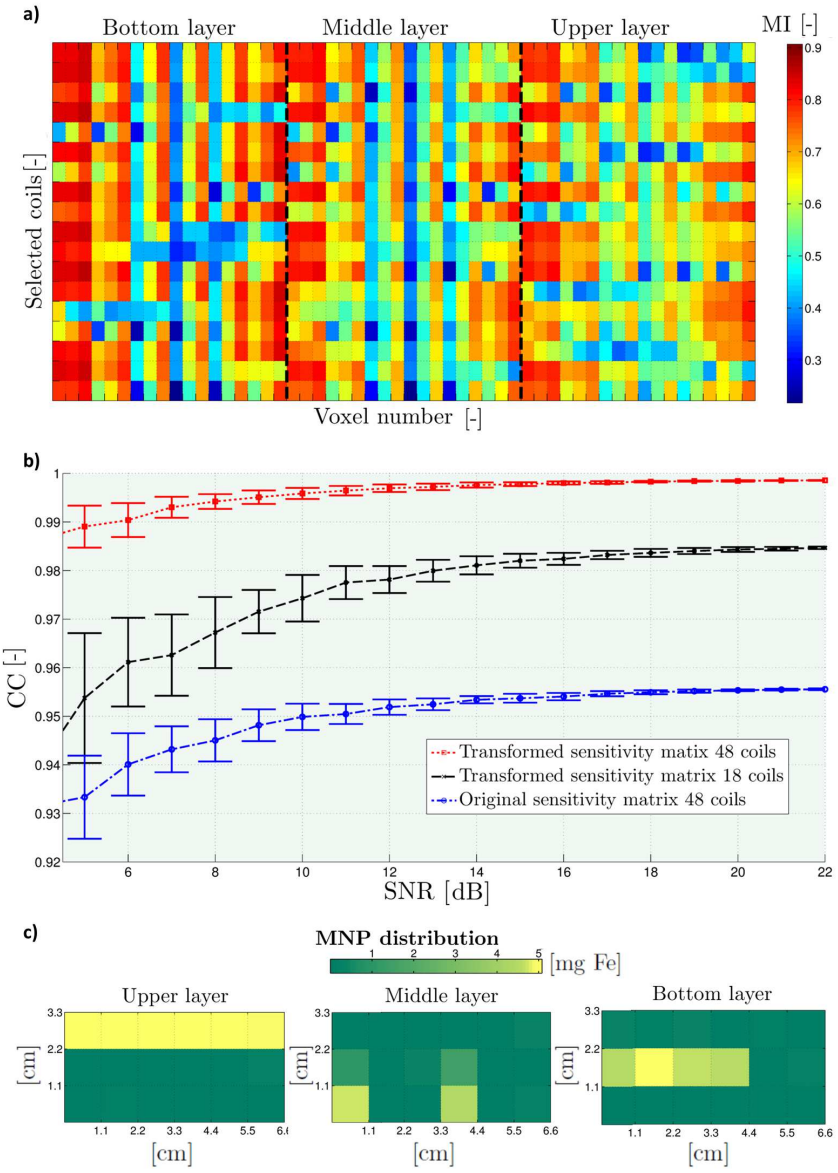

Figure 3.14: a) MI for a coil from the subset compared with the 17 other selected coils (same color scale as Fig. 3.13a)). A general reduction in MI is seen for each coil comparison. b) CC function of SNR for $\mathbf{T}(\mathbf{L})$ with 48 and 18 coils and $\mathbf{L}$ with 48 coils. The subset has a decreased performance but still shows an improved accuracy compared to the original approach. c) Reconstruction of the PTB Phantom for the selection of 18 coils using white Gaussian noise with SNR 20 dB (same color scale as Fig. 3.12c)).

for each voxel size up until 1.5 - 2 cm. Using a value of 2 cm significantly alters the information content of the problem, and is an indication that this voxel size is too rough for this setup. For other given coils and their pairwise comparison similar results are found. This gives an estimated lower limit for the PTB setup of 1.5 cm.

In a next step the transformation from Section 3.3.3 is performed and the resulting weights investigated for the 48 coils for each voxel size. Because of the smaller voxel sizes, the stability of the inverse problem deteriorates. This is also reflected in the higher amounts of MI. In the transformation we reduce the MI by adapting the weight of the 'lesser' model to minimize the MI. Because of the increased MI for reduced voxel sizes, this introduces weights equal to zero in some cases. This corresponds to removing the model for the corresponding voxel and this way instability issues are created, which deteriorate the inverse solution. Figure 3.15b) shows the values of $\mathbf{W}_q$ (with $q = 1,...,48$) for each voxel size. For decreasing voxel sizes, decreasing weights are employed. Fig. 3.15a) showed no additional information for the 3 mm voxels and Fig. 3.15b) shows instability issues due to the lower weightings. Therefore, a lower limit of 5 mm is suggested. The setup is thus ideally suited for reconstructions of voxels between 5 and 15 mm. Given the coil diameters of about 1 cm and SQUID pick-up coils with an area of 7×7 mm, these limits seem a good estimate.

3.3.6 Conclusion

In this section, *quantitative* MRX models were developed by making use of statistical parameters from information theory such as the conditional entropy and mutual information. This could be achieved by employing the sensitivity matrices of each forward model as input to the statistical measures. The measures can then provide quantitative information and allow one to determine which MRX model is the most suited for MNP imaging. Based on the quantitative information associated to each model, a weighting on the level of the forward model can be performed. This transformation results in improved MNP reconstructions and an increased spatial and noise stability of the inverse solution. The improvement was most significant for positions in the sample which initially had a lower spatial sensitivity, i.e. voxels further away from coils and sensors. For these voxels, correlations between actual and reconstructed MNP distributions amounted to 99.2 %, whereas the original approach only had 82.5 %.

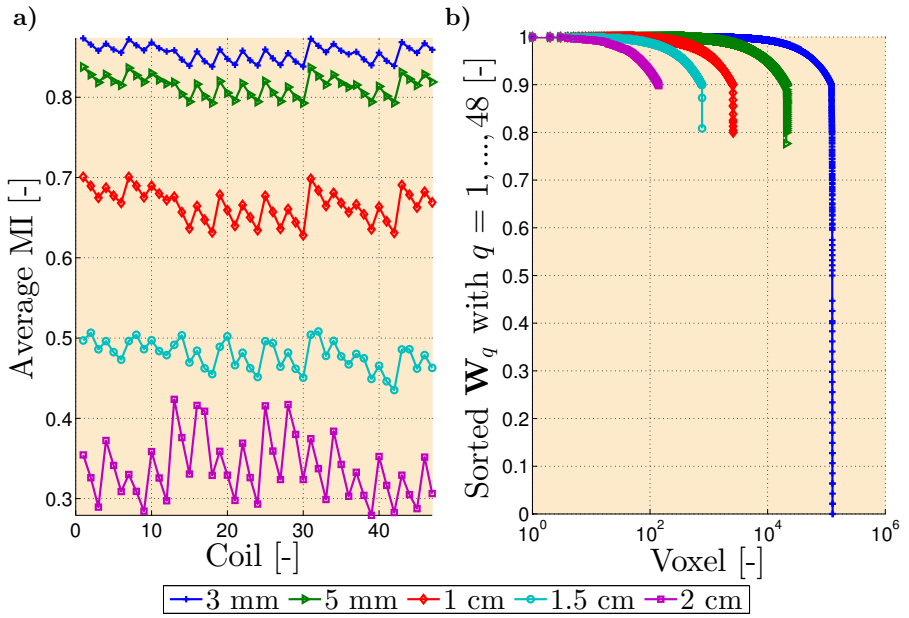

Figure 3.15: a) Average MI for a given coil with respect to the 47 other coils. Similar information content is seen for voxel sizes of 3 mm, 5 mm, 1 cm and 1.5 cm, suggesting an upper limit for the resolution of 1.5 cm for the setup. b) Visualization of $\mathbf{W}_q$ with $q = 1,...,48$ for different voxel sizes. For decreasing voxel sizes, the weights decrease due to a larger MI and increasing numerical instability. A voxel size of 3 mm requires a large decrease in the weights of the different models, causing instability issues.

It was additionally shown that the quantitative information could also be used *directly* to enhance MRX imaging setups. This way several aspects of a MRX imaging setup, having a coil array, could be optimized. For example, by only selecting the coils with the smallest mutual information in the measurement procedure, the measurement time could be reduced by 65 %, while still achieving small improvements in imaging accuracy and noise robustness. The statistical parameters also allow a *direct* measure of the relative information content within the setup models. This way the optimal voxel size for the given MRX setup could be determined to be between 5 and 15 mm, as other sizes showed a significant change in the statistical parameters.

To conclude, in this section a measure was presented which is able to compare, both quantitatively and accurately, different MRX models and setups independent of the MNP distribution.

3.4. Multi-color imaging

3.4.1 Introduction

In Section 1.2 an overview was given of the main biomedical MNP applications. This illustrates that many MNP applications exist, each with their specific particle type. From a clinical viewpoint it would be highly desirable and cost-effective to have an imaging tool that is capable of reconstructing the spatial distribution of multiple particle types simultaneously, so that multiple biomedical applications can be combined in a single experiment or platform. In the new field of theranostics (Section 1.2), combinations of particle types are envisioned that allow diagnosis followed by treatment in one experiment, such as the combined tracking of stem cells/drugs, the monitoring of disease progress and its adequate response [80, 82], or the specific targeting of cancer with MNP types suitable for imaging, drug targeting and thermoablation [63]. Also from the future perspective of personalized nanomedicine, in which nanomedicine is tailored to the needs of the patient, this platform would result in a more flexible, precise and non-invasive treatment of patients and would allow real-time monitoring and personalized treatment planning. Additionally, research should be performed to investigate what size, properties and composition the MNP need to treat any individual patient in the most effective way [62, 353]. Hence, inter-individual variability in therapeutic response can be reduced. Because MNP have been successful in both diagnostic and therapeutic applications, they have the potential to realize this platform and to provide personalized therapy.

For this reason, the MNP imaging research field has started to investigate the simultaneous imaging of multiple particle types. MPI for example, recently introduced a multi-color approach, which allows images of the spatial distribution of each particle type which can then be combined into a single color-coded image, hence the name multi-color MPI [221]. Using multi-color MPI, separation of suspended and immobilized particles seems feasible, but more than two types of particles still pose a challenging problem. Also AC susceptibility imaging proved successful [249], as the in- and out-of-phase component of the magnetic susceptibility are linked to MNP properties and their environment [122, 243]. We refer to Section 1.3.3 for information about the working principles of MPI and ACS and how they can be used to perform multi-color imaging.

Similarly, MRX imaging could be employed for the simultaneous imaging of multiple particle types, as its decaying signal also contains this information (Section 3.1.3) and would thus allow the measurement of various particle types or the imaging of the changing environment of the MNP. MRX imaging

has already been successfully performed to visualize immobilized and suspended particles simultaneously [330]. However as the dynamics, and as such the characteristic MRX signal, from fluid and immobilized MNP are significantly different, research still needs to be performed regarding the feasibility of MRX imaging of similar MNP types.

In this section a method is presented that separates the MRX signal into the relative contributions of various MNP types without the need of large differences in their MNP magnetization dynamics. This way it is possible to reconstruct the spatial distribution of each MNP type simultaneously using MRX imaging. These reconstructions, in a similar way to multi-color MPI, can then be combined in a color-coded image, i.e. *multi-color* MRX imaging. More specifically, the presented setup could be used to monitor the biodistribution (for example in the liver, lungs, large arteries and spleen) and clearance of multiple MNP types simultaneously or to assess magnetic drug targeting efficiency of these particles towards larger tissues (Section 3.1.5). Additionally, the presented technique could be used to image the binding processes of the MNP with their targets (antibodies, cells, molecules, biomarkers, etc.), as the magnetic dynamics change when the MNP bind with their target. This concept has already been successfully applied in MRX characterization (see Section 3.1.5), but could now be extended to spatial reconstructions. Six phantoms with different spatial particle configurations and multiple MNP types are considered to investigate the advantages and drawbacks of this technique. The final goal is to assess the ability of MRX imaging to differentiate between multiple types of particles. This way MRX opens the pathway to clinical examinations in which different types of particles can be detected, or the tissue surrounding the particles can be assessed.

Section 3.4.2 provides an overview of the setup and particles used in the multi-color measurements. In Section 3.4.3 the forward model of multi-color MRX imaging is developed and the corresponding inverse problems are discussed. Section 3.4.4 details the performed experiments and starts with a description of the MRX reference measurements of the various particle types and their phantom configurations. It emphasizes the main separation and reconstruction difficulties associated to each phantom. The section ends with a thorough analysis of the obtained phantom reconstructions in which various quality parameters are employed. This work was published in Ref. [354].

3.4.2 MRX imaging setup

Experiments were performed at the PTB for the experimental validation of the color MRX imaging approach. The sensors system employed was the 304

low-T_c SQUID magnetometers sensor setup [325], which was described in detail in Section 3.3.2. This device enables the spatial mapping of the magnetic induction vector due to the different orientations and positions of the SQUID magnetometers distributed along 4 layers in a large liquid helium Dewar of 25 cm inner diameter. A sampling frequency of 750 Hz was employed.

Beneath the Dewar, at a distance of 64 mm from the lowest SQUID sensors, a plexiglass mount (see Fig. 3.16a)) is positioned in which different configurations of MNP samples can be placed [330]. The mount consists of 5 layers with a size of 9.6 $\times$ 9.6 cm and a height of 1.2 cm. Using this mount the MNP samples can be fixed spatially, reducing the error on their position. The second layer is used for the spatial configurations of the particles (i.e. the MNP phantoms) by means of a holder. The holder consists of a grid pattern of 64 voxels with a size of 1.2 cm in which holes are placed following a checker board pattern. Each hole allows the placement of a closed cuboid sample container with dimensions of 0.9 $\times$ 0.9 $\times$ 2 cm, so that no leakage or evaporation of the particles is possible. The sample containers are fixed in the holes by non-magnetic tape. In each sample holder a maximum of 0.5 ml of particle fluid is inserted. The particles under consideration are commercially available ferrofluids (chemicell GmbH, Germany) consisting of an aqueous dispersion of magnetic iron oxides. See Table 3.4 for their properties.

Table 3.4: Properties of the MNP under study.

Name	Type	Size [nm]	Amount in sample holder [mg Fe]
F200	fluidMAG-D	200	6
F200 freeze-dried	fluidMAG-D	200	6
F300	fluidMAG-D	300	6.7
N500	nanoMAG-D	500	3.5

The particles are magnetized by 30 planar excitation coils each with a diameter of 36 mm. 15 of these coils are positioned between the Dewar and the phantom, the other 15 coils are below the phantom. Both coil layers are at a distance of 5.7 cm and 13.2 cm respectively from the lowest SQUID sensors. Figure 3.16b) depicts an overview of the complete MRX imaging setup. The second layer of the mount is used for the phantoms, due to the large height of the employed sample containers. The coil activation procedure is as follows: each time a single coil of the 30 coils is activated for 5 seconds with a stabilized current of 1.2 A, then switched off, after which the 304 SQUID sensors measure the MRX signal for 5 seconds ($S = 304$). Each coil generates a different magnetic field, so in total 30 spatially varying magnetic fields are considered and thus (30 $\times$ S) measurements are performed (with $Q = N_a =$

30, see Eq. (3.14)).

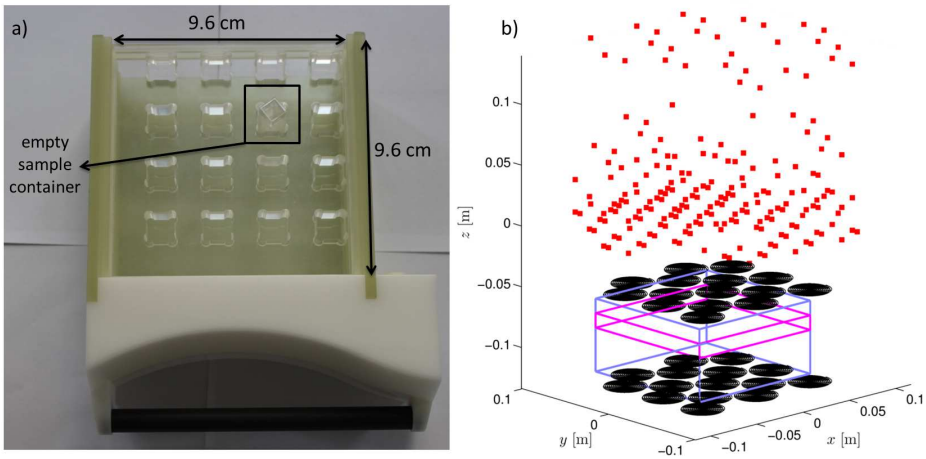

Figure 3.16: a) Top view of the plexiglass mount for the MNP phantoms. In the second layer of the mount a checkerboard pattern is inserted. This way multiple configurations of MNP samples can be realized by placing the particles in sample containers which can be fixed in the holes with tape. b) Complete overview of the MRX imaging setup at PTB. The 30 activation coils for magnetizing the MNP are represented as filled black circles. The red squares show the positions of the SQUID sensors. The orientation of the SQUIDs is omitted for clarity purposes. The blue lines depict the plexiglass mount. The second layer of the mount, in which the checkerboard pattern is placed, is highlighted in pink.

3.4.3 Multi-color model

Recall from Section 1.1.3 that 1) the particles can rotate as a whole, thereby changing the orientation of their magnetic moment, or 2) the orientation of the magnetic moment inside the particle cores can be altered. These mechanisms are characterized by a typical time constant called the Brownian relaxation time (Eq. (1.5)), τ_B, and the Néel relaxation time (Eq. (1.4)), τ_N respectively. τ_{eff} (Eq. (1.6)) is the effective relaxation constant when both Brownian and Néel relaxation phenomena are occurring in the particle. It represents the fact that the fastest relaxation of both mechanisms will define the effective relaxation mechanism of the particle. τ_{eff} depends on particle properties such as its anisotropy and core and hydrodynamic volumes. In Sections 3.1.2 and 3.1.3 it was clarified how these particle properties and their surrounding environment alter the shape of the MRX measurement signal. These sections showed that the MRX signal can be regarded as a summation of all effective relaxation times associated to the variety of particles in the

MNP sample. In this dissertation particle dynamics are captured through a reference MRX measurement of a sample with well-known MNP amount. This information was included in the forward model for MRX imaging (Eq. (3.14)) using the $\Delta\kappa_{t_1,t_2}$ term (Eq. (3.10)), which represents the temporal decay of the MNP sample between the time points t_1 and t_2. Therefore, it was of importance to use the same particle type (or combinations of particle types) in the actual experiment as in the reference measurement. Hence, the imaging model described in Section 3.1.4 was only valid for signals originating from one particle type in a homogeneous environment, as other environments or particle types could alter $\Delta\kappa_{t_1,t_2}$. In this section, a theoretical procedure is introduced that uses *a priori* information on the MNP properties to allow MRX imaging in which multiple MNP types in a homogeneous environment, or the same particle type in a heterogeneous environment, can be imaged simultaneously, i.e. multi-color MRX imaging.

Multiple particle types can be included in the forward model by representing the MRX signal as a combination of the MRX signals from each particle type. The forward model for 1 particle type (Eq. (3.14)) can thus be extended to Λ particle types as follows:

$$\mathbf{B}(\mathbf{c}) = \sum_{\lambda=1}^{\Lambda} \mathbf{L}_\lambda \cdot \mathbf{c}_\lambda = \left[\mathbf{L}_1, \ldots, \mathbf{L}_\lambda, \ldots, \mathbf{L}_\Lambda\right] \begin{bmatrix} \mathbf{c}_1 \\ \vdots \\ \mathbf{c}_\lambda \\ \vdots \\ \mathbf{c}_\Lambda \end{bmatrix} \tag{3.30}$$

with Λ the number of particle types under consideration, $\mathbf{L}_\lambda$ is the sensitivity matrix (with dimensions $(QS) \times V$) of particle type λ and $\mathbf{c}_\lambda$ (with dimensions $V \times 1$) its spatial distribution. Each $\mathbf{L}_\lambda$ differs in the $\Delta\kappa_\lambda(t_1,t_2)$ term as this term represents the effect of the particle's properties on the MRX signal. The reconstruction can then be solved in a similar way as described in Sections 1.4.3 and 3.1.4. Remember that Eq. (3.30) models the amplitude decrease of the MRX signal between two time points. However, by increasing the number of time points used, more temporal information about the particles can be obtained, which make the distinction between the particle types easier and stabilizes the inverse problem. Temporal information in the MRX model for a single particle type was included in Ref. [37] by using the Kronecker product, although it was shown to only make a difference for signals having a low SNR. In this work, temporal information is included by considering two sub-problems, one related to the time window (with J time points instead of only 2), and the other one related to the image reconstruction. This way, temporal information can be taken into account and more information is

available to solve the inverse problem.

By performing a MRX reference measurement of each particle type λ, taking into account sample location and sensor orientation, $\boldsymbol{\kappa}_\lambda$ can be determined similarly as in Section 3.1.3 :

$$\boldsymbol{\kappa}_\lambda(t_{\text{window}}) = \frac{\mathbf{B}_{\text{MRXref}_\lambda}(t_{\text{window}})}{Hc_{\text{calib}_\lambda}} \tag{3.31}$$

Remark that in Eq. (3.10) only the difference between two time points (t_1 and t_2) of the MRX curve was used, resulting in a scalar $\Delta\kappa_\lambda(t_1,t_2)$ instead of the $1 \times J$ vector $\boldsymbol{\kappa}_\lambda(t_{\text{window}})$. In Eq. (3.31) $\mathbf{B}_{\text{MRXref}_\lambda}(t_{\text{window}})$ is the MRX reference signal (dimensions $1 \times J$) for a time window with J time points for particle type λ with an iron amount of c_{calib_λ}, magnetized in a magnetic field with amplitude H, see also the lower part of Fig. 3.17. Then $\mathbf{B}(\boldsymbol{\delta}, t_{\text{window}})$ can be formulated as a linear combination of the Λ MRX reference measurements because the associated relaxation times do not change:

$$\begin{aligned}\mathbf{B}(\boldsymbol{\delta}, t_{\text{window}}) &= \sum_{\lambda=1}^{\Lambda} \boldsymbol{\delta}_\lambda \mathbf{B}_{\text{MRXref}_\lambda}(t_{\text{window}}) \\ &= \left[\boldsymbol{\delta}_1, \ldots, \boldsymbol{\delta}_\lambda, \ldots, \boldsymbol{\delta}_\Lambda\right] \begin{bmatrix} \mathbf{B}_{\text{MRXref}_1}(t_{\text{window}}) \\ \vdots \\ \mathbf{B}_{\text{MRXref}_\lambda}(t_{\text{window}}) \\ \vdots \\ \mathbf{B}_{\text{MRXref}_\Lambda}(t_{\text{window}}) \end{bmatrix}\end{aligned} \tag{3.32}$$

with $\boldsymbol{\delta}_\lambda$ (dimensions $(QS) \times 1$) the relative contribution of reference measurement λ for each measurement. This procedure is based on the MARIA technique described in Section 3.1.5, in which the distinction was made between unbound and bound particles in the MRX signal by fitting their respective reference curves (Eq. (3.15)). Then an inverse problem can be solved, which is the first sub-problem:

$$\boldsymbol{\delta}^* = \arg\min_{\boldsymbol{\delta}} \left\| \mathbf{B}(\boldsymbol{\delta}, t_{\text{window}}) - \mathbf{B}_{\text{MRX}}(t_{\text{window}}) \right\| \tag{3.33}$$

with $\mathbf{B}_{\text{MRX}}(t_{\text{window}})$ the MRX measurement, which corresponds to $\mathbf{S}_{\text{m}}$ in the general example of Eq. (1.19). The solution of this equation can be found through the methods described in Section 1.4.3. Here, NNLS (Eq. (1.26)) is used. The absolute contributions were assumed to be positive values, which is a correct approximation after signal filtering. By solving this equation the relative contributions of each particle type to the signals in the sensors could be found. The signal in the sensors originating from particle type λ is thus

equal to $\boldsymbol{\delta}_\lambda^* \mathbf{B}_{\mathrm{MRXref}_\lambda}(t_{\mathrm{window}})$.

The found relative contributions are then used to reconstruct the spatial distribution of each particle type (see Fig. 3.17). Now, only the difference of the MRX signal between the two time points t_1 and t_2 is considered, as the temporal information was already employed in Eq. (3.33). We then arrive at a forward model for each particle type λ, similar to Eq. (3.14):

$$\mathbf{B} = \mathbf{L}_\lambda \cdot \mathbf{c}_\lambda \qquad \lambda = 1, ..., \Lambda \tag{3.34}$$

For each particle type its particle distribution $\mathbf{c}_\lambda$ should be chosen such that the difference between the forward simulation $\mathbf{B}$ (using Eq. (3.34)) and the earlier found contribution of the particle type $\left(\boldsymbol{\delta}_\lambda^* \mathbf{B}_{\mathrm{MRXref}_\lambda}(t_{\mathrm{window}})\right)$ to the complete MRX signal $\mathbf{B}_{\mathrm{MRX}}(t_{\mathrm{window}})$ is minimized. The temporal information was reduced to the difference in amplitude between t_1 and t_2: $\boldsymbol{\delta}_\lambda^* B_{\mathrm{MRXref}_\lambda}$. This second sub-problem is again an inverse problem:

$$\mathbf{c}_\lambda^* = \arg\min_{\mathbf{c}_\lambda} \|\mathbf{B} - \boldsymbol{\delta}_\lambda^* B_{\mathrm{MRXref}_\lambda}\| \qquad \lambda = 1, ..., \Lambda \tag{3.35}$$

This problem can be solved with the techniques described earlier in Section 1.4.3. Similar as for Eq. (3.33), NNLS is employed (Eq (1.26)), because the considered phantoms have small and spatially fast varying sources instead of larger distributed sources [270]. Figure 3.17 shows an overview of the two presented methods for MRX imaging. The upper part depicts classical MRX imaging, i.e. one MNP type in a homogeneous environment, as explained in Section 3.1.4, while the lower part depicts multi-color MRX imaging in which multiple MNP types in a homogeneous environment are imaged as described in this section.

Note that the solution of an inverse problem depends on the ratio of the number of known values with respect to the unknowns (Section 1.4.3). If there are more unknowns than known values, the problem becomes underdetermined and multiple solutions are possible. In the other case only an approximation of the solution is possible. The associated forward model should be posed in such way as to have the largest amount of information available. In the first approach (Eq. (3.30)) there are (QS) known values and $\Lambda \times V$ unknowns. In the second approach, the total problem is split up in two sub-problems (Eqs. (3.32) and (3.34)), with $(QS) \times J$ and (QS) known values and $(QS) \times \Lambda$ and V unknowns respectively, that should be better stated than the initial problem.

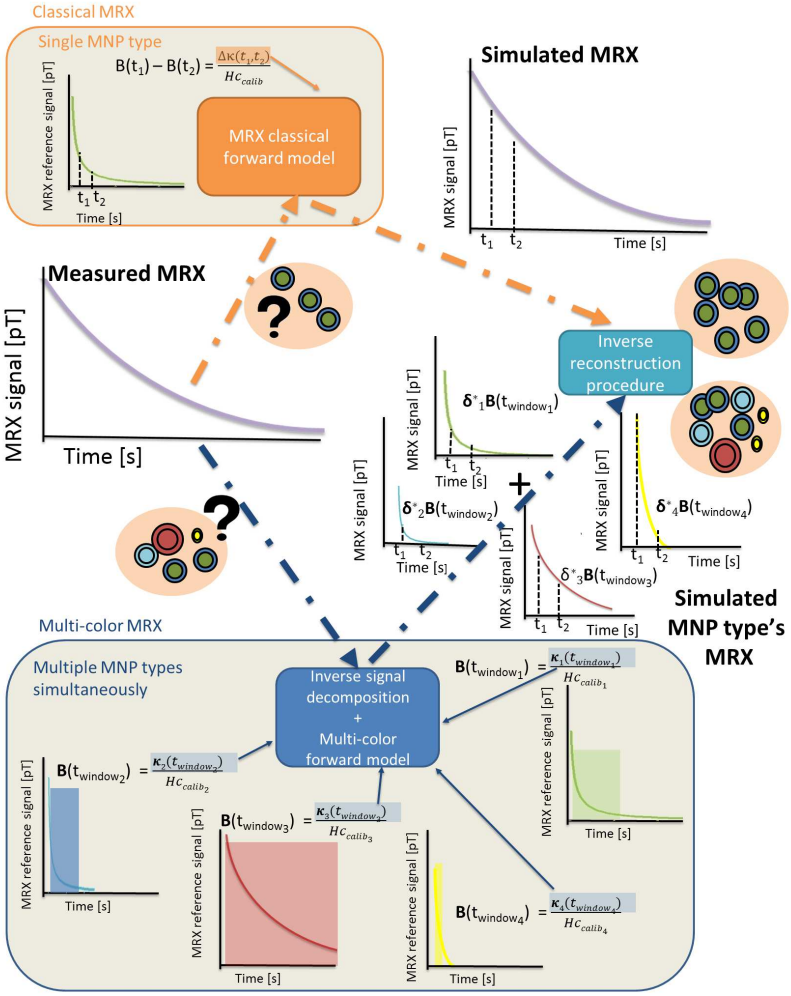

Figure 3.17: Overview of the presented methods. The upper part shows how a single MNP type distribution can be reconstructed using classical MRX imaging. Based on the reference curve of the MNP type a simulated MRX signal is generated with the classical forward model. The reconstructed MNP distribution is found with the inverse reconstruction procedure so that the differences between the simulated signal and measured MRX signal are minimal. The lower part depicts a reconstruction procedure for four MNP types. First, using the four measured MNP reference signals and their ideal time windows, the relative contribution ($\boldsymbol{\delta}_\lambda$) of each particle type to the measured MRX signal is determined. Then each particle type's component ($\boldsymbol{\delta}^*_\lambda \mathbf{B}_{\mathrm{MRXref}_\lambda}$) is simulated with the multi-color forward model and fed to the inverse reconstruction procedure. Remark that the main differences between the two techniques are situated in the use of multiple references, inclusion of temporal information for the signal decomposition and the use of multiple reconstructions in the multi-color approach.

Assessment of reconstruction quality

In this work various quantities are calculated to determine the reconstruction quality of the different phantoms. Besides the correlation coefficient (Eq. (1.27)), which has been used throughout this dissertation, two new quality parameters are employed.

The goal of this study is to investigate how well MRX is able to distinguish between the different types of particles. In a worst case scenario a wrong particle type is associated to a position. This evaluation is included in the spatial separation ratio (SSR) parameter. This parameter calculates the ratio of the reconstructed amount on the actual position of a particle type to the reconstructed amounts of other particle types on this position. Because there is only one particle type on each spatial position, this ratio should be as high as possible. This quantity was also used to asses the performance of MPI for separating different MNP types [221]. This parameter was added because it is not always clear from the reconstructed images whether other particle types are associated to the particle position. This happens when the reconstructed amount of the wrong particle type is significantly lower than that of the right reconstructed particle.

The final parameter is the relative deviation (RD) of the reconstructed total amount of MNP to the actual total MNP amount. All the reconstructed iron amounts for one particle type are added and the relative deviation with the actual amount of this particle type is calculated. Ideally, the reconstructed iron amount corresponds to the actual amount in the phantom for each particle type, which corresponds to a zero value for this parameter.

3.4.4 Experimental validation

We measured the MRX reference curves of the four particle types in their sample holders. In this case only one particle type is placed in the holder during each measurement. From Section 3.4.3 we know that this reference measurement is important, because it is used to determine the relative contributions of each particle type (Eq. (3.32)) and the resulting spatial distribution (Eq. (3.34)). Therefore, this measurement should be as accurate as possible. We used the MRX imaging setup to our benefit to improve the accuracy of the MRX reference curves, by employing the same activation procedure as was done with the phantoms (with total number of measurements equal to QS). Instead of a single reference (which is the common approach) from which $\boldsymbol{\kappa}_\lambda(t_{\text{window}})$ (Eq. (3.31)) can be obtained, now QS reference curves are fitted to $\boldsymbol{\kappa}_\lambda(t_{\text{window}})$. Based on these fitted values, an accurate MRX reference signal

can be simulated. Figure 3.18 shows the normalized simulated reference curves with corresponding shaded uncertainty band. The uncertainty bands show the standard deviation of the measured reference signals (after noise filtering) with respect to the simulated reference. As can be expected from Eqs. (1.4) and (1.5), particles in a similar fluid exhibiting a larger size show a slower MRX decay. By freeze-drying the F200 type (from a liquid environment to immobilized form) its decay time is also increased. Normalized curves were used to remove effects such as distances and amount of MNP, so we can focus on the shape of the MRX curve. Its shape is determined by magnetization dynamics and enables to differentiate between particle types. As can be seen from Fig. 3.18, large deviations exist between the simulated and measured references. This variability is a consequence of distortions and induced currents (ringing effects) in the sensor system after removing the magnetic fields. The F200 freeze-dried and F300 samples show a similar reference shape and also have interfering measurements which could make the separation very hard. The N500 sample also has some interferences with the F300 sample, but because of its different shape, the separation should still be feasible.

Note that MRX multi-color imaging is able to take dipolar effects into account that can occur in MNP accumulations in tissues or cells. This can be done by measuring the reference curves of the MNP for (a large) variation in MNP concentrations and considering these curves in the reconstruction procedure. Subsequently, the requirement of classical MRX (see Section 3.1.4), in which the reference should be measured for comparable MNP amounts as the experiment, is not necessary anymore. Also the effect of particle sedimentation, in which the local MNP concentration can significantly increase, can be taken into account in the experiment by measuring reference curves of a steady sample at different time points.

Figure 3.19a) shows the six MNP configurations under study. Three factors play an important role in the complexity of reconstructing multiple MNP types: the distance between the particle types, the number of particle types and the differences between the characteristic relaxometry signal of the particle types. Each phantom enables to investigate one or more of these aspects to show the possibilities and limitations of MRX for reconstructing multiple MNP types simultaneously. Phantom 1 has only two particle types with a large distance of 6 cm in between, which should make it the easiest phantom to reconstruct. Phantom 2 introduces 4 particle types instead of 2, which are still fairly wide (3.6 cm) apart. Due to the increased number of particle types, the first inverse problem (Eq. (3.33)) becomes harder to solve. Phantoms 3 and 4 have the complexity that the 4 particle types are only

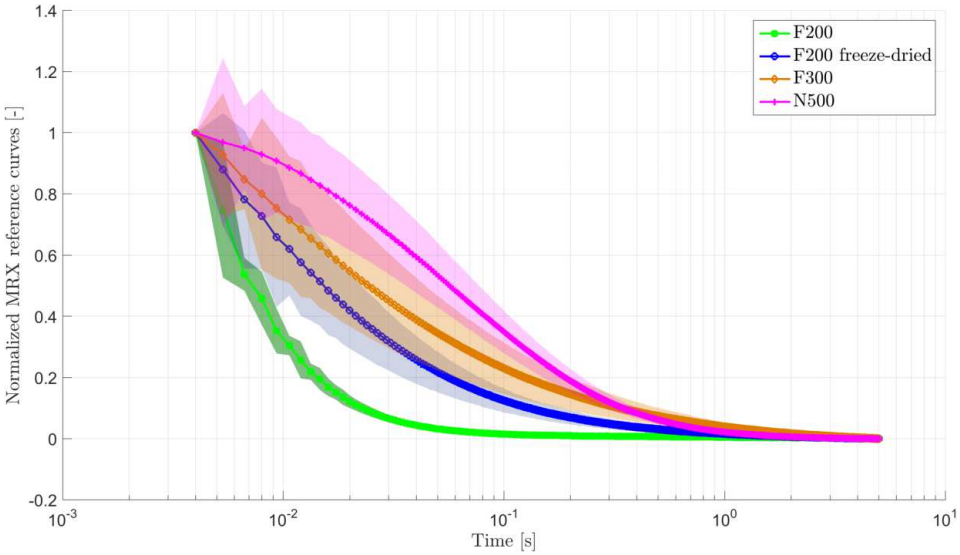

Figure 3.18: To increase the accuracy of the MRX reference curves (reduced ringing effects and distortions) reference signals were simulated based on a fit of $\boldsymbol{\kappa}_\lambda$ on QS measurements. The shaded uncertainty bands show the standard deviation of the measured reference curves with respect to the simulated reference. Especially the F200 freeze-dried and the F300 sample show overlap in their measurements, additionally they have a similar shape, making their separation very hard. The N500 sample also shows some interference with the F300 sample, but due to a different shape of the curve, the separation should be easier.

placed one voxel (1.2 cm) from each other, thereby increasing the difficulty of the second inverse problem. In phantom 3 the samples are arranged in such a way, that the most distinct reference curves are placed next to each other, while in phantom 4 similar reference curves are placed next to each other. This makes phantom 4 more complex to reconstruct than phantom 3. Because the samples are lined next to each other, the samples are measured by many different sensors. This should make the reconstructions of phantoms 3 and 4 easier than the reconstructions of phantoms 5 and 6 in which the samples are also separated by one voxel, but in this case the samples are also on a smaller area (3.6 cm $\times$ 3.6 cm). This means that in phantoms 5 and 6, there is less disconnected information from the sensors, and combined with a diameter size of about 36 mm for the magnetizing coils, it is hard to differentiate them. In phantom 5 only three particle types are measured, separated by a distance of one voxel (1.2 cm), while in phantom 6 four particle types are employed. Therefore, phantom 6 should be the most complex phantom to be reconstructed. A limitation of the considered phantoms is that the MNP types where physically separated and hence no mixture between MNP types

occurred. It is possible that due to particle interactions (clustering, dipolar interactions), the reference curves change. This could be solved by measuring mixtures of the MNP for varying amounts and use these reference curves in the reconstruction procedure. This way even clustering states of the MNP could be quantified.

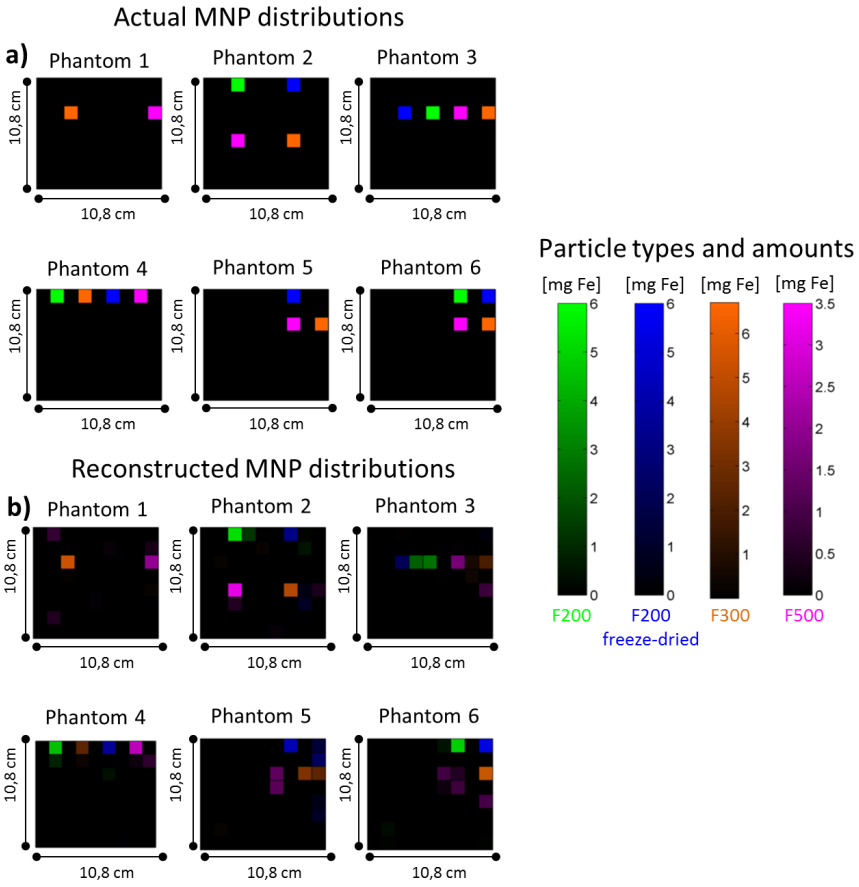

Figure 3.19: a) Actual MNP distribution of 6 phantoms with different spatial arrangements of multiple MNP types. b) Reconstructed MNP distributions of the 6 phantoms with the time windows from Table 3.5 following the theoretical procedure from Section 3.4.3.

The number of time points, J, plays a significant role in the first inverse problem (Eq. (3.33)), therefore the different phantoms from Fig. 3.19a) were reconstructed using different time windows. The time windows were selected based on reference properties (i.e. only the time points in which the reference

has a certain SNR or in which the amplitude difference between two reference curves is maximal are selected). Because the time window is chosen based on reference properties, this method can also be employed for various spatial particle distributions. MRX finds accurate MNP distributions for time windows starting from 4 ms after switching off the external magnetic field (the necessary time delay for recovery of the SQUID electronics). Especially for the F200 sample, a small time window ($<$ 20 ms) is required to avoid a deterioration of its reconstruction. The length of the time window increases for larger particle sizes up until $<$ 250 ms for the N500 particle. For all these time windows, the reconstructions were evaluated with the quality parameters defined in Section 3.4.3 and finally the time window that resulted in the best reconstructions for the considered particle type across the 6 phantoms was chosen (see Table 3.5).

Table 3.5: Chosen time windows for the reconstruction of the phantoms.

Particle name	t_{start} **[s]**	t_{end} **[s]**
F200	0.004	0.016
F200 freeze-dried	0.004	0.041
F300	0.004	0.061
N500	0.004	0.204

The chosen time windows all start directly after the necessary delay of 4 ms for the recovery of the SQUID electronics. It is thus important to start the measurement as early as possible, because the highest information content is in the earlier data points. A drawback of these points is the variability of the signal due to ringing effects after switching off the excitation field (see also Figure 3.18). The length of the time windows correlates with the typical decay time of the MRX reference curves. It should be noted that it is possible to achieve good reconstruction results for every phantom by adjusting the time window parameter. It was decided to have a fixed time window for each MNP type to present a fair comparison. The requirements for the time windows are very basic and in the future more advanced techniques should be considered which also depend on the shape of the reference curve. Furthermore, the same time window is now used for different particle type configurations (i.e. phantom 1 has only two particle types, phantom 5 has three particle types and the others have four particle types), as the properties (number of unknowns with respect to known values, eigenvalue distribution,...) of the matrix with the relative contributions (Eq. (3.32)), depend on the number of particle types, this could change the reconstruction results.

Figure 3.19b) shows the reconstructions of the phantoms and Table 3.6 lists their reconstruction quality parameters.Remark that these phantoms consist

of very small sources compared to the biologically more common distributed sources of several centimeters in the liver, spleen and lungs. This further increases the reconstruction complexity. It is especially apparent for phantoms 5 and 6 in which the combined challenge of point-sources and limited amount of useful information from the sensors deteriorate the reconstruction. Because of the fast relaxation of the F200 sample (Fig. 3.18), it was assumed that the MRX signal of this sample would be too low when the measurement started or it would be obscured by ringing effects. In reality, it is the easiest sample to separate because of its different shape of the reference curve compared to the other references. This way the range of possible samples for MRX imaging is further increased towards fast-relaxing samples. In some cases (phantoms 2 and 6), the RD on the total reconstructed amount is high for the F200 sample, which is due to broadening of the reconstruction and the small association to wrong particle types. Because this particle type has a fast relaxation, it is very likely that noisy behavior of other samples can be associated to this reference curve. However, with increased noise pre-processing this can be reduced.

In the case of only two particle types (phantom 1), the SSR shows a perfect distinction between the two particle types, a very good spatial agreement (CC of 91 and 99 %) and the respective reconstructed amounts show small RDs of 5 and 13%. Also when four particle types are considered, the spatial configuration is still very well reconstructed and MRX imaging is able to distinguish the four particle types. In some cases some amount is associated to the wrong particle type. In phantom 2 for example, the spatial quality parameters reflect a high spatial correspondence for the reconstructions (CC between 82 and 97 %), but a small fraction of other particle types are associated to the wrong particle type. However, the SSR is still 3 to 58 times higher compared to the wrongly reconstructed amounts, making the separation very successful. When the 4 particle types are lined up and placed closer together (phantoms 3 and 4), the types are still spatially very well reconstructed (CC between 74 and 99 % and SSR not lower than 3). The RDs on the total amount for these phantoms range between 6 and 39 %. Although phantom 4 is harder to reconstruct (similar particles next to each other) than phantom 3 it shows a better agreement to the actual distribution. This is due to the fact that some noisy channels were present directly above the samples of phantom 3. These were removed in the noise filtering, thus reducing useful sensor information. On the small areas present in phantoms 5 and 6 with 4 and 3 particle types respectively, SSR is still very good, but the spatial reconstruction starts to deteriorate: the CC varies between 23 and 99 % and also the RD on the reconstructed amounts is very high, ranging between 10 and 56 %. If the same spatial configuration would be considered for only 1 identical particle type, this would also be a difficult reconstruction. In phantom 5, a small amount of

the F300 is reconstructed on the position of F200 freeze-dried particle (SSR of 5). The other samples are perfectly distinguishable. In phantom 6, the spatial separation deteriorates a little bit (SSR from 1 to 11), because of the combined difficulty of the small area and 4 particle types instead of 3 and the modified properties of the matrix with the relative contributions of each reference.

Generally, MRX imaging allows to distinguish very well between the various particle types, both spatially as well as quantitatively. This is also supported by the reconstruction quality parameters in Table 3.6. Accurate reconstruction results can be obtained for multiple phantoms by using time windows that correlate to the signal length of the references in the reconstruction procedure. It is expected that the reconstructions can be further improved by optimizing the time windows and by employing imaging techniques such as adaptive targeting (Section 3.2), random activation of the coils [264], sensitivity targeting [272] or quantitative model selection (Section 3.3). Furthermore, advanced selection criteria should be used for determining the ideal time window. Possible examples are time windows depending on the shape of the reference curves, the number of employed particle types and their references, and the associated stability of the inverse problem (Eq. (3.32)). As this section is only a proof of concept showing that MRX has the ability to distinguish between multiple particle types simultaneously, we do not to go into detail on these techniques.

3.4.5 Conclusion

Although MRX imaging allows the reconstruction of a broad range of MNP types, little research has been done on imaging different MNP types simultaneously and separating them. Biomedical applications can benefit significantly from a measurement technique that allows the localization of different MNP types. In this section a theoretical procedure and experimental validation was presented to show the feasibility of MRX imaging in reconstructing multiple MNP types simultaneously. Because each particle type has its own characteristic MRX signal, it is possible to take this *a priori* information into account while solving the inverse problem. This way each particle type's signal can be separated and its spatial distribution reconstructed. By assigning a unique color code and intensity to each particle type's signal, an image can be obtained in which each spatial distribution is depicted in the resulting color and with the intensity a measure for the amount of particles of that type, hence the name multi-color MNP imaging.

Table 3.6: Reconstruction quality parameters for each phantom.

Phantom 1	**CC [-]**	**SSR [-]**				**RD [-]**
		F200	F200 freeze-dried	F300	N500	
F300	99%	-	-	-	∞	5%
N500	91%	-	-	∞	-	13%
Phantom 2	**CC [-]**	**SSR [-]**				**RD [-]**
		F200	F200 freeze-dried	F300	N500	
F200	87%	-	∞	∞	∞	50%
F200 freeze-dried	82%	3	-	5	∞	21%
F300	97%	3	3	-	∞	8%
N500	97%	58	∞	∞	-	51%
Phantom 3	**CC [-]**	**SSR [-]**				**RD [-]**
		F200	F200 freeze-dried	F300	N500	
F200	74%	-	17	∞	∞	23%
F200 freeze-dried	82%	∞	-	5	28	15%
F300	90%	∞	15	-	∞	39%
N500	88%	∞	∞	∞	-	6%
Phantom 4	**CC [-]**	**SSR [-]**				**RD [-]**
		F200	F200 freeze-dried	F300	N500	
F200	96%	-	102	∞	∞	26%
F200 freeze-dried	99%	6	-	3	∞	28%
F300	87%	∞	∞	-	117	26%
N500	94%	∞	∞	∞	-	31%
Phantom 5	**CC [-]**	**SSR [-]**				**RD [-]**
		F200	F200 freeze-dried	F300	N500	
F200 freeze-dried	84%	-	-	5	∞	58%
F300	55%	-	∞	-	∞	26%
N500	23%	-	∞	∞	-	21%
Phantom 6	**CC [-]**	**SSR [-]**				**RD [-]**
		F200	F200 freeze-dried	F300	N500	
F200	71%	-	8	∞	∞	65%
F200 freeze-dried	99%	2	-	11	∞	10%
F300	99%	1	∞	-	∞	11%
N500	26%	∞	∞	∞	-	31%

The theoretical procedure is validated by reconstructing 6 phantoms, with different spatial arrangements of multiple MNP types, using MRX imaging. It is observed that MRX imaging distinguishes between two particle types with similar reference curves and up to four particle types can easily be separated. Problems between discriminating particles do, however, arise when more than 3 particle types are present in a small area (3.6 cm $\times$ 3.6 cm), because of the combination of magnetizing coils with a diameter of 36 mm and the reduced independent information from the sensors. This could be improved

by using more closely spaced magnetometers, smaller coils and MRX imaging techniques such as adaptive targeting (Section 3.2), random activation of the coils [264], sensitivity targeting [272] or quantitative model selection (Section 3.3). These techniques could increase the attainable reconstruction quality of the reconstruction.

For the applications envisioned with this setup i.e. imaging the distribution of MNP in the liver, lungs and spleen, for investigating the MNP biodistribution, the phantoms represent a worst case scenario, as MNP tend to be rather homogeneously distributed in these larger tissues, while the phantoms represent point-sources. Distributed sources are easier to reconstruct using MRX, due to the broadening of sources inherent to the used technique. If the particles would be more distributed, possible better reconstructions could be obtained in smaller areas. A further increase in reconstruction quality is expected when more advanced models are employed to select the ideal time window based on i.e. the shape of the reference curves, the number of employed particle types and their references, and the associated stability of the inverse problem. Moreover, the effects of reference variability and how to incorporate this in the forward model should be investigated.

4

Conclusions and outlook

At the beginning of this chapter the main conclusions of this PhD are discussed (Section 4.1). This section considers the conclusions from the EPR and MRX part separately. Next, a more general conclusion of this dissertation is given. There, among others, it is shown that the non-invasive methods, developed in this dissertation, have in common that they induce various and independent responses from the MNP. This way, they stabilize the inverse problem and improve the accuracy of the reconstruction results. This general conclusion is further investigated in a preliminary study, in which the distinct EPR and MRX sensor data is combined, and the potential advantages of their fusion are investigated (Section 4.2). This chapter ends with the description of possible future work based on the conclusions from this dissertation and the preliminary study, and contributes some general ideas that could be of benefit to the MNP imaging community (Section 4.3).

4.1. Conclusions

In this dissertation, non-invasive spatial reconstruction methods were developed for the imaging of magnetic nanoparticle distributions. These methods fulfill the need of various MNP-based applications, such as magnetic targeting

and hyperthermia, that require knowledge on the spatial MNP distribution in order to operate safely and efficiently.

In chapter 1, the general framework in which this research is situated was sketched. It provided a general introduction to magnetic nanoparticles with an emphasis on their magnetic behavior and biomedical properties. Additionally, it showed how this typical behavior is useful in biomedical applications such as disease detection, magnetic targeting, magnetic hyperthermia and in enhancing the contrast of anatomic images. On the other hand, this chapter clearly expressed the need for a non-invasive quantitative MNP imaging technique, as the clinical implementation of aforementioned applications was hindered, among others, by an inaccurate knowledge of the particle biodistribution. A distinction was made between clinically established imaging methods and recent imaging methods specifically developed for the spatial reconstruction of magnetic nanoparticles. The more 'traditional' imaging techniques only allow a qualitative picture of the particle distribution, while the particle imaging techniques can quantitatively measure the particles through magnetic field measurements. Nevertheless, their reconstructions suffer from artifacts and inaccuracies, which originate from measurement noise, the ill-posedness of the inverse problem or from incorrect assumptions and errors in the forward model. Therefore, the main objective of this work is to improve the forward modeling, inverse problem solving and measurement techniques of two promising MNP imaging techniques, namely electron paramagnetic resonance (EPR) and magnetorelaxometry imaging (MRX).

4.1.1 Electron paramagnetic resonance imaging

Chapter 2 of this dissertation started with a general introduction to EPR and provided an overview of its main biomedical applications (Section 2.1). It made clear that current state-of-the-art setups lack the sensitivity to measure the particle biodistribution non-invasively, or could only provide the total number of particles in a sample, without information on its distribution. Therefore, in the next sections of this chapter, research was focused on developing an EPR imaging model and measurement procedure which allows to accurately reconstruct the spatial MNP distribution.

In Section 2.2 adaptions of the measurement procedure and forward model were investigated in order to obtain independent measurement data that could be used for finding the spatial MNP distribution in the sample. A forward model was developed based on the fact that the sample's response changed depending on its position with respect to the coils. This behavior can

be included in the forward model by measuring the response of a well-known MNP amount on various positions. The model assumes that the response varies linearly with the amount of MNP and was hence used to estimate the particle distribution. The measurement procedure was extended from a single measurement on one position to moving the sample along a line, in which for each new position a measurement was made. By minimizing the differences between the forward model solution and the obtained measurements using truncated singular value decomposition, the 1D distribution could be recovered for various MNP samples having a length of 16 mm with resolutions estimated to be between 1 mm to 5 mm.

Following this proof of concept, a sensitivity analysis was performed to investigate the strengths and weaknesses of the model (Section 2.3). This analysis included the development of error models, which allowed to simulate their impact on the MNP reconstruction. More specifically, measurement and positioning errors were considered. Additionally, setup parameters were investigated, such as the requirements on the response function's shape and on the stability of the sensitivity matrix in order to achieve accurate reconstructions. The analysis was performed for various particle distributions including constant, gradient and spatially varying distributions. The analysis revealed that the forward model showed the largest sensitivity towards positioning errors of the sample, that the response function should preferably have a constant slope and that the setup is not suitable for constant distributions, but has a high reconstruction accuracy for spatially varying distributions. The inverse solution procedure was extended from singular value decomposition to non-negative least squares as the first approach resulted in non-physical negative particle amounts. Their comparison learned that SVD showed broadening of particle spots, although the mean value of these spots corresponded to the actual particle amount, while NNLS accurately retrieved the spot's location, albeit with errors in its particle amount. Therefore, a combination of both solvers was suggested to combine their strengths and to overcome their weaknesses. This way, improved reconstructions could be obtained for distributions containing various spots of particles.

The forward model was furthermore extended to enable the reconstruction of 2D and 3D distributions (Section 2.4). Based on coarse experimental measurements of the response function it was shown that the response function had a symmetric component. This addition of linearly dependent information in the inverse problem had the effect that the inverse problem had a reduced stability for larger volumes ($>$ 200 voxels) and hence resulted in a decreased reconstruction quality. By removing this symmetric component, improved reconstructions can be obtained. Additionally, the inverse problem was

further stabilized by gradually inserting the sample to the sides of the setup so that only a well-defined part of the sample was activated. This principle was further exploited in Section 2.5, in which the Helmholtz coil pair in the setup was replaced by a coil array. This allows to speed up the measurements, while maintaining an increase in reconstruction accuracy.

4.1.2 Magnetorelaxometry imaging

Chapter 3 begins with a general introduction to MRX in which its measurement procedure, common decay and imaging models and its main biomedical applications are described (Section 3.1). The other sections review the performed research. This work is focused on MRX imaging setups using a coil array for the generation of spatially varying magnetic fields, since previous studies have shown their potential for improving MNP reconstructions. The performed research was specifically aimed at analyzing following three topics that are key in bringing MRX imaging closer to clinical practice: 1) how to activate the coils to obtain improved MNP reconstructions, 2) definition of a quantitative measure for comparison of different MRX forward models and imaging setups, and 3) development of a forward model to enable the distinct reconstruction of multiple particle types simultaneously.

The first topic was investigated in Section 3.2. It introduced a specific way to activate the coils based on *a priori* information on the particle distribution. In this approach the currents in the coils are adapted to specifically target voxels or sub-regions of the sample where particles are assumed to be present. This is achieved by assigning a larger spatial sensitivity to these regions compared to the regions in which no particles are assumed. Then the target currents for achieving the desired spatial sensitivity are calculated and employed in the next MRX measurement. The obtained reconstruction can then again be used as input for the targeting procedure. This procedure was iteratively repeated until no significant changes were observed in the obtained reconstructions. Results showed that it is possible to significantly improve the accuracy of the obtained particle distributions. This was especially apparent for regions that typically show a reduced reconstruction accuracy, i.e. regions further away from the sensors.

The second topic was realized in Section 3.3, which introduced quantitative MRX models. They resolve the lack of a quantitative measure. Such a measure compares the various MRX imaging setups and models to determine the optimal configuration for reconstructing the particle amount in a given voxel. Existing measures in MRX either did not allow a quantitative, voxel-based,

comparison or required the use of significant simulation time. Therefore, the use of statistical parameters in MRX imaging was introduced. By employing the sensitivity matrices as input to statistical measures, the MRX imaging models and setups can be quantitatively compared in a very fast fashion. These models are referred to as *quantitative* MRX models. As an example of the capabilities of this approach, the magnetizing coils of a given MRX imaging setup were considered as separate MRX imaging models. Based on the quantitative information associated to each coil model, the different models were combined into a larger sensitivity matrix according to a voxel-based weighting that takes the relative performances of the models into account. Compared to the case in which no weighting was used, a significant increase in reconstruction accuracy was obtained. Another advantage of the presented approach is that the quantitative information associated to each model can also be used *directly*. As such, a subset of coils was determined which realized small improvements in reconstructions, while significantly reducing measurement time. Additionally, based on the quantitative model's information content, it was possible to determine the optimal voxel size ($\approx$ 5 - 15 mm) for the given setup.

In Section 3.4, the third topic of investigation was pursued. In this section a MRX imaging model was developed that allowed to separately localize and quantify various particle types. In the final image a unique color code was associated to each particle type and its intensity determined the amount of particles for each given particle type. This model was referred to as the *MRX multi-color imaging model*, based on the name of its counterpart in MPI. The multi-color imaging could be realized by solving two inverse problems instead of one general inverse imaging problem. The first inverse problem determined the relative contributions of each particle type in the measurement data by using *a priori* information on the particle's relaxometry signal. After obtaining their relative contributions, they serve as input to a second inverse problem, which corresponds to the inverse problem of the original MRX imaging model. The second problem is solved for each particle type separately and encompasses the reconstruction of the spatial MNP distribution of the given particle type. Using this approach, up to 4 particle types could be easily separated in a 10 cm $\times$ 10 cm sample. Difficulties in the separation occurred however when the different particle types were concentrated on a smaller area. This is although more related to imaging setup parameters than to the imaging model.

4.1.3 General conclusion

The techniques developed during this PhD contribute to the biomedical field of MNP imaging in general. We were able to progress EPR from a sensitive MNP detection technique to a quantitative MNP imaging technique for the reconstruction of 3D MNP distributions. This was achieved by developing forward models with associated measurement protocols and inverse reconstruction procedures. Similarly, the MRX imaging technique was brought closer to clinical practice by allowing the localization and quantification of multiple particle types simultaneously and by realizing an adaptive measurement procedure that significantly improved MNP reconstructions. Furthermore, a quantitative measure was developed for MRX imaging in which statistical parameters were used to find the optimal forward model and setup configuration. This quantitative measure can also be useful in the general improvement of MNP imaging techniques employing a forward model.

Previously mentioned advancements resulted in a higher accuracy on the obtained spatial particle distributions. Therefore, MNP-based applications such as magnetic hyperthermia, disease detection and magnetic targeting could in turn benefit from these results so that an improved efficiency and patient safety is achieved.

The techniques presented in this work have in common that a variety of responses, originating from the MNP, are induced. This is realized for example by moving the sample and by exposing it to spatially varying magnetic fields. Moreover, the responses containing independent information about the particles' location and/or having a high signal content are selected for use in the inverse reconstruction procedure. In this dissertation this was achieved by making use of quantitative MRX models, the adaptive activation of the coils, or by performing in-depth sensitivity and stability analyses. One of the main conclusions of this work is that inducing the *right* responses of the particles (i.e. having enough variety and containing independent information and a large signal content) allows to stabilize the inverse solution and to improve MNP reconstructions. Additionally, this approach has the potential to be applied to other MNP imaging techniques such as MPI and ASI (Section 1.3.3). In Section 4.2 this concept is further investigated in a preliminary study in which the possible advantages of combining the distinct sensor data from EPR and MRX are analyzed. Among other things, Section 4.3 further elaborates on this topic and explains how, in future work, the MNP imaging community in general could benefit from this approach.

4.2. Preliminary study: combined EPR-MRX setup

4.2.1 Introduction

In this section a combination of EPR and MRX is presented and possible advantages of their fusion, such as improved reconstructions of the MNP distributions and increased stability of the inverse problem, are investigated. To date, many measurement procedures and forward models are under investigation with the aim to stabilize the inverse problem and to increase the reconstruction quality of the MNP distributions [37, 39, 272, 311, 349, 351]. As both EPR and MRX result in distinct measurements (resonant magnetic signal, decaying magnetic signal), it can be assumed that the forward models generate distinct information about the MNP sample under study. By combining both models, independent information can be added to subsequently increase the stability of the inverse problem. This results in improved noise robustness, enhanced MNP reconstructions, shorter measurement procedures and allows for the imaging of higher number of unknowns (i.e. larger volumes or finer resolutions).

The goal of this preliminary study is to investigate how above mentioned modalities (each of them characterized by an ill-posed inverse problem) need to be combined to improve the reconstruction of MNP distributions. The performance of both measurement techniques is first numerically compared on various MNP phantoms for different noise levels (3400 simulated configurations). Stability and sensitivity parameters are calculated next to investigating the reconstruction quality of the MNP distribution. Subsequently, the effect of various combinations of both modalities is explored to take advantage of the respective strengths of EPR and MRX so to ultimately increase the overall imaging performance. It is found that the combination of EPR and MRX, further referred to as EPR-MRX, results in an increase in MNP reconstruction quality, stability of the inverse problem, performance and a tremendous reduction of measurement time. These advantages offer promising opportunities for MNP visualization in clinical practice.

Section 4.2.2 discusses a possible implementation of the suggested EPR-MRX setup and describes the employed phantoms. Section 4.2.3 starts with a summary of the respective forward models of EPR and MRX and then explains how they can be combined. In Section 4.2.4 a comparison is performed between EPR and MRX with respect to the stability of their inverse problem, and their spatial and noise sensitivity. This way, their respective strengths and weaknesses are determined for the given setup. Finally, both modalities are combined in various ways and the previous analysis is repeated to investigate

if the combination of EPR and MRX is advantageous. This work was published in Ref. [355].

4.2.2 EPR-MRX imaging setup and phantoms

The considered virtual EPR-MRX imaging setup is based on an existing MRX imaging setup (Section 3.3.2) and EPR imaging setup (Section 2.5) in order to perform realistic simulations. The external magnetic field is generated by 16 magnetizing coils ($Q = 16$), each having a diameter of approximately 1 cm and 9 winding turns. The coils are used for generating the magnetizing field both for EPR and MRX. Next, the setup consists of an excitation and pickup coil which are used in the EPR measurements only, for generating the RF wave and for measuring the resonance signal respectively. The excitation and pickup coils, together with the sample, are positioned between 2 groups of 8 magnetizing coils (Section 2.5). The sample is moved through the excitation and pickup coils for the EPR measurements. Additionally, 304 SQUID magnetometers are employed for registering the MRX signal ($S = 304$). They are placed according to the 304 low-T_c SQUID magnetometers sensor setup in the PTB in Berlin [325]. A detailed description of the sensor configuration can be found in Section 3.3.2. Figure 4.1a) shows the complete EPR-MRX imaging setup. Only a limited number of SQUID sensors are shown (not to scale) because the diameter of the complete magnetic measurement system is significantly larger than the employed sample sizes.

A cylindrical tube consisting of different compartments allows the placement of various MNP amounts in each holder. In this proof of concept 5 cylindrical phantoms, each with different MNP concentration distributions, are numerically generated with the use of fractional Brownian motion [313]. See Fig. 4.1b) for an example. The fractional Brownian motion was also employed in creating the MNP distributions in the MRX adaptive targeting procedure (Section 3.2.2) and the EPR coil array (Section 2.5.3) sections. This way, clustered areas of MNP can be produced corresponding to e.g. MNP injection sites in magnetic hyperthermia (Section 1.2.3). These phantoms were calculated for increasing tube lengths from 2 to 68 mm and a fixed diameter of 8 mm to investigate the stability of the considered techniques for increasing numbers of unknowns. Although the sample sizes are rather small, many unknowns (order of 1000 voxels) are generated due to the fine resolution of 1 mm $\times$ 1 mm $\times$ 10° employed. The MNP amounts that we consider in our study, vary between 0 and 10 mg Fe for each voxel. One of the phantoms, indicated by phantom 5 (see Section 4.2.4), is considered the most demanding to reconstruct, as it only has small MNP amount differences between neighboring voxels and the MNP amounts vary only between 7 and

10 mg of Fe.

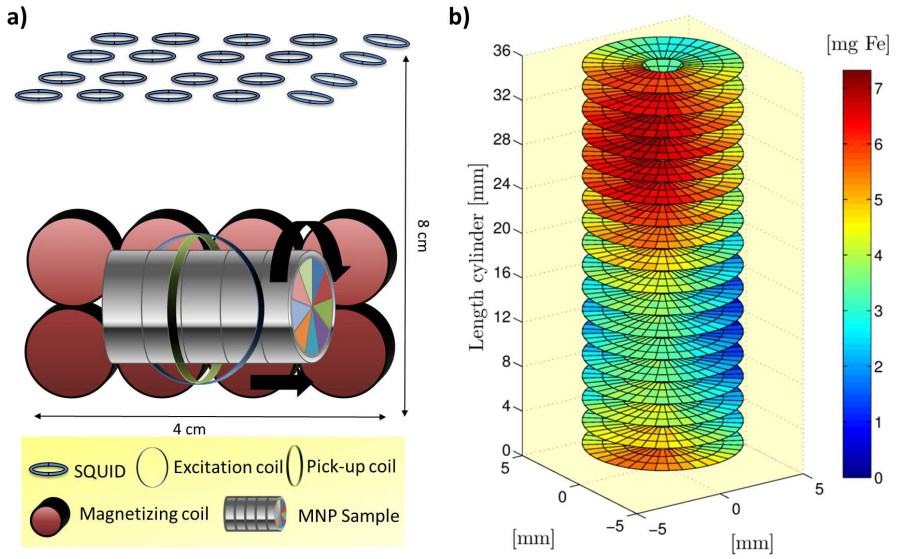

Figure 4.1: a) Overview of the EPR-MRX imaging setup. 16 magnetizing coils generate the magnetic field (only 8 are visualized for clarity reasons), an excitation coil produces the radio frequency wave, a pickup coil measures the resonance signal and SQUID sensors register the relaxometry signal. Cylindrical MNP sample holders are used. Only few SQUID sensors are depicted for clarity purposes. b) Example of a cylindrical MNP phantom with a length of 36 mm.

4.2.3 EPR-MRX imaging model

In this section the forward models of EPR and MRX are recalled and it is demonstrated how both models can be merged together. Remember that in total NQ EPR measurements are performed which originate from a measurement for each position of the sample, with in total N positions of the MNP sample through rotation and translation of the sample. This is performed for Q spatially varying magnetic fields resulting from the coil array (Section 2.5.2). These EPR measurements can be simulated using a forward model:

$$\mathbf{S}_{\mathrm{f_{EPR}}} = \mathbf{L}_{\mathrm{EPR}} \cdot \mathbf{c} \tag{4.1}$$

This is the same expression as derived earlier (Eq. (2.18)), although now explicitly the subscript EPR is used to distinct this forward model from the forward model derived for MRX imaging. We briefly repeat that $\mathbf{c}$ contains

the MNP amount in each voxel v ($v = 1, ..., V$) of the sample. $\mathbf{L}_{\mathrm{EPR}}$ is a $NQ \times V$ matrix with sensitivity constants, embedding the link between the MNP distribution and the measurements in the pickup coil. In practice, the elements in $\mathbf{L}_{\mathrm{EPR}}$ are obtained by calculating the corresponding response values for the position of each voxel in each measurement and the magnetic field at this voxel. The approach is detailed in Sections 2.4 and 2.5. As can be observed from Eq. (4.1), the response values need to be known very accurately. In Section 2.3, it was investigated how errors in the response function affect the image quality.

A forward model similar to Eq. (4.1) can be obtained for the MRX modality:

$$\mathbf{S}_{\mathrm{f}_{\mathrm{MRX}}} = \mathbf{L}_{\mathrm{MRX}} \cdot \mathbf{c} \tag{4.2}$$

This expression again corresponds to the forward model derived earlier for MRX (Eq. (3.14)) with $N_a = Q$. Hence, $\mathbf{L}_{\mathrm{MRX}}$ has dimensions $SQ \times V$ and is again a sensitivity matrix, $\mathbf{S}_{\mathrm{f}_{\mathrm{MRX}}}$ is a vector of SQ elements representing the amplitude decrease in the S sensors for Q spatially varying magnetic fields generated by the sequential activation of the Q coils and for the MNP distribution in the V voxels, $\mathbf{c}$.

The measurement techniques EPR and MRX can then be merged into EPR-MRX with their respective sensitivity matrices $\mathbf{L}_{\mathrm{EPR}}$ and $\mathbf{L}_{\mathrm{MRX}}$ (Eqs. (4.1 and 4.2)) joint into $\mathbf{L}_{\mathrm{EPR-MRX}}$. This yields following forward model for EPR-MRX imaging:

$$\mathbf{S}_{\mathrm{f}_{\mathrm{EPR-MRX}}} = \begin{bmatrix} \mathbf{L}_{\mathrm{EPR}} \\ \mathbf{L}_{\mathrm{MRX}} \end{bmatrix} \cdot \mathbf{c} = \mathbf{L}_{\mathrm{EPR-MRX}} \cdot \mathbf{c} \tag{4.3}$$

Fusing two complementary techniques, could stabilize the associated inverse problem and subsequently improve the MNP reconstruction quality.

The increased stability may hold another advantage; the measurement time of both techniques can be significantly reduced by minimizing the number of spatially varying magnetic fields and/or the number of displacements of the sample (in EPR). Next to minimal sample movement and number of spatially varying magnetic fields, it is also possible to halve the measurement time by alternating the employed technique for each spatial field. For example in the case of a magnetizing coil array in which each coil is sequentially activated, MRX is employed after activation of coil 1, EPR is performed during activation of coil 2 and then MRX is again employed for coil 3. This alternation between both techniques continues until all coils have been activated once. We refer to this as EPR-MRX alternation. Together with minimal sample movement these can reduce the measurement time. See Fig. 4.2 for a visual

explanation of the EPR-MRX alternation technique.

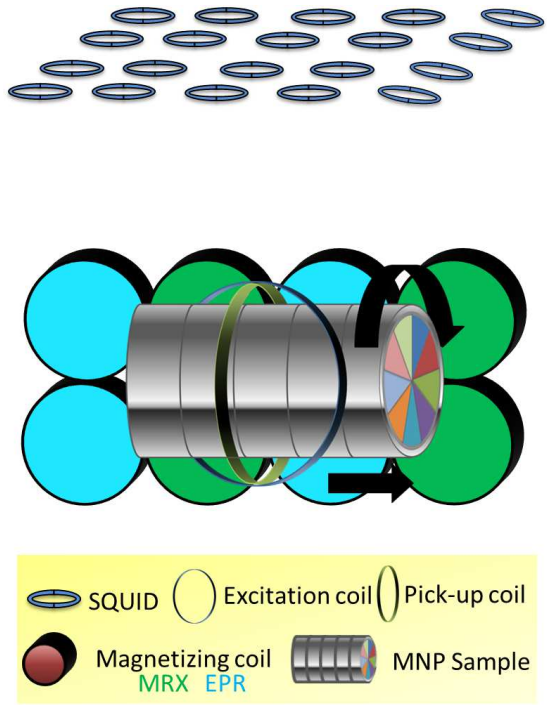

Figure 4.2: Principle of EPR-MRX alternation. Each coil is separately activated and then EPR (coils depicted in blue) or MRX (coils visualized in green) is used for acquiring sample information.

Recovery of the MNP distribution can be achieved by solving an inverse problem, as was done throughout this dissertation:

$$\mathbf{c}^*_{\text{type}} = \arg\min_{\mathbf{c}} \|(\mathbf{L}_{\text{type}} \cdot \mathbf{c}) - \mathbf{S}_{\text{m}_{\text{type}}}\| \tag{4.4}$$

with type referring to the employed technique i.e. EPR, MRX or EPR-MRX. The respective forward models can be found in Eqs. (4.1),(4.2) and (4.3) and the respective measurements are represented as $\mathbf{S}_{\text{m}_{\text{EPR}}}$, $\mathbf{S}_{\text{m}_{\text{MRX}}}$ and $\mathbf{S}_{\text{m}_{\text{EPR-MRX}}}$. The dimensionality of the sensitivity matrix $\mathbf{L}_{\text{type}}$ determines the type of the inverse problem (Section 1.4.3). In this section truncated SVD (Eq. (1.23)) is employed to solve the inverse problem.

4.2.4 Numerical validation

Different quality parameters (see Section 1.4.4) are calculated to allow a thorough comparison between EPR and MRX on different aspects such as SNR, independent information in the signal, etc. A total of 3400 configurations are simulated (i.e. 40 different noise levels, 17 phantom lengths and 5 MNP distributions). The stability of the sensitivity matrix $\mathbf{L}_{\text{type}}$ is investigated by inspecting the eigenvalues of the sensitivity matrix. The rate of decrease in amplitude of the eigenvalues is captured in the condition number β (Eq. (1.28). A relatively slow decrease corresponds to a high stability of the matrix. β should be as low as possible. The quality of the MNP reconstructions can be assessed using the correlation coefficient (CC) Eq. (1.27). Furthermore, the spatial sensitivity parameter $\mathbf{S}_{\text{p}}$ (Eq. (3.17)) is employed, which is a measure for the impact of a voxel on the measurements.

Comparison between EPR and MRX imaging

The benefits and drawbacks of both techniques are investigated by inspecting their sensitivity matrix properties and the reconstruction quality of the five MNP phantoms. Figure 4.3a) depicts the normalized eigenvalue distribution for both methods for increasing lengths of the phantom cylinder. The eigenvalues are sorted following decreasing amplitude. MRX shows a slightly reduced stability in the solving of the ill-posed inverse problem and is more sensitive to increasing the number of unknowns compared to EPR. This can also be observed when inspecting the condition number values (β) in the inset of Fig. 4.3a). One could conclude that MRX is less stable than EPR, however some side remarks need to be taken into account. EPR requires significantly more measurements (6 to 10 times the amount of MRX measurements) for the same number of unknowns (see Fig. 4.3b)). This is because the sample needs to be moved for each spatial magnetic field configuration, making the technique considerably more time-consuming than MRX, where the sample is not moved. The inset of Fig. 4.3b) additionally shows that MRX requires significantly less measurements for a similar β (i.e. for a β of $\approx$ 230, EPR requires 4.5 times more measurements compared to MRX). Another fact that is negatively influencing the MRX stability is the considered fine resolution of 1 mm $\times$ 1 mm $\times$ 10°. This type of MRX setup is more suited for resolutions in the range of 1 cm^3 (See Section 3.3.5). If a larger resolution is employed, the stability of the sensitivity matrix is improved because sufficient independent information can be added. The stability of MRX for the considered setup could be further improved by using smaller magnetization coils, more closely spaced magnetometers, cruder reconstruction resolution, extra magnetization coils above and below the sample or advanced MRX imaging techniques that

adapt the sensitivity of the matrix [272] or transform the sensitivity matrix (Section 3.3). The measurements with EPR can be made faster by reducing the number of movements or using multiple pickup coils for measuring the EPR signal.

Figure 4.4 shows reconstructions of a cylindrical phantom with a diameter of 8 mm and a length of 4 mm consisting of 576 voxels, for the case when white Gaussian noise is added to the sensor data. For each SNR level (from 0 to 40 dB), 50 reconstructions are carried out and the mean and standard deviations of the CC are calculated. MRX depicts a slightly worse reconstruction compared to EPR, especially for lower SNRs (0 - 10 dB), where it is observed that the reconstruction quality of MRX deteriorates faster than EPR due to the lower stability of the sensitivity matrix.

Figure 4.5a) and b) show the mean CC of 50 reconstructions in the case of a SNR of 20 dB, for the five phantoms with increasing lengths, when using MRX and EPR respectively. Strikingly, different relative performances can be seen regarding some phantoms for each technique. This is related to the spatial distribution of the MNP within the phantom and suggests that in some cases both techniques are sensitive to other aspects of the phantom.

This is further supported by the normalized spatial sensitivity profiles of EPR and MRX that show the sensitivity of the modalities to a certain voxel of the volume. In Fig. 4.6 part of the sensitivity profile is shown for the 4 middle coils for MRX (left) and EPR (right). In MRX, voxels that are close to an activation coil and close to the sensors (above) are easily registered. Therefore, voxels in the middle and central layers of the sample have a lower spatial sensitivity in the MRX setup compared to EPR, because they are less activated by the coils and further away from the sensors. Indeed, in EPR, the particles in the middle layers have the best resonance condition towards the pickup coil and have thus the highest sensitivity, while the voxels on the edge and central layers have a slightly lower sensitivity. There is additionally a translational and rotational symmetry of the volume, because of the movement of the sample. One should note that when the sample would be moved in MRX a similar sensitivity would occur. Based on these results we can conclude that EPR and MRX offer distinct information about the MNP sample under study and especially with respect to their sensitivity to the spatial distribution of the MNP. Therefore, combining them might offer interesting possibilities that can improve MNP reconstructions.

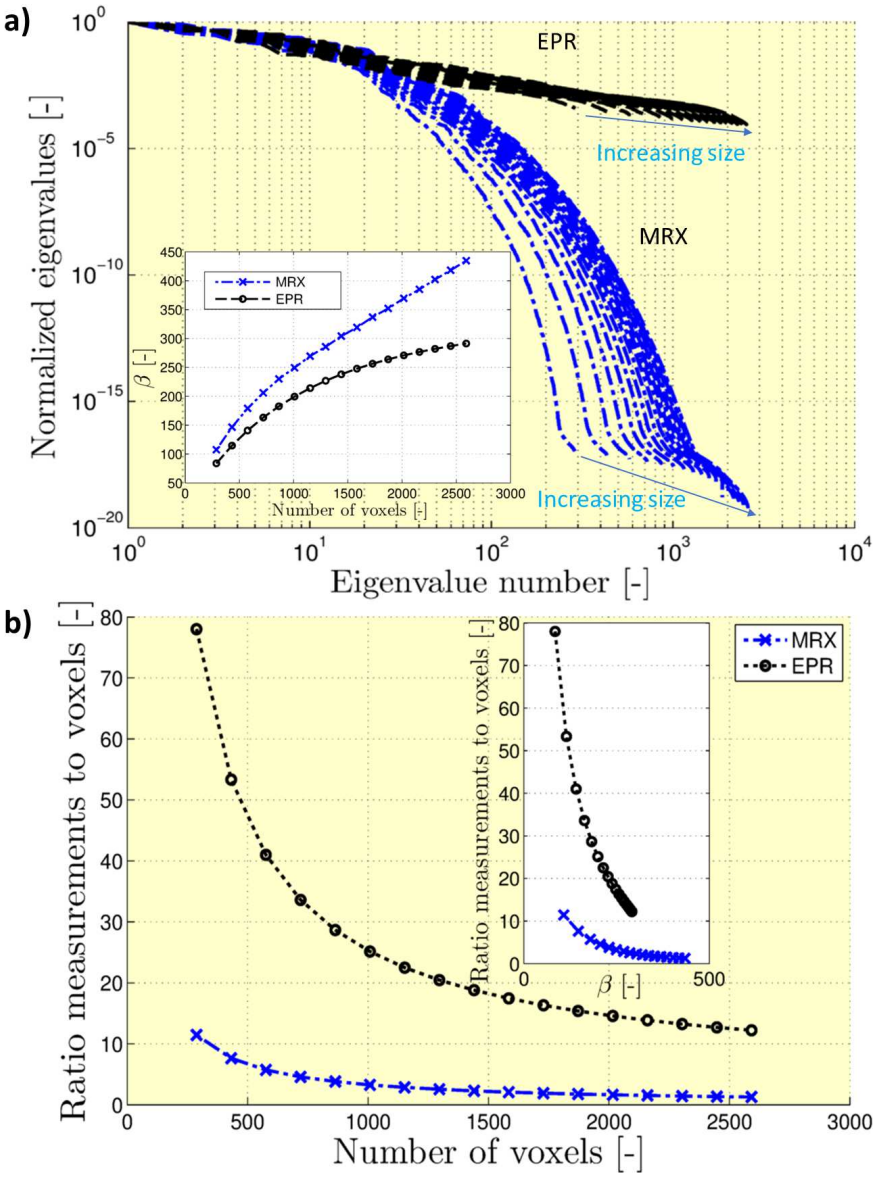

Figure 4.3: a) Normalized eigenvalues for the sensitivity matrices of EPR and MRX. Inset: β as function of phantom size. EPR has a slightly higher numerical stability than MRX for this setup configuration and is less sensitive to increasing number of voxels. b) Performed number of measurements for a given amount of voxels. EPR requires a large amount of measurements compared to MRX for equal sample sizes, making it time-consuming. Inset: MRX is able to achieve a similar condition number at far less measurements.

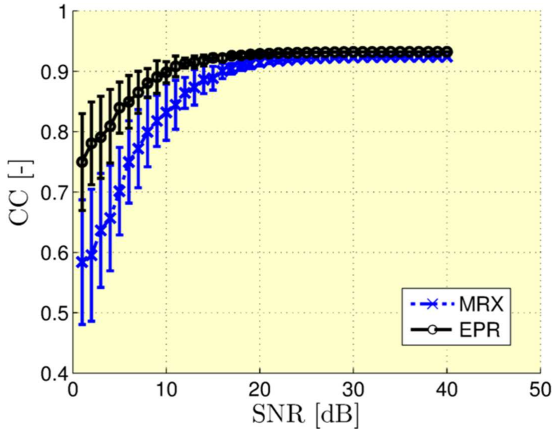

Figure 4.4: Averaged CC for 50 noise experiments for varying SNR using a fixed phantom. MRX and EPR achieve comparable reconstruction scores, however at lower SNRs the reconstruction quality deteriorates easier for MRX.

Advantages of EPR-MRX imaging

In this section we numerically combine the sensitivity matrices of EPR and MRX into EPR-MRX imaging (Eq. (4.3)) to resolve the drawbacks of both techniques and to increase the stability of the inverse problem.

In a first step the complete sensitivity matrices of both measurement techniques are combined to investigate the impact on imaging accuracy and stability (similar as for their comparison). Fig. 4.7a) and b) illustrate the anticipated increased stability of EPR-MRX compared to EPR. The relative amount of MRX measurements is small compared to the amount of EPR measurements resulting in limited increase of stability. We thus assume that the stability will further improve for similar measurements of both MRX and EPR.

The combined distinct information from both measurement modalities results in a higher CC for noisy MNP reconstructions (Fig. 4.8). For lower SNRs the CC becomes similar to the one obtained for EPR. These reconstructions are performed for the same phantom as in Figure 4.4, also for 50 averaged realizations. On average (considered over all phantoms, phantom sizes and noise levels, i.e. 3400 configurations) an increase of reconstruction quality of about 6 % can be achieved compared to EPR and MRX separately. In Fig. 4.7b) the number of measurements is still high because all the EPR and MRX measurements were added together. The amount of measurements was reduced by a factor two with EPR-MRX alternation in which each coil is activated separately with a certain measurement technique i.e. MRX is

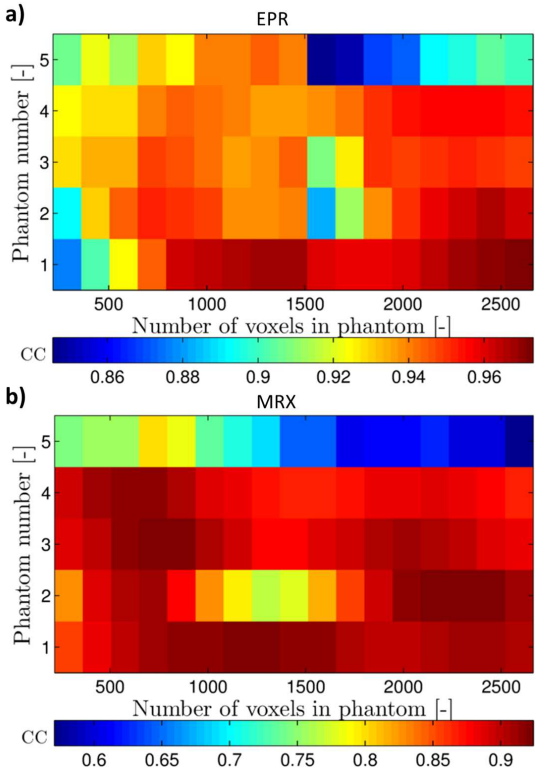

Figure 4.5: a) and b) Averaged CC for a SNR of 20 dB using 5 phantoms with increasing lengths in the case of EPR and MRX respectively. Both techniques are sensitive to different aspects of the phantoms. Note the different color scale to visualize dissimilarities in information content.

employed after activation of coil 1, while EPR is performed during activation of coil 2 and so on. This combined matrix has a similar stability (Fig. 4.7a) and b)) and a similar reconstruction quality compared to EPR, while requiring only half the number of measurements.

Finally, in Fig. 4.9, the correlation scores are visualized of 50 noisy reconstructions on the 5 phantoms at a noise level of 20 dB for increasing phantom lengths (similar as in Fig. 4.5) with EPR, MRX, EPR-MRX and EPR-MRX alternation respectively. Using EPR-MRX, improved MNP reconstructions can be obtained, while EPR-MRX alternation achieves similar to improved CC compared to EPR.

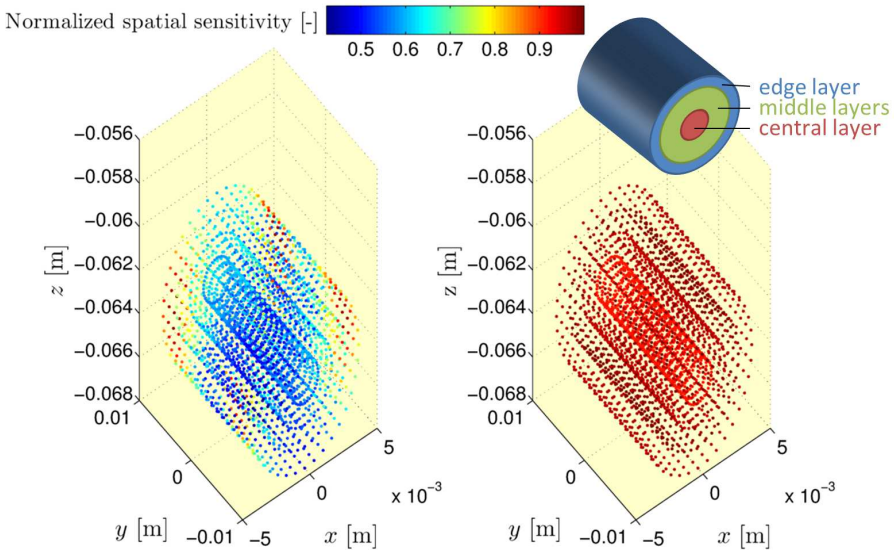

Figure 4.6: Normalized spatial sensitivity profile for MRX (left) and EPR (right) for the region of the four middle coils. In the case of MRX, particles in the vicinity of activation coils and SQUID sensors (above) have a higher spatial sensitivity and are thus more easily registered by the sensors. Particles in the middle and near the bottom of the sample have a lower sensitivity. In the case of EPR, an almost equal spatial sensitivity is observed for every voxel. Particles in the middle layers have the best spatial sensitivity, because in this region the right criteria of magnetic field and excitation are met resulting in a good registration of these particles in the pickup coil. The translational and rotational symmetry is due to movement of the sample.

The number of measurements for EPR-MRX was further reduced by minimizing the movement of the MNP sample (translational steps from 1 mm to 4 mm and rotation angles from 10 deg to 40 deg) and/or applying EPR-MRX alternation, see the black dashed curves in Fig. 4.10a), until measurement ratios similar to MRX are achieved. The measurement ratio scale is reduced for visualization purposes. Generally, the noise sensitivity is hardly affected by the measurement reduction in the case of EPR-MRX and a similar pattern as in Fig. 4.8 for EPR-MRX alternation is observed for all the reduced cases. When sample movement in EPR is limited, it becomes noise sensitive and similar noise behavior as for MRX in Fig. 4.4 is observed. The combined information of $\mathbf{S}_{\mathrm{m_{EPR}}}$ and $\mathbf{S}_{\mathrm{m_{MRX}}}$ thus results in an increased noise stability even when the number of measurements is significantly reduced. Fig. 4.10b) and c) show the average CC of noisy reconstructions for the 5 phantoms at 20 dB using a combination of reduced sample movement and measurement technique alternation for a measurement ratio of 11 and 13 for 288 unknowns for EPR-MRX and EPR respectively. This is a measurement reduction of

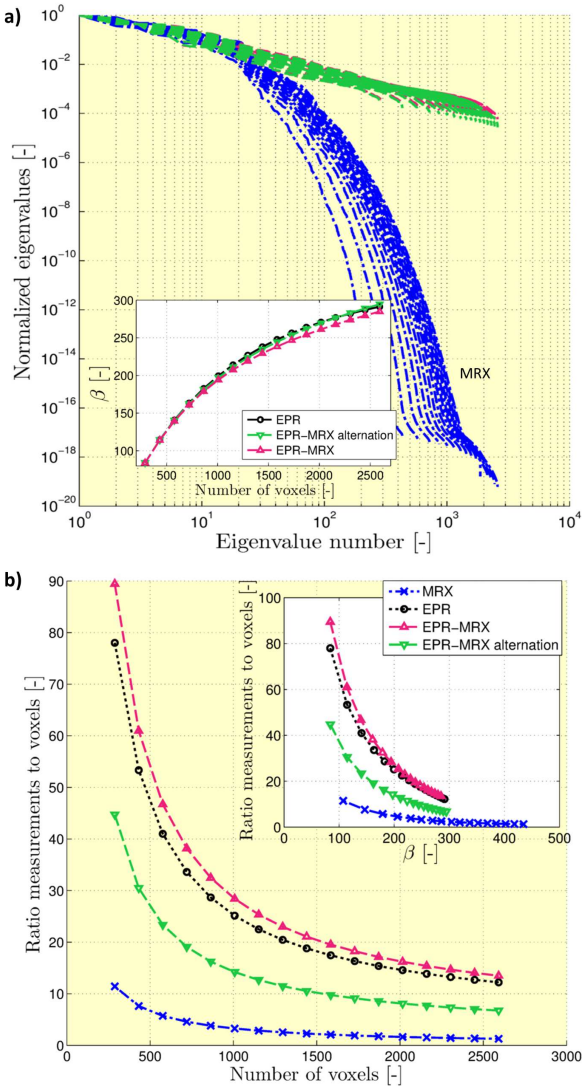

Figure 4.7: a) Normalized eigenvalues for the sensitivity matrices of EPR, MRX, EPR-MRX and EPR-MRX alternation. Inset: β as function of phantom size. EPR and EPR-MRX alternation have the same stability of the inverse problem and EPR-MRX shows a small increase in stability. b) Performed number of measurements for a given amount of voxels. EPR-MRX requires the total amount of MRX and EPR measurements, therefore EPR-MRX alternation was employed to significantly reduce measurement time. Inset: number of required measurements as function of β.

88 and 87 %. In the latter case all 16 coils are used and the sample is only limited in its movements through the magnetic field. Note that we did not

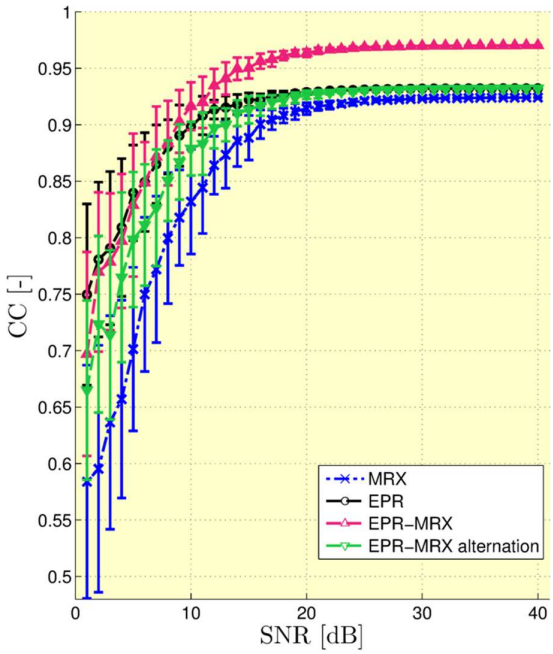

Figure 4.8: Averaged CC for 50 noise experiments for varying SNR using a fixed phantom. EPR-MRX shows an increased CC for typically used SNRs, however at lower SNRs, the reconstruction results are comparable to EPR. EPR-MRX alternation shows equivalent reconstruction scores compared to EPR.

explicitly include the time required to move the sample in the simulations, as this will be highly dependent on experimental realization. We assume this scales similarly as the reduction in sample movement. Due to the combined distinct information in EPR-MRX, MNP reconstructions do not deteriorate for decreased number of measurements and a similar reconstruction quality can be kept with respect to EPR with extensive measurements and a significant increase in CC compared to MRX is still achieved. Using EPR with reduced sample movement, reconstruction quality is diminished compared to EPR-MRX with similar reduction by on average 5 %. This becomes apparent for higher number of unknowns where the combination shows a higher stability and corresponding CC (as was predicted by the inset in Fig. 4.3b)). To conclude, the combined approach of EPR and MRX allows to significantly reduce measurement time (with 88 %), while keeping similar reconstruction results and noise sensitivity compared to EPR with extensive measurements and improved reconstruction scores to MRX and EPR independently with similar reduced measurements.

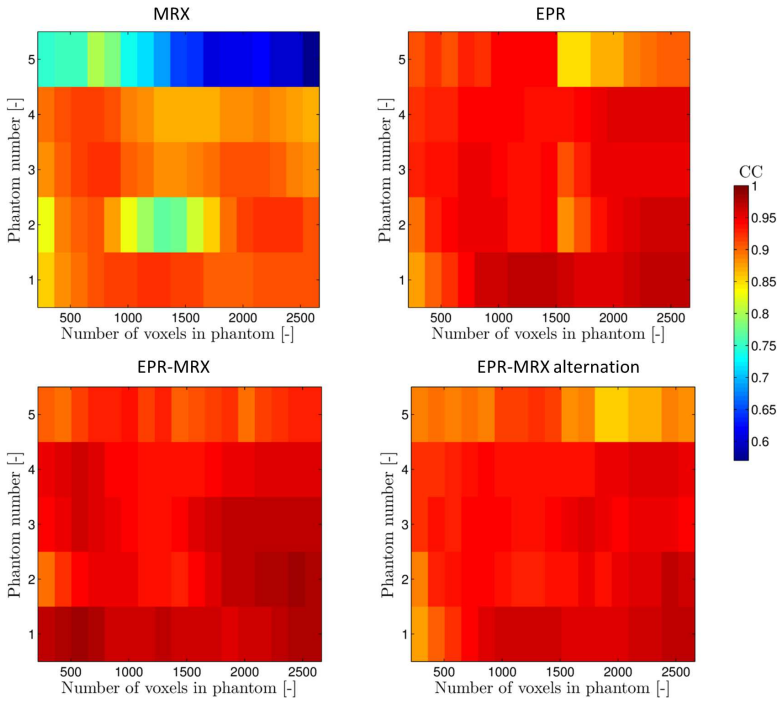

Figure 4.9: Averaged CC for a SNR of 20 dB using 5 phantoms with increasing lengths in the case of MRX, EPR, EPR-MRX and EPR-MRX alternation. The combined distinct information used in EPR-MRX yields (considered in 3400 configurations) increased reconstruction scores and on average an improvement of 6 % in CC can be obtained.

In this section the advantages of combining EPR and MRX were investigated. Of main interest was to analyze whether their combination can increase the quality of MNP reconstructions. Although both measurement methods can still be improved individually, their combination will always remain advantageous as long as their setup configurations generate distinct information from the sample. This can be investigated by calculating the spatial sensitivity profile or the stability of the matrices. In the case of MRX, the drawback of the lower stability of the inverse problem in this configuration could be improved by positioning the sensors more closely and using smaller coils. This allows to activate and measure smaller regions of the sample and in this way increase stability of the inverse problem and the resulting reconstruction quality. Additionally, advanced imaging techniques could be employed to increase reconstruction quality and stability of the inverse problem (see for example Sections 3.2 and 3.3 and Ref. [272]). In the case of EPR, the drawback of many sample positions can be reduced by employing multiple sensors, as

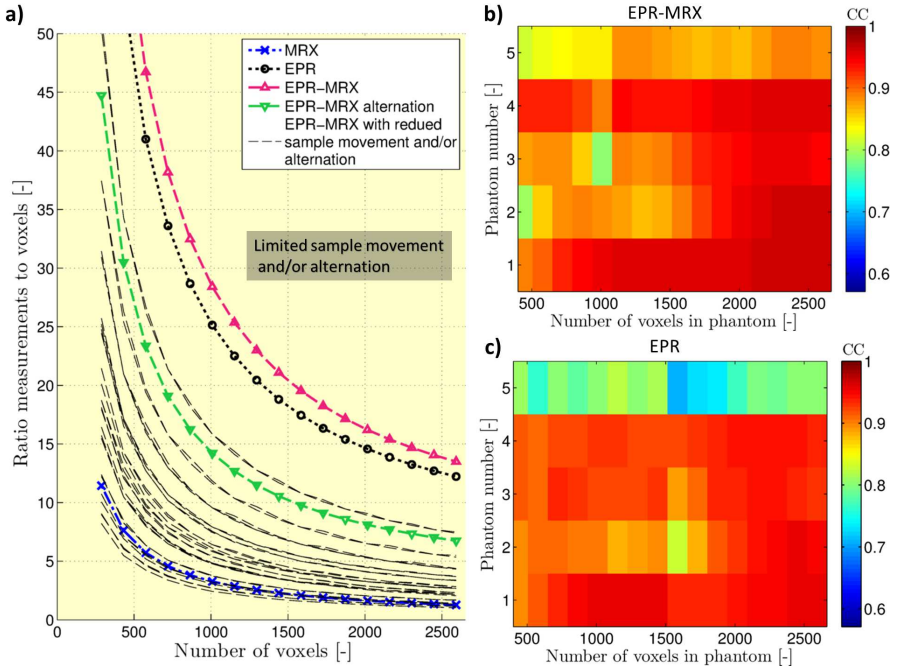

Figure 4.10: a) Performed number of measurements with respect to number of unknowns. Black dashed curves represent EPR-MRX results for reduced sample movement and/or alternating EPR-MRX. b) and c) Averaged CC of the 5 phantoms with increasing lengths for a noise level of 20 dB using EPR-MRX and EPR respectively. The EPR-MRX approach is less affected by the measurement reduction than EPR, which now becomes more noise sensitive and shows reduced CC. On average (from 3400 configurations) an improvement of 5 % can be obtained with EPR-MRX with reduced measurements compared to EPR.

in the case of MRX, instead of just one pickup coil. This however requires extensive measurements and modeling to take this behavior into account.

Note that accurate knowledge on the position of the sample is needed because the EPR measurements require movement of the sample. This can be realized by attaching small coils to the sample and feed these coils with a known AC current, as performed in Ref. [356]. These coils are then measured by the SQUIDs and can be accurately reconstructed with MRX as point sources, by employing their known magnetic moment. Hence, the coils are used as markers for determining the position of the sample. Other possible approaches to limit the accuracy requirements on sample positioning, are sample movement with use of a robot [43] or moving the sample only after all the required measurement at that position have been performed. Research still needs to be devoted regarding their up scaling to human sized objects so that their

combination can be useful in clinical practice. As sample movement is not ideal from clinical perspective, the excitation, pickup and magnetization coils could be moved instead of the sample. These could for example be inserted in a large, hollow tube which is able to internally rotate and translate. It is expected that the larger field of view, will necessitate increased power requirements for the coils. Currently, a lot of research is performed on smart coil designs to reduce this issue [233–235]. In MRX, investigations on this are performed using a rabbit-sized imaging setup [330].

4.2.5 Conclusion

A preliminary study is presented in which two promising MNP reconstruction techniques, EPR and MRX, are fused into EPR-MRX to improve their MNP reconstructions further. A comparative study between both techniques was performed in which sensitivity, stability and reconstruction quality parameters were calculated for 3400 simulated configurations, showing the complementarity in measurement data and sensitivity to the MNP distribution. By using their distinct information, we aimed at reducing the number of required measurements and at resolving the stability problems when solving the inverse problems, while improving MNP reconstructions. Their direct combination results in an average increase of MNP reconstruction quality with 6 % considered over all simulated configurations. To speed up the EPR measurements, EPR-MRX alternation was investigated in which both measurement techniques are alternated for each magnetic field configuration. This way, a speedup of the measurements by 50 % can be attained, another 38 % speedup is obtained by limiting movement of the sample. With this tremendous reduction in measurement time, a similar reconstruction quality compared to EPR with extensive measurements was achieved, while still having an increase in reconstruction quality of on average 5 % compared to MRX and EPR with similar reduction in measurements. Based on this preliminary study further steps can be made to investigate more advanced combinations of both modalities and to physically implement the EPR-MRX method with the intention to achieve high quality reconstructions of the spatial MNP distribution.

This preliminary study shows the importance of generating distinct MNP responses and selecting the specific responses that contain independent information on particle location. In principle, each MNP imaging technique can be combined as long as the merged modalities generate high-quality, distinct information from the MNP sample. This is one of the topics on which Section 4.3 elaborates. Additionally, it also considers some possibilities of

feedback between the imaging techniques, which could significantly increase reconstruction accuracy.

4.3. Future work

Although the presented techniques in this work resulted in significant progress in the accuracy, stability and speed of the MNP imaging techniques, still many advancements need to be made to improve this field and the nanomedicine field in general. Future work can be subdivided into various categories such as improving 1) the forward model, 2) the reconstruction procedure, 3) the imaging setup and 4) possible applications. In the following, some ideas on these subjects are presented and elaborated on.

The multi-color imaging model described in Section 3.4, for example, could result in new applications using MRX imaging in which the viscosity of the particle's surroundings needs to be visualized. Indeed, τ_B (Eq. (1.5)) depends on η and could hence reflect the surrounding environment of the particles. In order to achieve this, a reference MRX curve needs to be measured for the particle type in different environments or tissues, i.e. each tissue corresponds to a certain reference curve. This is particularly interesting when anatomical information is available from other modalities such as MRI. This data can be used to assign a tissue property to each voxel. When the relative contributions of each reference curve are determined (Eq. (3.33)), it is possible to constrain the second inverse problem (Eq. (3.35)). Hence, the actual localization and quantification of the MNP only works on a sub-region which corresponds to the given tissue. This way, there are less unknowns and the inverse problem should show an increased stability. On the other hand, it has been shown in some cases that τ_B becomes suppressed when MNP are injected in the body. Therefore, research needs to be performed to investigate the effect on the relaxation mechanisms when particles are injected in the body in order to find suitable particle types.

Additionally, the required *a priori* information on particle relaxation in the multi-color model could be omitted by employing for example Kaczmarz's algorithm to determine the various τ_{eff} (Eq. (1.6)) in the relaxation signal [357] (Section 1.4.3). However, care needs to be taken, as a single particle type typically expresses a distribution of relaxation constants and it will be difficult to determine the origin of a certain relaxation constant (i.e. original particle relaxation constant, or a particle in a different environment, or a particle interacting with other particles or tissues).

The multi-color model could also be employed in the EPR imaging technique. It makes use of the convenient property that spectrum broadening occurs in EPR (Sections 2.1.1 and 2.1.2), when paramagnetic materials such as oxygen are in the environment of the particle. In traditional EPR this effect has been

used, for example, to obtain oxygen maps and to determine the viscosity, pH and charge of the environment. In the imaging setup described in this dissertation, this has the effect that the response function of the particles changes. By measuring the response functions for the various tissue conditions, it is possible to relate tissue properties to a certain location. Nevertheless, experimental investigations are required to estimate the size of this effect and how it is related to changes in the response function.

The multi-color model can be especially of interest to the combined EPR-MRX setup. For example, the tissue information in the EPR signal can be extracted through the multi-color model to build a tissue map. This tissue map is then fed into the MRX multi-color model. Subsequently, the inverse problem of MRX could be constrained to certain organs or regions, as explained previously. This way, the inverse problem will be further stabilized as only sub-volumes are considered and thus improved MNP distributions will be obtained. This could also be used the other way around to constrain the inverse problem of EPR with the use of the MRX image. In fact, various feedback configurations between both techniques are possible, in which reconstructions of one technique are used as *a priori* information in the other technique. Future research should certainly be focused on how both can be combined and provide feedback to each other. The feedback could for example also allow for error estimation.

Also the other techniques specifically developed in this dissertation for MRX imaging could be employed for the EPR imaging setup with the coil array (Section 2.5) and the EPR-MRX imaging setup (Section 4.2). For example, the adaptive targeting procedure (Section 3.2) allows to adaptively activate the coils so that sensitivity is given where needed based on preliminary information on the particle distribution. In the EPR-MRX setup, the adaptive targeting procedure could also be used as a way to provide feedback between both modalities. One could for example perform a first reconstruction with EPR and, based on this reconstruction, MRX coils could be activated to target certain areas of the sample. As the EPR part currently provides a finer resolution, it could also be used to focus on certain parts of a preliminary MRX reconstruction where more detail is required. Additionally, the statistical parameters (Section 3.3) can be employed to allow comparison between coil configurations and to optimize the EPR and EPR-MRX setup in general. In fact, as the statistical measures take the sensitivity matrix as input, every technique using a forward model similar to Eq. (1.18) might benefit from this procedure.

Future work on the forward model and inverse reconstruction procedures should contain research on more advanced particle models that include the effect of particle interactions. Many lessons can also be learned from the advanced dipole models and reconstruction procedures from the field of MEG and EEG. Another possibility is the application of deep learning techniques in the reconstruction of the MNP distributions. They could offer a solution to the appearance of inaccuracies, blurring and artifacts in the reconstructed images. These effects originate in the approximations used in the forward model or nanoparticle model employed in the reconstruction procedure of current imaging techniques. Moreover, instability issues can arise when an ill-posed inverse problem is used. As deep learning techniques have already been successfully employed in data interpretation and recognition they should certainly be explored to analyze their applicability in MNP imaging [191].

Improvements can also be made with respect to the stability of the inverse problem. In other MNP-based imaging techniques, such as MPI and ASI (Section 1.3.3), research was also concentrated on stabilizing the inverse problem to enhance the imaging performance. So far, this was achieved by inducing MNP responses that contain increased amounts of independent information on particle location. By combining the various imaging techniques, it is expected that different MNP signals can be induced which stabilize the inverse problem. In Section 4.2, a preliminary numerical study of this principle was performed in which the combination of EPR and MRX was presented which showed that their combination can be advantageous. This is also a recent trend in clinically established techniques in which combinations of MRI, CT and positron emission tomography (PET) modalities are introduced. Especially beneficial for the nanomedicine field, would be the combination of MNP-based applications and imaging techniques into a single setup. Such a platform results in a more flexible and precise treatment of patients and allows real-time monitoring and personalized treatment planning.

Apart from some initial investigations in which the field-free-point of MPI was used for generating the magnetorelaxometry signal [319], the MNP imaging techniques have been developed rather independently. Therefore, in future research, it should be investigated which combinations of applied magnetic fields yield the largest amount of information on particle location. Especially sequences of magnetic fields are of interest as they probe the dynamic response of the MNP and hence contain large amounts of information. Initially, these sequences can be considered as combinations of current state-of-the-art techniques, which are gradually extended to contain both temporally and spatially varying magnetic fields, such as pulsed, gradient,

static, and AC fields. This is a challenging problem both from hardware and signal processing viewpoint. For example, in MPI and EPR it is sufficient to employ coils for the detection of the MNP signal, while MRX and ASI require SQUIDs, fluxgates or optical magnetometers. Moreover, the imaging techniques utilize a broad range of frequencies in their imaging procedures. On the other hand, some compromises could be made, such as the use of lower magnetic fields and a slower moving field-free-point [358]. Another challenge, from data analysis viewpoint, is the large amount of data that is generated from the possible combinations. Therefore, a method needs to be devised in order to select those data components which contain the desired particle information. This could for example be achieved using the quantitative models presented in Section 3.3, by performing in-depth sensitivity analyses (Sections 2.3 and 2.4), or with compressed sensing techniques [185]. The compressed sensing technique has been used in MPI to reduce computation time of the reconstructed MNP distribution and to reduce number of measurement positions for the system function. The latter technique could also be useful in MRX, ASI and EPR to reduce the sensitivity matrix and the calibration time. Another possibility to reduce the time-consuming measurement of the response functions and reference measurements is the use of a hybrid sensitivity matrix which is a combination of a magnetic nanoparticle model and measurements [183].

In the previous paragraph, the MNP imaging techniques were combined by fusing their magnetic field measurements. Another possibility to improve MNP reconstructions is to include feedback between the imaging techniques. This enables one to exploit the various strengths of each technique and to use their result as preliminary or *a priori* information in the other imaging techniques. This is similar to the feedback approaches suggested for the EPR-MRX imaging setup.

Also related to the stability of the inverse problem, is the use of a non-regular grid in the reconstructions of the particle distributions. The reconstructions in this dissertation have all been performed on a grid pattern consisting of volume-elements with a fixed size over the complete sample. It is possible to relate the particle distribution and imaging setup properties, together with the spatial sensitivity parameter and the quantitative models, to the geometrical properties of an adaptive grid which takes into account the local accuracy/resolution in a sub-region of the sample. This way, the condition of the inverse problem can be improved and hence an increase in reconstruction quality should be attainable.

Finally, although the presented techniques in this work have been used in the context of biomedical problems, the described techniques can also find applicability outside the biomedical field. They can, for example, be used in the non-destructive evaluation of magnetic materials, geomagnetic studies [359] and environmental applications such as waste management and water decontamination [360, 361].

Bibliography

[1] M. Arruebo, R. Fernández-Pacheco, M. R. Ibarra, and J. Santamaría. Magnetic nanoparticles for drug delivery. *Nano today*, 2(3):22–32, 2007.

[2] F. J. Heiligtag and M. Niederberger. The fascinating world of nanoparticle research. *Materials Today*, 16(78):262 – 271, 2013.

[3] W. Andrä and H. Nowak. *Magnetism in medicine: a handbook*, chapter 1. John Wiley & Sons, 2007.

[4] P. Colomban. The use of metal nanoparticles to produce yellow, red and iridescent colour, from bronze age to present times in lustre pottery and glass: solid state chemistry, spectroscopy and nanostructure. In *Journal of Nano Research*, volume 8, pages 109–132. Trans Tech Publ, 2009.

[5] M. Faraday. Preparation of colloidal gold. *Philos Trans R Soc London*, 147: 145–181, 1857.

[6] P. P. Edwards and J. M. Thomas. Gold in a metallic divided state - from faraday to present-day nanoscience. *Angewandte Chemie International Edition*, 46(29):5480–5486, 2007.

[7] C. Burda, X. Chen, R. Narayanan, and M. A. El-Sayed. Chemistry and properties of nanocrystals of different shapes. *Chemical Reviews*, 105(4): 1025–1102, 2005.

[8] R. Rossetti, J. L. Ellison, J. M. Gibson, and L. E. Brus. Size effects in the excited electronic states of small colloidal cds crystallites. *The Journal of Chemical Physics*, 80(9):4464–4469, 1984.

[9] R. Kodama. Magnetic nanoparticles. *Journal of Magnetism and Magnetic Materials*, 200(13):359 – 372, 1999.

[10] C. P. Bean and J. D. Livingston. Superparamagnetism. *Journal of Applied Physics*, 30(4):S120–S129, 1959.

[11] J. Dormann, D. Fiorani, and E. Tronc. Magnetic relaxation in fine-particle systems. *Advances in Chemical Physics, Volume 98*, pages 283–494.

[12] A. Einstein. *Investigations on the Theory of the Brownian Movement*. Courier Corporation, 1956.

[13] Néel, Louis. Théorie du traînage magnétique des substances massives dans le domaine de rayleigh. *J. Phys. Radium*, 11(2):49–61, 1950.

[14] Q. Pankhurst, J. Connolly, S. Jones, and J. Dobson. Applications of magnetic nanoparticles in biomedicine. *Journal of Physics D: Applied Physics*, 36:R167–R181, 2003.

[15] Q. Pankhurst, N. Thanh, S. Jones, and J. Dobson. Progress in applications of magnetic nanoparticles in biomedicine. *Journal of Physics D: Applied Physics*, 42:224001 (15pp), 2009.

[16] L. Trahms. Biomedical applications of magnetic nanoparticles. *Colloidal Magnetic Fluids, Lecture notes in physics*, 763:327–358, 2009.

[17] K. M. Krishnan. Biomedical nanomagnetics: A spin through possibilities in imaging, diagnostics, and therapy. *IEEE Transactions on Magnetics*, 46 (7):2523–2558, 2010.

[18] F. Ludwig, E. Heim, M. Schilling, and K. Enpuku. Characterization of superparamagnetic feo nanoparticles by fluxgate magnetorelaxometry for use in biomedical applications. *Journal of Applied Physics*, 103:07A314, 2008.

[19] H. Bryant, N. L. Adolphi, D. L. Huber, D. L. Fegan, T. C. Monson, T. E. Tessier, and E. R. Flynn. Magnetic properties of nanoparticles useful for SQUID relaxometry in biomedical applications. *Journal of Magnetism and Magnetic Materials*, 323(6):767 – 774, 2011.

[20] E. M. Cherry, P. G. Maxim, and J. K. Eaton. Particle size, magnetic field, and blood velocity effects on particle retention in magnetic drug targeting. *Medical Physics*, 37(1):175–182, 2010.

[21] C. Alexiou, W. Arnold, R. Klein, F. Parak, P. Hulin, C. Bergemann, W. Erhardt, S. Wagenpfeil, and A. Lübbe. Locoregional cancer treatment with magnetic drug targeting. *Cancer Research*, 60(23):6641–6648, 2000.

[22] P. E. Magnelind, Y. J. Kim, A. N. Matlashov, S. G. Newman, P. L. Volegov, and M. A. Espy. Toward early cancer detection using superparamagnetic relaxometry in a SQUID-based ULF-MRI system. *Superconductor Science and Technology*, 27(4):044031, 2014.

[23] D. Eberbeck, C. Bergemann, F. Wiekhorst, U. Steinhoff, and L. Trahms. Quantification of specific bindings of biomolecules by magnetorelaxometry. *Journal of Nanobiotechnology*, 6, 2008.

[24] A. Jordan, R. Scholz, P. Wust, H. Fähling, and R. Felix. Magnetic fluid hyperthermia (MFH): Cancer treatment with AC magnetic field induced excitation of biocompatible superparamagnetic nanoparticles. *Journal of Magnetism and Magnetic Materials*, 201(13):413 – 419, 1999.

[25] W. R. Sanhai, J. H. Sakamoto, R. Canady, and M. Ferrari. Seven challenges for nanomedicine. *Nature Nanotechnology*, 3(5):242–244, 2008.

[26] R. Kötitz, P. Fannin, and L. Trahms. Time domain study of Brownian and Néel relaxation in ferrofluids. *Journal of Magnetism and Magnetic Materials*, 149(1-2):42–46, 1995.

[27] W. Weitschies, R. Kötitz, T. Bunte, and L. Trahms. Determination of relaxing or remanent nanoparticle magnetization provides a novel binding-specific technique for the evaluation of immunoassays. *Pharmaceutical and Pharmacological Letters*, 7(1):5–8, 1997.

[28] D. Eberbeck, S. Hartwig, U. Steinhoff, and L. Trahms. Description of the magnetisation decay in ferrofluids with a narrow particle size distribution. *Magnetohydrodynamics*, 39:77–83, 2003.

[29] D. Eberbeck, F. Wiekhorst, U. Steinhoff, and L. Trahms. Aggregation behaviour of magnetic nanoparticle suspensions investigated by magnetorelaxometry. *Journal of Physics: Condensed Matter*, 18:S2829–S2847, 2006.

[30] F. Wiekhorst, C. Seliger, R. Jurgons, U. Steinhoff, D. Eberbeck, L. Trahms, and C. Alexiou. Quantification of magnetic nanoparticles by magnetorelaxometry and comparison to histology after magnetic drug targeting. *Journal of Nanoscience and Nanotechnology, 6*, 9(10):3222–3225, 2006.

[31] R. Tietze, R. Jurgons, S. Lyer, E. Schreiber, F. Wiekhorst, D. Eberbeck, H. Richter, U. Steinhoff, L. Trahms, and C. Alexiou. Quantification of drug-loaded magnetic nanoparticles in rabbit liver and tumor after in vivo administration. *Journal of Magnetism and Magnetic Materials*, 321 (10):1465–1468, 2009.

[32] F. Wiekhorst, U. Steinhoff, D. Eberbeck, K. Schwarz, H. Richter, R. Renner, M. Roessner, C. Rudolph, and L. Trahms. Quantification of magnetic nanoparticle concentration in pig lung tissue after magnetic aerosol drug targeting by magnetorelaxometry. In J. Sloten, P. Verdonck, M. Nyssen, and J. Haueisen, editors, *4th European Conference of the International Federation for Medical and Biological Engineering*, volume 22 of *IFMBE Proceedings*, pages 2326–2329. Springer Berlin Heidelberg, 2009.

[33] L. Warzemann, J. Schambach, P. Weber, W. Weitschies, and R. Kötitz. LTS SQUID gradiometer system for in vivo magnetorelaxometry. *Superconductor Science and Technology*, 12(11):953, 1999.

[34] E. Flynn and H. Bryant. A biomagnetic system for *in vivo* cancer imaging. *Physics in Medicine and Biology*, 50(6):1273–1293, 2005.

[35] F. Wiekhorst, R. Jurgons, D. Eberbeck, T. Sander, U. Steinhoff, S. Hartwig, C. Alexiou, and L. Trahms. SQUID system with integrated superconducting shield for monitoring of drug targeting with magnetic nanoparticles in animals. *Biomed. Tech*, 50(2):609–610, 2005.

[36] D. Baumgarten, M. Liehr, F. Wiekhorst, U. Steinhoff, P. Münster, P. Miethe, L. Trahms, and J. Haueisen. Magnetic nanoparticle imaging by means of minimum norm estimates from remanence measurements. *Medical & biological engineering & computing*, 46(12):1177–1185, 2008.

[37] D. Baumgarten and J. Haueisen. A spatio-temporal approach for the solution of the inverse problem in the reconstruction of magnetic nanoparticle distributions. *IEEE Transactions on Magnetics*, 46(8):3496–3499, 2010.

[38] F. Wiekhorst, D. Baumgarten, W. Haberkorn, U. Steinhoff, J. Haueisen, M. Bär, and L. Trahms. A physical phantom modeling extended magnetic nanoparticle distributions in biological systems. In *World Congress on Medical Physics and Biomedical Engineering, September 7-12, 2009, Munich, Germany*, pages 293–296. Springer, 2009.

[39] R. Eichardt, D. Baumgarten, B. Petković, F. Wiekhorst, L. Trahms, and J. Haueisen. Adapting source grid parameters to improve the condition of the magnetostatic linear inverse problem of estimating nanoparticle distributions. *Medical & biological engineering & computing*, 50(10):1081–1089, 2012.

[40] J. Wikswo, Y. Ma, N. Sepulveda, S. Tan, I. Thomas, U. Lauder, A. Steinhoff, G. Crevecoeur, F. Wiekhorst, M. Liebl, J. Haueisen, and L. Trahms. Magnetic susceptibility imaging for nondestructive evaluation (using SQUID magnetometer). *IEEE Transactions on Applied Superconductivity*, 3(1):1995–2002, 1993.

[41] U. Steinhoff, F. Wiekhorst, D. Baumgarten, J. Haueisen, and L. Trahms. Imaging of magnetic nanoparticles based on magnetorelaxometry with sequential activation of inhomogeneous magnetization fields. *Biomedical Engineering / Biomedizinische Technik*, 55:22–25, 2010.

[42] G. Crevecoeur, D. Baumgarten, U. Steinhoff, J. Haueisen, L. Trahms, and L. Dupré. Advancements in magnetic nanoparticle reconstruction using sequential activation of excitation coil arrays using magnetorelaxometry. *IEEE Transactions on Magnetics*, 48(4):1313 – 1316, 2012.

[43] B. Gleich and J. Weizenecker. Tomographic imaging using the nonlinear response of magnetic particles. *Nature*, 435(7046):1214–1217, 2005.

[44] J. Weizenecker, B. Gleich, J. Rahmer, H. Dahnke, and J. Borgert. Three-dimensional real-time in vivo magnetic particle imaging. *Physics in Medicine and Biology*, 54:L1, 2009.

[45] J. Weizenecker, B. Gleich, and J. Borgert. Magnetic particle imaging using a field free line. *Journal of Physics D: Applied Physics*, 41(10):105009, 2008.

[46] T. F. Sattel, T. Knopp, S. Biederer, B. Gleich, J. Weizenecker, J. Borgert, and T. M. Buzug. Single-sided device for magnetic particle imaging. *Journal of Physics D: Applied Physics*, 42(2):022001, 2009.

[47] T. Knopp, J. Rahmer, T. F. Sattel, S. Biederer, J. Weizenecker, B. Gleich, J. Borgert, and T. M. Buzug. Weighted iterative reconstruction for magnetic particle imaging. *Physics in Medicine and Biology*, 55(6):1577, 2010.

[48] P. Goodwill and S. Conolly. Multidimensional x-space magnetic particle imaging. *IEEE Transactions on Medical Imaging*, 30(9):1581–1590, 2011.

[49] U. Steinhoff, M. Liebl, M. Bauer, F. Wiekhorst, L. Trahms, D. Baumgarten, and J. Haueisen. Spatially resolved measurement of magnetic nanoparticles using inhomogeneous excitation fields in the linear susceptibility range ($<$ 1mT). In T. M. Buzug and J. Borgert, editors, *Magnetic Particle Imaging*, volume 140 of *Springer Proceedings in Physics*, pages 295–300. Springer Berlin Heidelberg, 2012.

[50] B. W. Ficko, P. M. Nadar, P. J. Hoopes, and S. G. Diamond. Development of a magnetic nanoparticle susceptibility magnitude imaging array. *Physics in Medicine and Biology*, 59(4):1047, 2014.

[51] P. Vaes and S. Teughels. Isolating active electron spin signals in EPR, 2012. WO/2012/126968.

[52] X. Li, G. Torfs, J. Vandewege, J. Bauwelinck, and J. Verbiest. Sensitive and quantitative pEPR detection system for SPIO nanoparticles. *Electronics Letters*, 49(25):1600–1601, 2013.

[53] M. Colombo, S. Carregal-Romero, M. F. Casula, L. Gutierrez, M. P. Morales, I. B. Boehm, J. T. Heverhagen, D. Prosperi, and W. J. Parak. Biological applications of magnetic nanoparticles. *Chemical Society Reviews*, 41(11):4306–4334, 2012.

[54] A. K. Gupta and M. Gupta. Synthesis and surface engineering of iron oxide nanoparticles for biomedical applications. *Biomaterials*, 26(18):3995 – 4021, 2005.

[55] L. H. Reddy, J. L. Arias, J. Nicolas, and P. Couvreur. Magnetic nanoparticles: design and characterization, toxicity and biocompatibility, pharmaceutical and biomedical applications. *Chemical Reviews*, 112(11):5818–5878, 2012.

[56] W. Wu, Z. Wu, T. Yu, C. Jiang, and W.-S. Kim. Recent progress on magnetic iron oxide nanoparticles: synthesis, surface functional strategies and biomedical applications. *Science and Technology of Advanced Materials*, 2016.

[57] C. Sun, J. S. Lee, and M. Zhang. Magnetic nanoparticles in MR imaging and drug delivery. *Advanced Drug Delivery Reviews*, 60(11):1252 – 1265, 2008. Inorganic Nanoparticles in Drug Delivery.

[58] J. Gao, H. Gu, and B. Xu. Multifunctional magnetic nanoparticles: design, synthesis, and biomedical applications. *Accounts of chemical research*, 42(8):1097–1107, 2009.

[59] R. Hao, R. Xing, Z. Xu, Y. Hou, S. Gao, and S. Sun. Synthesis, functionalization, and biomedical applications of multifunctional magnetic nanoparticles. *Advanced Materials*, 22(25):2729–2742, 2010.

[60] D.-E. Lee, H. Koo, I.-C. Sun, J. H. Ryu, K. Kim, and I. C. Kwon. Multifunctional nanoparticles for multimodal imaging and theragnosis. *Chemical Society Reviews*, 41(7):2656–2672, 2012.

[61] A. Singh and S. K. Sahoo. Magnetic nanoparticles: a novel platform for cancer theranostics. *Drug Discovery Today*, 19(4):474 – 481, 2014.

[62] G. T. Tietjen and W. M. Saltzman. Nanomedicine gets personal. *Science Translational Medicine*, 7(314):314fs47–314fs47, 2015.

[63] C. Li. A targeted approach to cancer imaging and therapy. *Nature materials*, 13(2):110–115, 2014.

[64] J. H. Ryu, S. Lee, S. Son, S. H. Kim, J. F. Leary, K. Choi, and I. C. Kwon. Theranostic nanoparticles for future personalized medicine. *Journal of Controlled Release*, 190:477–484, 2014.

[65] Z. Cheng, A. Al Zaki, J. Z. Hui, V. R. Muzykantov, and A. Tsourkas. Multifunctional nanoparticles: cost versus benefit of adding targeting and imaging capabilities. *Science*, 338(6109):903–910, 2012.

[66] S. Bogren, A. Fornara, F. Ludwig, M. del Puerto Morales, U. Steinhoff, M. F. Hansen, O. Kazakova, and C. Johansson. Classification of magnetic nanoparticle systemssynthesis, standardization and analysis methods in the nanomag project. *International Journal of Molecular Sciences*, 16(9): 20308–20325, 2015.

[67] nanomag eu fp7 project.

[68] J. M. Coey. *Magnetism and magnetic materials*. Cambridge University Press, 2010.

[69] J. Frenkel and J. Dorfman. Spontaneous and induced magnetisation in ferromagnetic bodies. *Nature*, 126(3173):274–275, 1930.

[70] F. Ahrentorp, A. Astalan, J. Blomgren, C. Jonasson, E. Wetterskog, P. Svedlindh, A. Lak, F. Ludwig, L. J. Van IJzendoorn, F. Westphal, et al. Effective particle magnetic moment of multi-core particles. *Journal of Magnetism and Magnetic Materials*, 380:221–226, 2015.

[71] J. Leliaert, A. Coene, G. Crevecoeur, A. Vansteenkiste, D. Eberbeck, F. Wiekhorst, B. Van Waeyenberge, and L. Dupré. Regarding the Néel relaxation time constant in magnetorelaxometry. *Journal of Applied Physics*, 116(16):163914, 2014.

[72] O. Laslett, S. Ruta, R. Chantrell, J. Barker, G. Friedman, and O. Hovorka. Consistent energy barrier distributions in magnetic particle chains. *Physica B: Condensed Matter*, 2015.

[73] O. Laslett, S. Ruta, J. Barker, R. W. Chantrell, G. Friedman, and O. Hovorka. Interaction effects enhancing magnetic particle detection based on magneto-relaxometry. *Applied Physics Letters*, 106(1):012407, 2015.

[74] A. G. Kolhatkar, A. C. Jamison, D. Litvinov, R. C. Willson, and T. R. Lee. Tuning the magnetic properties of nanoparticles. *International Journal of Molecular Sciences*, 14(8):15977, 2013.

[75] W. T. Coffey and Y. P. Kalmykov. Thermal fluctuations of magnetic nanoparticles: Fifty years after brown. *Journal of Applied Physics*, 112 (12):121301, 2012.

[76] F. Wiekhorst, U. Steinhoff, D. Eberbeck, and L. Trahms. Magnetorelaxometry assisting biomedical applications of magnetic nanoparticles. *Pharmaceutical Research*, 29(5):1189–1202, 2012.

[77] F. Ludwig, E. Heim, and M. Schilling. Characterization of superparamagnetic nanoparticles by analyzing the magnetization and relaxation dynamics using fluxgate magnetometers. *Journal of Applied Physics*, 101 (11):113909, 2007.

[78] T. Yoshida and K. Enpuku. Simulation and quantitative clarification of AC susceptibility of magnetic fluid in nonlinear Brownian relaxation region. *Japanese Journal of Applied Physics*, 48(12R):127002, 2009.

[79] M. K. Yu, J. Park, and S. Jon. Targeting strategies for multifunctional nanoparticles in cancer imaging and therapy. *Theranostics*, 2(1):3, 2012.

[80] I. Cuadrado, M. J. G. M. Piedras, I. Herruzo, M. del Carmen Turpin, B. Castejón, P. Reventun, A. Martin, M. Saura, J. L. Zamorano, and C. Zaragoza. EMMPRIN-Targeted magnetic nanoparticles for in vivo visualization and regression of acute myocardial infarction. *Theranostics*, 6(4):545, 2016.

[81] L. Hajba and A. Guttman. The use of magnetic nanoparticles in cancer theranostics: Toward handheld diagnostic devices. *Biotechnology Advances*, 34(4):354 – 361, 2016.

[82] B. Zheng, P. Marc, E. Yu, B. Gunel, K. Lu, T. Vazin, D. V. Schaffer, P. W. Goodwill, and S. M. Conolly. Quantitative magnetic particle imaging monitors the transplantation, biodistribution, and clearance of stem cells in vivo. *Theranostics*, 6(3):291, 2016.

[83] H. M. Azzazy and M. M. Mansour. In vitro diagnostic prospects of nanoparticles. *Clinica Chimica Acta*, 403(12):1 – 8, 2009.

[84] K. J. Widder, A. E. Senyei, and D. G. Scarpelli. Magnetic microspheres: a model system for site specific drug delivery in vivo. *Experimental Biology and Medicine*, 158(2):141–146, 1978.

[85] Y. Gao, Y. Liu, and C. Xu. Magnetic nanoparticles for biomedical applications: From diagnosis to treatment to regeneration. In *Engineering in Translational Medicine*, pages 567–583. Springer, 2014.

[86] S. Y. Lee, S. I. Jeon, S. Jung, I. J. Chung, and C.-H. Ahn. Targeted multimodal imaging modalities. *Advanced Drug Delivery Reviews*, 76(0):60 – 78, 2014. Targeted imaging.

[87] U. O. Häfeli, K. Gilmour, A. Zhou, S. Lee, and M. E. Hayden. Modeling of magnetic bandages for drug targeting: Button vs. halbach arrays. *Journal of Magnetism and Magnetic Materials*, 311(1):323 – 329, 2007. Proceedings of the Sixth International Conference on the Scientific and Clinical Applications of Magnetic CarriersSCAMC-06.

[88] L. C. Barnsley, D. Carugo, J. Owen, and E. Stride. Halbach arrays consisting of cubic elements optimised for high field gradients in magnetic

drug targeting applications. *Physics in Medicine and Biology*, 60(21):8303, 2015.

[89] O. Felfoul, A. T. Becker, G. Fagogenis, and P. E. Dupont. Simultaneous steering and imaging of magnetic particles using MRI toward delivery of therapeutics. *Scientific Reports*, 6, 2016.

[90] R. Tietze, S. Lyer, S. Dürr, and C. Alexiou. Nanoparticles for cancer therapy using magnetic forces. *Nanomedicine*, 7(3):447–457, 2012.

[91] P. Radon, N. Löwa, D. Gutkelch, and F. Wiekhorst. Design and characterization of a device to quantify the magnetic drug targeting efficiency of magnetic nanoparticles in a tube flow phantom by magnetic particle spectroscopy. *Journal of Magnetism and Magnetic Materials*, pages –, 2016.

[92] V. Mody, A. Cox, S. Shah, A. Singh, W. Bevins, and H. Parihar. Magnetic nanoparticle drug delivery systems for targeting tumor. *Applied Nanoscience*, 4(4):385–392, 2014.

[93] J. Estelrich, E. Escribano, J. Queralt, and M. A. Busquets. Iron oxide nanoparticles for magnetically-guided and magnetically-responsive drug delivery. *International journal of molecular sciences*, 16(4):8070–8101, 2015.

[94] B. Shapiro, S. Kulkarni, A. Nacev, S. Muro, P. Y. Stepanov, and I. N. Weinberg. Open challenges in magnetic drug targeting. *Wiley Interdisciplinary Reviews: Nanomedicine and Nanobiotechnology*, 7(3):446–457, 2015.

[95] C. J. Cheng, G. T. Tietjen, J. K. Saucier-Sawyer, and W. M. Saltzman. A holistic approach to targeting disease with polymeric nanoparticles. *Nature Reviews Drug Discovery*, 14(4):239–247, 2015.

[96] P. G. Kyrtatos, P. Lehtolainen, M. Junemann-Ramirez, A. Garcia-Prieto, A. N. Price, J. F. Martin, D. G. Gadian, Q. A. Pankhurst, and M. F. Lythgoe. Magnetic tagging increases delivery of circulating progenitors in vascular injury. *JACC: Cardiovascular Interventions*, 2(8):794 – 802, 2009.

[97] A. Yanai, U. O. Häfeli, A. L. Metcalfe, P. Soema, L. Addo, C. Y. Gregory-Evans, K. Po, X. Shan, O. L. Moritz, and K. Gregory-Evans. Focused magnetic stem cell targeting to the retina using superparamagnetic iron oxide nanoparticles. *Cell transplantation*, 21(6):1137–1148, 2012.

[98] G. Frasca, F. Gazeau, and C. Wilhelm. Formation of a three-dimensional multicellular assembly using magnetic patterning. *Langmuir*, 25(4): 2348–2354, 2009.

[99] J. Dobson, S. H. Cartmell, A. Keramane, and A. J. E. Haj. Principles and design of a novel magnetic force mechanical conditioning bioreactor for tissue engineering, stem cell conditioning, and dynamic in vitro screening. *IEEE Transactions on NanoBioscience*, 5(3):173–177, 2006.

[100] S. K. Samal, V. Goranov, M. Dash, A. Russo, T. Shelyakova, P. Graziosi, L. Lungaro, A. Riminucci, M. Uhlarz, et al. Multilayered magnetic

gelatin membrane scaffolds. *ACS Applied Materials & Interfaces*, 7(41): 23098–23109, 2015.

[101] J. Dobson. Remote control of cellular behaviour with magnetic nanoparticles. *Nature Nanotechnology*, 3(3):139–143, 2008.

[102] C. Plank, O. Zelphati, and O. Mykhaylyk. Magnetically enhanced nucleic acid delivery. Ten years of magnetofectionprogress and prospects. *Advanced drug delivery reviews*, 63(14):1300–1331, 2011.

[103] D. Ibraheem, A. Elaissari, and H. Fessi. Gene therapy and DNA delivery systems. *International Journal of Pharmaceutics*, 459(12):70 – 83, 2014.

[104] R. Gilchrist, R. Medal, W. D. Shorey, R. C. Hanselman, J. C. Parrott, and C. B. Taylor. Selective inductive heating of lymph nodes. *Annals of surgery*, 146(4):596, 1957.

[105] W. J. Atkinson, I. A. Brezovich, and D. P. Chakraborty. Usable frequencies in hyperthermia with thermal seeds. *IEEE Transactions on Biomedical Engineering*, (1):70–75, 1984.

[106] S. Dutz and R. Hergt. Magnetic nanoparticle heating and heat transfer on a microscale: Basic principles, realities and physical limitations of hyperthermia for tumour therapy. *International Journal of Hyperthermia*, 29(8):790–800, 2013.

[107] R. Rosensweig. Heating magnetic fluid with alternating magnetic field. *Journal of Magnetism and Magnetic Materials*, 252:370–374, 2002.

[108] J. Carrey, B. Mehdaoui, and M. Respaud. Simple models for dynamic hysteresis loop calculations of magnetic single-domain nanoparticles: Application to magnetic hyperthermia optimization. *Journal of Applied Physics*, 109(8):083921, 2011.

[109] C. L. Dennis and R. Ivkov. Physics of heat generation using magnetic nanoparticles for hyperthermia. *International Journal of Hyperthermia*, 29 (8):715–729, 2013.

[110] J.-P. Fortin, C. Wilhelm, J. Servais, C. Ménager, J.-C. Bacri, and F. Gazeau. Size-sorted anionic iron oxide nanomagnets as colloidal mediators for magnetic hyperthermia. *Journal of the American Chemical Society*, 129(9): 2628–2635, 2007.

[111] R. Hergt and S. Dutz. Magnetic particle hyperthermia - biophysical limitations of a visionary tumour therapy. *Journal of Magnetism and Magnetic Materials*, 311(1):187 – 192, 2007. Proceedings of the Sixth International Conference on the Scientific and Clinical Applications of Magnetic Carriers SCAMC-06.

[112] W. Andrä, C. d'Ambly, R. Hergt, I. Hilger, and W. Kaiser. Temperature distribution as function of time around a small spherical heat source of local magnetic hyperthermia. *Journal of Magnetism and Magnetic Materials*, 194(13):197 – 203, 1999.

[113] W. L. Nyborg. Solutions of the bio-heat transfer equation. *Physics in Medicine and Biology*, 33(7):785, 1988.

[114] S. Dutz and R. Hergt. Magnetic particle hyperthermia - a promising tumour therapy? *Nanotechnology*, 25(45):452001, 2014.

[115] I. Hilger. In vivo applications of magnetic nanoparticle hyperthermia. *International Journal of Hyperthermia*, 29(8):828–834, 2013.

[116] K. Maier-Hauff, R. Rothe, R. Scholz, U. Gneveckow, P. Wust, B. Thiesen, A. Feussner, A. von Deimling, N. Waldoefner, R. Felix, et al. Intracranial thermotherapy using magnetic nanoparticles combined with external beam radiotherapy: results of a feasibility study on patients with glioblastoma multiforme. *Journal of Neuro-Oncology*, 81(1):53–60, 2007.

[117] M. Johannsen, U. Gneveckow, B. Thiesen, K. Taymoorian, C. Cho, N. Waldöfner, R. Scholz, A. Jordan, S. Loening, and P. Wust. Thermotherapy of prostate cancer using magnetic nanoparticles: feasibility, imaging, and three-dimensional temperature distribution. *European urology*, 52(6):1653–1662, 2007.

[118] E. A. Prigo, G. Hemery, O. Sandre, D. Ortega, E. Garaio, F. Plazaola, and F. J. Teran. Fundamentals and advances in magnetic hyperthermia. *Applied Physics Reviews*, 2(4):041302, 2015.

[119] S. Dutz, M. Kettering, I. Hilger, R. Müller, and M. Zeisberger. Magnetic multicore nanoparticles for hyperthermia - influence of particle immobilization in tumour tissue on magnetic properties. *Nanotechnology*, 22 (26):265102, 2011.

[120] R. Di Corato, A. Espinosa, L. Lartigue, M. Tharaud, S. Chat, T. Pellegrino, C. Ménager, F. Gazeau, and C. Wilhelm. Magnetic hyperthermia efficiency in the cellular environment for different nanoparticle designs. *Biomaterials*, 35(24):6400 – 6411, 2014.

[121] C. L. Dennis, K. L. Krycka, J. A. Borchers, R. D. Desautels, J. van Lierop, N. F. Huls, A. J. Jackson, C. Gruettner, and R. Ivkov. Internal magnetic structure of nanoparticles dominates time-dependent relaxation processes in a magnetic field. *Advanced Functional Materials*, 2015.

[122] D. Soukup, S. Moise, E. Céspedes, J. Dobson, and N. D. Telling. In situ measurement of magnetization relaxation of internalized nanoparticles in live cells. *ACS nano*, 9(1):231–240, 2015.

[123] L. C. Branquinho, M. S. Carrião, A. S. Costa, N. Zufelato, M. H. Sousa, R. Miotto, R. Ivkov, and A. F. Bakuzis. Effect of magnetic dipolar interactions on nanoparticle heating efficiency: Implications for cancer hyperthermia. *Scientific Reports*, 3, 2013.

[124] C. Martinez-Boubeta, K. Simeonidis, A. Makridis, M. Angelakeris, O. Iglesias, P. Guardia, A. Cabot, L. Yedra, S. Estradé, F. Peiró, et al. Learning from nature to improve the heat generation of iron-oxide

nanoparticles for magnetic hyperthermia applications. *Scientific Reports*, 3, 2013.

[125] S. Ruta, R. Chantrell, and O. Hovorka. Unified model of hyperthermia via hysteresis heating in systems of interacting magnetic nanoparticles. *Scientific Reports*, 5, 2015.

[126] S. Ota, T. Yamada, and Y. Takemura. Dipole-dipole interaction and its concentration dependence of magnetic fluid evaluated by alternating current hysteresis measurement. *Journal of Applied Physics*, 117(17): 17D713, 2015.

[127] K. Murase, M. Aoki, N. Banura, K. Nishimoto, A. Mimura, T. Kuboyabu, and I. Yabata. Usefulness of magnetic particle imaging for predicting the therapeutic effect of magnetic hyperthermia. *Open Journal of Medical Imaging*, 5(02):85, 2015.

[128] P. Debbage and W. Jaschke. Molecular imaging with nanoparticles: giant roles for dwarf actors. *Histochemistry and Cell Biology*, 130(5):845–875, 2008.

[129] C. P. Slichter. *Principles of magnetic resonance*, volume 1. Springer Science & Business Media, 2013.

[130] S. Laurent, C. Henoumont, D. Stanicki, S. Boutry, E. Lipani, S. Belaid, R. N. Muller, and L. Vander Elst. MRI contrast agents: from molecules to particles. *SpringerBriefs in applied sciences and technology, Nanotheranostics*, 2016.

[131] J. Huang, X. Zhong, L. Wang, L. Yang, and H. Mao. Improving the magnetic resonance imaging contrast and detection methods with engineered magnetic nanoparticles. *Theranostics*, 2(1):86–102, 2012.

[132] J. Estelrich, M. J. Sánchez-Martín, and M. A. Busquets. Nanoparticles in magnetic resonance imaging: from simple to dual contrast agents. *International journal of nanomedicine*, 10:1727, 2015.

[133] T.-H. Shin, Y. Choi, S. Kim, and J. Cheon. Recent advances in magnetic nanoparticle-based multi-modal imaging. *Chem. Soc. Rev.*, pages –, 2015.

[134] Y.-X. J. Wang. Superparamagnetic iron oxide based MRI contrast agents: current status of clinical application. *Quantitative imaging in medicine and surgery*, 1(1):35, 2011.

[135] L. Sandiford, A. Phinikaridou, A. Protti, L. K. Meszaros, X. Cui, Y. Yan, G. Frodsham, P. A. Williamson, N. Gaddum, R. M. Botnar, et al. Bisphosphonate-anchored PEGylation and radiolabeling of superparamagnetic iron oxide: long-circulating nanoparticles for in vivo multimodal (T1 MRI-SPECT) imaging. *Acs Nano*, 7(1):500–512, 2012.

[136] H.-Y. Lee, Z. Li, K. Chen, A. R. Hsu, C. Xu, J. Xie, S. Sun, and X. Chen. PET/MRI dual-modality tumor imaging using arginine-glycine-aspartic (RGD)–conjugated radiolabeled iron oxide nanoparticles. *Journal of Nuclear Medicine*, 49(8):1371–1379, 2008.

[137] E. S. Shibu, K. Ono, S. Sugino, A. Nishioka, A. Yasuda, Y. Shigeri, S.-i. Wakida, M. Sawada, and V. Biju. Photouncaging nanoparticles for MRI and fluorescence imaging in vitro and in vivo. *ACS nano*, 7(11):9851–9859, 2013.

[138] O. Girard, J. Du, L. Agemy, K. Sugahara, V. Kotamraju, E. Ruoslahti, G. Bydder, and R. Mattrey. Optimization of iron oxide nanoparticle detection using ultrashort echo time pulse sequences: Comparison of T1, T2*, and synergistic T1- T2* contrast mechanisms. *Magnetic resonance in medicine*, 65(6):1649–1660, 2011.

[139] M. A. Bernstein, J. Huston, and H. A. Ward. Imaging artifacts at 3.0 T. *Journal of Magnetic Resonance Imaging*, 24(4):735–746, 2006.

[140] M. Mehrmohammadi, J. Oh, S. Mallidi, and S. Y. Emelianov. Pulsed magneto-motive ultrasound imaging using ultrasmall magnetic nanoprobes. *Molecular imaging*, 10(2):102, 2011.

[141] M. Mehrmohammadi, T.-H. Shin, M. Qu, P. Kruizinga, R. L. Truby, J.-H. Lee, J. Cheon, and S. Y. Emelianov. In vivo pulsed magneto-motive ultrasound imaging using high-performance magnetoactive contrast nanoagents. *Nanoscale*, 5:11179–11186, 2013.

[142] M. Mehrmohammadi, M. Qu, L. L. Ma, D. K. Romanovicz, K. P. Johnston, K. V. Sokolov, and S. Y. Emelianov. Pulsed magneto-motive ultrasound imaging to detect intracellular accumulation of magnetic nanoparticles. *Nanotechnology*, 22(41):415105, 2011.

[143] G. Hu and B. He. Magnetoacoustic imaging of magnetic iron oxide nanoparticles embedded in biological tissues with microsecond magnetic stimulation. *Applied Physics Letters*, 100(1):013704, 2012.

[144] L. Mariappan, Q. Shao, C. Jiang, K. Yu, S. Ashkenazi, J. C. Bischof, and B. He. Magneto acoustic tomography with short pulsed magnetic field for in-vivo imaging of magnetic iron oxide nanoparticles. *Nanomedicine: Nanotechnology, Biology and Medicine*, 12(3):689 – 699, 2016.

[145] Y. Wang, X. Xie, X. Wang, G. Ku, K. L. Gill, D. P. O'Neal, G. Stoica, and L. V. Wang. Photoacoustic tomography of a nanoshell contrast agent in the in vivo rat brain. *Nano Letters*, 4(9):1689–1692, 2004.

[146] L. V. Wang and S. Hu. Photoacoustic tomography: in vivo imaging from organelles to organs. *Science*, 335(6075):1458–1462, 2012.

[147] Y. Jin, C. Jia, S.-W. Huang, M. O'Donnell, and X. Gao. Multifunctional nanoparticles as coupled contrast agents. *Nature communications*, 1:41, 2010.

[148] M. Qu, S. Mallidi, M. Mehrmohammadi, R. Truby, K. Homan, P. Joshi, Y.-S. Chen, K. Sokolov, and S. Emelianov. Magneto-photo-acoustic imaging. *Biomedical optics express*, 2(2):385–396, 2011.

[149] J. Li, B. Arnal, C.-W. Wei, J. Shang, T.-M. Nguyen, M. O'Donnell, and X. Gao. Magneto-optical nanoparticles for cyclic magnetomotive photoacoustic imaging. *ACS nano*, 9(2):1964–1976, 2015.

[150] B. Arnal, C.-W. Wei, J. Li, X. Gao, and M. O'Donnell. Highly sensitive magneto-motive photoacoustic and ultrasound (PAUS) imaging with cyclic excitations. *Journal of Optics*, 18(2):024009, 2016.

[151] R. John, R. Rezaeipoor, S. G. Adie, E. J. Chaney, A. L. Oldenburg, M. Marjanovic, J. P. Haldar, B. P. Sutton, and S. A. Boppart. In vivo magnetomotive optical molecular imaging using targeted magnetic nanoprobes. *Proceedings of the National Academy of Sciences*, 107(18):8085–8090, 2010.

[152] K. Bayer, H. Eckert, F. Wiekhorst, L. Trahms, M. Krause, and S. Odenbach. Magnetic nanoparticles in tumor xenografts detected and quantified by micro-computer tomography. *Biomedical Physics & Engineering Express*, 1(3):035002, 2015.

[153] O. M. Girard, L. de Rochefort, M. Poirier-Quinot, L. Darrasse, and R. F. Mattrey. Quantification strategies for MRI. *Molecular imaging techniques: new frontiers. London: Future Science Ltd*, pages 66–80, 2013.

[154] R. Kuhlpeter, H. Dahnke, L. Matuszewski, T. Persigehl, A. von Wallbrunn, T. Allkemper, W. L. Heindel, T. Schaeffter, and C. Bremer. R2 and R2* mapping for sensing cell-bound superparamagnetic nanoparticles: in vitro and murine in vivo testing. *Radiology*, 245(2):449–457, 2007.

[155] J. Zhang, H. L. Ring, K. R. Hurley, Q. Shao, C. S. Carlson, D. Idiyatullin, N. Manuchehrabadi, P. J. Hoopes, C. L. Haynes, J. C. Bischof, et al. Quantification and biodistribution of iron oxide nanoparticles in the primary clearance organs of mice using T1 contrast for heating. *Magnetic Resonance in Medicine*, 2016.

[156] U. Gneveckow, A. Jordan, R. Scholz, V. Brüss, N. Waldöfner, J. Ricke, A. Feussner, B. Hildebrandt, B. Rau, and P. Wust. Description and characterization of the novel hyperthermia - and thermoablation - system MFH® 300F for clinical magnetic fluid hyperthermia. *Medical Physics*, 31(6):1444–1451, 2004.

[157] N. L. Adolphi, K. S. Butler, D. M. Lovato, T. Tessier, J. E. Trujillo, H. J. Hathaway, D. L. Fegan, T. C. Monson, T. E. Stevens, D. L. Huber, et al. Imaging of Her2-targeted magnetic nanoparticles for breast cancer detection: comparison of SQUID-detected magnetic relaxometry and MRI. *Contrast Media & Molecular Imaging*, 7(3):308–319, 2012.

[158] J. Zhang, R. Chamberlain, M. Etheridge, D. Idiyatullin, C. Corum, J. Bischof, and M. Garwood. Quantifying iron-oxide nanoparticles at high concentration based on longitudinal relaxation using a three-dimensional SWIFT look-locker sequence. *Magnetic resonance in medicine*, 71(6):1982–1988, 2014.

[159] L. Wang, C. A. Corum, D. Idiyatullin, M. Garwood, and Q. Zhao. T1 estimation for aqueous iron oxide nanoparticle suspensions using a variable flip angle SWIFT sequence. *Magnetic Resonance in Medicine*, 70(2): 341–347, 2013.

[160] C. A. Gharagouzloo, P. N. McMahon, and S. Sridhar. Quantitative contrast-enhanced MRI with superparamagnetic nanoparticles using ultrashort time-to-echo pulse sequences. *Magnetic Resonance in Medicine*, 74(2):431–441, 2015.

[161] D. M. Grodzki, P. M. Jakob, and B. Heismann. Ultrashort echo time imaging using pointwise encoding time reduction with radial acquisition (PETRA). *Magnetic Resonance in Medicine*, 67(2):510–518, 2012.

[162] L. O. Sillerud. Quantitative [Fe]MRI of PSMA-targeted SPIONs specifically discriminates among prostate tumor cell types based on their PSMA expression levels. *International journal of nanomedicine*, 11:357, 2016.

[163] O. M. Girard, R. Ramirez, S. McCarty, and R. F. Mattrey. Toward absolute quantification of iron oxide nanoparticles as well as cell internalized fraction using multiparametric MRI. *Contrast Media & Molecular Imaging*, 7(4):411–417, 2012.

[164] F. Schweser, A. Deistung, B. W. Lehr, and J. R. Reichenbach. Quantitative imaging of intrinsic magnetic tissue properties using MRI signal phase: an approach to in vivo brain iron metabolism? *Neuroimage*, 54(4):2789–2807, 2011.

[165] P. H. Mills, T. K. Hitchens, L. M. Foley, T. Link, Q. Ye, C. R. Weiss, J. D. Thompson, W. D. Gilson, A. Arepally, J. A. Melick, P. M. Kochanek, C. Ho, J. W. M. Bulte, and E. T. Ahrens. Automated detection and characterization of SPIO-labeled cells and capsules using magnetic field perturbations. *Magnetic Resonance in Medicine*, 67(1):278–289, 2012.

[166] W. A. Kalender. *Computed tomography: fundamentals, system technology, image quality, applications*. John Wiley & Sons, 2011.

[167] A. L. Dias, R. Künzel, R. S. Levenhagen, and E. Okuno. Application of computed tomography images in the evaluation of magnetic nanoparticles biodistribution. *Journal of Magnetism and Magnetic Materials*, 322 (16):2405 – 2407, 2010.

[168] H. Rahn and S. Odenbach. X-ray microcomputed tomography as a tool for the investigation of the biodistribution of magnetic nanoparticles. *Nanomedicine*, 4(8):981–990, 2009.

[169] A. Attaluri, R. Ma, Y. Qiu, W. Li, and L. Zhu. Nanoparticle distribution and temperature elevations in prostatic tumours in mice during magnetic nanoparticle hyperthermia. *International Journal of Hyperthermia*, 27(5):491–502, 2011.

[170] A. LeBrun, N. Manuchehrabadi, A. Attaluri, F. Wang, R. Ma, and L. Zhu. MicroCT image-generated tumour geometry and sar distribution for tumour temperature elevation simulations in magnetic nanoparticle hyperthermia. *International Journal of Hyperthermia*, 29(8):730–738, 2013. PMID: 24074039.

[171] H. Rahn, S. Lyer, R. Tietze, H. Richter, C. Alexiou, D. Eberbeck, F. Wiekhorst, L. Trahms, F. Beckmann, and S. Odenbach. SRCT and MRX analysis of ferrofluid accumulation in bovine arteries: a step further in the understanding of magnetic drug targeting. *Physics Procedia*, 9:258–261, 2010.

[172] H. Rahn, C. Alexiou, L. Trahms, and S. Odenbach. 3-dimensional quantitative detection of nanoparticle content in biological tissue samples after local cancer treatment. *Journal of Magnetism and Magnetic Materials*, 360:92–97, 2014.

[173] M. Mehrmohammadi, J. Oh, L. Ma, E. Yantsen, T. Larson, S. Mallidi, S. Park, K. Johnston, K. Sokolov, T. Milner, et al. Imaging of iron oxide nanoparticles using magneto-motive ultrasound. In *Ultrasonics Symposium, 2007. IEEE*, pages 652–655. IEEE, 2007.

[174] M. Mehrmohammadi, K. Y. Yoon, M. Qu, K. P. Johnston, and S. Y. Emelianov. Enhanced pulsed magneto-motive ultrasound imaging using superparamagnetic nanoclusters. *Nanotechnology*, 22(4):045502, 2011.

[175] J. Weizenecker, J. Borgert, and B. Gleich. A simulation study on the resolution and sensitivity of magnetic particle imaging. *Physics in Medicine and Biology*, 52:6363–6374, 2007.

[176] B. Gleich, J. Weizenecker, and J. Borgert. Experimental results on fast 2D-encoded magnetic particle imaging. *Physics in Medicine and Biology*, 53(6):N81, 2008.

[177] K. Grafe, G. Bringout, M. Graeser, T. Sattel, and T. Buzug. System matrix recording and phantom measurements with a single-sided magnetic particle imaging device. *IEEE Transactions on Magnetics*, 51(2):1–3, 2015.

[178] J. Weaver. Perpendicular magnetic particle imaging, pMPI. *IEEE Transactions on Magnetics*, 51(2):1–4, 2015.

[179] T. Knopp, S. Biederer, T. Sattel, J. Weizenecker, B. Gleich, J. Borgert, and T. Buzug. Trajectory analysis for magnetic particle imaging. *Physics in Medicine and Biology*, 54(2):385, 2008.

[180] P. W. Goodwill, J. J. Konkle, B. Zheng, E. U. Saritas, and S. M. Conolly. Projection x-space magnetic particle imaging. *IEEE Transactions on Medical Imaging*, 31(5):1076–1085, 2012.

[181] J. J. Konkle, P. W. Goodwill, O. M. Carrasco-Zevallos, and S. M. Conolly. Projection reconstruction magnetic particle imaging. *IEEE Transactions on Medical Imaging*, 32(2):338–347, 2013.

[182] J. Rahmer, J. Weizenecker, B. Gleich, and J. Borgert. Signal encoding in magnetic particle imaging: properties of the system function. *BMC Medical Imaging*, 9(1):4, 2009.

[183] T. Knopp, T. F. Sattel, S. Biederer, J. Rahmer, J. Weizenecker, B. Gleich, J. Borgert, and T. M. Buzug. Model-based reconstruction for magnetic particle imaging. *IEEE Transactions on Medical Imaging*, 29(1):12–18, 2010.

[184] T. Knopp and A. Weber. Sparse reconstruction of the magnetic particle imaging system matrix. *IEEE Transactions on Medical Imaging*, 32(8): 1473–1480, 2013.

[185] A. Weber and T. Knopp. Reconstruction of the magnetic particle imaging system matrix using symmetries and compressed sensing. *Advances in Mathematical Physics*, 2015, 2015.

[186] A. Weber, J. Weizenecker, U. Heinen, M. Heidenreich, and T. Buzug. Reconstruction enhancement by denoising the magnetic particle imaging system matrix using frequency domain filter. *IEEE Transactions on Magnetics*, 51(2):1–5, 2015.

[187] P. W. Goodwill and S. M. Conolly. The x-space formulation of the magnetic particle imaging process: 1-D signal, resolution, bandwidth, SNR, SAR, and magnetostimulation. *IEEE Transactions on Medical Imaging*, 29 (11):1851–1859, 2010.

[188] P. W. Goodwill, A. Tamrazian, L. R. Croft, C. D. Lu, E. M. Johnson, R. Pidaparthi, R. M. Ferguson, A. P. Khandhar, K. M. Krishnan, and S. M. Conolly. Ferrohydrodynamic relaxometry for magnetic particle imaging. *Applied Physics Letters*, 98(26):262502, 2011.

[189] P. W. Goodwill, E. U. Saritas, L. R. Croft, T. N. Kim, K. M. Krishnan, D. V. Schaffer, and S. M. Conolly. X-space MPI: Magnetic nanoparticles for safe medical imaging. *Advanced Materials*, 24(28):3870–3877, 2012.

[190] A. Tateo, A. Iurino, G. Settanni, A. Andrisani, P. F. Stifanelli, P. Larizza, F. Mazzia, R. M. Mininni, S. Tangaro, and R. Bellotti. Hybrid x-space: a new approach for MPI reconstruction. *Physics in Medicine and Biology*, 61(11):4061, 2016.

[191] T. Hatsuda, T. Takagi, A. Matsuhisa, M. Arayama, H. Tsuchiya, S. Takahashi, and Y. Ishihara. Basic study of image reconstruction method using neural networks with additional learning for magnetic particle imaging. *International Journal on Magnetic Particle Imaging*, 2(2), 2016.

[192] L. M. Bauer, S. F. Situ, M. A. Griswold, and A. C. S. Samia. Magnetic particle imaging tracers: State-of-the-art and future directions. *J. Phys. Chem. Lett*, 6(13):2509–2517, 2015.

[193] S. Biederer, T. Knopp, T. Sattel, K. Lüdtke-Buzug, B. Gleich, J. Weizenecker, J. Borgert, and T. Buzug. Magnetization response spectroscopy of superparamagnetic nanoparticles for magnetic particle imaging. *Journal of Physics D: Applied Physics*, 42(20):205007, 2009.

[194] D. Eberbeck, F. Wiekhorst, S. Wagner, and L. Trahms. How the size distribution of magnetic nanoparticles determines their magnetic particle imaging performance. *Applied Physics Letters*, 98(18):182502, 2011.

[195] N. Löwa, P. Knappe, F. Wiekhorst, D. Eberbeck, A. Thunemann, and L. Trahms. How hydrodynamic fractionation influences MPI performance of resovist. *IEEE Transactions on Magnetics*, 51(2):1–4, 2015.

[196] J. Rahmer, A. Antonelli, C. Sfara, B. Tiemann, B. Gleich, M. Magnani, J. Weizenecker, and J. Borgert. Nanoparticle encapsulation in red blood cells enables blood-pool magnetic particle imaging hours after injection. *Physics in Medicine and Biology*, 58(12):3965, 2013.

[197] L. R. Croft, P. W. Goodwill, and S. M. Conolly. Relaxation in x-space magnetic particle imaging. *IEEE Transactions on Medical Imaging*, 31(12): 2335–2342, 2012.

[198] H. Mamiya and B. Jeyadevan. Nonequilibrium magnetic response of anisotropic superparamagnetic nanoparticles and possible artifacts in magnetic particle imaging. *PLoS ONE*, 10(3):e0118156, 2015.

[199] R. M. Ferguson, K. R. Minard, and K. M. Krishnan. Optimization of nanoparticle core size for magnetic particle imaging. *Journal of Magnetism and Magnetic Materials*, 321(10):1548 – 1551, 2009. Proceedings of the Seventh International Conference on the Scientific and Clinical Applications of Magnetic Carriers.

[200] R. M. Ferguson, K. R. Minard, A. P. Khandhar, and K. M. Krishnan. Optimizing magnetite nanoparticles for mass sensitivity in magnetic particle imaging. *Medical Physics*, 38(3):1619–1626, 2011.

[201] A. P. Khandhar, R. M. Ferguson, H. Arami, and K. M. Krishnan. Monodisperse magnetite nanoparticle tracers for in vivo magnetic particle imaging. *Biomaterials*, 34(15):3837 – 3845, 2013.

[202] F. Ludwig, H. Remmer, C. Kuhlmann, T. Wawrzik, H. Arami, R. M. Ferguson, and K. M. Krishnan. Self-consistent magnetic properties of magnetite tracers optimized for magnetic particle imaging measured by ac susceptometry, magnetorelaxometry and magnetic particle spectroscopy. *Journal of Magnetism and Magnetic Materials*, 360:169–173, 2014.

[203] H. Arami and K. M. Krishnan. Intracellular performance of tailored nanoparticle tracers in magnetic particle imaging. *Journal of Applied Physics*, 115(17):17B306, 2014.

[204] S. A. Shah, D. B. Reeves, R. M. Ferguson, J. B. Weaver, and K. M. Krishnan. Mixed brownian alignment and néel rotations in superparamagnetic iron oxide nanoparticle suspensions driven by an ac field. *Physical Review B*, 92(9):094438, 2015.

[205] R. M. Ferguson, A. P. Khandhar, C. Jonasson, J. Blomgren, C. Johansson, and K. M. Krishnan. Size-dependent relaxation properties of monodisperse magnetite nanoparticles measured over seven decades of fre-

quency by AC susceptometry. *IEEE Transactions on Magnetics*, 49(7): 3441–3444, 2013.

[206] R. M. Ferguson, A. P. Khandhar, S. J. Kemp, H. Arami, E. U. Saritas, L. R. Croft, J. Konkle, P. W. Goodwill, A. Halkola, J. Rahmer, J. Borgert, S. M. Conolly, and K. M. Krishnan. Magnetic particle imaging with tailored iron oxide nanoparticle tracers. *IEEE Transactions on Medical Imaging*, 34 (5):1077–1084, 2015.

[207] C. Kuhlmann, A. Khandhar, R. Ferguson, S. Kemp, T. Wawrzik, M. Schilling, K. Krishnan, and F. Ludwig. Drive-field frequency dependent MPI performance of single-core magnetite nanoparticle tracers. *IEEE Transactions on Magnetics*, 51(2):1–4, 2015.

[208] N. Gehrke, D. Heinke, D. Eberbeck, F. Ludwig, T. Wawrzik, C. Kuhlmann, and A. Briel. Magnetic characterization of clustered core magnetic nanoparticles for MPI. *IEEE Transactions on Magnetics*, 51(2): 1–4, 2015.

[209] T. Yoshida, Y. Matsugi, N. Tsujimura, T. Sasayama, K. Enpuku, T. Viereck, M. Schilling, and F. Ludwig. Effect of alignment of easy axes on dynamic magnetization of immobilized magnetic nanoparticles. *Journal of Magnetism and Magnetic Materials*, 427:162–167, 2017.

[210] R. Dhavalikar, D. Hensley, L. Maldonado-Camargo, L. Croft, S. Ceron, P. Goodwill, S. Conolly, and C. Rinaldi. Finite magnetic relaxation in x-space magnetic particle imaging: comparison of measurements and ferrohydrodynamic models. *Journal of Physics D: Applied Physics*, 49(30): 305002, 2016.

[211] K. Them, J. Salamon, P. Szwargulski, S. Sequeira, M. G. Kaul, C. Lange, H. Ittrich, and T. Knopp. Increasing the sensitivity for stem cell monitoring in system-function based magnetic particle imaging. *Physics in Medicine and Biology*, 61(9):3279, 2016.

[212] N. Löwa, M. Seidel, P. Radon, and F. Wiekhorst. Magnetic nanoparticles in different biological environments analyzed by magnetic particle spectroscopy. *Journal of Magnetism and Magnetic Materials*, 427:133–138, 2017.

[213] J. Gehrcke, M. Rückert, T. Kampf, W. Kullmann, P. Jakob, and V. Behr. Investigation of the magnetic particle imaging signals dependency on ferrofluid concentration. In *Magnetic nanoparticles: Particle science, imaging technology, and clinical application. Proceedings of the First International Workshop on Magnetic Particle Imaging, edited by Buzug TM, Borgert J., Knopp T., Biederer S., Sattel TF, Erbe M., and Lüdtke-Buzug K., Lübeck, Germany*, pages 73–78, 2010.

[214] T. Wawrzik, T. Yoshida, M. Schilling, and F. Ludwig. Debye-based frequency-domain magnetization model for magnetic nanoparticles in

magnetic particle spectroscopy. *IEEE Transactions on Magnetics*, 51(2): 1–4, 2015.

[215] A. M. Rauwerdink and J. B. Weaver. Measurement of molecular binding using the Brownian motion of magnetic nanoparticle probes. *Applied Physics Letters*, 96(3):033702, 2010.

[216] A. M. Rauwerdink and J. B. Weaver. Concurrent quantification of multiple nanoparticle bound states. *Medical Physics*, 38(3):1136–1140, 2011.

[217] J. B. Weaver, A. M. Rauwerdink, and E. W. Hansen. Magnetic nanoparticle temperature estimation. *Medical Physics*, 36(5):1822–1829, 2009.

[218] W. C. Poller, N. Löwa, F. Wiekhorst, M. Taupitz, S. Wagner, K. Möller, G. Baumann, V. Stangl, L. Trahms, and A. Ludwig. Magnetic particle spectroscopy reveals dynamic changes in the magnetic behavior of very small superparamagnetic iron oxide nanoparticles during cellular uptake and enables determination of cell-labeling efficacy. *Journal of Biomedical Nanotechnology*, 12(2):337–346, 2016.

[219] A. M. Rauwerdink, A. J. Giustini, and J. B. Weaver. Simultaneous quantification of multiple magnetic nanoparticles. *Nanotechnology*, 21(45): 455101, 2010.

[220] K. Murase, R. Song, and S. Hiratsuka. Magnetic particle imaging of blood coagulation. *Applied Physics Letters*, 104(25):252409, 2014.

[221] J. Rahmer, A. Halkola, B. Gleich, I. Schmale, and J. Borgert. First experimental evidence of the feasibility of multi-color magnetic particle imaging. *Physics in Medicine and Biology*, 60(5):1775, 2015.

[222] J. Haegele, S. Vaalma, N. Panagiotopoulos, J. Barkhausen, F. M. Vogt, J. Borgert, and J. Rahmer. Multi-color magnetic particle imaging for cardiovascular interventions. *Physics in Medicine and Biology*, 61(16):N415, 2016.

[223] T. Viereck, C. Kuhlmann, S. Draack, M. Schilling, and F. Ludwig. Dual-frequency magnetic particle imaging of the Brownian particle contribution. *Journal of Magnetism and Magnetic Materials*, 427:156–161, 2017.

[224] T. Kuboyabu, I. Yabata, M. Aoki, N. Banura, K. Nishimoto, A. Mimura, and K. Murase. Magnetic particle imaging for magnetic hyperthermia treatment: Visualization and quantification of the intratumoral distribution and temporal change of magnetic nanoparticles in vivo. *Open Journal of Medical Imaging*, 6(01):1, 2016.

[225] A. Ohki, T. Kuboyabu, M. Aoki, M. Yamawaki, and K. Murase. Quantitative evaluation of tumor response to combination of magnetic hyperthermia treatment and radiation therapy using magnetic particle imaging. *International Journal of Nanomedicine and Nanosurgery*, 2:1–6, 2016.

[226] L. M. Bauer, S. F. Situ, M. A. Griswold, and A. C. S. Samia. High-performance iron oxide nanoparticles for magnetic particle imaging–guided hyperthermia (hMPI). *Nanoscale*, 2016.

[227] T. Kuboyabu, A. Ohki, N. Banura, and K. Murase. Usefulness of magnetic particle imaging for monitoring the effect of magnetic targeting. *Open Journal of Medical Imaging*, 6(02):33, 2016.

[228] E. U. Saritas, P. W. Goodwill, L. R. Croft, J. J. Konkle, K. Lu, B. Zheng, and S. M. Conolly. Magnetic particle imaging (MPI) for NMR and MRI researchers. *Journal of Magnetic Resonance*, 229(0):116 – 126, 2013. Frontiers of In Vivo and Materials MRI Research.

[229] B. Zheng, T. Vazin, P. W. Goodwill, A. Conway, A. Verma, E. U. Saritas, D. Schaffer, and S. M. Conolly. Magnetic particle imaging tracks the long-term fate of in vivo neural cell implants with high image contrast. *Scientific Reports*, 5, 2015.

[230] J. Borgert, J. D. Schmidt, I. Schmale, C. Bontus, B. Gleich, B. David, J. Weizenecker, J. Jockram, C. Lauruschkat, O. Mende, et al. Perspectives on clinical magnetic particle imaging. *Biomedizinische Technik/Biomedical Engineering*, 58(6):551–556, 2013.

[231] P. Vogel, M. A. Rückert, P. Klauer, W. H. Kullmann, P. M. Jakob, and V. C. Behr. Traveling wave magnetic particle imaging. *IEEE Transactions on Medical Imaging*, 33(2):400–407, 2014.

[232] E. Saritas, P. Goodwill, G. Zhang, and S. Conolly. Magnetostimulation limits in magnetic particle imaging. *IEEE Transactions on Medical Imaging*, 32(9):1600–1610, 2013.

[233] T. Knopp, T. F. Sattel, and T. M. Buzug. Efficient magnetic gradient field generation with arbitrary axial displacement for magnetic particle imaging. *IEEE Magnetics Letters*, 3:6500104–6500104, 2012.

[234] C. Kaethner, M. Ahlborg, T. Knopp, T. F. Sattel, and T. M. Buzug. Efficient gradient field generation providing a multi-dimensional arbitrary shifted field-free point for magnetic particle imaging. *Journal of Applied Physics*, 115(4):044910, 2014.

[235] I. Schmale, J. Rahmer, B. Gleich, J. Kanzenbach, J. Schmidt, C. Bontus, O. Woywode, and J. Borgert. First phantom and in vivo MPI images with an extended field of view. In *SPIE Medical Imaging*, pages 796510–796510. International Society for Optics and Photonics, 2011.

[236] P. Vogel, M. A. Rückert, P. Klauer, W. H. Kullmann, P. M. Jakob, and V. C. Behr. First in vivo traveling wave magnetic particle imaging of a beating mouse heart. *Physics in Medicine and Biology*, 61(18):6620, 2016.

[237] T. Sasayama, Y. Tsujita, M. Morishita, M. Muta, T. Yoshida, and K. Enpuku. Three-dimensional magnetic nanoparticle imaging using small field gradient and multiple pickup coils. *Journal of Magnetism and Magnetic Materials*, 427:144–150, 2017.

[238] P. Fannin, B. Scaife, and S. Charles. The measurement of the frequency dependent susceptibility of magnetic colloids. *Journal of Magnetism and Magnetic Materials*, 72(1):95 – 108, 1988.

[239] S. H. Chung, A. Hoffmann, S. D. Bader, C. Liu, B. Kay, L. Makowski, and L. Chen. Biological sensors based on Brownian relaxation of magnetic nanoparticles. *Applied Physics Letters*, 85(14):2971–2973, 2004.

[240] C.-Y. Hong, C. C. Wu, Y. C. Chiu, S. Y. Yang, H. E. Horng, and H. C. Yang. Magnetic susceptibility reduction method for magnetically labeled immunoassay. *Applied Physics Letters*, 88(21):212512, 2006.

[241] F. Ludwig, E. Heim, and M. Schilling. Characterization of magnetic coreshell nanoparticles by fluxgate magnetorelaxometry, ac susceptibility, transmission electron microscopy and photon correlation spectroscopy - a comparative study. *Journal of Magnetism and Magnetic Materials*, 321(10):1644 – 1647, 2009. Proceedings of the Seventh International Conference on the Scientific and Clinical Applications of Magnetic Carriers.

[242] K. Enpuku, H. Watanabe, Y. Higuchi, T. Yoshida, H. Kuma, N. Hamasaki, M. Mitsunaga, H. Kanzaki, and A. Kandori. Characterization of magnetic markers for liquid-phase immunoassays using Brownian relaxation. *Japanese Journal of Applied Physics*, 51(2R):023002, 2012.

[243] K. Park, T. Harrah, E. B. Goldberg, R. P. Guertin, and S. Sonkusale. Multiplexed sensing based on Brownian relaxation of magnetic nanoparticles using a compact AC susceptometer. *Nanotechnology*, 22(8):085501, 2011.

[244] F. Öisjöen, J. F. Schneiderman, A. P. Astalan, A. Kalabukhov, C. Johansson, and D. Winkler. A new approach for bioassays based on frequency- and time-domain measurements of magnetic nanoparticles. *Biosensors and Bioelectronics*, 25(5):1008–1013, 2010.

[245] F. Ludwig, O. Kazakova, L. Fernandez Barquin, A. Fornara, L. Trahms, U. Steinhoff, P. Svedlindh, E. Wetterskog, Q. Pankhurst, P. Southern, et al. Magnetic, structural, and particle size analysis of single-and multicore magnetic nanoparticles. *IEEE Transactions on Magnetics*, 50(11):1–4, 2014.

[246] F. Ludwig, C. Balceris, T. Viereck, O. Posth, U. Steinhoff, H. Gavilan, R. Costo, L. Zeng, E. Olsson, C. Jonasson, and C. Johansson. Size analysis of single-core magnetic nanoparticles. *Journal of Magnetism and Magnetic Materials*, 427:19–24, 2017.

[247] A. P. Astalan, C. Jonasson, K. Petersson, J. Blomgren, D. Ilver, A. Krozer, and C. Johansson. Magnetic response of thermally blocked magnetic nanoparticles in a pulsed magnetic field. *Journal of Magnetism and Magnetic Materials*, 311(1):166–170, 2007.

[248] N. Sepulveda, I. Thomas, and J. P. Wikswo. Magnetic susceptibility tomography for three-dimensional imaging of diamagnetic and paramagnetic objects. *IEEE Transactions on Magnetics*, 30(6):5062–5069, 1994.

[249] B. W. Ficko, P. M. Nadar, and S. G. Diamond. Spectroscopic AC susceptibility imaging (sASI) of magnetic nanoparticles. *Journal of Magnetism and Magnetic Materials*, 375(0):164 – 176, 2015.

[250] B. W. Ficko, P. Giacometti, and S. G. Diamond. Nonlinear susceptibility magnitude imaging of magnetic nanoparticles. *Journal of Magnetism and Magnetic Materials*, 378(0):267 – 277, 2015.

[251] B. W. Ficko, P. Giacometti, and S. G. Diamond. Extended arrays for nonlinear susceptibility magnitude imaging. *Biomedical Engineering/Biomedizinische Technik*, 60(5):457–463, 2015.

[252] B. W. Ficko, C. NDong, P. Giacometti, K. E. Griswold, and S. G. Diamond. A feasibility study of nonlinear spectroscopic measurement of magnetic nanoparticles targeted to cancer cells. *IEEE Transactions on Biomedical Engineering*, 64(5):972–979, 2017.

[253] B. W. Ficko, M. Liebl, C. Knopke, M. Q. Phan, U. Steinhoff, F. Wiekhorst, and S. G. Diamond. Nonlinear spectroscopic characterization and volterra series inspired modeling of magnetic nanoparticles. *IEEE Transactions on Magnetics*, 53(2):1–12, 2017.

[254] J. Clarke and A. I. Braginski. *The SQUID handbook, vol 2: applications of SQUIDs and SQUID systems*. Wiley-VCH, New York, 2006.

[255] A. Coene, G. Crevecoeur, J. Leliaert, and L. Dupré. Toward 2D and 3D imaging of magnetic nanoparticles using EPR measurements. *Medical Physics*, 42(9):5007–5014, 2015.

[256] A. Coene, G. Crevecoeur, L. Dupré, and P. Vaes. Quantitative estimation of magnetic nanoparticle distributions in one dimension using low-frequency continuous wave electron paramagnetic resonance. *Journal of Physics D: Applied Physics*, 46(24):245002, 2013.

[257] M. Denoual, S. Saez, F. Kauffman, and C. Dolabdjian. Magnetorelaxometry using improved giant magnetoresistance magnetometer. *Sensors and Actuators A: Physical*, 159(2):184–188, 2010.

[258] F. Ludwig, S. Mäuselein, E. Heim, and M. Schilling. Magnetorelaxometry of magnetic nanoparticles in magnetically unshielded environment utilizing a differential fluxgate arrangement. *Review of Scientific Instruments*, 76:106102, 2005.

[259] J. Dieckhoff, M. Schilling, and F. Ludwig. Fluxgate based detection of magnetic nanoparticle dynamics in a rotating magnetic field. *Applied Physics Letters*, 99(11):112501, 2011.

[260] J. Clarke and A. I. Braginski. *The SQUID handbook: fundamentals and technology of SQUIDs and SQUID Systems, Volume I*. Wiley-VCH Verlag GmbH&Co, KGaA, Weinheim, 2004.

[261] N. L. Adolphi, D. L. Huber, H. C. Bryant, T. C. Monson, D. L. Fegan, J. Lim, J. E. Trujillo, T. E. Tessier, D. M. Lovato, K. S. Butler, et al. Characterization of single-core magnetite nanoparticles for magnetic imaging

by SQUID relaxometry. *Physics in Medicine and Biology*, 55(19):5985 – 6003, 2010.

[262] C. Johnson, N. L. Adolphi, K. L. Butler, D. M. Lovato, R. Larson, P. D. Schwindt, and E. R. Flynn. Magnetic relaxometry with an atomic magnetometer and SQUID sensors on targeted cancer cells. *Journal of Magnetism and Magnetic Materials*, 324(17):2613 – 2619, 2012.

[263] M. Liebl, U. Steinhoff, F. Wiekhorst, J. Haueisen, and L. Trahms. Quantitative imaging of magnetic nanoparticles by magnetorelaxometry with multiple excitation coils. *Physics in Medicine and Biology*, 59(21):6607–6620, 2014.

[264] D. Baumgarten, R. Eichardt, G. Crevecoeur, E. Supriyanto, and J. Haueisen. Magnetic nanoparticle imaging by random and maximum length sequences of inhomogeneous activation fields. In *Engineering in Medicine and Biology Society (EMBC), 2013 35th Annual International Conference of the IEEE*, pages 3258–3260. IEEE, 2013.

[265] R. Penrose. A generalized inverse for matrices. In *Mathematical proceedings of the Cambridge philosophical society*, volume 51, pages 406–413. Cambridge Univ Press, 1955.

[266] P. Hansen. The truncated SVD as a method for regularization. *BIT Numerical Mathematics*, 27(4):534–553, 1987.

[267] A. N. Tikhonov and V. Y. Arsenin. Solutions of ill-posed problems. 1977.

[268] P. C. Hansen. *The L-curve and its use in the numerical treatment of inverse problems*. IMM, Department of Mathematical Modelling, Technical Universityof Denmark, 1999.

[269] C. L. Lawson and R. J. Hanson. *Solving least squares problems*, volume 161. SIAM, 1974.

[270] M. Liebl, U. Steinhoff, F. Wiekhorst, A. Coene, J. Haueisen, and L. Trahms. Quantitative reconstruction of a magnetic nanoparticle distribution using a non-negativity constraint. *Biomedical Engineering/Biomedizinische Technik*, 58:2, 2013.

[271] S. Kaczmarz. Angenäherte auflösung von systemen linearer gleichungen. *Bulletin International de l'Academie Polonaise des Sciences et des Lettres*, 35:355–357, 1937.

[272] D. Baumgarten, F. Braune, E. Supriyanto, and J. Haueisen. Plane-wise sensitivity based inhomogeneous excitation fields for magnetorelaxometry imaging of magnetic nanoparticles. *Journal of Magnetism and Magnetic Materials*, 380:255–260, 2015.

[273] M. Brustolon and G. Giamello. *Electron paramagnetic resonance: a practitioner's toolkit*. John Wiley & Sons Inc, 2009.

[274] J. Weil and J. Bolton. *Electron paramagnetic resonance: elementary theory and practical applications*. Wiley, 2007.

[275] S. Misra. *Multifrequency Electron Paramagnetic Resonance: Theory and Applications*. Wiley-VCH, 2011.

[276] E. Zavoisky. Spin-magnetic resonance in paramagnetics. *J Phys USSR*, 9:211–245, 1945.

[277] F. Bloch. Nuclear induction. *Physical review*, 70(7-8):460, 1946.

[278] B. Gallez and H. Swartz. *In vivo* EPR: when, how and why? *NMR in Biomedicine*, 17(5):223–225, 2004.

[279] P. Danhier and B. Gallez. Electron paramagnetic resonance: a powerful tool to support magnetic resonance imaging research. *Contrast Media & Molecular Imaging*, 10(4):266–281, 2015.

[280] S. Subramanian, K. Matsumoto, J. Mitchell, and M. Krishna. Radio frequency continuous-wave and time-domain EPR imaging and overhauser-enhanced magnetic resonance imaging of small animals: instrumental developments and comparison of relative merits for functional imaging. *NMR in Biomedicine*, 17(5):263–294, 2004.

[281] K. A. Radermacher, S. Boutry, S. Laurent, L. V. Elst, I. Mahieu, C. Bouzin, J. Magat, V. Gregoire, O. Feron, R. N. Muller, B. F. Jordan, and B. Gallez. Iron oxide particles covered with hexapeptides targeted at phosphatidylserine as MR biomarkers of tumor cell death. *Contrast Media & Molecular Imaging*, 5(5):258–267, 2010.

[282] H. Yasui, S. Matsumoto, N. Devasahayam, J. P. Munasinghe, R. Choudhuri, K. Saito, S. Subramanian, J. B. Mitchell, and M. C. Krishna. Low-field magnetic resonance imaging to visualize chronic and cycling hypoxia in tumor-bearing mice. *Cancer Research*, 70(16):6427–6436, 2010.

[283] C. Berthier, L. P. Levy, and G. Martinez. *High Magnetic Fields: Applications in Condensed Matter Physics and Spectroscopy*, volume 595. Springer, 2008.

[284] S. Subramanian, N. Devasahayam, S. Matsumoto, K. Saito, J. Mitchell, and M. Krishna. Echo-based single point imaging (ESPI): A novel pulsed EPR imaging modality for high spatial resolution and quantitative oximetry. *Journal of Magnetic Resonance*, 218:105–114, 2012.

[285] S. Subramanian and M. C. Krishna. Dancing with the electrons: Time-domain and CW in vivo EPR imaging. *Magnetic Resonance Insights*, 2: 43–74, 2008.

[286] K. Yamada, R. Murugesan, N. Devasahayam, J. Cook, J. Mitchell, S. Subramanian, and M. Krishna. Evaluation and comparison of pulsed and continuous wave radiofrequency electron paramagnetic resonance techniques for in vivo detection and imaging of free radicals. *Journal of Magnetic Resonance*, 154(2):287–297, 2002.

[287] M. C. Krishna, S. Matsumoto, H. Yasui, K. Saito, N. Devasahayam, S. Subramanian, and J. B. Mitchell. Electron paramagnetic resonance imaging of tumor pO_2. *Radiation Research*, 177(4):376–386, 2012.

[288] H. Swartz, N. Khan, J. Buckey, R. Comi, L. Gould, O. Grinberg, A. Hartford, H. Hopf, H. Hou, E. Hug, et al. Clinical applications of EPR: overview and perspectives. *NMR in Biomedicine*, 17(5):335–351, 2004.

[289] H. M. Swartz, B. B. Williams, B. I. Zaki, A. C. Hartford, L. A. Jarvis, E. Y. Chen, R. J. Comi, M. S. Ernstoff, H. Hou, N. Khan, et al. Clinical EPR: unique opportunities and some challenges. *Academic Radiology*, 21(2): 197–206, 2014.

[290] R. Ahmad and P. Kuppusamy. Theory, instrumentation, and applications of electron paramagnetic resonance oximetry. *Chemical Reviews*, 110(5):3212–3236, 2010.

[291] C. M. Desmet, A. Lafosse, S. Vériter, P. E. Porporato, P. Sonveaux, D. Dufrane, P. Levêque, and B. Gallez. Application of electron paramagnetic resonance (EPR) oximetry to monitor oxygen in wounds in diabetic models. *PLoS ONE*, 10(12):e0144914, 2015.

[292] H. M. Swartz, G. Burke, M. Coey, E. Demidenko, R. Dong, O. Grinberg, J. Hilton, A. Iwasaki, P. Lesniewski, M. Kmiec, et al. In vivo EPR for dosimetry. *Radiation Measurements*, 42(6):1075–1084, 2007.

[293] A. Iannone, M. Federico, A. Tomasi, R. L. Magin, A. Casasco, and V. Vannini. Detection and quantitation in rat tissues of the superparamagnetic magnetic resonance contrast agent dextran magnetite as demonstrated by electron spin resonance spectroscopy. *Investigative Radiology*, 27(6): 450–455, 1992.

[294] L. Gamarra, W. M. Pontuschka, E. Amaro, A. daCosta Filho, G. Brito, E. Vieira, S. Carneiro, D. Escriba, A. Falleiros, and V. Salvador. Kinetics of elimination and distribution in blood and liver of biocompatible ferrofluids based on $Fe_3\,O_4$ nanoparticles: An EPR and XRF study. *Materials Science and Engineering: C*, 28(4):519–525, 2008.

[295] B. Chertok, A. J. Cole, A. E. David, and V. C. Yang. Comparison of electron spin resonance spectroscopy and inductively-coupled plasma optical emission spectroscopy for biodistribution analysis of iron-oxide nanoparticles. *Molecular Pharmaceutics*, 7(2):375–385, 2010.

[296] L. Gamarra, A. daCosta Filho, and J. Mamani. Ferromagnetic resonance for the quantification of superparamagnetic iron oxide nanoparticles in biological materials. *International Journal of Nanomedicine*, 5(1):203–211, 2010.

[297] P. Danhier, G. De Preter, J. Magat, Q. Godechal, P. E. Porporato, B. F. Jordan, O. Feron, P. Sonveaux, and B. Gallez. Multimodal cell tracking of a spontaneous metastasis model: comparison between MRI, electron paramagnetic resonance and bioluminescence. *Contrast Media & Molecular Imaging*, 9(2):143–153, 2014.

[298] M. Levy, N. Luciani, D. Alloyeau, D. Elgrabli, V. Deveaux, C. Pechoux, S. Chat, G. Wang, N. Vats, F. Gendron, C. Factor, S. Lotersztajn, A. Lu-

ciani, C. Wilhelm, and F. Gazeau. Long term in vivo biotransformation of iron oxide nanoparticles. *Biomaterials*, 32(16):3988 – 3999, 2011.

[299] C. Wilhelm, F. Gazeau, and J.-C. Bacri. Magnetophoresis and ferromagnetic resonance of magnetically labeled cells. *European Biophysics Journal*, 31(2):118–125, 2002.

[300] P. Danhier, G. De Preter, S. Boutry, I. Mahieu, P. Levêque, J. Magat, V. Haufroid, P. Sonveaux, C. Bouzin, O. Feron, et al. Electron paramagnetic resonance as a sensitive tool to assess the iron oxide content in cells for MRI cell labeling studies. *Contrast Media & Molecular Imaging*, 7 (3):302–307, 2012.

[301] P. Danhier, J. Magat, P. Levêque, G. De Preter, P. E. Porporato, C. Bouzin, B. F. Jordan, G. Demeur, V. Haufroid, O. Feron, et al. In vivo visualization and ex vivo quantification of murine breast cancer cells in the mouse brain using MRI cell tracking and electron paramagnetic resonance. *NMR in Biomedicine*, 28(3):367–375, 2015.

[302] H. Fujii, K. Yoshikawa, and L. J. Berliner. In vivo fate of superparamagnetic iron oxides during sepsis. *Magnetic Resonance Imaging*, 20(3): 271–276, 2002.

[303] K. A. Radermacher, N. Beghein, S. Boutry, S. Laurent, L. Vander Elst, R. N. Muller, B. F. Jordan, and B. Gallez. In vivo detection of inflammation using pegylated iron oxide particles targeted at E-selectin: a multimodal approach using MR imaging and EPR spectroscopy. *Investigative Radiology*, 44(7):398–404, 2009.

[304] P. Vaes and S. Teughels. Pulsed EPR detection, 2011.

[305] P. Duraiswamy. *Data Acquisition and Digital Signal Processing for Electron Paramagnetic Resonance Spectrometers*. PhD thesis, Ugent, 2013.

[306] X. Li, G. Torfs, S. Teughels, and J. Bauwelinck. First demonstration of RF pulse pEPR detection system for SPIO nanoparticles. *Electronics Letters*, 51(19):1486–1488, 2015.

[307] G. Eaton, S. Eaton, and D. Barr. *Quantitative EPR*. Springer Verlag Wien, 2010.

[308] O. L. Gobbo, F. Wetterling, P. Vaes, S. Teughels, F. Markos, D. Edge, C. M. Shortt, K. Crosbie-Staunton, M. W. Radomski, Y. Volkov, et al. Biodistribution and pharmacokinetic studies of SPION using particle electron paramagnetic resonance, MRI and ICP-MS. *Nanomedicine*, 10(11):1751–1760, 2015.

[309] D. Edge, C. M. Shortt, O. L. Gobbo, S. Teughels, A. Prina-Mello, Y. Volkov, P. MacEneaney, M. W. Radomski, and F. Markos. Pharmacokinetics and bio-distribution of novel super paramagnetic iron oxide nanoparticles (SPIONs) in the anaesthetized pig. *Clinical and Experimental Pharmacology and Physiology*, 43(3):319–326, 2016.

[310] G. Crevecoeur, A. Coene, L. Dupré, and P. Vaes. Methods and systems for determining a particle distribution by means of electron paramagnetic resonance data, 2014. WO Patent App. PCT/EP2013/070,136.

[311] A. Coene, G. Crevecoeur, and L. Dupré. Robustness assessment of 1-D electron paramagnetic resonance for improved magnetic nanoparticle reconstructions. *IEEE Transactions on Biomedical Engineering*, 62(6):1635–1643, 2015.

[312] A. Coene, G. Crevecoeur, and L. Dupré. Magnetic nanoparticle imaging using multiple electron paramagnetic resonance activation sequences. *Journal of Applied Physics*, 117(17):17D105, 2015.

[313] B. Mandelbrot and J. Van Ness. Fractional Brownian motions, fractional noises and applications. *SIAM Review*, 10(4):422–437, 1968.

[314] H. Matz, D. Drung, S. Hartwig, H. Gro, R. Kötitz, W. Mller, A. Vass, W. Weitschies, and L. Trahms. A SQUID measurement system for immunoassays. *Applied Superconductivity*, 6(1012):577 – 583, 1999.

[315] F. Ludwig, E. Heim, S. Mäuselein, D. Eberbeck, and M. Schilling. Magnetorelaxometry of magnetic nanoparticles with fluxgate magnetometers for the analysis of biological targets. *Journal of Magnetism and Magnetic Materials*, 293(1):690–695, 2005.

[316] V. Dolgovskiy, V. Lebedev, S. Colombo, A. Weis, B. Michen, L. Ackermann-Hirschi, and A. Petri-Fink. A quantitative study of particle size effects in the magnetorelaxometry of magnetic nanoparticles using atomic magnetometry. *Journal of Magnetism and Magnetic Materials*, 379:137 – 150, 2015.

[317] E. Romanus, D. Berkov, S. Prass, C. Groß, W. Weitschies, and P. Weber. Determination of energy barrier distributions of magnetic nanoparticles by temperature dependent magnetorelaxometry. *Nanotechnology*, 14(12): 1251, 2003.

[318] D. Eberbeck, M. Kettering, C. Bergemann, P. Zirpel, I. Hilger, and L. Trahms. Quantification of the aggregation of magnetic nanoparticles with different polymeric coatings in cell culture medium. *Journal of Physics D: Applied Physics*, 43(40):405002, 2010.

[319] S. Sarangi, I. C. Tan, and A. Brazdeikis. Magnetic imaging method based on magnetic relaxation of magnetic nanoparticles. *Journal of Applied Physics*, 105(9):093926, 2009.

[320] R. Eichardt and J. Haueisen. Influence of sensor variations on the condition of the magnetostatic linear inverse problem. *IEEE Transactions on Magnetics*, 46(8):3449–3452, 2010.

[321] N. K. Hoo, M. Klemm, E. Supriyanto, and D. Baumgarten. Effects of excitation coil configurations in magnetorelaxometry imaging of magnetic nanoparticles. In *2014 IEEE Conference on Biomedical Engineering and Sciences (IECBES)*, pages 715–718, 2014.

[322] M.-X. Huang, B. Anderson, C. W. Huang, G. J. Kunde, E. C. Vreeland, J. W. Huang, A. N. Matlashov, T. Karaulanov, C. P. Nettles, A. Gomez, K. Minser, C. Weldon, G. Paciotti, M. Harsh, R. R. Lee, and E. R. Flynn. Development of advanced signal processing and source imaging methods for superparamagnetic relaxometry. *Physics in Medicine and Biology*, 62(3):734, 2017.

[323] L. P. De Haro, T. Karaulanov, E. C. Vreeland, B. Anderson, H. J. Hathaway, D. L. Huber, A. N. Matlashov, C. P. Nettles, A. D. Price, T. C. Monson, et al. Magnetic relaxometry as applied to sensitive cancer detection and localization. *Biomedical Engineering/Biomedizinische Technik*, 60 (5):445–455, 2015.

[324] J. Bork, H. Hahlbohm, R. Klein, and A. Schnabel. The 8-layered magnetically shielded room of the PTB: Design and construction. In *Biomag2000, Proc. 12th Int. Conf. on Biomagnetism*, pages 970–73. Espoo, Finland, 2001.

[325] A. Schnabel, M. Burghoff, S. Hartwig, F. Petsche, U. Steinhoff, D. Drung, and H. Koch. A sensor configuration for a 304 SQUID vector magnetometer. *Neurology & Clinical Neurophysiology*, 2004:70, 2004.

[326] R. Chantrell, S. Hoon, and B. Tanner. Time-dependent magnetization in fine-particle ferromagnetic systems. *Journal of Magnetism and Magnetic Materials*, 38(2):133 – 141, 1983.

[327] D. Berkov and R. Kötitz. Irreversible relaxation behaviour of a general class of magnetic systems. *Journal of Physics in Condensed Matter*, 8:1257–1266, 1996.

[328] R. Kötitz, W. Weitschies, L. Trahms, W. Brewer, and W. Semmler. Determination of the binding reaction between avidin and biotin by relaxation measurements of magnetic nanoparticles. *Journal of Magnetism and Magnetic Materials*, 194(13):62 – 68, 1999.

[329] F. Wiekhorst, W. Haberkorn, U. Steinhoff, S. Lyer, C. Alexiou, M. Bär, and L. Trahms. Principal moments of a multipole expansion to quantify the magnetic nanoparticle distributions in arteries. *Biomedical Engineering/Biomedizinische Technik*, 57(SI-1 Track-M):751–754, 2012.

[330] M. Liebl, F. Wiekhorst, D. Eberbeck, P. Radon, D. Gutkelch, D. Baumgarten, U. Steinhoff, and L. Trahms. Magnetorelaxometry procedures for quantitative imaging and characterization of magnetic nanoparticles in biomedical applications. *Biomedical Engineering/Biomedizinische Technik*, 60(5):427–443, 2015.

[331] J. Lange, R. Kötitz, A. Haller, L. Trahms, W. Semmler, and W. Weitschies. Magnetorelaxometry - a new binding specific detection method based on magnetic nanoparticles. *Journal of Magnetism and Magnetic Materials*, 252:381–383, 2002.

[332] H. Grossman, W. Myers, V. Vreeland, R. Bruehl, M. Alper, C. Bertozzi, and J. Clarke. Detection of bacteria in suspension by using a supercon-

ducting quantum interference device. *Proceedings of the National Academy of Sciences*, 101(1):129–134, 2004.

[333] D. Eberbeck, C. Bergemann, S. Hartwig, U. Steinhoff, and L. Trahms. Binding kinetics of magnetic nanoparticles on latex beads and yeast cells studied by magnetorelaxometry. *Journal of Magnetism and Magnetic Materials*, 289(0):435 – 438, 2005. Proceedings of the 10th International Conference on Magnetic Fluids.

[334] D. Eberbeck, F. Wiekhorst, U. Steinhoff, K. O. Schwarz, A. Kummrow, M. Kammel, J. Neukammer, and L. Trahms. Specific binding of magnetic nanoparticle probes to platelets in whole blood detected by magnetorelaxometry. *Journal of Magnetism and Magnetic Materials*, 321(10): 1617 – 1620, 2009. Proceedings of the Seventh International Conference on the Scientific and Clinical Applications of Magnetic Carriers.

[335] D. Eberbeck, F. Wiekhorst, U. Steinhoff, and L. Trahms. Quantification of biomolecule agglutination by magnetorelaxometry. *Applied Physics Letters*, 95(21):213701, 2009.

[336] F. Ludwig, E. Heim, D. Menzel, and M. Schilling. Investigation of superparamagnetic Fe_3O_4 nanoparticles by fluxgate magnetorelaxometry for use in magnetic relaxation immunoassays. *Journal of Applied Physics*, 99(8):08P106, 2006.

[337] N. L. Adolphi, D. L. Huber, J. E. Jaetao, H. C. Bryant, D. M. Lovato, D. L. Fegan, E. L. Venturini, T. C. Monson, T. E. Tessier, H. J. Hathaway, C. Bergemann, R. S. Larson, and E. R. Flynn. Characterization of magnetite nanoparticles for SQUID-relaxometry and magnetic needle biopsy. *Journal of Magnetism and Magnetic Materials*, 321(10):1459 – 1464, 2009. Proceedings of the Seventh International Conference on the Scientific and Clinical Applications of Magnetic Carriers.

[338] P. Radon, M. Liebl, N. Pompner, M. Stapf, F. Wiekhorst, K. Gitter, I. Hilger, S. Odenbach, and L. Trahms. Magnetic particle spectroscopy to determine the magnetic drug targeting efficiency of different magnetic nanoparticles in a flow phantom. *IEEE Transactions on Magnetics*, 51(2): 1–4, 2015.

[339] P. Dames, B. Gleich, A. Flemmer, K. Hajek, N. Seidl, F. Wiekhorst, D. Eberbeck, I. Bittmann, C. Bergemann, T. Weyh, et al. Targeted delivery of magnetic aerosol droplets to the lung. *Nature Nanotechnology*, 2 (8):495–499, 2007.

[340] C. Seliger, R. Jurgons, F. Wiekhorst, D. Eberbeck, L. Trahms, H. Iro, and C. Alexiou. In vitro investigation of the behaviour of magnetic particles by a circulating artery model. *Journal of Magnetism and Magnetic Materials*, 311(1):358–362, 2007.

[341] H. Richter, F. Wiekhorst, K. Schwarz, S. Lyer, R. Tietze, C. Alexiou, and L. Trahms. Magnetorelaxometric quantification of magnetic nanoparti-

cles in an artery model after ex vivo magnetic drug targeting. *Physics in Medicine and Biology*, 54(18):N417, 2009.

[342] E. R. Flynn, H. Bryant, C. Bergemann, R. S. Larson, D. Lovato, and D. A. Sergatskov. Use of a SQUID array to detect T-cells with magnetic nanoparticles in determining transplant rejection. *Journal of Magnetism and Magnetic Materials*, 311(1):429 – 435, 2007. Proceedings of the Sixth International Conference on the Scientific and Clinical Applications of Magnetic Carriers SCAMC-06.

[343] J. E. Jaetao, K. S. Butler, N. L. Adolphi, D. M. Lovato, H. C. Bryant, I. Rabinowitz, S. S. Winter, T. E. Tessier, H. J. Hathaway, C. Bergemann, E. R. Flynn, and R. S. Larson. Enhanced leukemia cell detection using a novel magnetic needle and nanoparticles. *Cancer Research*, 69(21):8310–8316, 2009.

[344] H. J. Hathaway, K. S. Butler, N. L. Adolphi, D. M. Lovato, R. Belfon, D. Fegan, T. C. Monson, J. E. Trujillo, T. E. Tessier, H. C. Bryant, D. L. Huber, R. S. Larson, and E. R. Flynn. Detection of breast cancer cells using targeted magnetic nanoparticles and ultra-sensitive magnetic field sensors. *Breast Cancer Research*, 13(5):R108, 2011.

[345] R. Jurgons, C. Seliger, A. Hilpert, L. Trahms, S. Odenbach, and C. Alexiou. Drug loaded magnetic nanoparticles for cancer therapy. *Journal of Physics: Condensed Matter*, 18(38):S2893, 2006.

[346] H. Richter, M. Kettering, F. Wiekhorst, U. Steinhoff, I. Hilger, and L. Trahms. Magnetorelaxometry for localization and quantification of magnetic nanoparticles for thermal ablation studies. *Physics in Medicine and Biology*, 55:623–633, 2010.

[347] M. Kettering, H. Richter, F. Wiekhorst, S. Bremer-Streck, L. Trahms, W. A. Kaiser, and I. Hilger. Minimal-invasive magnetic heating of tumors does not alter intra-tumoral nanoparticle accumulation, allowing for repeated therapy sessions: an in vivo study in mice. *Nanotechnology*, 22(50):505102, 2011.

[348] A. Coene, G. Crevecoeur, and L. Dupré. Adaptive control of excitation coil arrays for targeted magnetic nanoparticle reconstruction using magnetorelaxometry. *IEEE Transactions on Magnetics*, 48:2842 – 2845, 2012.

[349] A. Coene, G. Crevecoeur, M. Liebl, F. Wiekhorst, L. Dupré, and U. Steinhoff. Uncertainty of reconstructions of spatially distributed magnetic nanoparticles under realistic noise conditions. *Journal of Applied Physics*, 115(17):17B509, 2014.

[350] S. Baillet, L. Garnero, G. Marin, and J.-P. Hugonin. Combined MEG and EEG source imaging by minimization of mutual information. *IEEE Transactions on Biomedical Engineering*, 46(5):522–534, 1999.

[351] A. Coene, J. Leliaert, L. Dupré, and G. Crevecoeur. Quantitative model selection for enhanced magnetic nanoparticle imaging in magnetorelaxometry. *Medical Physics*, 42(12):6853–6862, 2015.

[352] C. E. Shannon. A mathematical theory of communication. *The Bell System Technical Journal*, 27:379423, 1948.

[353] M. A. Miller, S. Gadde, C. Pfirschke, C. Engblom, M. M. Sprachman, R. H. Kohler, K. S. Yang, A. M. Laughney, G. Wojtkiewicz, N. Kamaly, et al. Predicting therapeutic nanomedicine efficacy using a companion magnetic resonance imaging nanoparticle. *Science Translational Medicine*, 7(314):314ra183–314ra183, 2015.

[354] A. Coene, J. Leliaert, M. Liebl, N. Löwa, U. Steinhoff, G. Crevecoeur, L. Dupré, and F. Wiekhorst. Multi-color magnetic nanoparticle imaging using magnetorelaxometry. *Physics in Medicine and Biology*, 62(8):3139, 2017.

[355] A. Coene, J. Leliaert, G. Crevecoeur, and L. Dupré. Sensor fusion of electron paramagnetic resonance and magnetorelaxometry data for quantitative magnetic nanoparticle imaging. *Journal of Physics D: Applied Physics*, 50(8):085008, 2017.

[356] F. Wiekhorst, M. Liebl, U. Steinhoff, L. Trahms, S. Lyer, S. Dürr, and C. Alexiou. Magnetorelaxometry for in-vivo quantification of magnetic nanoparticle distributions after magnetic drug targeting in a rabbit carcinoma model. In T. M. Buzug and J. Borgert, editors, *Magnetic Particle Imaging*, volume 140 of *Springer Proceedings in Physics*, pages 301–305. Springer Berlin Heidelberg, 2012.

[357] J. Leliaert, D. Schmidt, O. Posth, M. Liebl, D. Eberbeck, A. Coene, U. Steinhoff, F. Wiekhorst, B. V. Waeyenberge, and L. Dupré. Interpreting the magnetorelaxometry signal of suspended magnetic nanoparticles with kaczmarz' algorithm. 50(19), 2017.

[358] S. Colombo, V. Lebedev, A. Tonyushkin, Z. D. Grujic, V. Dolgovskiy, and A. Weis. Towards a mechanical MPI scanner based on atomic magnetometry. *arXiv preprint arXiv:1611.09047*, 2016.

[359] R. Eichardt, D. Baumgarten, L. Di Rienzo, S. Linzen, V. Schultze, and J. Haueisen. Localisation of buried ferromagnetic objects based on minimum-norm-estimations: A simulation study. *COMPEL: The International Journal for Computation and Mathematics in Electrical and Electronic Engineering*, 28(5):1327–1337, 2009.

[360] S. C. Tang and I. M. Lo. Magnetic nanoparticles: essential factors for sustainable environmental applications. *Water research*, 47(8):2613–2632, 2013.

[361] C. Toumey. Quick lessons on environmental nanotech. *Nature Nanotechnology*, 10(7):566–567, 2015.